Force Tracking of Hydraulic Manipulators Within an Impedance Control Framework

by

Amir Ali Akbar Khayyat

A thesis
presented to the University of Manitoba
in fulfillment of the
thesis requirement for the degree of
Doctor of Philosophy
in
Mechanical & Industrial Engineering

Winnipeg, Manitoba, Canada, 2000

THE UNIVERSITY OF MANITOBA

FACULTY OF GRADUATE STUDIES

*****

COPYRIGHT PERMISSION PAGE

Force Tracking of Hydraulic Manipulators within an Impedance Control Framework

BY

Amir Ali Akbar Khayyat

A Thesis/Practicum submitted to the Faculty of Graduate Studies of The University of Manitoba in partial fulfillment of the requirements of the degree

of

Doctor of Philosophy

Abstract

The objective of this thesis is to develop, implement and analyze the performance of force control algorithms as applied to hydraulic manipulators. This work, which comprises both experimental and simulation studies, is built upon the concept of impedance control technique; this technique accommodates stable transition between unconstrained and constrained motions. Position-based formulation of impedance control is employed here because of the difficulty in implementing controlled torques on hydraulic actuators. First, a nonlinear proportional-integral position controller is developed. It is shown that the controller accurately tracks position trajectories to within 0.2° of error, and regulates static trajectories to within 0.05° on a Unimate MK-II hydraulic manipulator. The controller has these capabilities despite large manipulator inertia, joint stiction, valve deadband and other nonlinearities. The positioner is then used to implement the position-based impedance controller (PBIC) to the manipulator. Various tests are performed to show that the PBIC can successfully replace the actual manipulator dynamics with those of the target impedance. Regulation of the end-effector force, however, cannot be achieved using the PBIC alone. Various available methods that potentially enable a PBIC to regulate the force are identified, studied, and modified as required. They are then applied, for the first time, to the hydraulic manipulator to improve the force control capability of the PBIC. The improvements thus made are twofold: through estimation of environmental parameters and through modification of the position reference. Accurate estimation of the environmental parameters is shown to be possible through an off-line identification procedure. The on-line identification method, which is built upon minimization of the force prediction error, gives estimates that do not

truly reflect the nature of the environment. The combination of these estimates, however, can modify the position reference toward accurate force regulation. It is also shown that the estimation part can be avoided by directly modifying the position reference to minimize the force error.

Acknowledgements

Completing a Ph.D. program of study in general and a doctoral dissertation in particular, in a society other than my society of origin, and in a language other than my mother tongue was not something I could have done without a high degree of motivation and enormous support. Various people and agencies have helped me make it possible.

I would first like to thank the members of my dissertation committee, Dr. Steve Onyshko and Dr. David Strong, for the careful reading of my thesis and useful comments. In addition, I am grateful to Dr. Abdie Kazemipur, Mr. Rob Rostecki and Mr. Navid Niksefat for proofreading this manuscript. I am also thankful to Mr. Al Lohse who provided technical assistance during the control implementation and experiments on the Unimate hydraulic manipulator throughout the course of this research.

Above all, however, I would like to express my special gratitude to my advisor, Dr. Nariman Sepehri, who was a great source of inspiration for me, with his hard-working, caring personality and academic knowledge.

The scholarship, provided by the Iranian Ministry of Culture and Higher Education, the grant provided by Manitoba Hydro, and the fellowship awarded by the University of Manitoba were instrumental in the success of my studies.

I wish to thank my beloved parents for their sacrifices, encouragement, and for always being supportive of my decisions.

Finally, I reserve my warmest gratitude for the support, kindness and patience of my dearest wife, Azar.

Table of Contents

Chapter 4

Chapter 5

List of Figures

Chapter 1

Introduction

1.1 Preliminary Remarks

The field of robotic manipulation has been growing rapidly over the past two decades. Industry has successfully adopted many robots which can be generally attributed to two modes of operation. The first one involves unconstrained motion in space, in which it is sufficient for the manipulator to track a trajectory in space. The second involves motion that is constrained through contact with the environment*. Examples of this include robots that perform such tasks as assembling, grinding, scraping, drilling, nuclear waste remediation and extraterrestrial exploration.

An issue of central importance in all these applications is the problem of controlling the interaction forces, i.e., the interaction forces must be accommodated rather than resisted in order to comply with the environmental constraints. Control of constrained manipulators has been approached using two basic strategies. The first strategy, *hybrid position/force control* (Raibert and Craig, 1981), is based on the observation that when

* Environment is the work piece with which the manipulator makes contact for applying a certain force.

the manipulator end-effector is in contact with the environment, the space of the end-effector coordinates can naturally be decomposed into a 'position subspace' and a 'force subspace'. These two subspaces correspond to the directions in which the end-effector is, respectively, free to move and constrained by the environment. This strategy achieves compliant motion by explicitly controlling the end-effector position in the position subspace, and controlling the interaction force in the force subspace. This strategy is intuitively appealing, as it permits the contact force to be explicitly controlled, which allows for the successful completion of many robotic tasks, such as performing consistent swipes in nuclear applications or contact-based surface inspections. However, as a consequence of treating the position-control and force-control tasks separately, the hybrid position/force-control methodology requires significant task planning and control-law switching during implementation. Moreover, this strategy runs into robustness problems, particularly during the transition between unconstrained and constrained motions (Seraji and Colbaugh, 1997).

The second strategy, *impedance control* (Hogan, 1985; Kazerooni et al., 1986), is concerned with regulating the 'mechanical impedance' of the robot end-effector. The goal is to maintain a desired dynamic relationship between the end-effector position and the end-effector/environment contact force. Hogan (1985) indicated that a generalized, nonlinear impedance consisting of some inertial, damping and stiffness characteristics may model this relationship. Consequently, Hogan hypothesized that a viable control strategy for contact tasks would be to give the manipulator an impedance complementary to that of the environment. The combined manipulator-environment system should then

be well behaved, much like a matched impedance electric circuit (Hogan, 1985; McCormick and Schwartz, 1993).

Impedance control provides a unified framework for considering both constrained and unconstrained motion control problems, and possesses certain advantages for many applications over hybrid position/force control. Unlike hybrid control methods that attempt to control forces and motions in orthogonal directions, impedance control consists of a single control law that accommodates external forces. As a result, it requires little off-line task planning, provides robustness to uncertainties and disturbances, and accommodates stable transition between unconstrained and constrained motions (Hogan, 1987; 1988).

The goal of an impedance control law is, as mentioned earlier, to achieve some target dynamics consisting of selected inertial, damping, and stiffness parameters. Kazerooni (1986) proposed a control law that implements the target dynamics of a generalized n-dimensional damped linear spring on an n-degree-of-freedom manipulator. Anderson and Spong (1987) proposed an inverse dynamics controller that implements a second-order linear target dynamics. Colgate and Hogan (1988) suggested a methodology for implementing a generalized single-degree-of-freedom impedance controller. However, all the implementations reviewed thus far are based on the assumption that the manipulator to be controlled can exert controllable torques (Hogan, 1987). While this assumption is acceptable for electrically actuated manipulators, it is not suitable for hydraulic manipulators.

The main reason the assumption of controllable torques does not hold for hydraulic manipulators is that while an electric actuator exerts a torque which is directly

proportional to the control current (D'Souza, 1988), the control current in a hydraulic actuator acts to move the spool valve which controls the flow of hydraulic fluid into the piston. This flow in turn causes a pressure build-up proportional to the actuator torque. Even if the spool valve dynamics are ignored, what the control current fundamentally controls is the derivative of the actuator torque, rather than the torque itself. Therefore, there is some lag automatically introduced into the system. Even if this lag is small in comparison to the target dynamics, the problem of controlling the force in the piston will be a real challenge (Conrad and Jensen, 1987). Another concern with torque-based impedance control is that it requires a great deal of knowledge of the dynamic and kinematic parameters of the robot, which may not be practical in many applications.

Field and Stepanenko (1993) have recently outlined an alternative approach to impedance control concept, called *model reference impedance control*, in which the controller is actually a position controller nested within a force feedback loop. Force feedback is used in a digital model of the target impedance to modify the position set-point. The concept has been implemented on a six-degree-of-freedom electric manipulator. They have demonstrated that the control system could exhibit the target dynamic behavior under a series of tests of step changes in position or end-effector loading. This type of impedance control is particularly suited to industrial manipulators that come equipped with built-in position controllers. Pelletier and Doyon (1994) have discussed the typical application and performance of such an impedance control scheme on an electrically actuated manipulator. Nakashima et al. (1995) have also shown the successful implementation of a similar concept applied to a semi-automatic, dual-armed electric manipulator aimed at hot-line maintenance work. This concept, which is herewith termed 'position-based

impedance control', is suitable for application to hydraulic manipulators, given that it does not require controlled actuator torques. In addition, the method requires no dynamic model of the robot, a feature that further simplifies the control.

1.2 The Scope and Organization of the Study

The goal of this study is to develop an impedance-based computer-control system capable of unsupervised interaction of industrial hydraulic manipulators with the environment. Hydraulic manipulators are extensively utilized in mining, construction, and forestry industries, as well as underwater explorations/inspections. They constantly interact with the environment for which they have no model, and experience different loading. They are built based on the achievement of adequate performance with extreme environmental tolerance and contamination. Therefore, they may show some non-ideal characteristics that have not been fully investigated in the literature. To the best of the author's knowledge, there is no document available on impedance-based force tracking/regulating in hydraulic manipulators.

The focus of this thesis is on the application of the position-based impedance control concept for force control studies in hydraulic manipulators. The method seems attractive, since any control algorithm with path tracking ability can be adapted for this application. Moreover, many manipulator-programming systems are based on position controllers. Therefore, the most appropriate implementation in practice is to use force feedback to modify position commands. The success of such an impedance controller, however, depends on three conditions. Firstly, it depends on the behavior of the underlying position controller. Secondly, it depends on the selection of the manipulator's target impedance

parameters. During constrained manipulation, the dynamics of the manipulator coupled with its environment must be considered, and the target impedance should adapt to variations in the environment impedance. Thirdly, it depends on the controller's ability to track desired forces during contact – a problem common to both position-based and torque-based impedance controls. It will be discussed later that, in an impedance control mode, the end-effector force can only be controlled indirectly, and a reference force generally cannot be specified. In the ideal case, where the parameters of the environment (i.e. location and stiffness) are known, a reference position trajectory can be synthesized a priori to produce the desired contact force. However, in practical cases where the environmental parameters are not known, an impedance controller tends to exhibit poor force tracking characteristics. In fact, the inability of the system to track a reference contact force has been considered the major disadvantage of impedance control over hybrid position/force control. This last issue constitutes the main focus of the present study, and will be addressed in more detail.

In this thesis, Chapter Two explains impedance control and classifies it into torque-based and position-based. After the inability of impedance control to regulate the end-effector force is shown, a background of efforts put forth by other researchers to provide force-tracking ability within an impedance control framework is presented. Chapter Three discusses the kinematics and dynamics of the hydraulic manipulator used as the test station. In the modeling work, detailed dynamics of the manipulator including nonlinear hydraulic valve characteristics, flow deadband, saturation and stick-slip friction are incorporated. Based on this modeling, a complete simulation program is developed that closely resembles the actual hydraulic manipulator. Chapter Four is devoted to

application of position-based impedance control to the hydraulic manipulator. Since the performance of a position-based impedance controller greatly depends on the tracking and regulating performance of its nested positioner, this chapter starts with the development of a novel nonlinear PI position controller appropriate for rugged hydraulic manipulators. Chapter Five is devoted to providing force-tracking capability to a position-based impedance controlled manipulator. Existing techniques for force regulation, using the impedance control concept, are adapted and modified as required to improve the force control capability of the PBIC. Comprehensive simulation studies are performed followed by experiments, through formally designed set of tests, aiming at evaluating their capability in force regulation of hydraulic manipulators.

Chapter 2

Background

2.1 What is Impedance Control?

Impedance control* is a general approach to the control of manipulation. The method is intended to encompass the traditional positioning tasks performed by robots while including the capability to handle static and dynamic interactions between the manipulator and the environment. Impedance control establishes a desired user-specified dynamic relationship, referred to as the target impedance, between the end-effector position, x, and the contact force, f. The most common implementation of impedance control computes a control torque which transforms the existing robot dynamics into a desired form (Field and Stepanenko, 1993). Consider an n-degree-of-freedom manipulator whose dynamics in Cartesian space, are described by

* The term 'impedance control' was first introduced by Neville Hogan (1985) in his three-part paper as a unified approach to all manipulation. Inspired by electrical systems, Hogan argued that physical systems come in two types: admittances which accept effort (force, voltage) inputs and yield flow (motion, current) outputs; and impedances which accept flow (motion, current) inputs and yield effort (force, voltage) outputs. Seen from the environment, a manipulator must be an impedance type. The role of impedance control is, therefore, to maintain a desired dynamic relationship between the end-effector position and the end-effector/environment contact force.

$$H_x(x)\ddot{x} + C_x(x,\dot{x})\dot{x} + g_x(x) + f_x(\dot{x}) = J^{-T}\tau - f \tag{2.1}$$

where τ is the vector of the joint torques supplied by the actuators, x is the vector representing the position and orientation of the manipulator's endpoint, $H_x(x)$ is the inertia matrix, and $C_x(x,\dot{x})$, $g_x(x)$, and $f_x(\dot{x})$ represent centrifugal/Coriolis forces, gravitational forces and friction forces, respectively. Finally, J is the Jacobian* matrix of the manipulator and f is the external force applied at the implement. In impedance control, the desired dynamics at the end-effector are often specified by a second-order dynamics that mimics a mass-spring-damper system. The three common formulations of the target impedance are (Seraji and Colbaugh, 1997):

$$M\ddot{x} + C\dot{x} + K(x - x_r) = -f \tag{2.2a}$$
$$M\ddot{x} + C(\dot{x} - \dot{x}_r) + K(x - x_r) = -f \tag{2.2b}$$
$$M(\ddot{x} - \ddot{x}_r) + C(\dot{x} - \dot{x}_r) + K(x - x_r) = -f \tag{2.2c}$$

where the term $(x - x_r)$ denotes the change in Cartesian position from the commanded trajectory, x_r. M, C, and K are, respectively, the diagonal mass, damping and stiffness matrices of the target impedance, specified by the user. Given the manipulator dynamics in (2.1), the required control torque to achieve the target dynamics (2.2c) for example, is given by

$$\tau = J^T\left(H_x\left(\ddot{x}_r - M^{-1}[C(\dot{x} - \dot{x}_r) + K(x - x_r) + f]\right) + C_x\dot{x} + g_x + f_x + f\right) \tag{2.3}$$

In robotics literature, this computed torque technique is referred to as 'torque-based impedance control'. In this equation, it is seen that the technique is highly dependent on the position and velocity dependent dynamic characteristics of the manipulator,

* $J^{-T} = (J^T)^{-1} = (J^{-1})^T$

represented by terms $H_x(x)$, $C_x(x,\dot{x})$, $g_x(x)$, and $f_x(\dot{x})$. These terms are not readily available for most industrial manipulators.

An alternative implementation of impedance control is shown in Fig. 2.1. This implementation, which has been termed 'model-reference impedance control' by Field and Stepanenko (1993), utilizes the interaction force, sensed by a sensor, and computes the corresponding motion of a linear mass-spring-damper model. The existing robot position controller (shown as a PID controller) is then used to track the model's output. This type of implementation does not necessarily require a robot model or even torque-driven actuators. All that is required is a suitable position controller capable of path tracking. This type of impedance control is suitable for manipulators with hydraulic actuators.

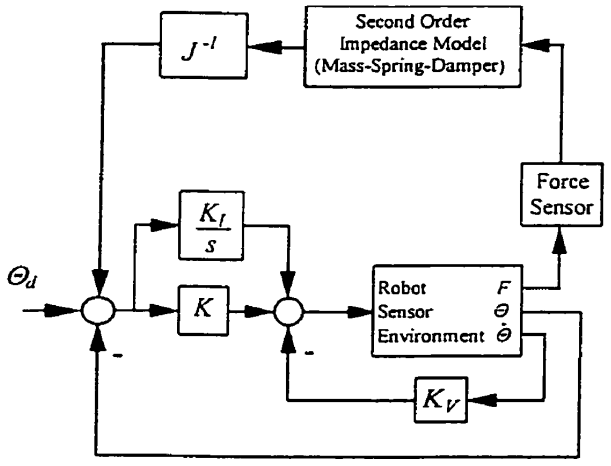

Fig. 2.1. Model reference impedance control system

The model-reference impedance control, as described above, is actually the extension of two previously developed force control algorithms by Whitney (1977) and Salisbury (1980). Whitney (1977) introduced the concept of damping control, which he called 'accommodation'. In this control (see Fig. 2.2a), sensed forces at the end-effector give

rise to a velocity vector which is used to modify a commanded velocity trajectory. The gain matrix, K_D, determines the degree of modification. Salisbury (1980) introduced a stiffness control scheme where instead of interpreting the sensed forces as velocity modifications, they are transformed into position modifications in the implement coordinate system (see Fig. 2.2b). The apparent stiffness at the end-effector is set by a stiffness matrix gain, K_S. Model-reference impedance control technique actually expands upon the above two methods by combining them and adding an inertial term. Hogan (1985) noted that no physically realizable system could eliminate the inertial effects of the manipulator. By adding the inertial term, the apparent inertia as seen at the end-effector could also be modified.

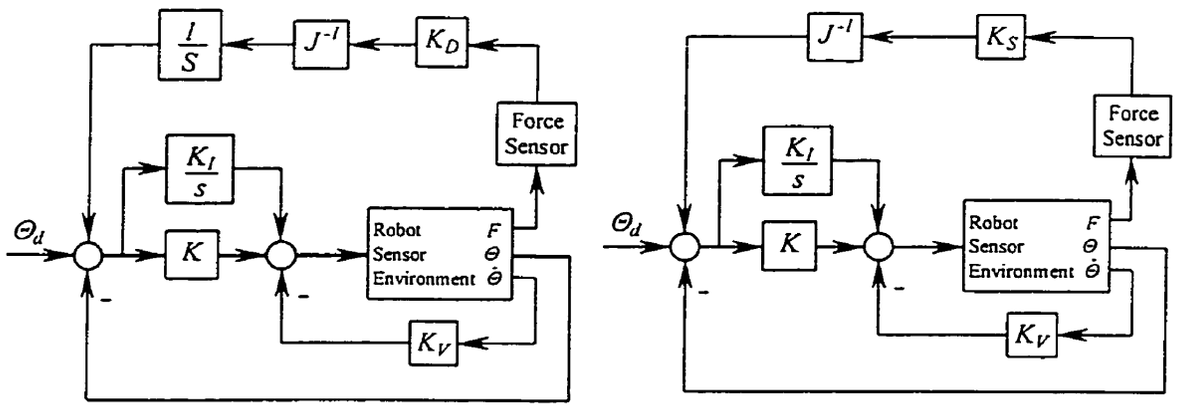

(a) Damping (Accommodation) Control **(b)** Stiffness Control

Fig. 2.2. Damping (accommodation) and stiffness control systems

2.2 Impedance Control and Force Tracking

In the beginning, impedance control, as defined by Eqs. (2.2), was employed only to provide a compliant and stable transition between unconstrained and constrained motions and it did not have any force reference. However, using impedance control as a method

for force tracking has been the focus of many papers as there has been a growing interest in this problem. Goldenberg (1988) suggested adding a reference force to the force required by the target impedance. This is equivalent to adding another impedance in parallel with the target impedance. The superposition property of impedance control makes such an approach permissible (Hogan, 1985). Therefore, to accomplish force tracking, a force set-point, f_r, is specified by the user and the target impedance is driven by the contact force error, $e = f_r - f$, rather than just the contact force, f. In contact tasks, the force set-point, f_r, is usually specified as a constant. The three target impedances are then described by

$$M\ddot{x} + C\dot{x} + K(x - x_r) = e \tag{2.4a}$$

$$M\ddot{x} + C(\dot{x} - \dot{x}_r) + K(x - x_r) = e \tag{2.4b}$$

$$M(\ddot{x} - \ddot{x}_r) + C(\dot{x} - \dot{x}_r) + K(x - x_r) = e \tag{2.4c}$$

During the free-space motion in which there is no contact with the environment, $e = 0$. Using the target impedance model in (2.4c), for instance, the following differential equation is obtained

$$M\frac{d^2}{dt^2}(x(t) - x_r(t)) + C\frac{d}{dt}(x(t) - x_r(t)) + K(x(t) - x_r(t)) = 0 \tag{2.5}$$

Since Eq. (2.5) is a stable differential equation, $x(t) \to x_r(t)$ as $t \to \infty$. Hence, the end-effector position, x, tracks the reference position trajectory, x_r, accurately according to the dynamics specified by Eq. (2.5). When the end-effector comes into contact with the environment, the dynamic interaction between the manipulator and the environment is dictated by the target impedance of Eq. (2.4c), which results in a compromise between the position deviation, $(x - x_r)$, and the force error, e, so neither accurate position control

nor accurate force control is accomplished. Therefore, impedance control by itself is incapable of force tracking. There have been some efforts to provide force control ability to impedance control. Some of these methods are explained in the next section.

2.3 Review on Force Tracking in Impedance Control

The fundamental task of the impedance control, as laid out by Hogan (1985), is to make the manipulator dynamics conform to the target impedance. This impedance should then be selected and modulated as required by the task at hand. Two approaches have been taken in addressing this issue: (1) to change the form or parameters of the target impedance, or (2) to alter the reference position trajectory.

Pelletier and Daneshmend (1990) presented a model reference adaptive control scheme to compensate for variations in environmental stiffness during compliant motion using damping control. Although the stability limits of their controller were not derived formally, they predicted that stability and convergence might not be achieved in situations which do not satisfy their initial low-friction and decoupling hypotheses. Lasky and Hsia (1991) examined the usefulness of further modifying the reference trajectory for the purpose of force tracking. Their approach was to modify each coordinate of the reference trajectory in direct proportion to the error in the corresponding component of the end-effector force. The effectiveness of the proposed modification was tested on a simulation of a two-link direct-drive manipulator. The task was to deburr a surface modeled as a pure stiffness. The results showed much improved force tracking when the proposed trajectory modification was used. This modification proved to be robust to multiple orders of magnitude of error in estimation of environmental stiffness. Chan

et al. (1991) developed a variable structure control scheme for robust impedance control in the presence of parametric uncertainties and external disturbances. Their strategy, however, required precise knowledge of the location and stiffness of the environment in order to achieve accurate force control. Lu and Meng (1991) examined the performance of two adaptive implementations of impedance control. They found that the injection of adaptive control techniques could compensate for errors in the dynamic model of the manipulator, resulting in robust control. Lyapunov analysis and simulation of a two-link direct-drive manipulator led to this conclusion. Cohen and Flash (1991) examined the possibility of designing a higher-level controller in which the controlled variables were the target dynamics of the manipulator. Simulation studies were carried out for a two-link, direct-drive manipulator performing a wiping task. The target impedance was a 'linear simple impedance', a term defined by Hogan (1988) meaning an impedance described by $f = A\dot{x} + Bx$. An associative search network was used to learn the impedance parameters using a reward function involving the sum of absolute errors in velocity and force. The errors were taken with respect to reference trajectories. An important element of this particular work was that no feedforward torque was used. The commanded torques were simply those required by the impedance relation in the static case using a fixed inertial matrix. It was found that the impedance parameter modulation scheme was fairly successful, but was unable to deal with abrupt changes in environmental admittance. A reference trajectory modification scheme was then added in an attempt to deal with this problem, with the result that stability and trajectory tracking were both improved.

Dawson, Lewis and Dorsey (1992) applied impedance control to force tracking tasks. They compensated for contact force errors in the dynamic model of the manipulator using a Lyapunov-based auxiliary signal to augment a PD-type position controller. Given controllable actuator torques and exact kinematics information, the global ultimate boundedness of the tracking error was proven, and simulation showed good force regulation.

McCormick and Schwartz (1993) compared the results of using a linearized impedance controller with a fully nonlinear one, in terms of force trajectory tracking and contact stability. A second-order target impedance was chosen, and the force-offset method of Colgate and Hogan (1988) was used to specify the reference force trajectory. Using a direct-drive, five-bar linkage, a slightly better response was observed for the nonlinear controller. However, simulation showed kinematic instabilities in the nonlinear controller that were absent in its linearized counterpart. Contact studies showed that, for improper impedance parameter selection, instability was present even when the surface of the environment was covered with a rubber pad. Increasing the target inertia and other parameters proportionately resulted in a stable contact. Another study of impedance parameter modulation (Johansson and Spong, 1994) used a quadratic optimization scheme to minimize deviations from the velocity and force trajectories. Again, a linear simple impedance was used on a simulation of a two-link, direct-drive robot. The authors only considered constant interaction forces.

Lu and Goldenberg (1995) adopted a sliding-mode-based impedance controller to formulate a force regulation scheme. Since the scheme needed information about environmental parameters, they also developed a simple off-line method to estimate the

location and stiffness of the environment to be used in a trajectory modification approach to accurate force regulation.

Seraji and Colbaugh (1997) developed two force control schemes for automatically generating a reference position trajectory that could facilitate the force-tracking capability of impedance controllers. The first scheme was based on generating the reference position on-line as a function of the force tracking error. The scheme used a direct adaptive control approach. In the second scheme, the environmental parameters were estimated on-line using an indirect adaptive control approach and the required reference position was computed based on these estimates. The force tracking performances of each scheme was demonstrated through simulation studies and some laboratory experimentation on an electric-driven manipulator.

2.4 Summary

In this chapter, impedance control was briefly explained and classified into torque-based and position-based. It was shown that position-based impedance control is a suitable candidate for implementation on hydraulic manipulators. Impedance control was shown to be incapable of force tracking by itself. Finally, some efforts put forth by other researchers to provide force-tracking capability for impedance control were listed.

The off-line environmental parameters estimation method by Lu and Goldenberg (1988), the simple position reference modification method by Lasky and Hsia (1993), and two (direct and indirect) adaptive methods by Seraji and Colbaugh (1997) that can be also applied in position-based impedance control framework will be adopted for the force control of a hydraulic manipulator later in this study in Chapter 5.

Chapter 3

The Unimate MKII-2000 Hydraulic Research Robot

3.1 Description of the Manipulator

The Unimate MKII-2000 robot, shown in Fig. 3.1, was used for all the experiments described in this work. The robot is an industrial hydraulic manipulator with a spherical geometry, i.e., the first three degrees of freedom are left/right, up/down, and in/out, in that order. Its hydraulic actuators are supplied by a constant-pressure source operating at approximately 7000 ± 500 KPa. The spool valve has circular ports (parabolic orifice area to spool displacement function) and a deadband of approximately 6% of the maximum spool stroke due to the spool overlap. Actuator/joint stiction provides some delay in the response that worsens this deadband.

Position feedback is obtained using digital encoders with resolutions of 0.028°, 0.028°, and 0.105mm on links 1, 2, and 3, respectively. The readings are taken by a 486-66MHz personal computer, which also performs all control actions. The control signals saturate at 3V. The force between the manipulator implement and the environment is measured by a sensor, built in-house, based on a standard strain gauge bridge. It has a range of

measurement in a single direction of 0 to 700N with ±10N of noise. This level of noise is due to transmission from the sensor to the computer, and is not atypical (Field and Stepanenko, 1993).

Kinematic and dynamic properties of the first three degrees of freedom of this manipulator as well as nonlinear dynamics of the hydraulic system are derived in this chapter and used in a simulation program.

3.2 The Kinematics and Dynamics of the Manipulator

The kinematics of the robot are derived using the descriptive conventions established by Denavit and Hartenburg (Paul, 1981). Link coordinate frame attachment to the first three links, are shown in a schematic view of the manipulator in Fig. 3.2.

The manipulator parameters are shown in Table 3.1, where Denavit and Hartenburg parameters, θ_n, d_n, α_n and a_n are as defined in Paul (1981).

Table 3.1. Denavit-Hartenburg parameters for Unimate MKII-2000.

Link	*Variable*	θ_n	d_n	a_n	α_n
1	θ_1	θ_1	0	0	-90°
2	θ_2	$\theta_2 + 90°$	0	$-a_2$	90°
3	d_3	0	d_3	0	0

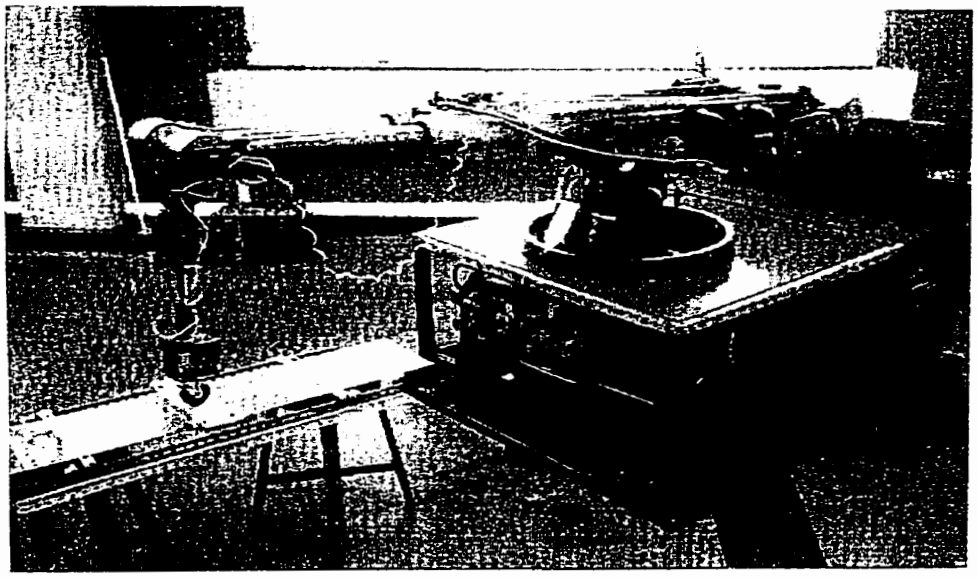

Fig. 3.1. Unimate MKII-2000 hydraulic manipulator and test station

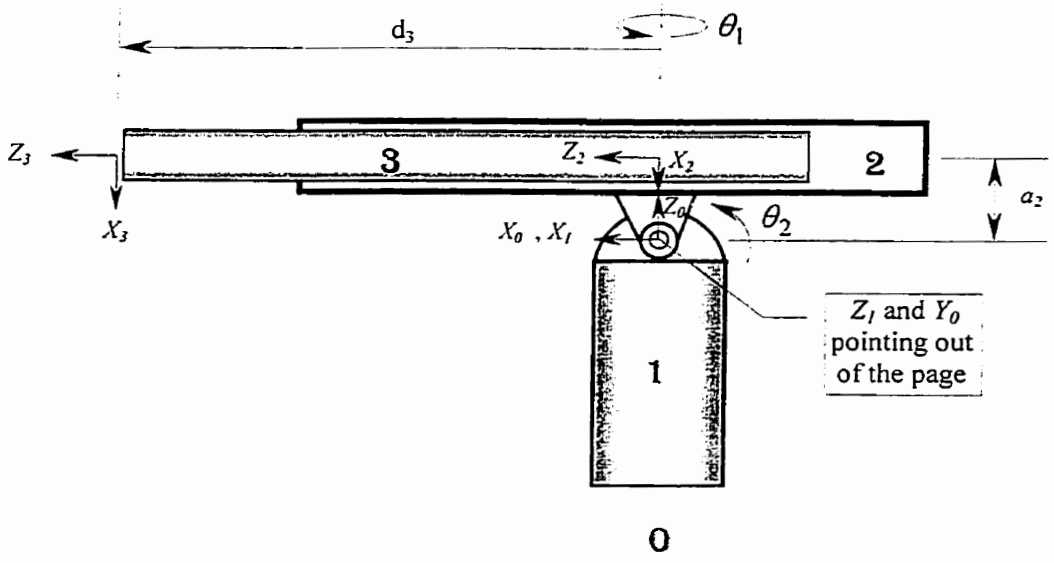

Fig. 3.2. Schematic of Unimate MKII-2000 and joint coordinates

Using parameters defined in Table 3.1, the transformation matrix of each link is obtained as follows:

$$A_1 = \begin{bmatrix} \cos\theta_1 & 0 & -\sin\theta_1 & 0 \\ \sin\theta_1 & 0 & \cos\theta_1 & 0 \\ 0 & -1 & 0 & 0 \\ 0 & 0 & 0 & 1 \end{bmatrix}$$

$$A_2 = \begin{bmatrix} -\sin\theta_2 & 0 & \cos\theta_2 & a_2\sin\theta_2 \\ \cos\theta_2 & 0 & \sin\theta_2 & -a_2\cos\theta_2 \\ 0 & 1 & 0 & 0 \\ 0 & 0 & 0 & 1 \end{bmatrix} \qquad (3.1)$$

$$A_3 = \begin{bmatrix} 1 & 0 & 0 & 0 \\ 0 & 1 & 0 & 0 \\ 0 & 0 & 1 & d_3 \\ 0 & 0 & 0 & 1 \end{bmatrix}$$

where A_i is the transformation matrix that relates the coordinate frame of link i to the coordinate frame of link $i-1$. Transformations T_i $(i = 1,2,3)$ of each link coordinate frame with respect to the base coordinate system, $\{X_0Y_0Z_0\}$, are obtained by the products of the A_i transformations.

$$T_1 = A_1 = \begin{bmatrix} \cos\theta_1 & 0 & -\sin\theta_1 & 0 \\ \sin\theta_1 & 0 & \cos\theta_1 & 0 \\ 0 & -1 & 0 & 0 \\ 0 & 0 & 0 & 1 \end{bmatrix} \qquad (3.2)$$

The location and orientation of the coordinate frame of link 1 is

$$\bar{P}_1 = T_1(1:3,4) = \begin{bmatrix} 0 \\ 0 \\ 0 \end{bmatrix}$$

$$\bar{i}_1 = T_1(1:3,1) = \begin{bmatrix} \cos\theta_1 \\ \sin\theta_1 \\ 0 \end{bmatrix},\ \bar{j}_1 = T_1(1:3,2) = \begin{bmatrix} 0 \\ 0 \\ -1 \end{bmatrix},\ \bar{k}_1 = T_1(1:3,3) = \begin{bmatrix} -\sin\theta_1 \\ \cos\theta_1 \\ 0 \end{bmatrix} \qquad (3.3)$$

where $\bar{P}_1$ is the vector describing the location of the origin of frame $\{X_1Y_1Z_1\}$ with respect to the base coordinate frame, $\{X_0Y_0Z_0\}$. $\bar{i}_1$, $\bar{j}_1$ and $\bar{k}_1$ are, respectively, the directions of the unit vectors of the X_1, Y_1 and Z_1 axes with respect to the base coordinate frame. Similarly,

$$T_2 = A_1 \cdot A_2 = \begin{bmatrix} -\cos\theta_1 \sin\theta_2 & -\sin\theta_1 & \cos\theta_1 \cos\theta_2 & a_2 \cos\theta_1 \sin\theta_2 \\ -\sin\theta_1 \sin\theta_2 & \cos\theta_1 & \sin\theta_1 \cos\theta_2 & a_2 \sin\theta_1 \sin\theta_2 \\ -\cos\theta_2 & 0 & -\sin\theta_2 & a_2 \cos\theta_2 \\ 0 & 0 & 0 & 1 \end{bmatrix} \tag{3.4}$$

$$\bar{P}_2 = T_2(1:3,4) = \begin{bmatrix} a_2 \cos\theta_1 \sin\theta_2 \\ a_2 \sin\theta_1 \sin\theta_2 \\ a_2 \cos\theta_2 \end{bmatrix} \tag{3.5}$$

$$\bar{i}_2 = T_2(1:3,1) = \begin{bmatrix} -\cos\theta_1 \sin\theta_2 \\ -\sin\theta_1 \sin\theta_2 \\ -\cos\theta_2 \end{bmatrix}, \quad \bar{j}_2 = T_2(1:3,2) = \begin{bmatrix} -\sin\theta_1 \\ \cos\theta_1 \\ 0 \end{bmatrix}, \quad \bar{k}_2 = T_2(1:3,3) = \begin{bmatrix} \cos\theta_1 \cos\theta_2 \\ \sin\theta_1 \cos\theta_2 \\ -\sin\theta_2 \end{bmatrix}$$

and

$$T_3 = A_1 \cdot A_2 \cdot A_3 = \begin{bmatrix} -\cos\theta_1 \sin\theta_2 & -\sin\theta_1 & \cos\theta_1 \cos\theta_2 & a_2 \cos\theta_1 \sin\theta_2 + d_3 \cos\theta_1 \cos\theta_2 \\ -\sin\theta_1 \sin\theta_2 & \cos\theta_1 & \sin\theta_1 \cos\theta_2 & a_2 \sin\theta_1 \sin\theta_2 + d_3 \sin\theta_1 \cos\theta_2 \\ -\cos\theta_2 & 0 & -\sin\theta_2 & a_2 \cos\theta_2 - d_3 \sin\theta_2 \\ 0 & 0 & 0 & 1 \end{bmatrix} \tag{3.6}$$

$$\bar{P}_3 = \bar{r}_{0,e} = T_3(1:3,4) = \begin{bmatrix} a_2 \cos\theta_1 \sin\theta_2 + d_3 \cos\theta_1 \cos\theta_2 \\ a_2 \sin\theta_1 \sin\theta_2 + d_3 \sin\theta_1 \cos\theta_2 \\ a_2 \cos\theta_2 - d_3 \sin\theta_2 \end{bmatrix} \tag{3.7}$$

$$\bar{i}_3 = T_3(1:3,1) = \begin{bmatrix} -\cos\theta_1 \sin\theta_2 \\ -\sin\theta_1 \sin\theta_2 \\ -\cos\theta_2 \end{bmatrix}, \quad \bar{j}_3 = T_3(1:3,2) = \begin{bmatrix} -\sin\theta_1 \\ \cos\theta_1 \\ 0 \end{bmatrix}, \quad \bar{k}_3 = T_3(1:3,3) = \begin{bmatrix} \cos\theta_1 \cos\theta_2 \\ \sin\theta_1 \cos\theta_2 \\ -\sin\theta_2 \end{bmatrix}$$

Forward kinematics gives the location of the end-effector in Cartesian base coordinate system in terms of the joint positions:

$$\begin{cases} x = \cos\theta_1 (a_2 \sin\theta_2 + d_3 \cos\theta_2) \\ y = \sin\theta_1 (a_2 \sin\theta_2 + d_3 \cos\theta_2) \\ z = a_2 \cos\theta_2 - d_3 \sin\theta_2 \end{cases} \quad \text{(Forward Kinematics)} \qquad (3.8)$$

Solving the above equations for joint positions θ_1, θ_2 and d_3, the inverse kinematics solution is obtained:

$$\begin{cases} \theta_1 = \tan^{-1}\left(\dfrac{y}{x}\right) \\ d_3 = \sqrt{x^2 + y^2 + z^2 - a_2^2} \\ \theta_2 = \tan^{-1}\left(\dfrac{a_2\sqrt{x^2+y^2} - d_3 z}{d_3\sqrt{x^2+y^2} + a_2 z}\right) \end{cases} \quad \text{(Inverse Kinematics)} \qquad (3.9)$$

The Jacobian matrix, $\boldsymbol{J}$, relates the velocity of the end-effector in Cartesian coordinates system, $\dot{\vec{X}}$, to the joint velocities, $\dot{\vec{\Theta}}$, as $\dot{\vec{X}} = \boldsymbol{J} \cdot \dot{\vec{\Theta}}$. It also translates the effect of forces at the end-effector, F, to the joint torques, τ, as $\tau = \boldsymbol{J}^T F$.

The Jacobian matrix, $\boldsymbol{J}$, is found as follows:

$$\begin{aligned} J &= \begin{bmatrix} J_{t_1} & J_{t_2} & J_{t_3} \end{bmatrix} = \begin{bmatrix} \vec{k}_0 \times \vec{r}_{0,e} & \vec{k}_1 \times \vec{r}_{1,e} & \vec{k}_2 \end{bmatrix} = \begin{bmatrix} \vec{k}_0 \times \vec{P}_3 & \vec{k}_1 \times (\vec{P}_3 - \vec{P}_1) & \vec{k}_2 \end{bmatrix} \\ &= \begin{bmatrix} \begin{bmatrix} 0 \\ 0 \\ 1 \end{bmatrix} \times \begin{bmatrix} a_2\cos\theta_1\sin\theta_2 + d_3\cos\theta_1\cos\theta_2 \\ a_2\sin\theta_1\sin\theta_2 + d_3\sin\theta_1\cos\theta_2 \\ a_2\cos\theta_2 - d_3\sin\theta_2 \end{bmatrix} & \begin{bmatrix} -\sin\theta_1 \\ \cos\theta_1 \\ 0 \end{bmatrix} \times \begin{bmatrix} a_2\cos\theta_1\sin\theta_2 + d_3\cos\theta_1\cos\theta_2 \\ a_2\sin\theta_1\sin\theta_2 + d_3\sin\theta_1\cos\theta_2 \\ a_2\cos\theta_2 - d_3\sin\theta_2 \end{bmatrix} & \begin{bmatrix} \cos\theta_1\cos\theta_2 \\ \sin\theta_1\cos\theta_2 \\ -\sin\theta_2 \end{bmatrix} \end{bmatrix} \\ &= \begin{bmatrix} -\sin\theta_1(a_2\sin\theta_2 + d_3\cos\theta_2) & \cos\theta_1(a_2\cos\theta_2 - d_3\sin\theta_2) & \cos\theta_1\cos\theta_2 \\ \cos\theta_1(a_2\sin\theta_2 + d_3\cos\theta_2) & \sin\theta_1(a_2\cos\theta_2 - d_3\sin\theta_2) & \sin\theta_1\cos\theta_2 \\ 0 & -(a_2\sin\theta_2 + d_3\cos\theta_2) & -\sin\theta_2 \end{bmatrix} \end{aligned} \qquad (3.10)$$

where $\vec{r}_{i,e}$ $(i = 1,2,3)$ is the vector that describes the location of the end-effector with respect to the origin of link i in the base coordinate system. The dynamics of the manipulator are defined by the following equations:

$$\tau_i = \sum_{j=1}^{3} D_{ij}\ddot{\theta}_j + I_{a_i}\ddot{\theta}_i + \sum_{j=1}^{3}\sum_{k=1}^{3} D_{ijk}\dot{\theta}_j\dot{\theta}_k + D_i + (\boldsymbol{J}^T F)_i \qquad (i = 1,2,3) \qquad (3.11)$$

where the last term, $(\boldsymbol{J}^T F)_i$, is the effect of end-point forces on joint torques/forces,

$$\text{and} \qquad \begin{cases} D_{ij} = \sum_{p=\max(i,j)}^{3} Trace\left(\dfrac{\partial \boldsymbol{T}_p}{\partial \theta_j} \boldsymbol{J}_p \dfrac{\partial \boldsymbol{T}_p^T}{\partial \theta_i} \right) \\ D_{ijk} = \sum_{p=\max(i,j,k)}^{3} Trace\left(\dfrac{\partial^2 \boldsymbol{T}_p}{\partial \theta_j \partial \theta_k} \boldsymbol{J}_p \dfrac{\partial \boldsymbol{T}_p^T}{\partial \theta_i} \right) \\ D_i = \sum_{p=i}^{3} -m_p \boldsymbol{g}^T \dfrac{\partial \boldsymbol{T}_p}{\partial \theta_i} {}^p\bar{\mathbf{r}}_p \end{cases} \tag{3.12}$$

$$\text{and} \qquad \boldsymbol{J}_p = \begin{bmatrix} \dfrac{-I_{xx_p} + I_{yy_p} + I_{zz_p}}{2} & I_{xy_p} & I_{xz_p} & m_p \bar{x}_p \\ I_{xy_p} & \dfrac{I_{xx_p} - I_{yy_p} + I_{zz_p}}{2} & I_{yz_p} & m_p \bar{y}_p \\ I_{xz_p} & I_{yz_p} & \dfrac{I_{xx_p} + I_{yy_p} - I_{zz_p}}{2} & m_p \bar{z}_p \\ m_p \bar{x}_p & m_p \bar{y}_p & m_p \bar{z}_p & m_p \end{bmatrix} \tag{3.13}$$

τ_i is the joint torque/force at joint i, I_{a_i} is the joint i actuator inertia, $\boldsymbol{J}_p$ is the pseudo-inertia matrix of link p, $\boldsymbol{g} = [g_x \quad g_y \quad g_z \quad 0]^T$ is the gravitational acceleration vector in the base coordinate system, and ${}^p\bar{\mathbf{r}}_p = \left[\bar{x}_p \quad \bar{y}_p \quad \bar{z}_p \quad 0\right]^T$ is the vector of the coordinates of the center of gravity of link p with respect to the same link coordinate system. D_{ii} represents the effective inertia at joint i. D_{ij} represents the coupling inertia between joints i and j. D_{ijj} represents the centripetal forces at joint i due to velocity at joint j. D_{ijk} represents the Coriolis forces at joint i due to velocities at joints j and k. Finally, D_i represents the gravity loading at joint i (R. P. Paul, 1981). These inertial terms for the Unimate manipulator are derived and listed in the Appendix.

Assuming the joint torques/forces τ_i $(i = 1,2,3)$ are known, the three equations of (3.11) are solved simultaneously for the three joint accelerations, $\ddot{\theta}_1$, $\ddot{\theta}_2$ and $\ddot{\theta}_3$. These

accelerations are integrated to get the joint velocities and positions in simulation programs. The Cartesian position of the end-effector is then calculated through forward kinematics as presented by (3.8). All of the dynamics computation starts with known joint torques; but in hydraulic actuators, unlike electrical ones, the joint torque is not simply proportional to the control signal. The following section is devoted to describing the hydraulic functions.

3.3 Hydraulic Actuation System

The schematic diagram of a hydraulic actuator operated by a closed-center valve and in contact with the environment is shown in Fig. 3.3. The actuator is coupled with the environment through the force sensor. The sensor with stiffness, k_s, and damping, c_s, connects the actuator rod represented by the mass, M, and viscous damping, B, to the environment. The environment is represented by mass m_e, damping c_e, and stiffness k_e. The dynamic equations pertaining to this system are described as follows:

$$M\ddot{x} = F_a - k_s(x - x_e) - c_s(\dot{x} - \dot{x}_e) - B\dot{x} \tag{3.14a}$$

$$m_e\ddot{x}_e = k_s(x - x_e) - k_e x_e + c_s(\dot{x} - \dot{x}_e) - c_e\dot{x}_e \tag{3.14b}$$

where x and x_e are the actuator's displacement and environmental displacement, respectively. The net actuator force, f_a, that provides the joint force/torque in hydraulic manipulators is:

$$f_a = p_i A_i - p_o A_o \tag{3.15}$$

where A_i and A_o are the piston effective areas. p_i and p_o are the input and output line pressures, respectively, and the sensed force, f, is:

$$f = k_s(x - x_e) \tag{3.16}$$

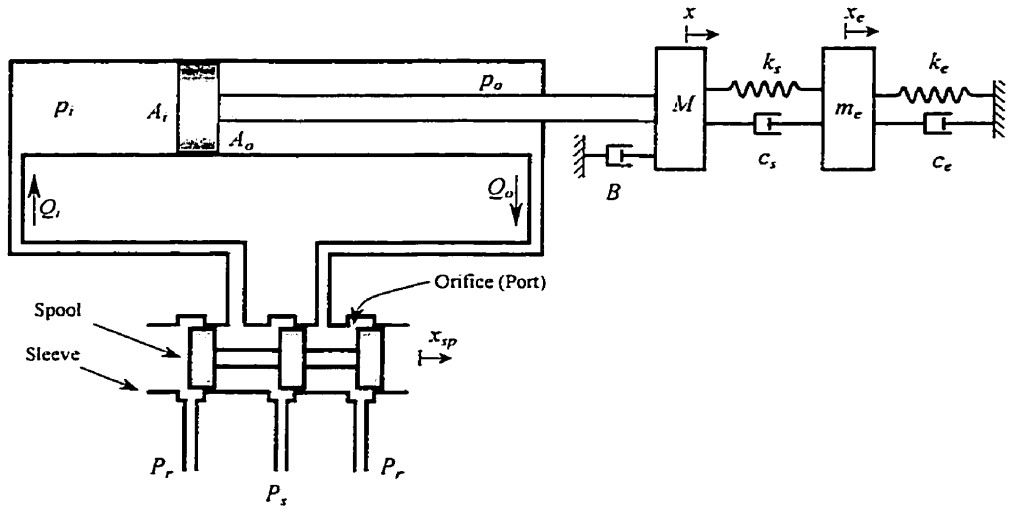

Fig. 3.3. Hydraulic system parameters

The governing nonlinear pressure/flow relationships in hydraulic valve, in their simplest form, can be written as follows (Merritt, 1967):

$$Q_i = \begin{cases} C_d A_{port} \sqrt{\frac{2}{\rho}(p_s - p_i)} & \text{extending } (x_{sp} \geq 0) \\ C_d A_{port} \sqrt{\frac{2}{\rho}(p_i - p_r)} & \text{retracting } (x_{sp} < 0) \end{cases} \tag{3.17}$$

$$Q_o = \begin{cases} C_d A_{port} \sqrt{\frac{2}{\rho}(p_o - p_r)} & \text{extending } (x_{sp} \geq 0) \\ C_d A_{port} \sqrt{\frac{2}{\rho}(p_s - p_o)} & \text{retracting } (x_{sp} < 0) \end{cases} \tag{3.18}$$

where Q_i and Q_o represent fluid flows from the valve into and out of the actuator. p_s is the supply (pump) pressure and p_r is the return (tank) pressure. ρ is the mass density of the fluid and C_d is the orifice discharge coefficient. x_{sp} is the spool displacement and A_{port} is the orifice (port) area. Each orifice in the Moog valves used in the Unimate manipulator consists of six holes drilled on the sleeve of the valve. Two larger holes each

have a radius of $r_1 = 0.125$ in and four smaller ones each have a radius of $r_2 = 0.11$ in. Fig. 3.4 shows the schematic of the holes arrangement. The port opening area is mathematically described as follows:

$$A_{port} = \begin{cases} 2\left(r_1^2 \cos^{-1}\left(\frac{r_1 - x_{sp}}{r_1}\right) - (r_1 - x_{sp})\sqrt{2r_1 x_{sp} - x_{sp}^2}\right) & \text{if } 0 \le x_{sp} \le (r_1 - r_2) \\ 2\left(r_1^2 \cos^{-1}\left(\frac{r_1 - x_{sp}}{r_1}\right) - (r_1 - x_{sp})\sqrt{2r_1 x_{sp} - x_{sp}^2}\right) & \text{if } (r_1 - r_2) < x_{sp} \\ \quad + 4\left(r_2^2 \cos^{-1}\left(\frac{r_2 - \left(x_{sp} - (r_1 - r_2)\right)}{r_2}\right) - \left(r_2 - \left(x_{sp} - (r_1 - r_2)\right)\right)\sqrt{2r_2\left(x_{sp} - (r_1 - r_2)\right) - \left(x_{sp} - (r_1 - r_2)\right)^2}\right) & \\ -2\left(r_1^2 \cos^{-1}\left(\frac{r_1 + x_{sp}}{r_1}\right) - (r_1 + x_{sp})\sqrt{-2r_1 x_{sp} - x_{sp}^2}\right) & \text{if } (r_2 - r_1) \le x_{sp} \le 0 \\ -2\left(r_1^2 \cos^{-1}\left(\frac{r_1 + x_{sp}}{r_1}\right) - (r_1 + x_{sp})\sqrt{-2r_1 x_{sp} - x_{sp}^2}\right) & \text{if } x_{sp} \le (r_2 - r_1) \\ -4\left(r_2^2 \cos^{-1}\left(\frac{r_2 + \left(x_{sp} + (r_1 - r_2)\right)}{r_2}\right) - \left(r_2 + \left(x_{sp} + (r_1 - r_2)\right)\right)\sqrt{-2r_2\left(x_{sp} + (r_1 - r_2)\right) - \left(x_{sp} + (r_1 - r_2)\right)^2}\right) & \end{cases} \tag{3.19}$$

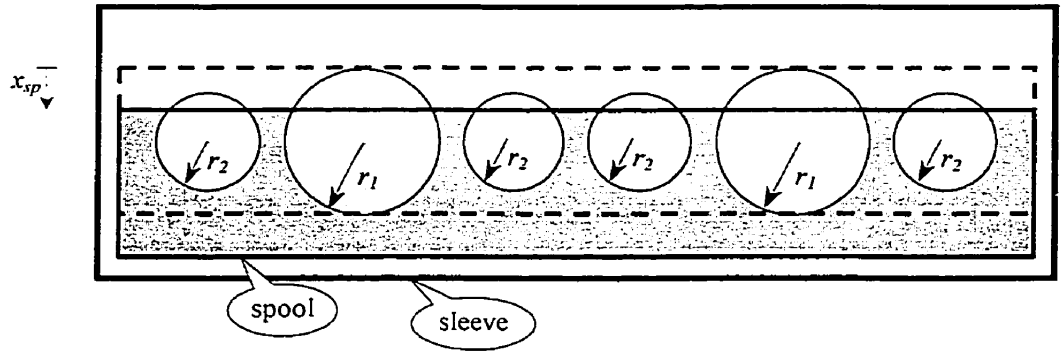

Fig. 3.4. Peripheral expansion of spool and sleeve in a typical orifice in Moog hydraulic valve

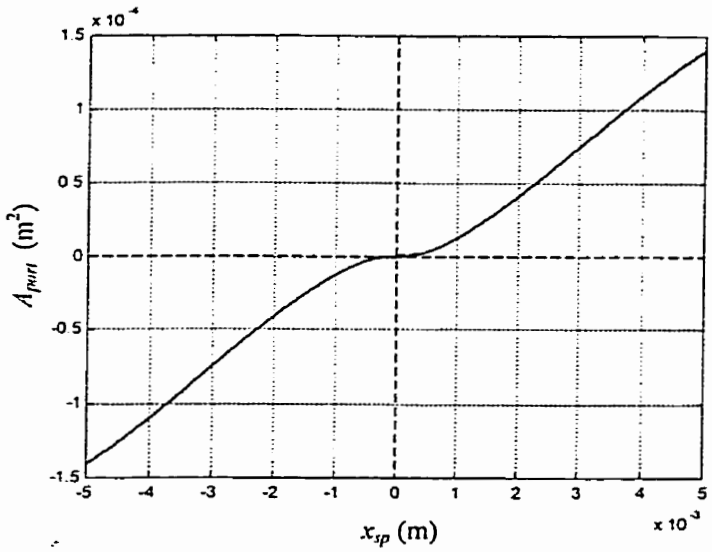

Fig. 3.5. Port opening area versus spool displacement

The port opening area, A_{port}, versus spool displacement, x_{sp}, is plotted in Fig. 3.5. As seen in Fig. 3.5, the valve is designed so that the orifice (port) area is as linear as possible with respect to the spool displacement, x_{sp}:

$$A_{port} \approx w x_{sp} \tag{3.20}$$

where w is the orifice gradient. Continuity equations for oil flow through the cylinder, neglecting the leakage flows, are:

$$\begin{aligned} Q_i &= \frac{V_i}{\beta}\dot{p}_i + A_i\dot{x} = C_i\dot{p}_i + A_i\dot{x} \\ Q_o &= -\frac{V_o}{\beta}\dot{p}_o + A_o\dot{x} = -C_o\dot{p}_o + A_o\dot{x} \end{aligned} \tag{3.21}$$

where β is the effective bulk modulus of the hydraulic fluid. C_i and C_o are hydraulic compliance (in/out), and V_i and V_o are the volumes of fluid trapped at the sides of the piston (in/out), and can be expressed as functions of actuator displacement:

$$V_i(x) = \overline{V}_i + A_i x$$
$$V_o(x) = \overline{V}_o - A_o x \tag{3.22}$$

where $\overline{V}_i$ and $\overline{V}_o$ are the initial fluid volumes trapped in the blind end and the rod side of the actuator, respectively.

The relationship between the spool displacement, x_{sp}, and the input voltage, u, is usually expressed as a simple lag (first-order model) which is accurate enough to model low-cost proportional valves (Liu and Alleyne, 2000):

$$X_{sp}(s) = \frac{k_{sp}}{\tau s + 1} U(s) \tag{3.23}$$

where τ and k_{sp} are, respectively, the time constant and gain describing the valve dynamics. The valves used in the Unimate manipulator, however, have fast responses (small time constant); therefore, the above valve dynamics are reduced to a simple proportional relationship:

$$x_{sp} = k_{sp}\, u \tag{3.24}$$

Equations (3.14) to (3.24) express the relationship between the contact force, f, and the input control voltage, u.

These differential equations are dependent on the joint positions and velocities. Thus, they cannot be solved independently to yield the joint force/torque to be used in the manipulator's dynamics. These differential equations, however, can be added to the system of differential equations that defines the dynamics of the manipulator, integrated and solved with them simultaneously.

3.4 Linearized Actuator Dynamics

The nonlinear hydraulic equations of (3.17) and (3.18) can be linearized by using a Taylor's series expansion about a zero spool displacement operating point and neglecting the higher order terms. The following linearized model is obtained:

$$\begin{aligned} Q_t &= k_{x_t} x_{sp} - k_{p_t} p_t = C_t \dot{p}_t + A_t \dot{x} \\ Q_o &= k_{x_o} x_{sp} + k_{p_o} p_o = -C_o \dot{p}_o + A_o \dot{x} \end{aligned} \tag{3.25}$$

where metering coefficients, k_x and k_p (also called flow and pressure sensitivity gains, respectively) for extension and retracting cases, are given as follows:

for Extending ($x_{sp} \geq 0$)	for Retracting ($x_{sp} < 0$)
$k_{x_t} = C_d w \sqrt{\frac{2}{\rho}(p_s - p_t)}$	$k_{x_t} = C_d w \sqrt{\frac{2}{\rho}(p_t - p_r)}$
$k_{p_t} = \frac{C_d w x_{sp}}{\sqrt{2\rho(p_s - p_t)}}$	$k_{p_t} = \frac{-C_d w x_{sp}}{\sqrt{2\rho(p_t - p_r)}}$
$k_{x_o} = C_d w \sqrt{\frac{2}{\rho}(p_o - p_r)}$	$k_{x_o} = C_d w \sqrt{\frac{2}{\rho}(p_s - p_o)}$
$k_{p_o} = \frac{C_d w x_{sp}}{\sqrt{2\rho(p_o - p_r)}}$	$k_{p_o} = \frac{-C_d w x_{sp}}{\sqrt{2\rho(p_s - p_o)}}$

(3.26)

Note that coefficients k_{x_t} (or k_{x_o}) and k_{p_t} (or k_{p_o}) are load- and pressure-dependent variables and can only be considered as constants for a small range of operations. It is also helpful to mention that all the above coefficients are positive values for cases of both extension and retraction. The above linearized equations can be written in Laplace form:

$$P_i(s) = \frac{k_{x_i}}{C_i s + k_{p_i}} X_{sp}(s) - \frac{A_i s}{C_i s + k_{p_i}} X(s)$$
$$P_o(s) = \frac{-k_{x_o}}{C_o s + k_{p_o}} X_{sp}(s) + \frac{A_o s}{C_o s + k_{p_o}} X(s) \qquad (3.27)$$

Incorporating (3.27) into (3.15),

$$F_a = P_i A_i - P_o A_o = \left[\frac{k_{x_i} A_i}{C_i s + k_{p_i}} + \frac{k_{x_o} A_o}{C_o s + k_{p_o}}\right] X_{sp} - \left[\frac{A_i^2 s}{C_i s + k_{p_i}} + \frac{A_o^2 s}{C_o s + k_{p_o}}\right] X \qquad (3.28)$$

and equations (3.14) to (3.16) are combined to form the following transfer functions:

$$\frac{F}{F_a} = \frac{k_s(m_e s^2 + c_e s + k_e)}{(Ms^2 + Bs)(m_e s^2 + (c_s + c_e)s + (k_s + k_e)) + (c_s s + k_s)(m_e s^2 + c_e s + k_e)} \qquad (3.29a)$$

$$\frac{F}{X} = \frac{k_s(m_e s^2 + c_e s + k_e)}{m_e s^2 + (c_s + c_e)s + (k_s + k_e)} \qquad (3.29b)$$

from equations (3.28), (3.29) and (3.24), the actuator position and actuator/environment contact force will be:

$$\frac{X}{U} = \frac{k_{sp}(\boldsymbol{Z}_s + \boldsymbol{Z}_e)[k_{x_i} A_i (C_o s + k_{p_o}) + k_{x_o} A_o (C_i s + k_{p_i})]}{(C_i s + k_{p_i})(C_o s + k_{p_o})[\boldsymbol{Z}_a \boldsymbol{Z}_s + \boldsymbol{Z}_a \boldsymbol{Z}_e + \boldsymbol{Z}_s \boldsymbol{Z}_e] + [A_o^2 s(C_i s + k_{p_i}) + A_i^2 s(C_o s + k_{p_o})](\boldsymbol{Z}_s + \boldsymbol{Z}_e)} \qquad (3.30)$$

$$\frac{F}{U} = \frac{k_{sp} k_s \boldsymbol{Z}_e[k_{x_i} A_i (C_o s + k_{p_o}) + k_{x_o} A_o (C_i s + k_{p_i})]}{(C_i s + k_{p_i})(C_o s + k_{p_o})[\boldsymbol{Z}_a \boldsymbol{Z}_s + \boldsymbol{Z}_a \boldsymbol{Z}_e + \boldsymbol{Z}_s \boldsymbol{Z}_e] + [A_o^2 s(C_i s + k_{p_i}) + A_i^2 s(C_o s + k_{p_o})](\boldsymbol{Z}_s + \boldsymbol{Z}_e)} \qquad (3.31)$$

where $\boldsymbol{Z}_a = (Ms^2 + Bs)$, $\boldsymbol{Z}_s = (c_s s + k_s)$ and $\boldsymbol{Z}_e = (m_e s^2 + c_e s + k_e)$.

Assuming a special condition in which $C_i = C_o = C$, $k_{x_i} = k_{x_o} = k_x$, and $k_{p_i} = k_{p_o} = k_p$, the transfer functions (3.30) and (3.31) are reduced to:

$$\frac{X}{U} = \frac{k_{sp}k_x(A_i + A_o)(\boldsymbol{Z}_s + \boldsymbol{Z}_e)}{(Cs + k_p)[(\boldsymbol{Z}_a\boldsymbol{Z}_s + \boldsymbol{Z}_a\boldsymbol{Z}_e + \boldsymbol{Z}_s\boldsymbol{Z}_e) + (A_i^2 s + A_o^2 s)(\boldsymbol{Z}_s + \boldsymbol{Z}_e)]} \tag{3.32}$$

$$\frac{F}{U} = \frac{k_{sp}k_s k_x \boldsymbol{Z}_e(A_i + A_o)}{(Cs + k_p)[(\boldsymbol{Z}_a\boldsymbol{Z}_s + \boldsymbol{Z}_a\boldsymbol{Z}_e + \boldsymbol{Z}_s\boldsymbol{Z}_e) + (A_i^2 s + A_o^2 s)(\boldsymbol{Z}_s + \boldsymbol{Z}_e)]} \tag{3.33}$$

When the manipulator performs unconstrained motion in space, $\boldsymbol{Z}_e = 0$. Thus, Eq. (3.29) is reduced to the following fourth-order, type one transfer function:

$$\begin{aligned}\frac{X}{U} &= \frac{k_{sp}(k_{x_i}A_iC_o + k_{x_o}A_oC_i)s + (k_{x_i}A_ik_{p_o} + k_{x_o}A_ok_{p_i})}{D(s)} \\ D(s) &= MC_iC_os^4 + [M(k_{p_i}C_o + k_{p_o}C_i) + BC_iC_o]s^3 \\ &\quad + [Mk_{p_i}k_{p_o} + B(k_{p_i}C_o + k_{p_o}C_i) + (A_i^2C_o + A_o^2C_i)]s^2 \\ &\quad + [Bk_{p_i}k_{p_o} + (A_i^2k_{p_o} + A_o^2k_{p_i})]s\end{aligned} \tag{3.34}$$

3.5 Environment

A simply supported aluminum plate was used as the environment for force control tests. By varying the support spacing, the environmental stiffness could be varied over an order of magnitude. Stiffnesses of ≈10,000N/m and ≈42,000N/m were used as low stiffness and high stiffness environments in experimental force control tests. Accurate stiffness measures were not needed since the force control methods were expected to work properly over a wide range of environmental stiffnesses. The range of

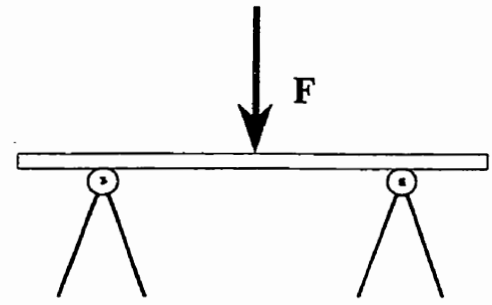

Fig. 3.6. Pure stiffness environment

environmental stiffnesses could be wider as, in the simulation tests, stiffnesses up to 140,000N/m are tested. Experimental tests, however, are limited to lower forces and lower stiffness environments, because the force sensor could not be used for forces over 500N.

3.6 Simulation Program

A complete simulation program for the hydraulic manipulator under investigation has been developed. Almost all non-idealities and nonlinear aspects such as nonlinear dynamics, flow deadband, saturation, stick-slip friction have been considered in the simulation program. In the simulation program, every attempt has been made to have the structure and physical parameters of the manipulator resemble the Unimate hydraulic robot. The accuracy of the simulation results has already been verified. Fig. 3.7 shows an example of the compatibility between the simulation and the experimental results. This figure compares the open loop response of the system to sinusoidal, ramp and step inputs in simulation and experiment.

This simulation program proved to be very instrumental in this research since many different design alternatives and scenarios that would possibly happen could be evaluated before applying them to the real system.

3.7 Summary

In this chapter, the kinematic and dynamic models of the Unimate MK-II hydraulic manipulator were derived. In this modeling work, detailed dynamics of the manipulator were incorporated. This includes nonlinear hydraulic valve characteristics, flow

deadband, saturation and stick-slip friction at the manipulator's joints. The environment was modeled as a pure stiffness. This type of environment has enjoyed popularity amongst many similar researches. The simulation software is running on a C program, and is capable of approximating the dynamics of the physical system sufficiently. There still exists a slight quantitative mismatch between the simulated and measured line pressures. Nevertheless, the resulting movement of each link is accurately simulated. Therefore, the model provides simulation capabilities to facilitate controller design. In particular, as will be shown later, the simulation model is instrumental in performance analysis of various position and impedance-based force-tracking controllers before they are actually tested on the real manipulator.

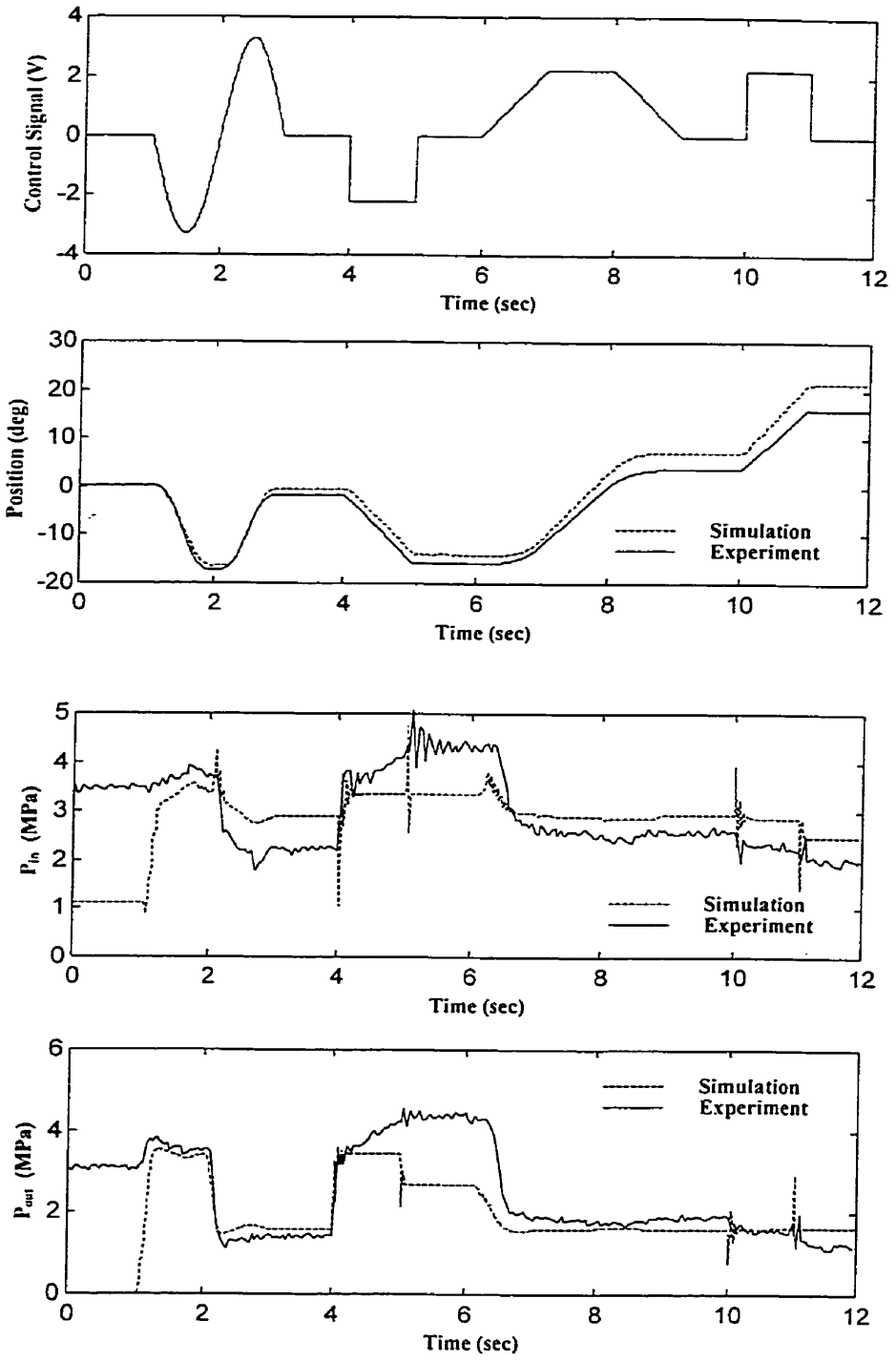

Fig. 3.7. Comparison of simulation with actual system (open loop) response to same specified input control signal to the up/down link including sinusoidal, step and ramp inputs

Chapter 4

The Application of Position-Based Impedance Control to Hydraulic Manipulators

Design of an impedance control for the Unimate hydraulic manipulator is addressed in this chapter which will be used later for the purpose of force control. As previously explained, the suitable form of impedance control for hydraulic manipulators is a position-based one. First, the structure of the position-based impedance controller (PBIC) is described and it is shown that the technique involved relies heavily on the accuracy of the nested positioner. Next, the step-by-step development of the position controller is described. The performance of the PBIC is then studied through three different tests.

4.1 Position-Based Impedance Controller Structure

The general block diagram of the position-based impedance control for the Unimate hydraulic manipulator is shown in Fig. 4.1.

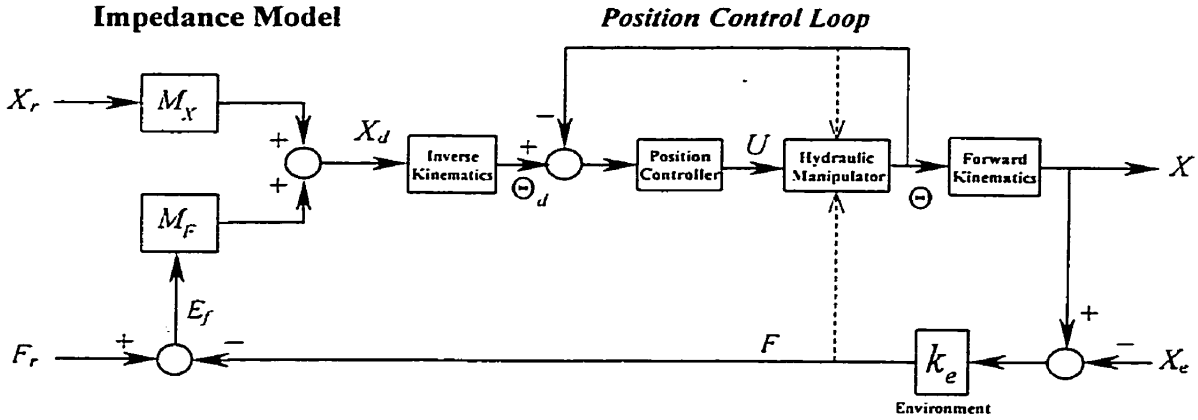

Fig. 4.1. Position-based impedance controller as applied to a hydraulic manipulator

X_r and F_r are the position and force set-points, respectively. M_X and M_F are second-order transfer functions that work on position reference, X_r, and force error, $E_f = F_r - F$, to form the desired end-effector Cartesian position, X_d. Through inverse kinematics, the desired position is transferred from Cartesian coordinates to the joint space coordinates to form Θ_d, the desired joint space trajectory. Θ_d is then passed to the position controller in the inner loop.

With reference to Fig. 4.1, the impedance model is broken into two parts: M_X is a transfer function modifying the position reference, and M_F modifies the force error.

$$X = X_d = M_X X_r + M_F(F_r - F) \tag{4.1}$$

Three different formulations of the linear second-order target impedance, Eq. (2.4), have been used in different occasions throughout this research.

The first formulation of second-order target impedance, Eq. (2.4a), has been used in direct adaptive force control, as discussed in Section 5.6.

$$M\ddot{x}(t) + C\dot{x}(t) + K(x(t) - x_r(t)) = e_f(t)$$

This formulation corresponds to the illustration in Fig. 4.2.

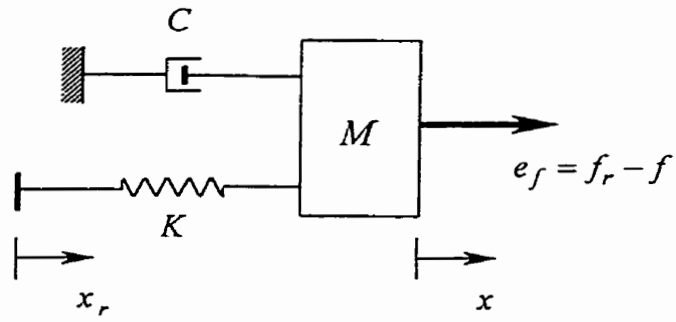

Fig. 4.2. Physical interpretation of target impedance model of Eq. (2.4a)

M_X and M_F are therefore

$$M_X = \frac{K}{Ms^2 + Cs + K}\ ,\ M_F = \frac{1}{Ms^2 + Cs + K} \tag{4.2}$$

The second formulation of second-order target impedance, Eq. (2.4b), has been used in Section 4.3 to study the behavior of position-based impedance control.

$$M\ddot{x}(t) + C\big(\dot{x}(t) - \dot{x}_r(t)\big) + K\big(x(t) - x_r(t)\big) = e_f(t)$$

This formulation corresponds to the illustration in Fig. 4.3 and gives a good physical sense.

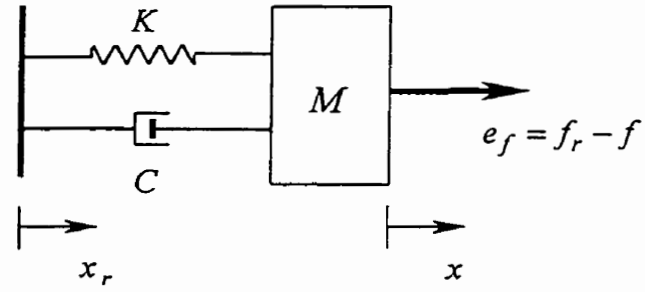

Fig. 4.3. Physical interpretation of target impedance model of Eq. (2.4b)

M_X and M_F are therefore

$$M_X = \frac{Cs + K}{Ms^2 + Cs + K}\ ,\ M_F = \frac{1}{Ms^2 + Cs + K} \tag{4.3}$$

The third formulation of second-order target impedance, Eq. (2.4c), has been used in indirect adaptive force control discussed in Section 5.4.

$$M\left(\ddot{x}(t)-\ddot{x}_r(t)\right)+C\left(\dot{x}(t)-\dot{x}_r(t)\right)+K\left(x(t)-x_r(t)\right)=e_f(t)$$

This formulation corresponds to the illustration in Fig. 4.4.

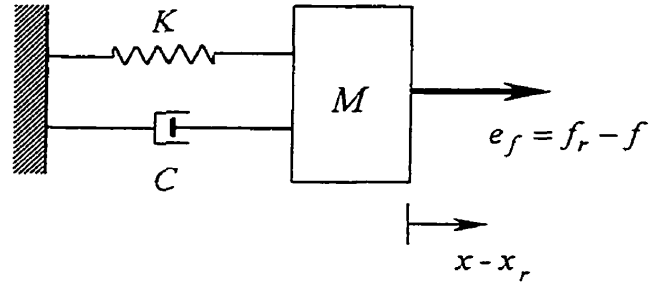

Fig. 4.4. Physical interpretation of target impedance model of Eq. (2.4c)

M_X and M_F are therefore

$$M_X = \frac{Ms^2+Cs+K}{Ms^2+Cs+K} = 1 \;,\; M_F = \frac{1}{Ms^2+Cs+K} \tag{4.4}$$

4.2 Development of a Nonlinear PI Position Controller

Position-based impedance control technique requires a positioner that performs very well at both regulating and tracking, as well as with large and small commanded inputs. Conventional PI(D) position controllers are widely used in practice even in some of the most recent advanced applications. This is mainly due to their simplicity, reliability and a favorable ratio between performance and cost in industrial environments. Due to this popularity, there are many studies that deal with the tuning rules and implementation details of such conventional controllers (Brambilla et al., 1989; Khayyat et al., 1996). In particular, integral action has received much attention. Integral controls are mainly used to compensate for steady-state errors without the need of a high proportional gain.

However, they may cause limit cycling due to the existence of unavoidable dry friction in the mechanical part of the components to be controlled, or may develop large overshoots and long settling times due to the actuator saturation. Some techniques have been proposed to circumvent these shortcomings (Bohn and Atherton, 1995; Khayyat et al., 1996).

In spite of many articles on PI(D) control applications in process or electric-servo control systems, the application of PI controls to hydraulic manipulators has received less attention. Here, for the first time, a performance qualification of the application of the patented integration technique by Morse et al. (1988) on hydraulic functions is presented. The goal is to identify a suitable method that requires a minimum knowledge of the machine model, can be easily adopted and tuned in practical situations, and demands minimum computational effort. Furthermore, the controller must contend with many nonlinearities in hydraulic function, such as nonlinear dynamics, actuator flow deadband, saturation and stiction. Finally, it should be equally well-behaved in both regulating and tracking tasks – traditionally, integral controllers are designed either as regulating or as tracking controllers (Eitelberg 1987; Khayyat et al. 1996).

The simulation and experimental study is performed using the up/down link of the Unimate hydraulic manipulator. The experimental benchmark test consists of both step and ramp tracking set-points for the purpose of comparing different characteristics of the featured integrators. The purpose of the step-input test is to evaluate the regulating ability and to display transient responses, while the purpose of the trajectory tracking experiment is to test the capability of the controller to follow reference changes. Furthermore, a 1Hz sine wave of diminishing amplitude input is tested which is believed

to be a demanding test to characterize the performance of different position controllers in response to fast changes in both position and velocity of the set-point. The above mentioned tests are also repeated for a tenfold different amplitude. Thus, each controller is evaluated with three tests. The first two tests include step and ramp inputs with tenfold different amplitudes, and the last two tests are diminishing sine waves, again with tenfold different amplitudes.

4.2.1 Proportional Control

A simple P-controller with best performing proportional gain was the first to be tested. The P-controller performed poorly both in tracking and regulating. Since the dynamics of the hydraulic actuator are of type one [see Eq. (3.34)], in theory the P-controller should have no steady-state error in regulating. However, due to the existence of valve deadband and stiction in the hydraulic actuators, some steady-state error in regulating is unavoidable (see Figs. 4.5 and 4.6). In the tracking portion of the responses, a zero position error would result in the proportional controller closing the valve and stopping the motion; thus, some error must appear in tracking. Therefore, the P-controller has a lag following the commanded tracking set-point (see Figs. 4.5 to 4.8). Finally, the effects of stiction and valve deadband are most apparent in the complete failure to track the fine sine wave pattern (Fig. 4.8).

4.2.2 Conventional PI Controller

A conventional linear PI-controller, with the same proportional gain and best performing integral gain was the next to be tested. The PI-controller improved the steady-state error and performed much better in tracking a ramp (see Figs. 4.9 and 4.10). It, however, had

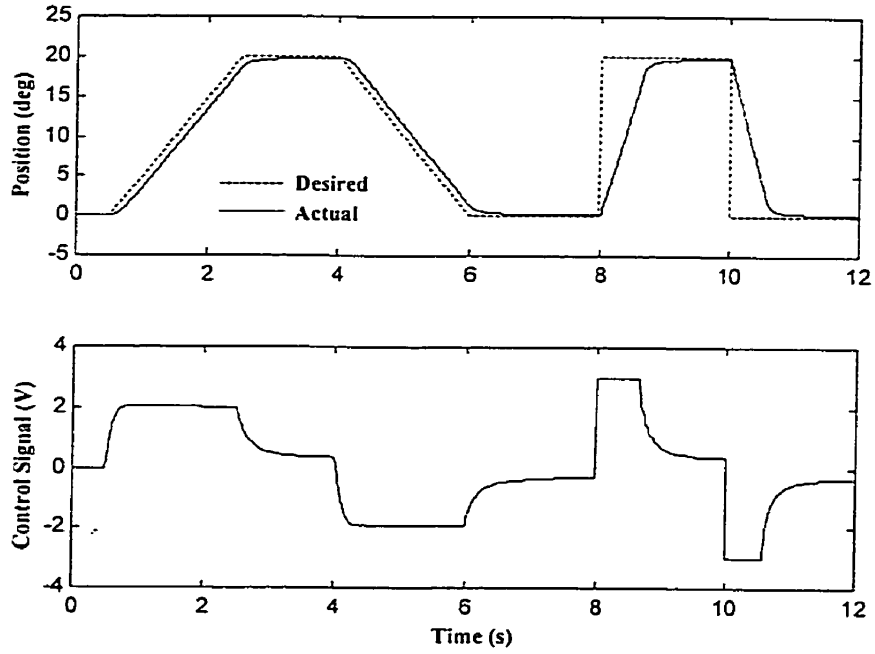

Fig. 4.5. Large step and ramp input responses of proportional controller: simulations ($k_p = 950$)

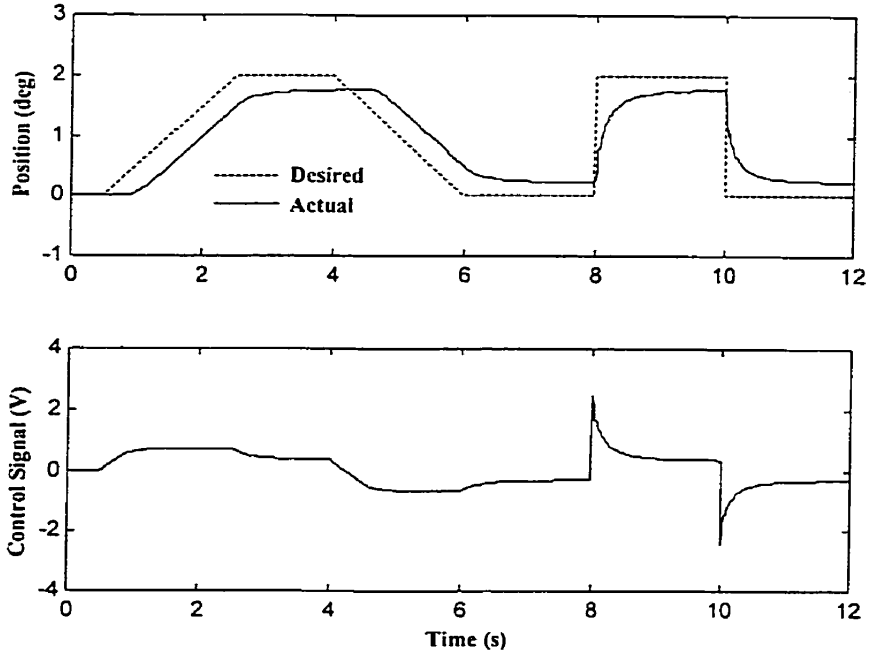

Fig. 4.6. Small step and ramp input responses of proportional controller: simulations ($k_p = 950$)

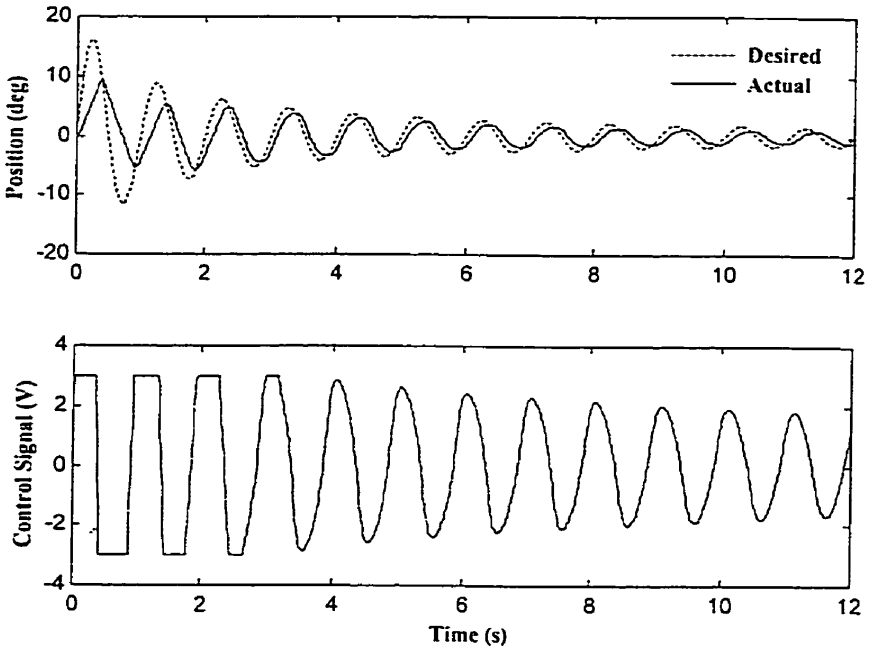

Fig. 4.7. Large diminishing sine wave input response of proportional controller: simulations ($k_p = 950$)

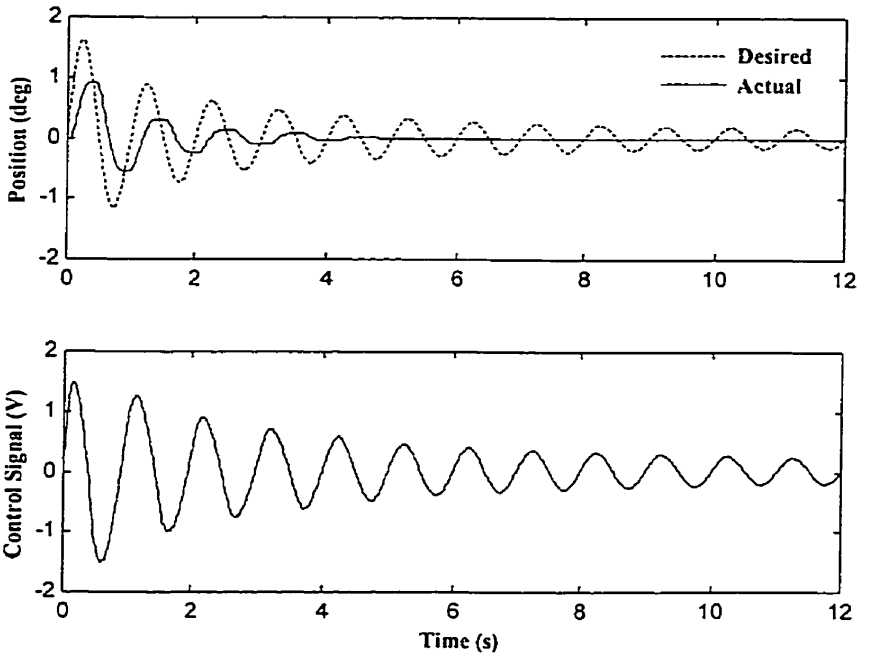

Fig. 4.8. Small diminishing sine wave input response of proportional controller: simulations ($k_p = 950$)

large overshoots in regulation due to the integral wind-up (see Figs. 4.9 and 4.10). Because of saturation phenomenon, conventional PI-controllers face integral wind-up during step regulations, especially for large input commands (Aström and Hägglund, 1988). With reference to Fig. 4.12, it is seen that the controller did not show much improvement overcoming the stiction and valve deadband problem, which is apparent in its failure to follow the fine sine wave pattern. The PI-controller followed the large sine wave pattern only slightly better than its counterpart, the P-controller (see Fig. 4.11).

4.2.3 Anti-wind-up Integral

The large overshoot and long settling time seen in Fig. 4.9 is due to integral wind-up. Since a controller operates over a wide range of operating conditions, it may happen that the control variable reaches the actuator's limit. When this happens the feedback loop is effectively broken because the actuator remains at its limit independent of the process output. If a controller with integral action is used, the error will continue to be integrated. This means that the integral term may become very large or, colloquially, it "winds up". It is then required that the error change sign for a long period before things return to normal. The consequence of this is that any controller with integral action may give large transients when the actuator saturates as can be seen in Fig. 4.9. The set-point change at $t = 8\,\mathrm{s}$ is so large that the actuator saturates. The integrator increases initially because the error is positive, and it reaches its largest value at time $t = 8.6\,\mathrm{s}$ when the error goes through zero. The control signal remains saturated at this point because of the large value

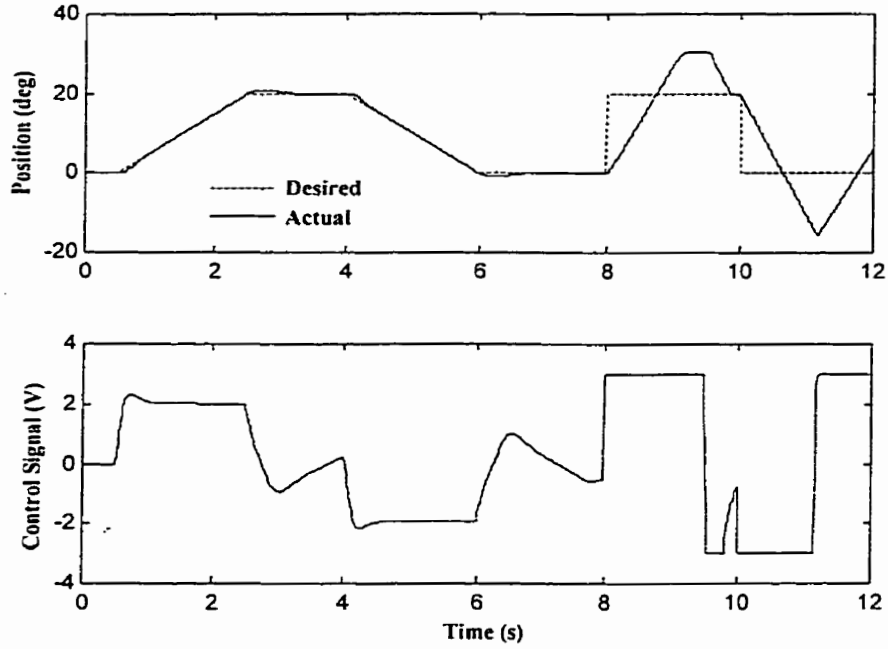

Fig. 4.9. Large step and ramp input responses of PI controller: simulations ($k_p = 950$, $k_i = 6000$)

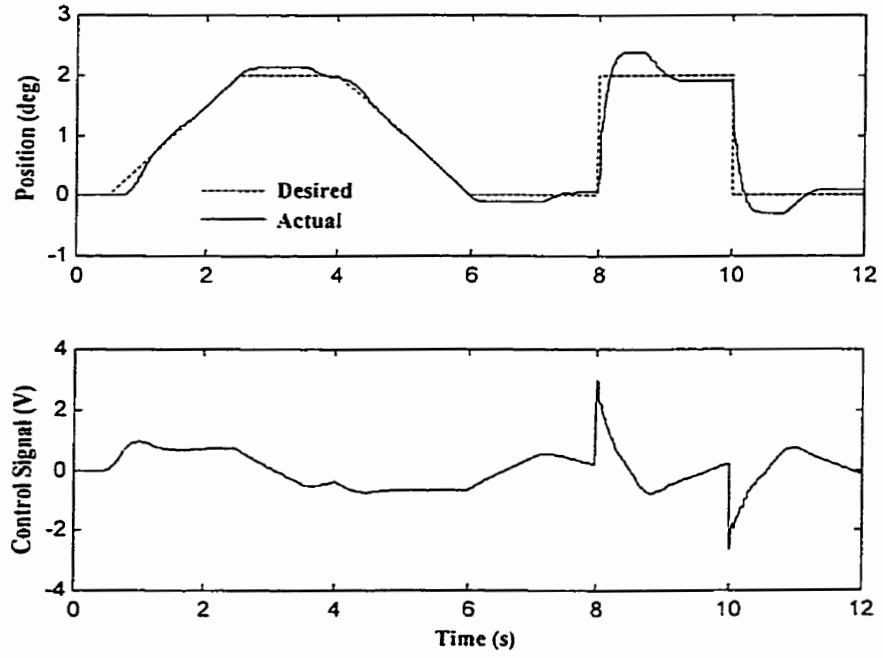

Fig. 4.10. Small step and ramp input responses of PI controller: simulations ($k_p = 950$, $k_i = 6000$)

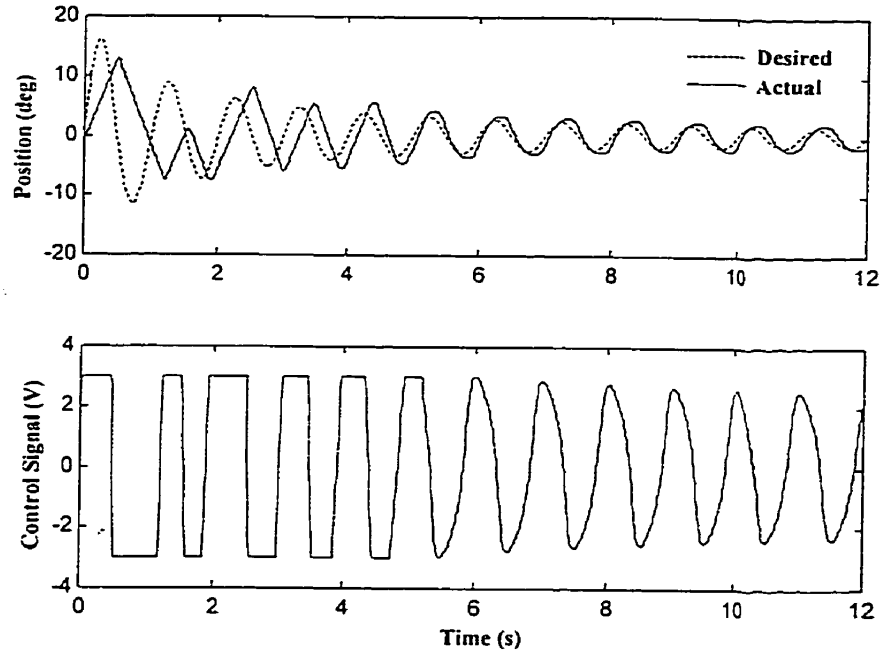

Fig.4.11. Large diminishing sine wave input response of PI controller: simulations ($k_p = 950$, $k_i = 6000$)

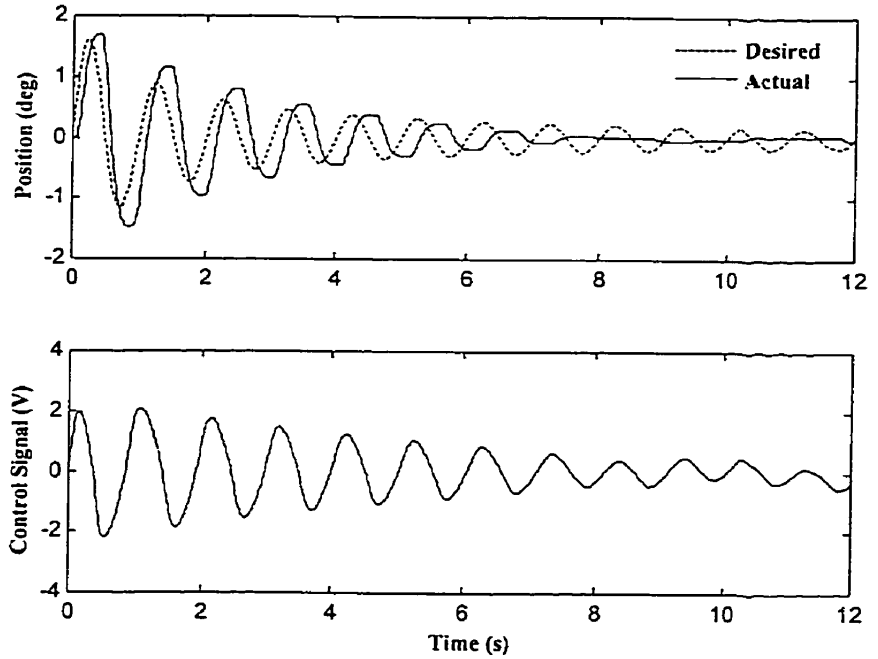

Fig. 4.12. Small diminishing sine wave input response of PI controller: simulations ($k_p = 950$, $k_i = 6000$)

of the integral component, and it does not leave the saturation limit until the error has been negative for a sufficiently long time to let the integral part wind down to an appropriate level. The net effect is a large overshoot, which is noticeable in Fig. 4.9.

Tracking anti-wind-up integral action as suggested by Aström and Hägglund (1988), was first applied to eliminate overshoot caused by integral wind-up. The tracking anti-wind-up integrator is formulated as below and is shown in Fig. 4.13.

$$I(t) = \left[I(t - \Delta t) + k_i e_\theta(t)\Delta t - k_t e_s(t)\Delta t \right] \tag{4.5}$$

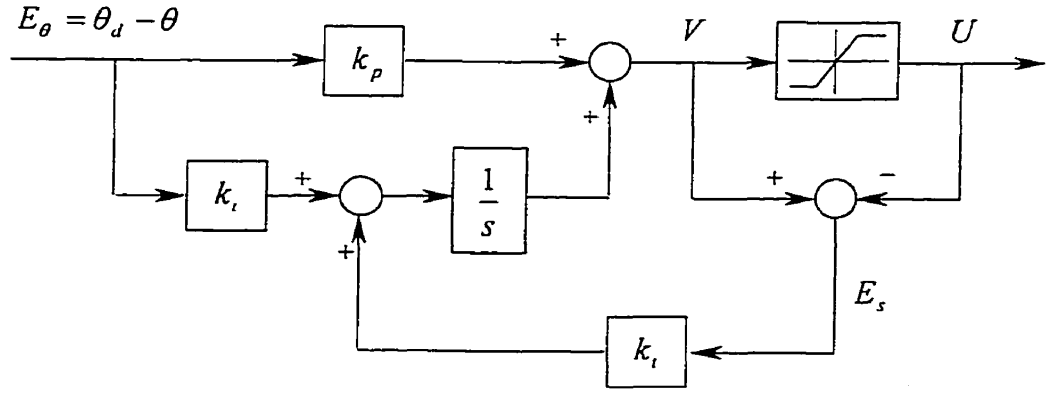

Fig. 4.13. Anti-wind-up applied to the PI controller

An extra feedback path is provided in the controller by measuring the actual actuator output and forming an error signal, e_s, as the difference between the output of the controller, v, and the actuator output, u. The error signal, e_s, is fed back to the input of the integrator through the feedback gain, k_t. The signal is zero when there is no saturation. It will thus have no effect on normal operation when the actuator does not saturate. However, when the actuator saturates, the feedback signal will attempt to drive

the error, e_s, to zero. This means that it will attempt to drive the integrator to a value such that the controller output is exactly at the saturation limit. This will clearly prevent the integrator from winding up. The rate at which the controller output is reset is governed by the feedback gain, k_t.

Using the same proportional gain as before, Aström's anti-wind-up integral allowed a sixfold higher integral gain and removed the overshoot problem. This controller improved both regulating and tracking responses (see Figs. 4.14 to 4.17). However, it only worked well for the large amplitudes of inputs that it was adjusted for (see Figs. 4.14 and 4.15). It also still had problems with stiction and valve deadband, and also had some significant overshoots in tracking the fine sine wave pattern (see Fig. 4.17). The slight oscillations about the set-point in steady-state (also called hunting) is due to high integral gain combined with the joint stick-slip friction. The integral action initially builds up its signal until the manipulator breaks free from the stick friction at the arm joint; the arm then experiences overshoot and comes to rest on the opposite side of the origin. The reaction continues again on the return motion.

4.2.4 Rate-Varying Integral

Seeking a better controller performance, Morse et al.'s (1988) patented rate-varying integral control was examined. This controller uses a proportional plus nonlinear integral method. The algorithm differs from the linear PI-control in the calculation of the error integral $I(t)$:

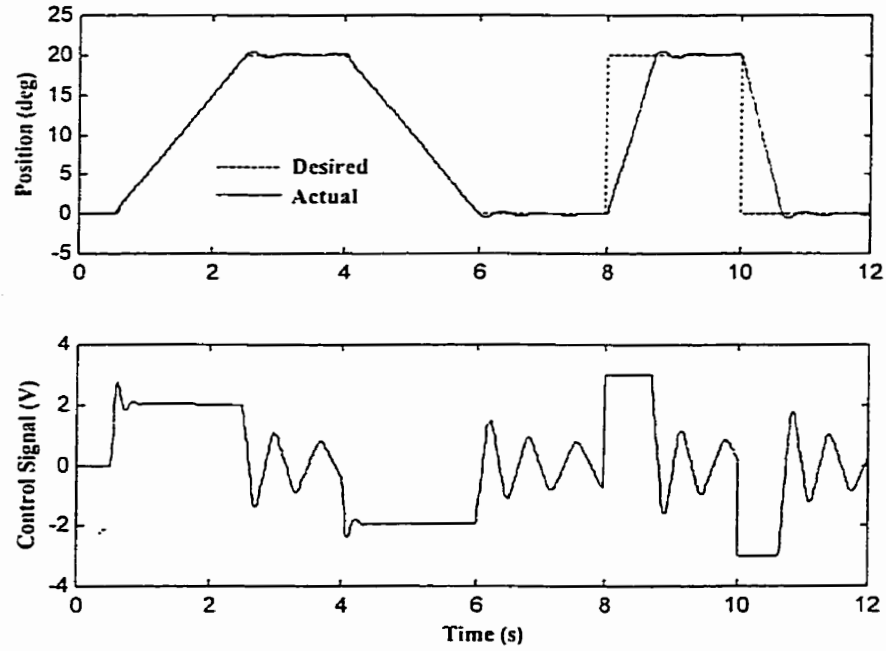

Fig. 4.14. Large step and ramp input responses of anti-wind-up integral controller: simulations ($k_p = 950$, $k_i = 38000$, $k_t = 650$)

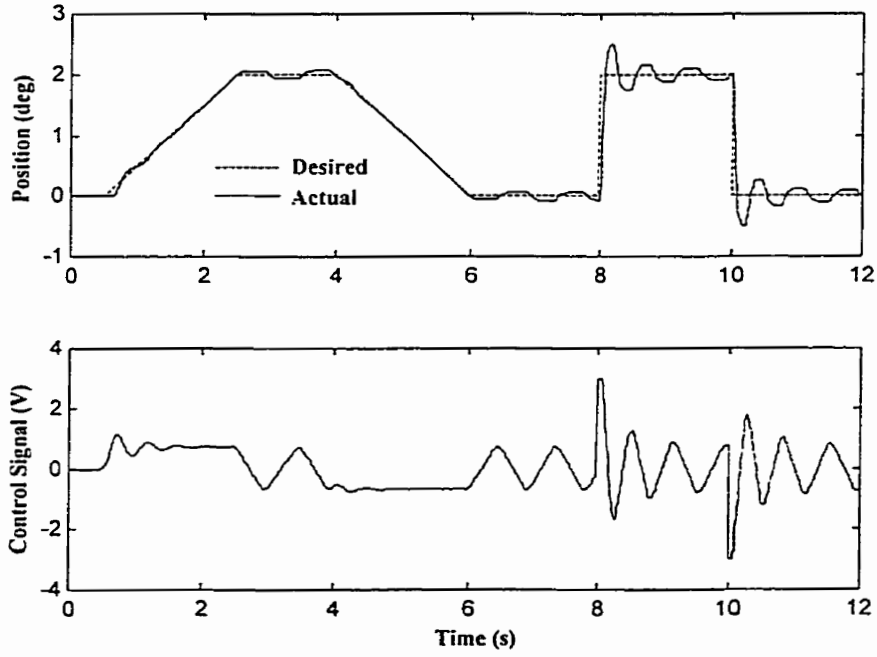

Fig. 4.15. Small step and ramp input responses of anti-wind-up integral controller: simulations ($k_p = 950$, $k_i = 38000$, $k_t = 650$)

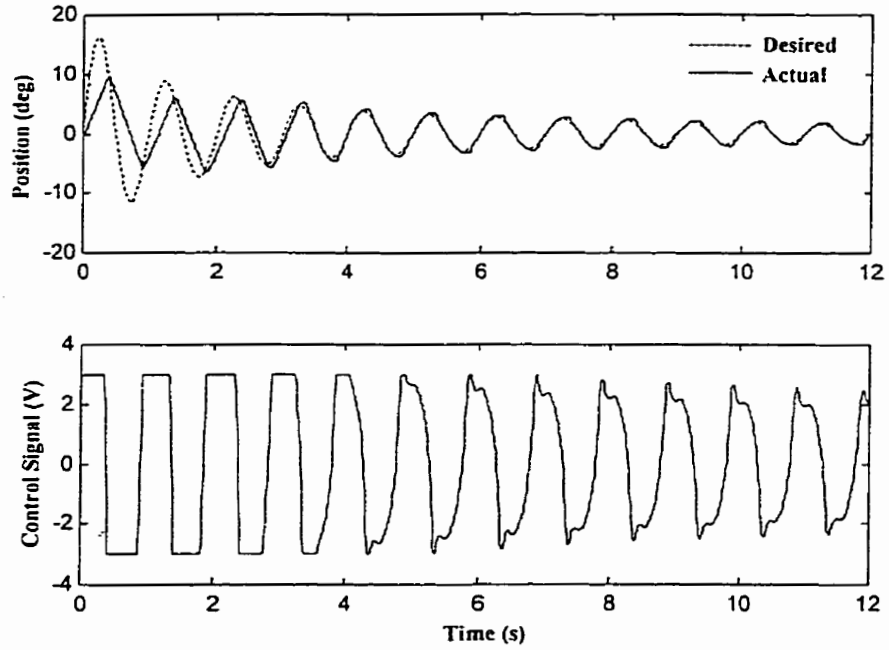

Fig. 4.16. Large diminishing sine wave input responses of anti-wind-up integral controller: simulations ($k_p = 950$, $k_i = 38000$, $k_t = 650$)

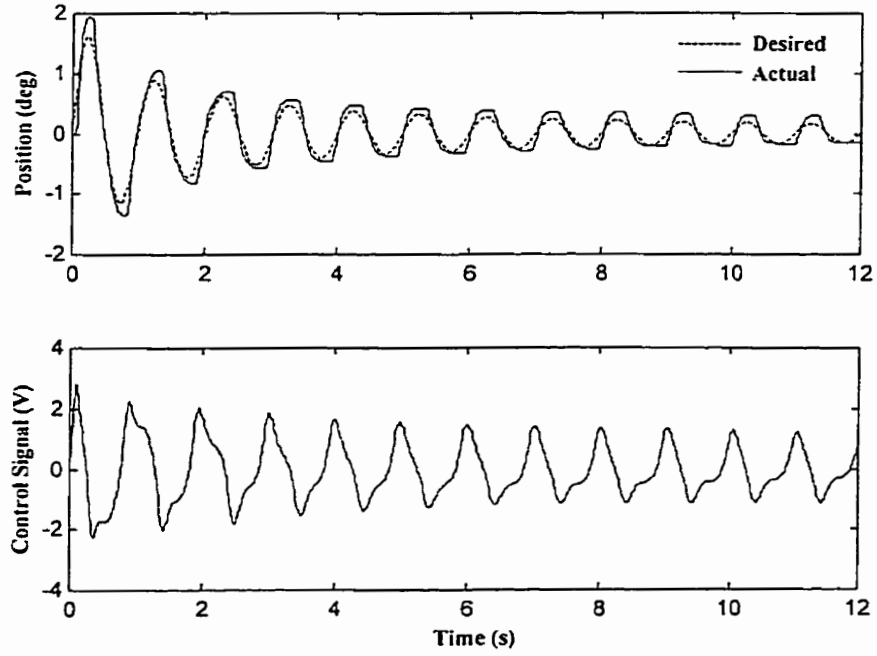

Fig. 4.17. Small decreasing sine wave input responses of anti-wind-up integral controller: simulations ($k_p = 950$, $k_i = 38000$, $k_t = 650$)

$$I(t) = (I(t - \Delta t) + e_\theta(t)\Delta t)\frac{\alpha}{\alpha + \dot{\theta}^2(t)} \tag{4.6}$$

where α is an arbitrary constant, θ is the controlled joint angle, $e_\theta = \theta_d - \theta$ is the joint position error, θ_d is the joint position set-point and Δt is the sampling time interval. The nonlinear multiplier (rate-varying factor)

$$f_{rv} = \frac{\alpha}{\alpha + \dot{\theta}^2(t)} \tag{4.7}$$

is as high as unity when the velocity $\dot{\theta}(t)$ approaches zero, indicating that the integrator is at full power; it approaches zero in a continuous fashion as the velocity increases. This factor is less than unity for any non-zero joint velocity, allowing the use of higher integral gains and increasing the control action at low speeds. Therefore, the method is most active when the load velocity is low, in which period, sticking is imminent. Figs. 4.18 and 4.19 show no sign of stiction or hunting due to stick-slip friction. The constant gain α determines a cutoff between high and low velocities. Also, because the entire accumulated integral was iteratively multiplied by this factor, the integral resets itself at high velocities, thereby eliminating the problems of windup and overshoot (see Figs. 4.18 and 4.19). For the same reason, however, the integrator failed to perform well during the trajectory tracking test, being no better than straight P-control (see Figs. 4.18 to 4.21). This is due to the fact that the method specifically pertains to controllers where the rate varying factor goes to zero as the velocity approaches infinity. Therefore, there will always be velocities at which the system is not effective in ensuring proper tracking along the selected trajectory. This approach, therefore, works well for regulating; however, if high-speed trajectory tracking is desired, it is no better than a pure P-controller.

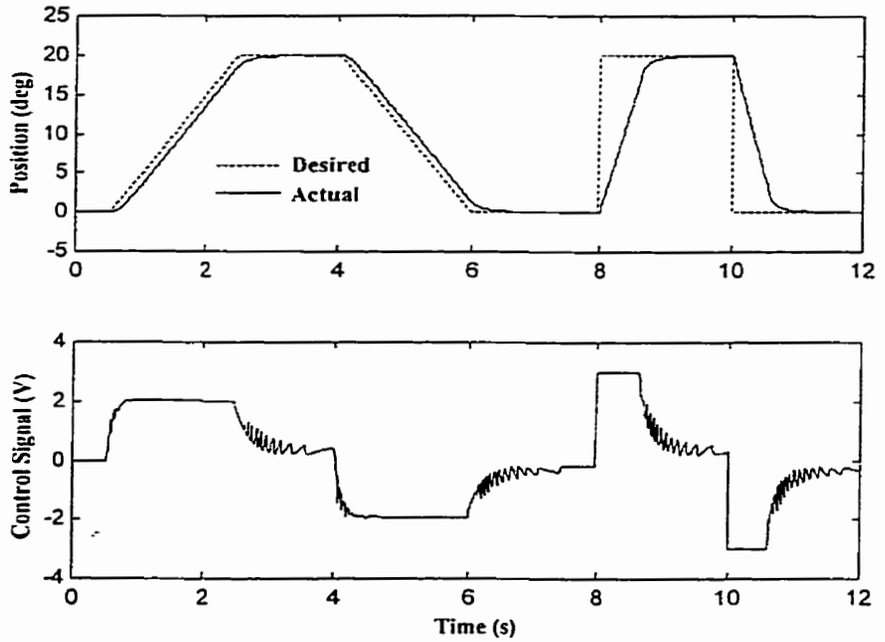

Fig. 4.18. Large step and ramp input responses of rate-varying integral controller: simulations ($k_p = 950$, $k_i = 38000$, $\alpha = 0.01$)

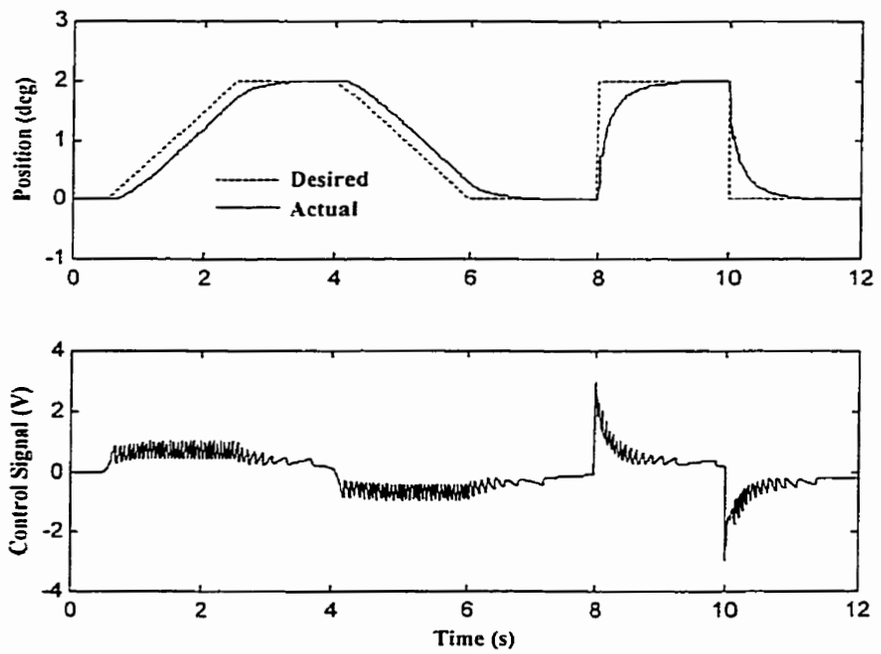

Fig. 4.19. Small step and ramp input responses of rate-varying integral controller: simulations ($k_p = 950$, $k_i = 38000$, $\alpha = 0.01$)

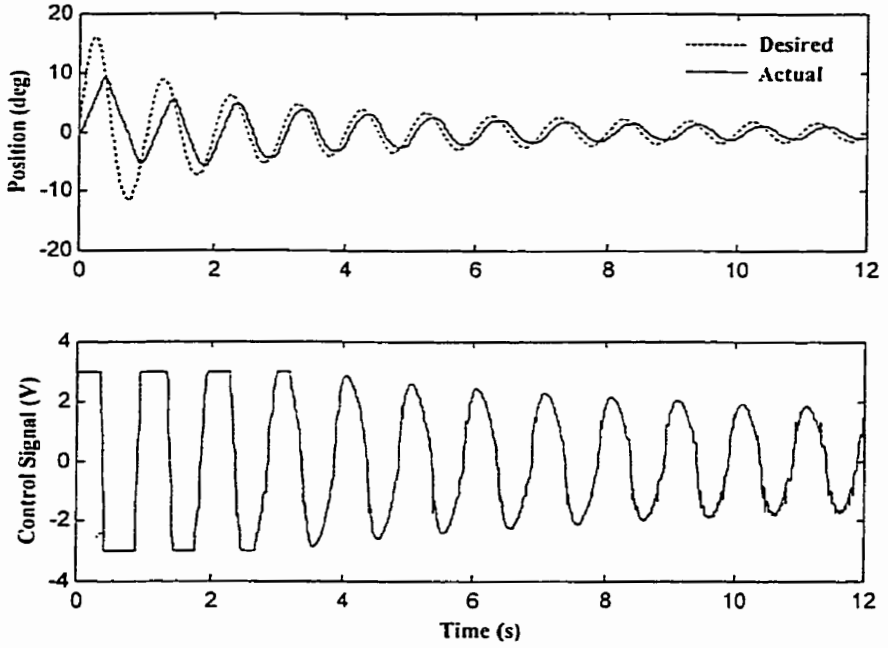

Fig. 4.20. Large diminishing sine wave input response of rate-varying integral controller: simulations ($k_p = 950$, $k_i = 38000$, $\alpha = 0.01$)

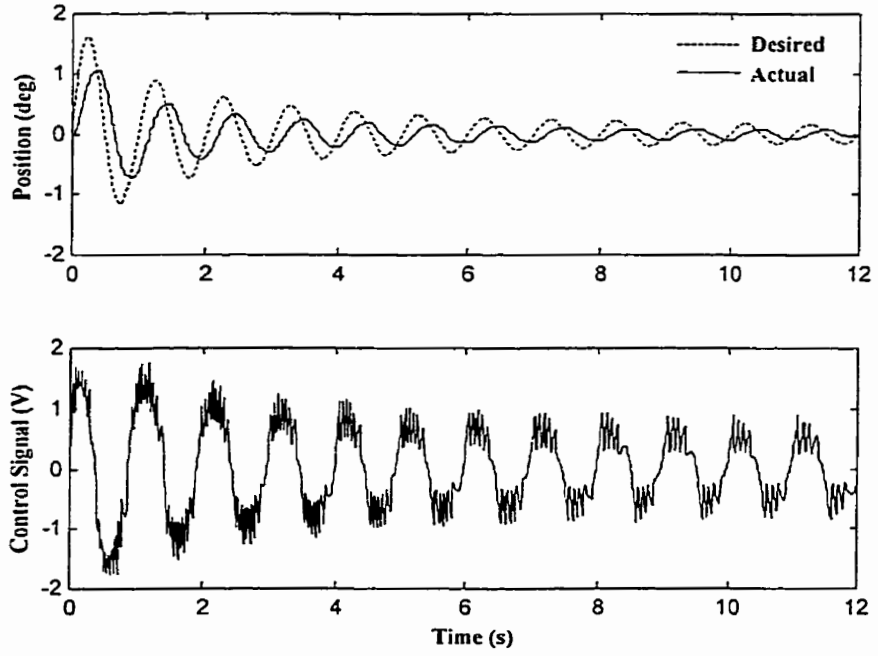

Fig. 4.21. Small diminishing sine wave input response of rate-varying integral controller: simulations ($k_p = 950$, $k_i = 38000$, $\alpha = 0.01$)

4.2.5 Modified Rate-Varying Integral

In order to improve the tracking capability of the rate-varying integral method by Morse et al. (1988), the error-rate (velocity error), $\dot{e}_\theta(t) = \dot{\theta}_d(t) - \dot{\theta}(t)$, was used in the nonlinear factor, f_{rv}, instead of the velocity, $\dot{\theta}(t)$.

$$I(t) = \left(I(t-\Delta t) + e_\theta(t)\Delta t\right)\frac{\alpha}{\alpha + \dot{e}_\theta^2(t)} \tag{4.8}$$

The proposed modification has two advantages. The first is that the controller has no problem tracking high velocity ramps since the integral will only reset in situations where integral wind-up is a possibility, i.e. when the error is rapidly changing. Figs. 4.22 to 4.25 show the superior capability of the modified method in tracking the set-point. The second advantage is that for regulation (i.e. step changes in the set-point), aside from having a relatively larger value for α, the modified method is almost indistinguishable from the original. Figs. 4.22 and 4.23 show a fast step response with almost no overshoot.

The disadvantage to this modification is that the anti-stiction property of the original method by Morse et al. (1988) is slightly degraded, and the larger α incorporated in modified method leads to a stronger integral during the steady-state which leads to hunting due to stick-slip friction. This phenomenon is shown in Figs. 4.22 and 4.23. When the set-point is not being followed due to the effects of stiction friction, the joint velocity, $\dot{\theta}(t)$, is zero but the velocity error, $\dot{e}_\theta$, is large. The rate varying factor, $f_{rv} = \frac{\alpha}{\alpha + \dot{\theta}^2(t)}$, belonging to the original method by Morse et al., is unity during this period and provides full controller action, whereas the present modified rate-varying factor,

$f_{nl} = \frac{\alpha}{\alpha + \dot{e}_\theta^2(t)}$, is small when stiction occurs, and is therefore not as effective as the original factor. However, simulation and experimental results showed that the higher gains allowed by the incorporation of the nonlinear factor still provided improved response time over the conventional PI controller.

To assist in fine movements, especially to remove the hunting effect created by the previous modification, a second modification is applied to the rate-varying integral controller. From Eq. (4.8), it is apparent that a large α leads to a stronger and more linear integral. On the other hand, a small α leads to a relatively weaker but more nonlinear integral, because a small α brings the integral to zero very quickly after any movement. The cutoff velocity parameter, α, in this modification is linked to the set-point velocity, $\dot{\theta}_d$. The controller is tuned using a certain maximum velocity, $\dot{\theta}_{\max}$, and the value of $\alpha_{\max}$ thereby obtained is then used in the calculation of α as follows:

$$\alpha = \alpha_{\max}\left(\gamma + \frac{|\dot{\theta}_d|}{\dot{\theta}_{\max}}\right) \tag{4.9}$$

where γ is a small constant that defines the ratio between $\alpha_{\max}$ (at maximum commanded joint velocity) and minimum α (at steady-state or zero commanded joint velocity).

Linking the nonlinear factor α to the set-point velocity, $\dot{\theta}_d$, as described by Eq. (4.9), leads to a relatively weaker integral when the set-point is barely changing, as in steady-state, compared to the case of tracking a steep ramp. Therefore, this modification reduces the hunting effect seen in the steady state portions of Figs. 4.22 and 4.23. Figs. 4.26 and 4.27 show that this modification not only has a great capability of tracking ramps, but

also is faster than the original method developed by Morse et al. during step input changes. Figs. 4.28 and 4.29 show this modified version's great capability of tracking sine waves; however, they also illustrate that the problems with deadband and stiction still remains.

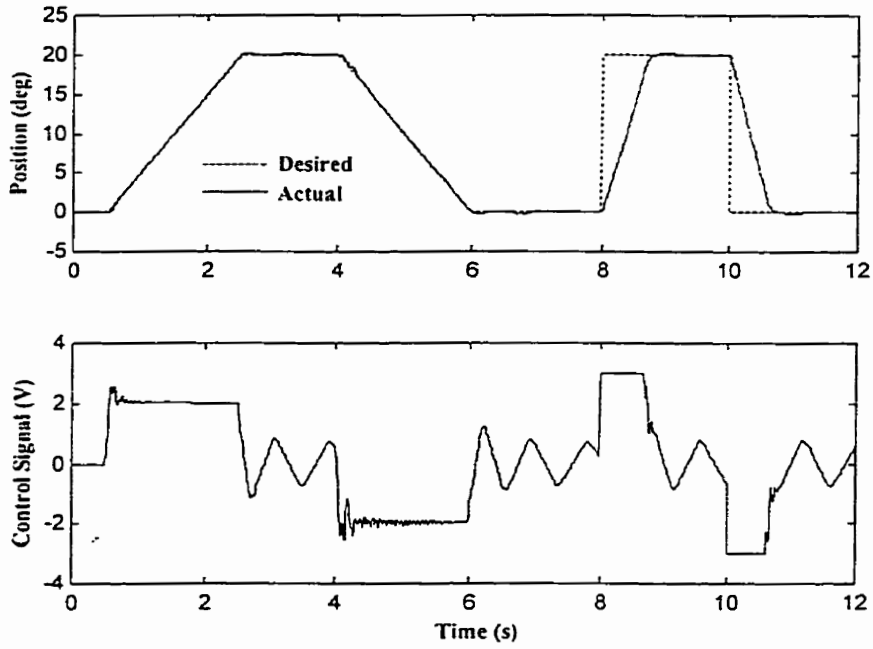

Fig. 4.22. Large step and ramp input responses of modified rate-varying integral Controller: simulations ($k_p = 950$, $k_i = 38000$, $\alpha = 15000$)

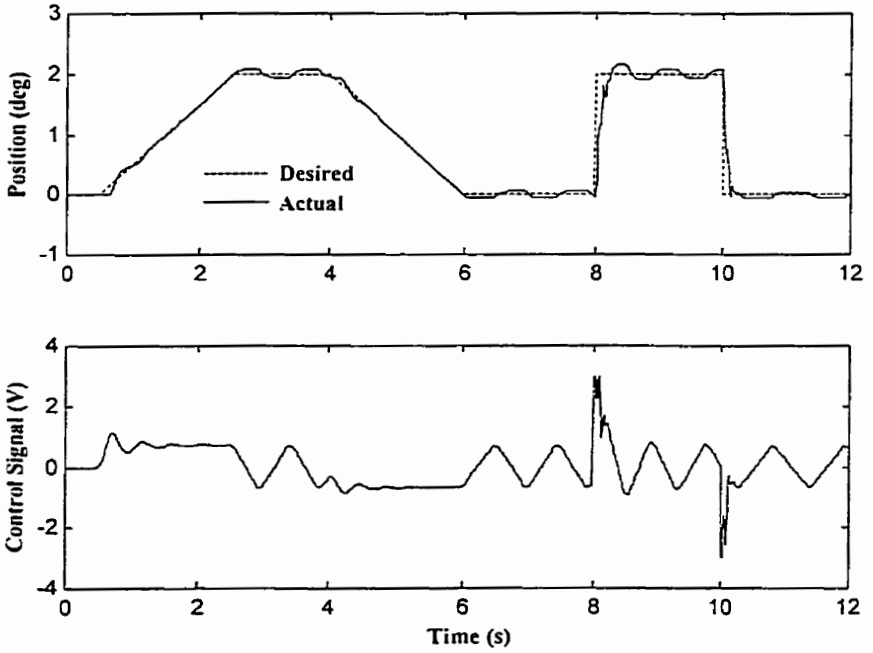

Fig. 4.23. Small step and ramp input responses of modified rate-varying integral Controller: simulations ($k_p = 950$, $k_i = 38000$, $\alpha = 15000$)

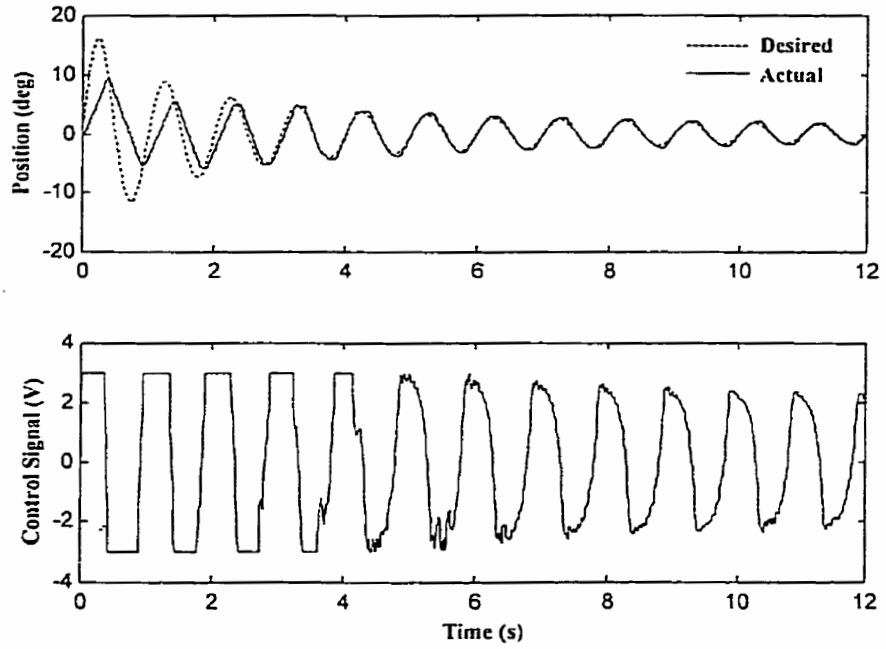

Fig. 4.24. Large diminishing sine wave input response of modified rate-varying integral Controller: simulations ($k_p = 950$, $k_i = 38000$, $\alpha = 15000$)

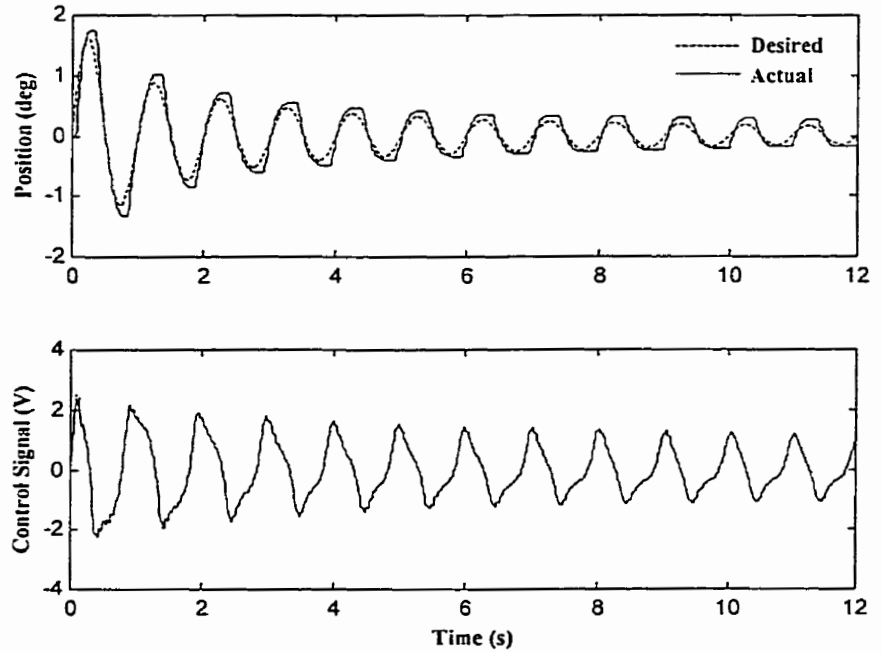

Fig. 4.25. Small diminishing sine wave input response of modified rate-varying integral Controller: simulations ($k_p = 950$, $k_i = 38000$, $\alpha = 15000$)

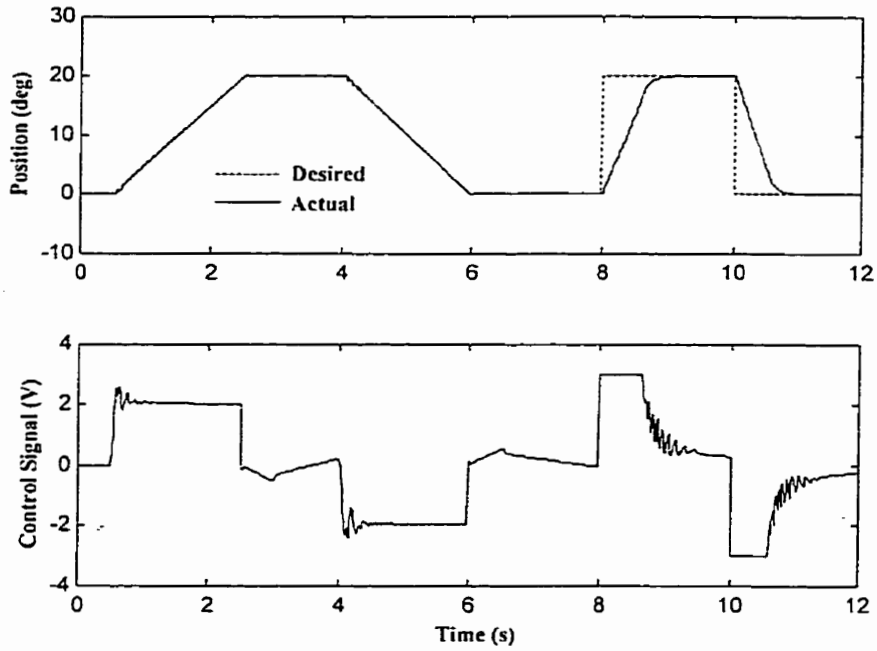

Fig. 4.26. Large step and ramp input responses of modified rate-varying integral controller: simulations ($k_p = 950$, $k_i = 38000$, $\alpha_{\max} = 15000$, $\dot{\theta}_{\max} = 14$ deg/s)

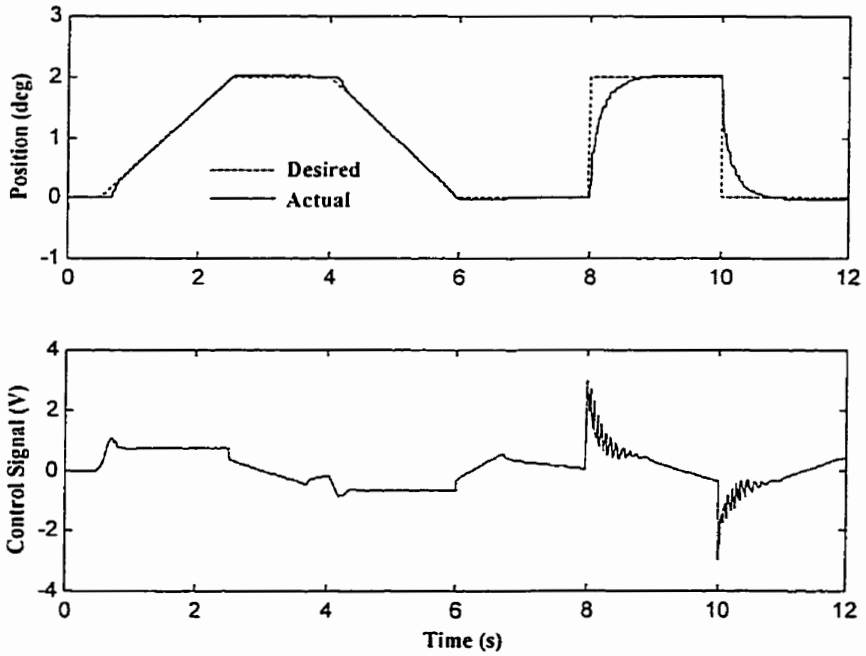

Fig. 4.27. Small step and ramp input responses of modified rate-varying integral controller: simulations ($k_p = 950$, $k_i = 38000$, $\alpha_{\max} = 15000$, $\dot{\theta}_{\max} = 14$ deg/s)

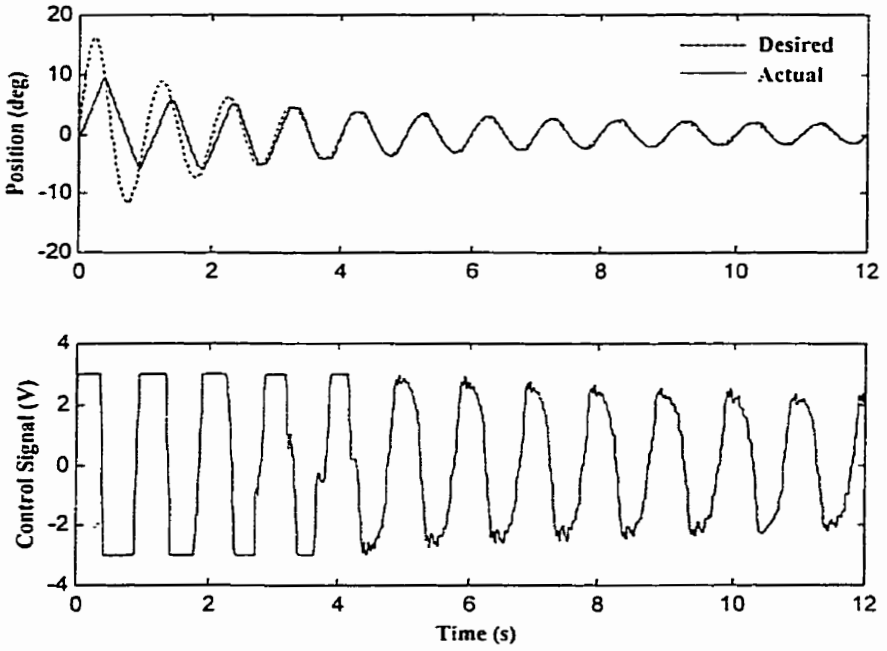

Fig. 4.28. Large diminishing sine wave input response of modified rate-varying integral controller: simulations ($k_p = 950$, $k_i = 38000$, $\alpha_{\max} = 15000$, $\dot{\theta}_{\max} = 14$ deg/s).

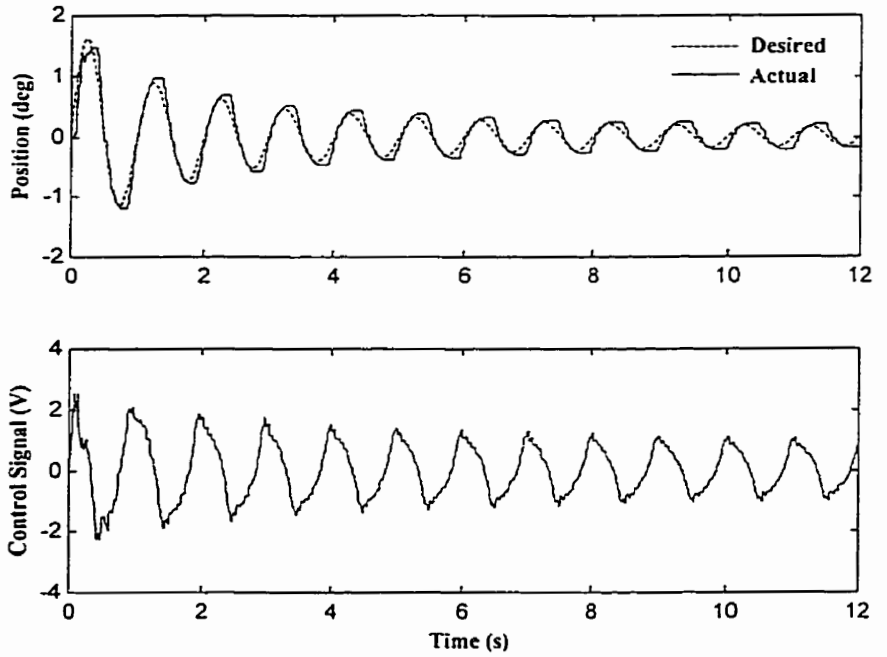

Fig. 4.29. Small diminishing sine wave input response of modified rate-varying integral controller: simulations ($k_p = 950$, $k_i = 38000$, $\alpha_{\max} = 15000$, $\dot{\theta}_{\max} = 14$ deg/s).

4.2.6 Deadband and Stiction Compensation

In this section, we introduce an approach which negates the effect of actuator deadband nonlinearity due to overlap and stiction in the spool valve as well as stiction at the manipulator joints. A number of techniques were reviewed and tested as discussed below.

Conventional Deadband Compensation:

The conventional deadband compensation method is based on the observation that the control signal always has to exceed a threshold before any motion occurs. Thus, a signal augmentation function $u_{aug}(t)$ can be defined as shown in Fig. 4.30. This signal is added to the control signal $u(t)$, which is calculated by equations (4.8) and (4.9).

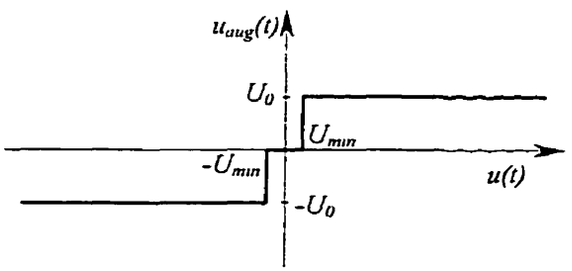

Fig. 4.30. Augmentation signal for conventional deadband compensation

Excellent trajectory tracking for large displacements was achieved by adding this augmentation signal (with $U_{\min} = 0.09\,\text{V}$, and $U_0 = 0.9\,\text{V}$) on the control signal obtained from Eqs. (4.8) and (4.9). This method, however, was less successful when tracking the small sine wave input. Rapid bang-bang action occurred in the augmentation signal when tracking the small diminishing sine wave pattern (note the circled parts of the control signal in Fig. 4.31), inducing vibrations in the system. When controlling the force on an environment of any reasonable stiffness, the commanded motions will be small ones, thus

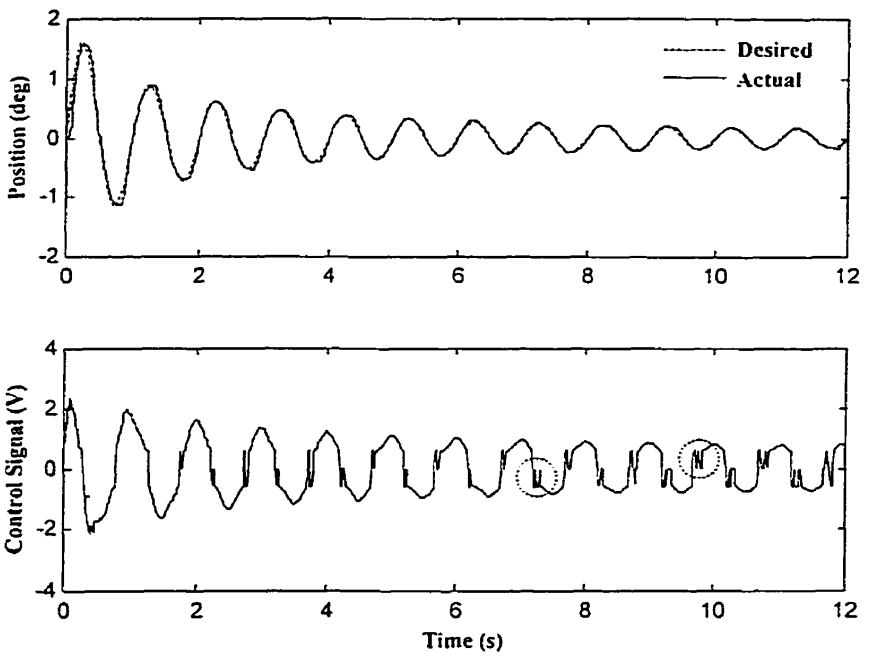

Fig 4.31. Small diminishing sine wave input response of modified rate-varying integral controller with deadband compensation: simulations ($U_{min} = 0.09$ V, $U_0 = 0.9$ V)

making this method of deadband compensation unsuitable for application to impedance control.

In an attempt to prevent the aforementioned vibrations and bang-bang action, a variant of deadband compensation that includes hysteresis was implemented. In this implementation, the added control signal (shown in Fig. 4.32) changed only after the underlying control signal, $u(t)$, had definitely switched signs.

The same parameters as the previous case ($U_{min} = 0.09$ V, and $U_0 = 0.9$ V) were used in this experiment. With reference to Fig. 4.33, inclusion of hysteresis eliminated the vibrations and rapid signal switching, and improved the tracking capability of the controller for small motions. However, while this modification successfully improved the

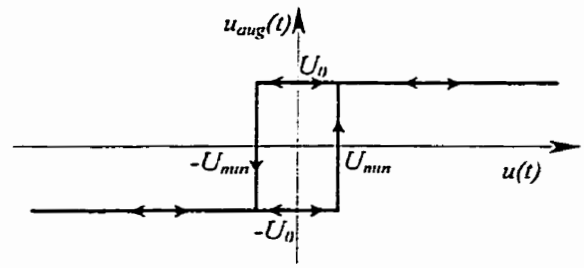

Fig. 4.32. Deadband compensation with hysteresis

controller's trajectory-tracking abilities, it degraded its static regulation abilities. As Fig. 4.34 shows, when tested with step inputs, the controller brings the manipulator to the desired position very quickly but cannot hold it steady since the added signal has no 'off' position. To improve the static stability and eliminate the hunting effect seen in Fig. 4.34, the added signal U_0 may be decreased. However, this action would increase the time required for the control signal to reach the levels required to overcome deadband and stiction. Therefore, improving the static stability would inversely affect the controller's ability to reduce deadband and stiction, which is precisely the reason for its introduction.

Nonlinear Velocity Feedback:

The use of a nonlinear velocity feedback was explored as another avenue of stiction compensation. The motivation for this approach comes from the observation that the largest error signal, during an occurrence of stiction, is the velocity error. Fig. 4.35 shows the first second of tracking a $\theta_d(t) = 0.1 - 0.1\cos(t)$ function. The figure represents the position error (in degrees), $e_\theta(t)$, its time derivative, $\dot{e}_\theta(t)$, and its time integral, $\int e_\theta(t)dt$. Inspection of Fig. 4.35 shows that integral based methods of stiction compensation rely on the smallest signal. The velocity error provides a much stronger signal. However, a nonlinear factor must be incorporated in any use of this signal to

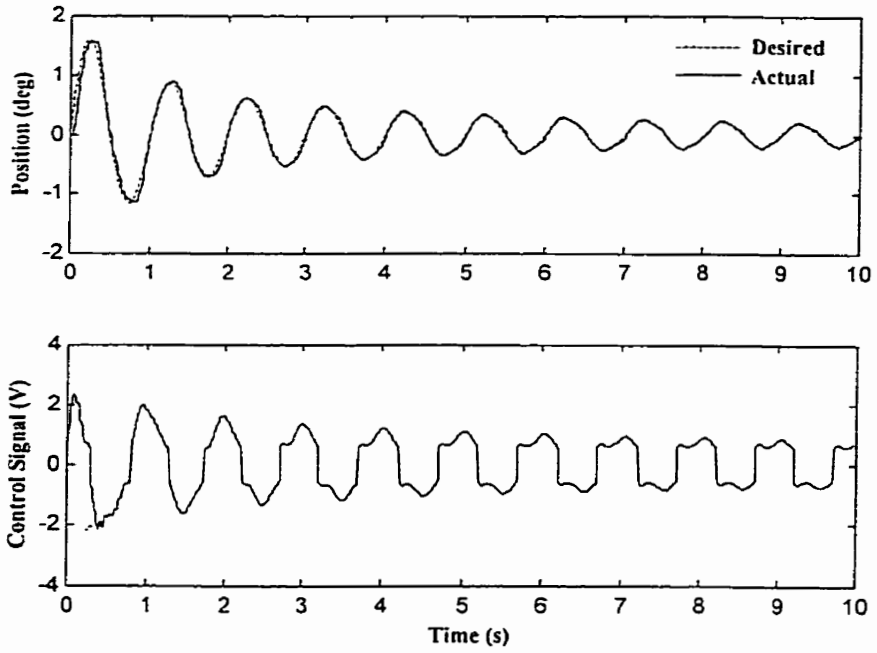

Fig. 4.33. Small diminishing sine wave input response of modified rate-varying integral controller and deadband with hysteresis compensation: simulations ($U_{min} = 0.09$ V, $U_0 = 0.9$ V)

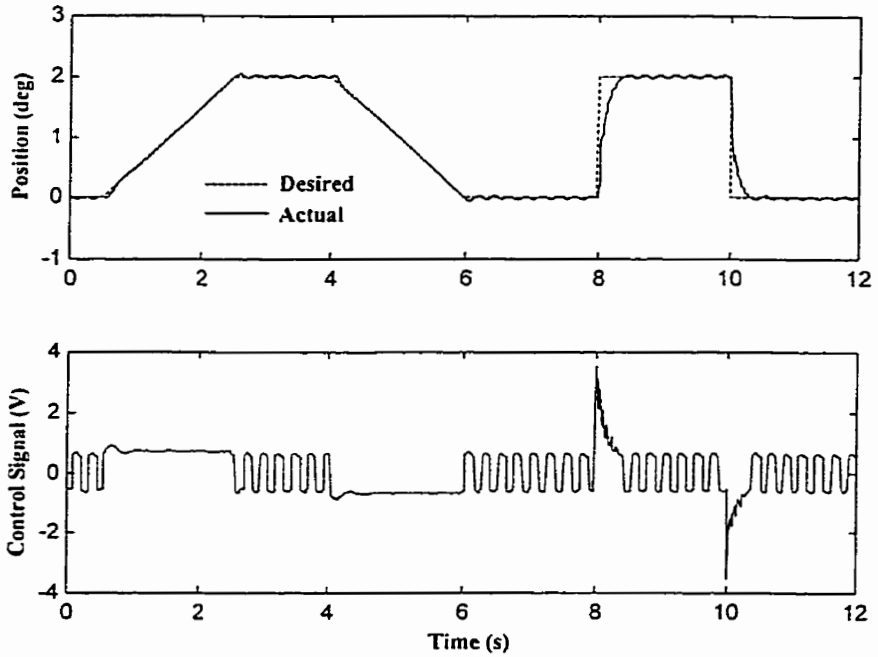

Fig. 4.34. Small step and ramp input responses of modified rate-varying integral controller and deadband with hysteresis compensation: simulations ($U_{min} = 0.09$ V, $U_0 = 0.9$ V)

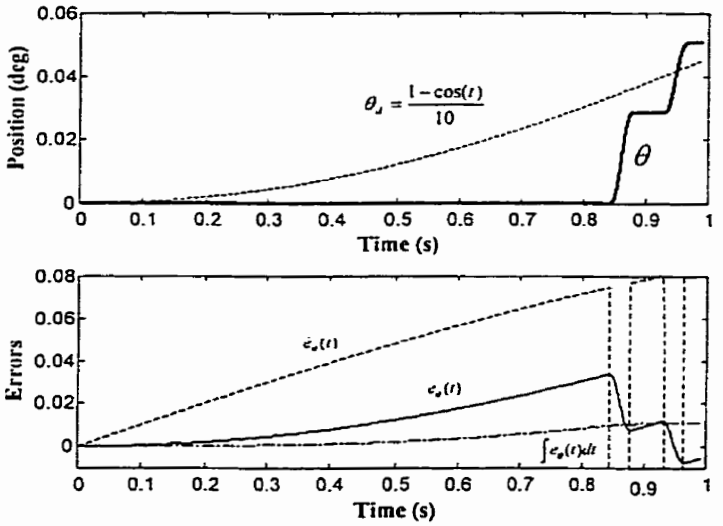

Fig. 4.35. Velocity error, position error, and position error integral signal patterns during stiction period (static friction broken at $t \approx 0.84$s)

avoid the damping action of derivative feedback. The result of this nonlinear filtering is an estimate of the velocity error caused by stiction:

$$\dot{e}_{stiction} = \frac{\dot{\theta}_d - \dot{\theta}}{1 + \beta\left(\frac{\dot{\theta}}{\dot{\theta}_d}\right)^2} \tag{4.10}$$

where $\dot{e}_{stiction}$ is herewith called the stiction-induced velocity error estimate, $\dot{\theta}$ and $\dot{\theta}_d$ are the actual and desired joint velocities, and β is a parameter that increases selectivity. This velocity error estimate is greatest when actual velocity, $\dot{\theta}$, is zero, which is when stiction occurs. $\dot{\theta}_d$ has been incorporated in the above estimate so that the estimate would be zero when the set-point is not changing (steady-state). Otherwise, the velocity error estimate in feedback would cause extra damping when the manipulator was slowly approaching its set-point, which in effect, would work against any integral terms attempting to eliminate

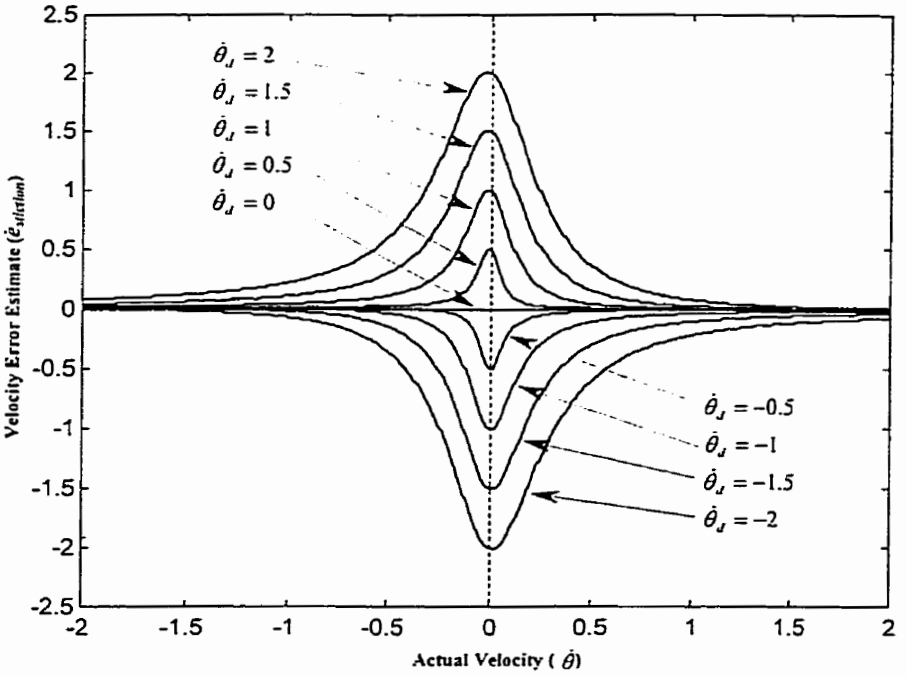

Fig. 4.36. Stiction detection signal graph ($\beta = 50$)

steady-state error. The inclusion of the set-point velocity, $\dot{\theta}_d$, prevents this scenario from occurring.

The velocity error, $\dot{e}_{stiction}$, as formulated in Eq. (4.10), is graphically presented in Fig. 4.36. As is seen, the estimate is appreciable only in the vicinity of $\dot{\theta} = 0$, where stiction occurs. The role of β is to avoid the damping action of derivative feedback. For high values of β, this function sharply discriminates between velocity errors due to sticking and those due to other causes, i.e. the estimate is close to zero unless there is a velocity error at low actual velocities. In other words, the estimate is large when the set-point is moving but the manipulator is not. This results in an estimate of the velocity error caused by stiction. In this work, the value for $\beta = 50$ was found through trial and error.

Velocity Error Triggered Integral Augmentation:

The method, which is herewith called velocity error triggered integral augmentation, uses nonlinear velocity feedback, as a switching signal. Once the experimentally determined threshold $\dot{e}_{\min}$ is met, deadband compensation is employed by directly adding an extra signal to the integral term. The algorithm used is formulated below (Sepehri et al. 1997):

$$u(t) = k_p e_\theta(t) + k_i I(t)$$

$$I(t) = \begin{cases} \dfrac{-U_{lower} - k_p e_\theta(t)}{k_i} & \dot{e}_{stiction} < -\dot{e}_{\min} \quad \& \quad -U_{lower} < u(t) < 0 \\ (I(t-\Delta t) + e_\theta(t)\Delta t)\dfrac{\alpha(\dot{\theta})}{\alpha(\dot{\theta}) + \dot{e}_\theta^2(t)} & |\dot{e}_{stiction}| \le \dot{e}_{\min} \\ \dfrac{U_{upper} - k_p e_\theta(t)}{k_i} & \dot{e}_{\min} < \dot{e}_{stiction} \quad \& \quad 0 < u(t) < U_{upper} \end{cases} \tag{4.11}$$

In short, when sticking is detected, the integral is immediately brought to the level necessary to overcome it, instead of waiting for the error to accumulate. Note that the integral augmentation should occur only once when the stiction-induced velocity error is first detected, so that the integral does not get perpetually reset if motion does not instantly ensue. U_{lower} and U_{upper} are chosen based on the observation that the control signals always have to exceed these thresholds, in either direction, before motion occurs. Inspection of the simulation results (see Figs. 4.37 to 4.40) shows the superior trajectory tracking abilities obtained by augmenting the controller with this method. Fig. 4.40 in particular shows how the control action is modified to improve the response time. The control signal is augmented as appropriate to reach the necessary levels for actuation. Therefore, while the response time is quickened, the ensuing control signal action is unchanged. The only undesirable behavior remaining in the new position controller is the slight overshoot seen in tracking the sine wave pattern. It will be dealt with by a final modification added to the above controller.

4.2.7 Overshoot Reduction

Figs. 4.37 to 4.40 show how the proposed method of integral augmentation eliminates sticking. However, the same graphs show slight recurrent overshoots in tracking a 1Hz sinusoidal input. In applications where accurate tracking of small motions must be achieved, such an overshoot is not permissible.

The cause of the problematic overshoot is the same as that of the excellent set-point tracking during the rest of the trajectory: namely, the integral portion of the controller. In order to maintain a very small error, the control signal must rely, almost entirely, on the integral term. However, while allowing for excellent tracking at constant velocities, the integral is slow to change, resulting in poor tracking of velocity changes. Even with the addition of the previously described rate varying integration scheme, the integral is too slow to die down when the velocity set-point is brought to zero. Some means is therefore needed to further decrease the integral term when braking accelerations are specified. This has been accomplished by including a set-point acceleration based term (braking acceleration, $\ddot{\theta}_{braking}$) in the calculation of the position error integral, i.e.,

$$I(t) = [I(t-\Delta t) + e_\theta(t)\Delta t + k_a \ddot{\theta}_{braking}\Delta t]\frac{\alpha(\dot{\theta})}{\alpha(\dot{\theta}) + \dot{e}_\theta^2(t)} \tag{4.12}$$

where

$$\ddot{\theta}_{braking} = \begin{cases} \ddot{\theta}_d & \text{if } \ddot{\theta}_d\dot{\theta}_d < 0 \\ 0 & \text{if } \ddot{\theta}_d\dot{\theta}_d \geq 0 \end{cases} \tag{4.13}$$

and k_a is a gain.

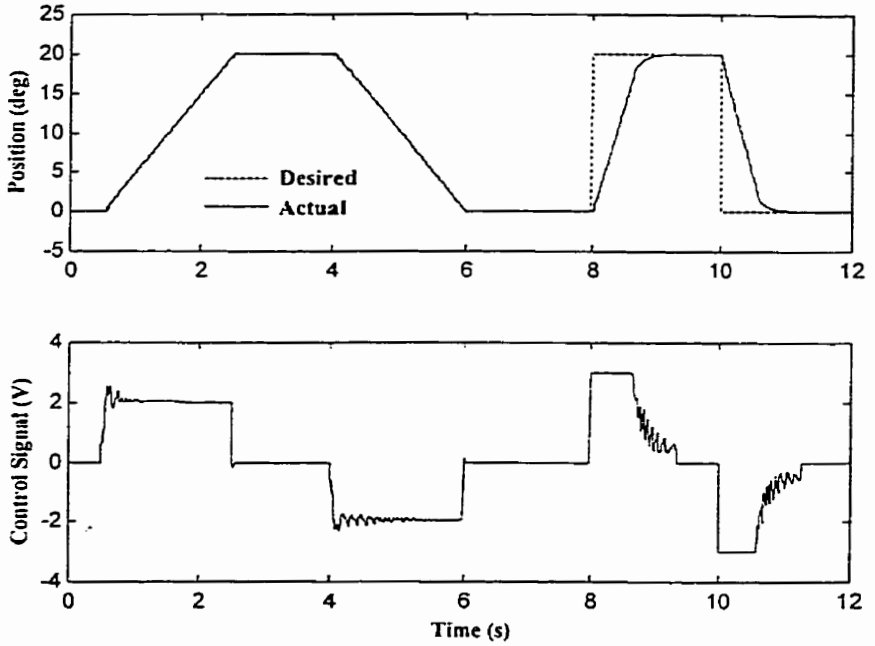

Fig. 4.37. Large step and ramp input responses of modified rate-varying integral controller with deadband and stiction compensation: simulations
($k_p = 950$, $k_i = 38000$, $\alpha_{\max} = 15000$, $\dot{\theta}_{\max} = 14$ deg/s, $U_{lower} = U_{upper} = 0.9$ V)

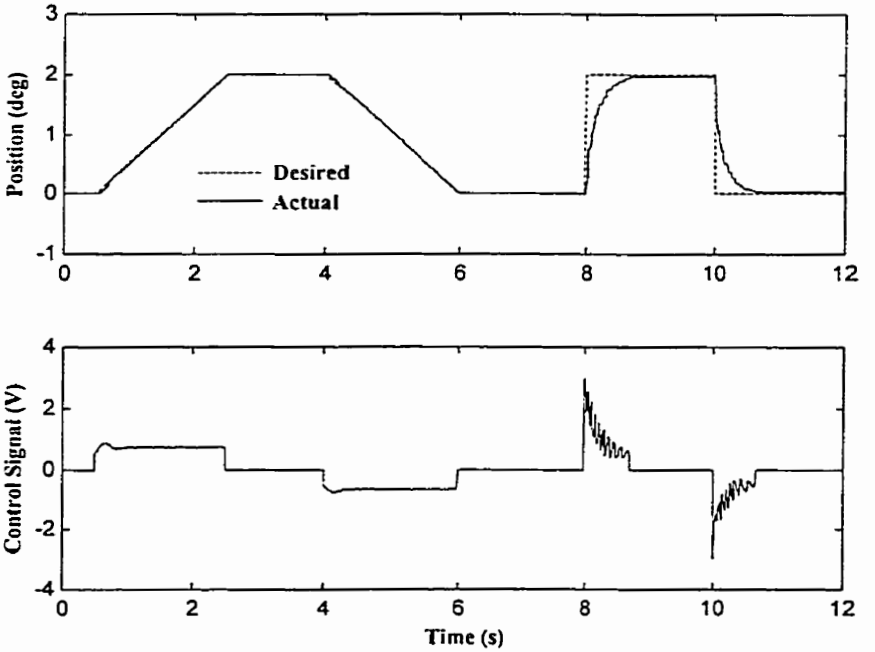

Fig. 4.38. Small step and ramp input responses of modified rate-varying integral controller with deadband and stiction compensation: simulations
($k_p = 950$, $k_i = 38000$, $\alpha_{\max} = 15000$, $\dot{\theta}_{\max} = 14$ deg/s, $U_{lower} = U_{upper} = 0.9$ V)

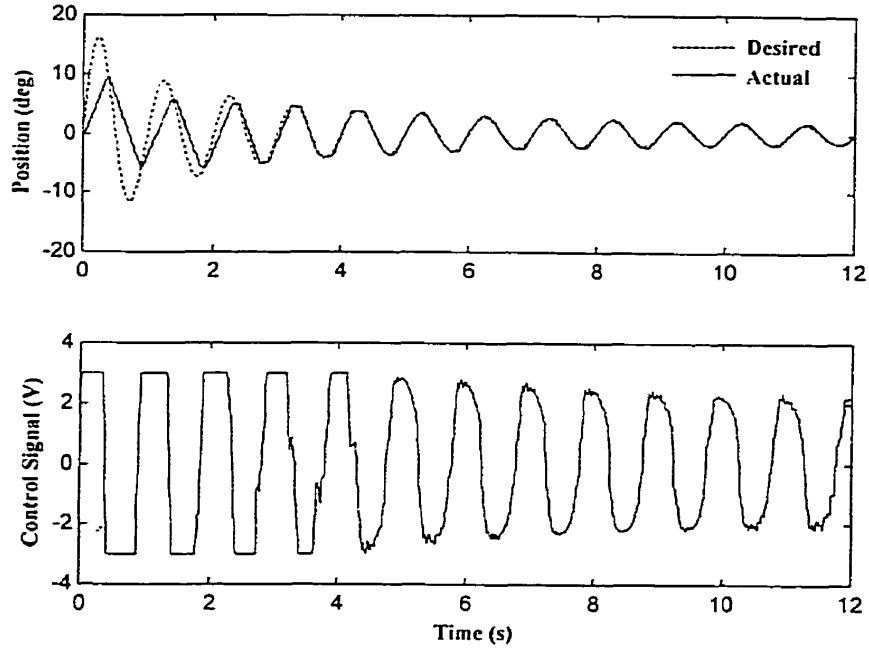

Fig. 4.39. Large diminishing sine wave input response of modified rate-varying integral controller with deadband and stiction compensation: simulations
($k_p = 950$, $k_i = 38000$, $\alpha_{\max} = 15000$, $\dot{\theta}_{\max} = 14$ deg/s, $U_{lower} = U_{upper} = 0.9$ V)

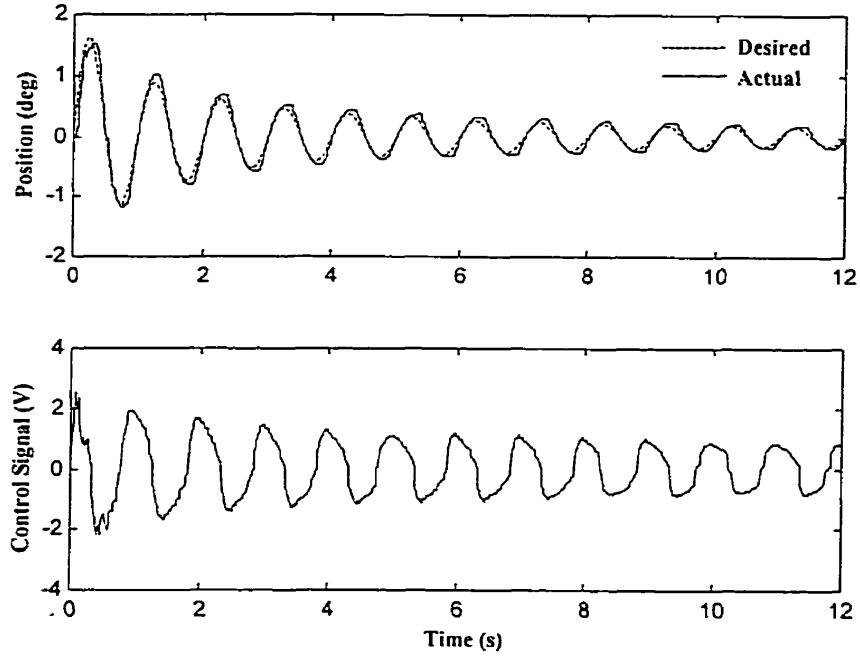

Fig. 4.40. Small diminishing sine wave input response of modified rate-varying integral controller with deadband and stiction compensation: simulations
($k_p = 950$, $k_i = 38000$, $\alpha_{\max} = 15000$, $\dot{\theta}_{\max} = 14$ deg/s, $U_{lower} = U_{upper} = 0.9$ V)

Without the nonlinear factor $f_{nr} = \frac{\alpha}{\alpha + \dot{e}_\theta^2}$, integrating the desired acceleration trajectory is equivalent to adding a velocity feedback, provided that the desired and actual trajectories are practically identical, which has been demonstrated to be the case here. Limiting the accelerations to be integrated to braking accelerations will therefore reduce the integral when the desired velocity is approaching zero, which is when the problems with overshoot are observed.

Figs. 4.41 to 4.44 show the responses resulting from this final modification. In no trial did the control signal reduction appear to reduce the speed of response. Fig. 4.44 gives the most striking illustration of the improvement in set-point tracking. The manipulator can now follow the sine wave closely.

4.2.8 Experimental Results

The nonlinear PI controller with the following parameters

$$k_p = 1200, \quad k_i = 11000, \qquad \alpha_{\max} = 8000, \qquad \dot{\theta}_{\max} = 10\,\text{deg/s},$$

$$\dot{e}_{\min} = 0.15\,\text{deg/s}, \qquad U_{lower} = U_{upper} = 1.1\,\text{V}, \qquad k_a = 150$$

was applied to the second link (up/down motion) of the Unimate hydraulic manipulator and the same benchmark tests as applied in the simulation studies were applied. The controller was implemented according to the scheme outlined by equations (4.11), (4.12) and (4.13).

Figs. 4.45 to 4.48 show the performance of the manipulator under the NPI controller in experiments. The ramp and step trials illustrated in Figs. 4.45 and 4.46 show that the steady-state positioning error is about 0.05°, or almost two encoder resolution widths.

Fig. 4.48 shows that the final controller still has difficulty following the diminishing sine wave once the peak-to-peak amplitude drops to about 0.2°. This amplitude corresponds to about seven times the encoder resolution. Tracking such small changes accurately while retaining stability in the face of large changes in set-point is a very difficult task because the effects of stiction and actuator deadband are most apparent in this region of operation. These errors were concluded to be the limits of the positioning ability of the controller developed here.

In summary, the aforementioned modifications and refinements led to a fine nonlinear PI (NPI) controller; the resultant controller was able to accurately track position trajectories down to seven encoder resolutions of error (~0.2°), and regulate static trajectories to within two encoder resolutions (~0.05°). This nonlinear controller has provided a good position controller to be used as the core (inner loop) of the position-based impedance control. Figures 4.49 to 4.51 show more simulation results which are also compared with results from the experiments taken from the M.Sc. thesis by B. Heinrichs (1995). These figures further prove that the simulation model developed during the course of this thesis is indeed accurate and represents all the nonlinearities inherent in the hydraulic manipulator under investigation.

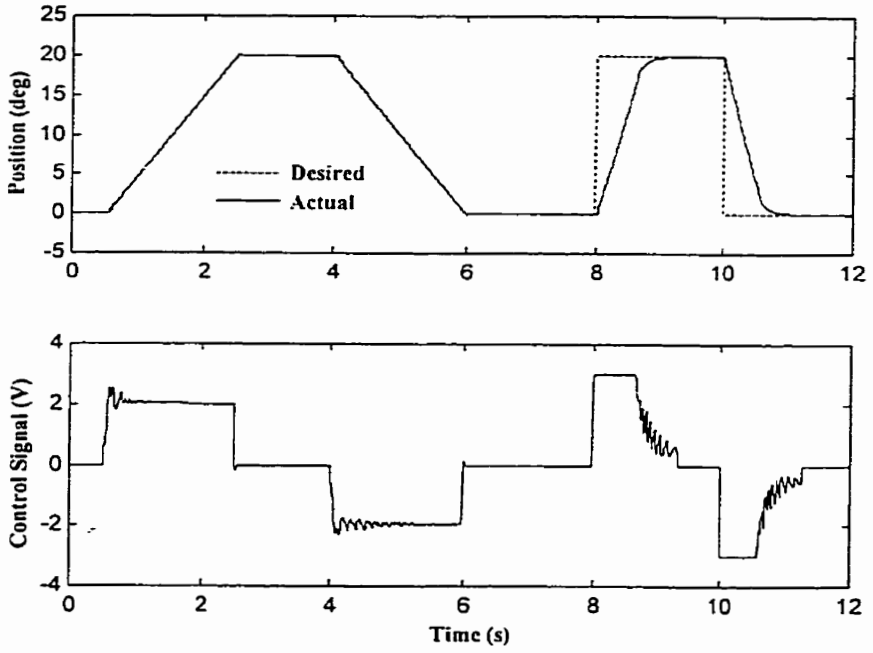

Fig. 4.41. Large step and ramp input responses of NPI controller: simulations ($k_p = 950$, $k_i = 38000$, $\alpha_{\max} = 15000$, $\dot{\theta}_{\max} = 14$ deg/s, $U_{up} = 0.9$ V, $K_a = 150$)

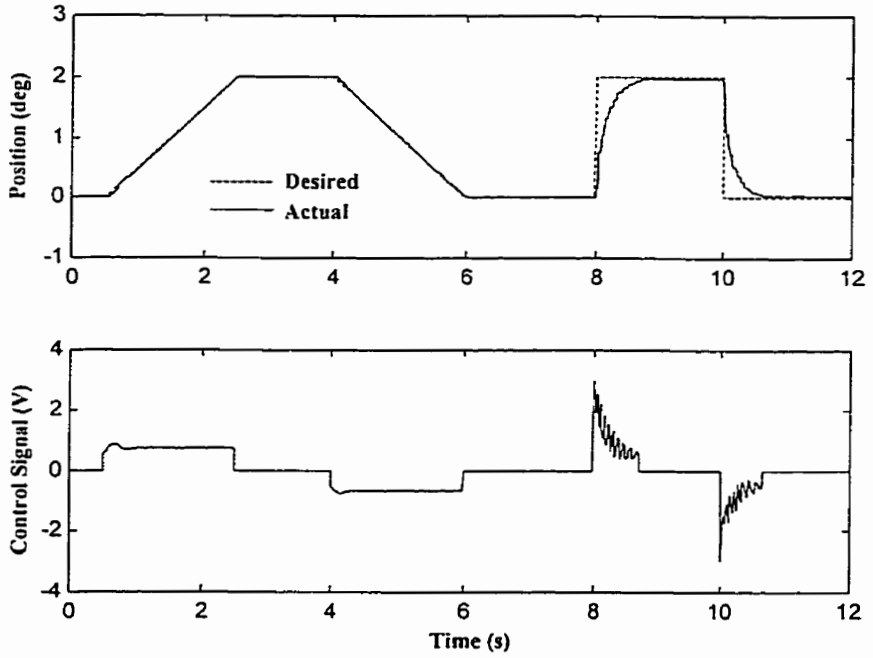

Fig. 4.42. Small step and ramp input responses of NPI controller: simulations ($k_p = 950$, $k_i = 38000$, $\alpha_{\max} = 15000$, $\dot{\theta}_{\max} = 14$ deg/s, $U_{up} = 0.9$ V, $K_a = 150$)

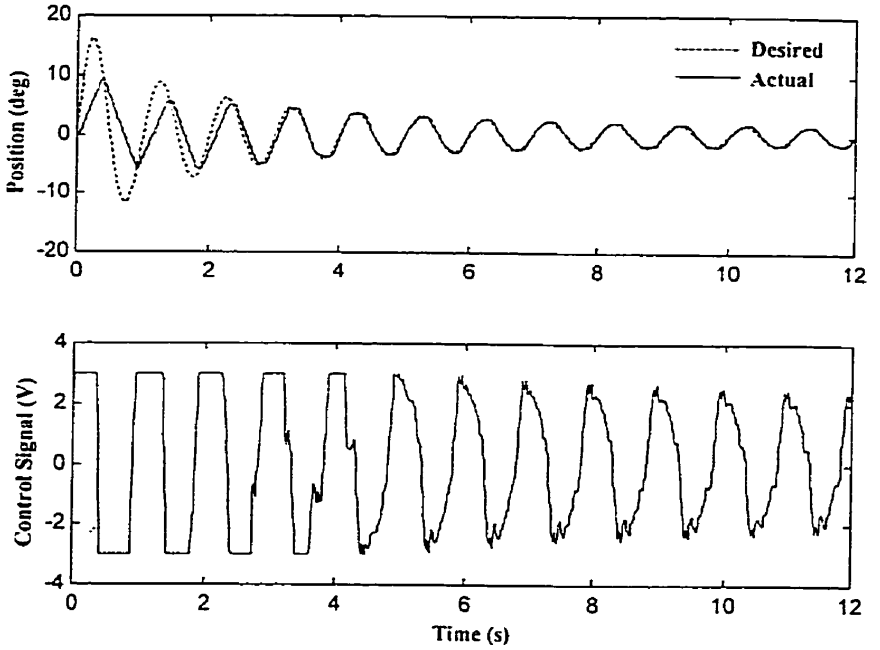

Fig. 4.43. Large diminishing sine wave input response of NPI controller: simulations ($k_p = 950$, $k_i = 38000$, $\alpha_{\max} = 15000$, $\dot{\theta}_{\max} = 14$ deg/s, $U_{up} = 0.9$ V, $K_a = 150$)

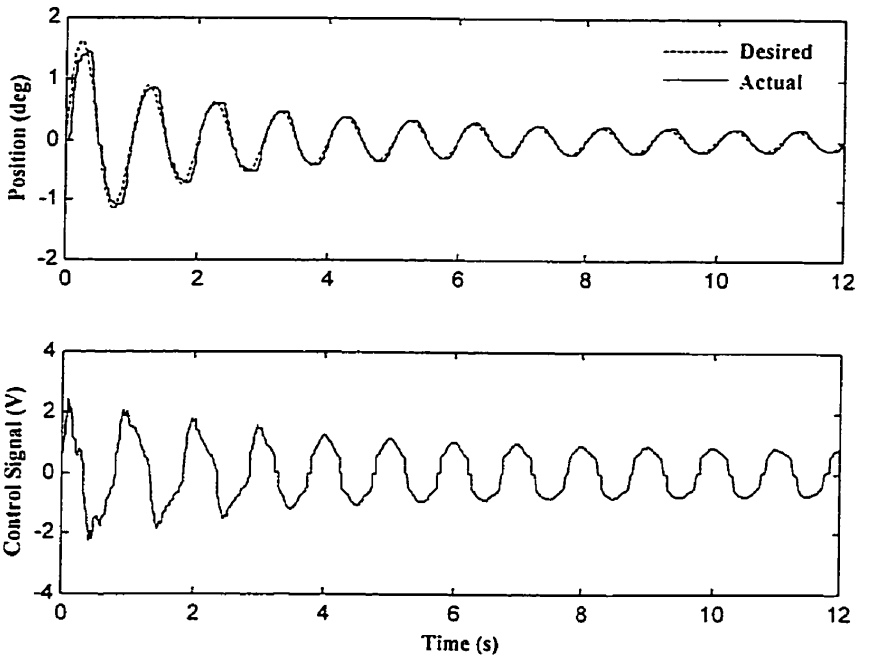

Fig. 4.44. small diminishing sine wave input response of NPI controller: simulations ($k_p = 950$, $k_i = 38000$, $\alpha_{\max} = 15000$, $\dot{\theta}_{\max} = 14$ deg/s, $U_{up} = 0.9$ V, $K_a = 150$)

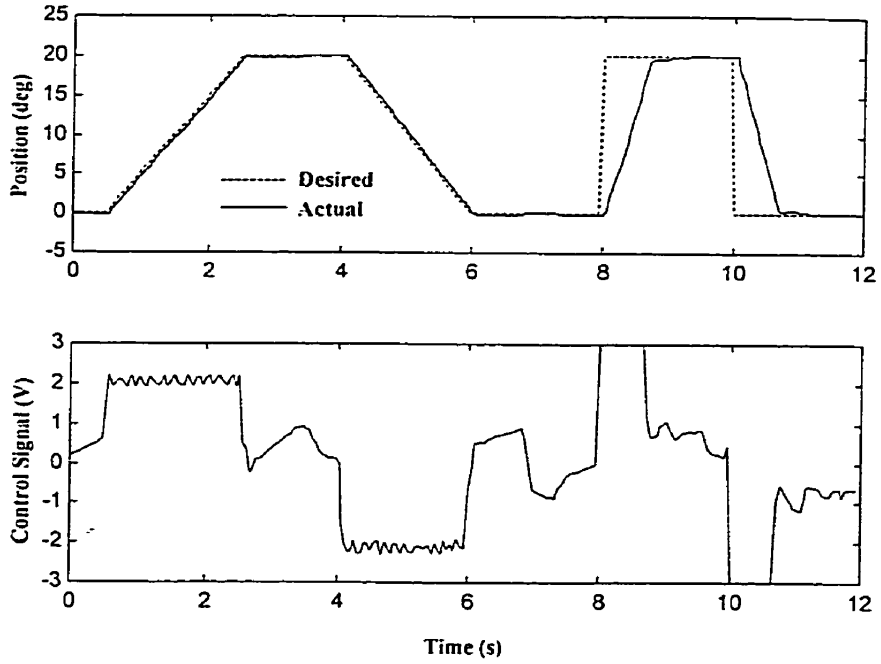

Fig. 4.45. Large step and ramp input responses of NPI controller: experiments ($k_p = 1200$, $k_i = 11000$, $\alpha_{\max} = 8000$, $\dot{\theta}_{\max} = 10$ deg/s, $U_{up} = 1.1$ V, $K_a = 150$)

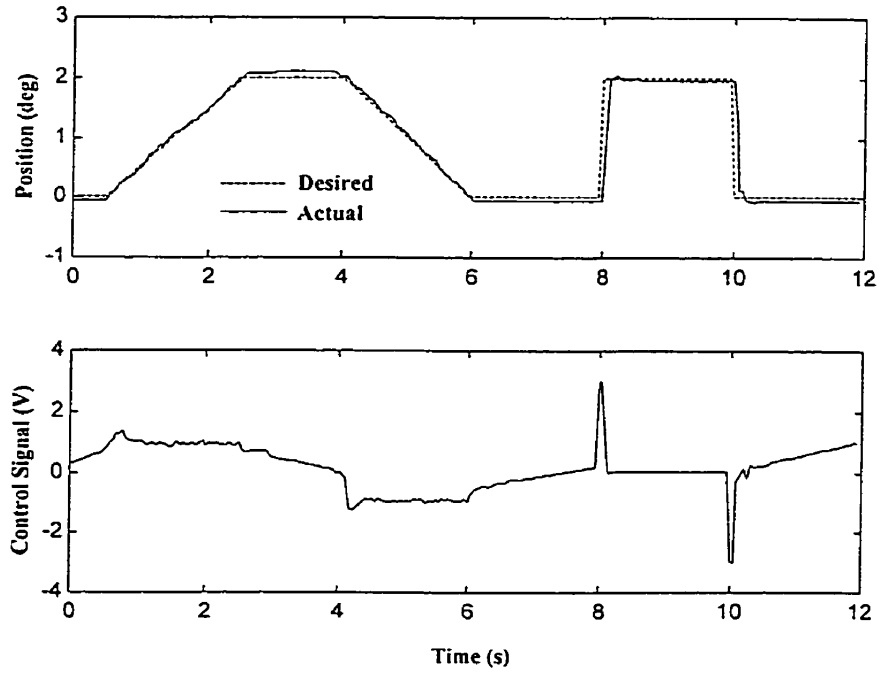

Fig. 4.46. Small step and ramp input responses of NPI controller: experiments ($k_p = 1200$, $k_i = 11000$, $\alpha_{\max} = 8000$, $\dot{\theta}_{\max} = 10$ deg/s, $U_{up} = 1.1$ V, $K_a = 150$)

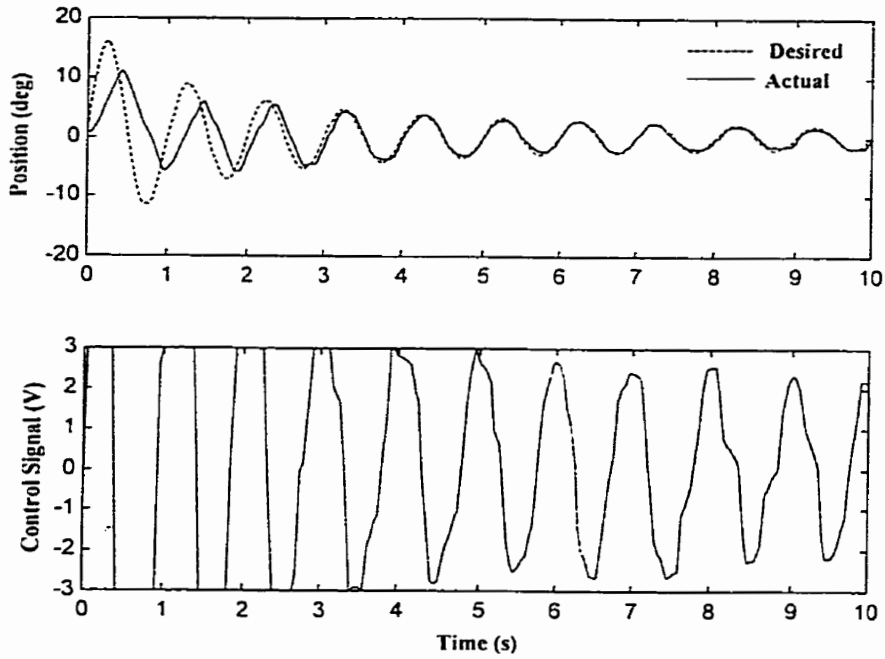

Fig. 4.47. Large diminishing sine wave input response of NPI controller: experiments ($k_p = 1200$, $k_i = 11000$, $\alpha_{\max} = 8000$, $\dot{\theta}_{\max} = 10$ deg/s, $U_{up} = 1.1$ V, $K_a = 150$)

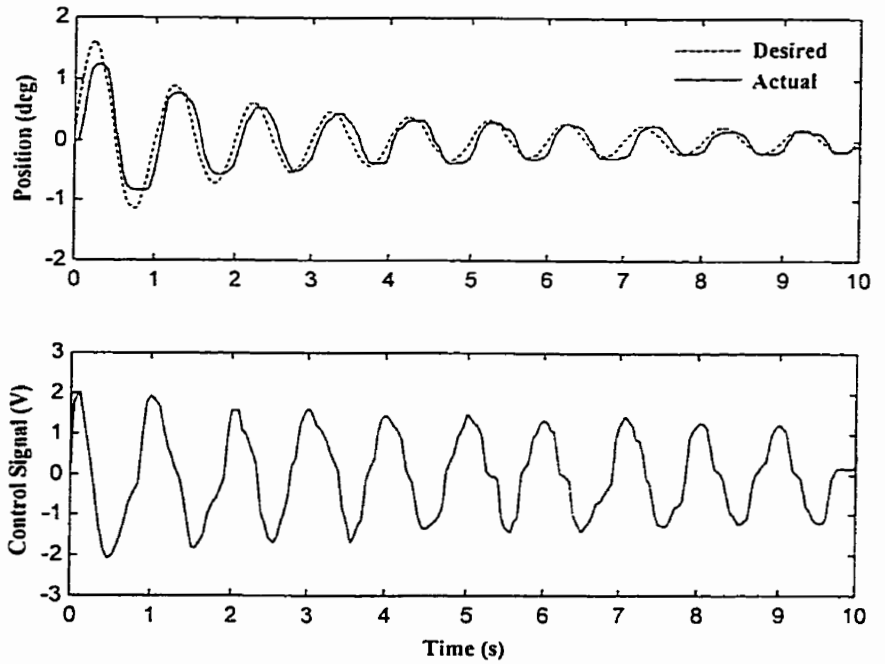

Fig. 4.48. Small diminishing sine wave input response of NPI controller: experiments ($k_p = 1200$, $k_i = 11000$, $\alpha_{\max} = 8000$, $\dot{\theta}_{\max} = 10$ deg/s, $U_{up} = 1.1$ V, $K_a = 150$)

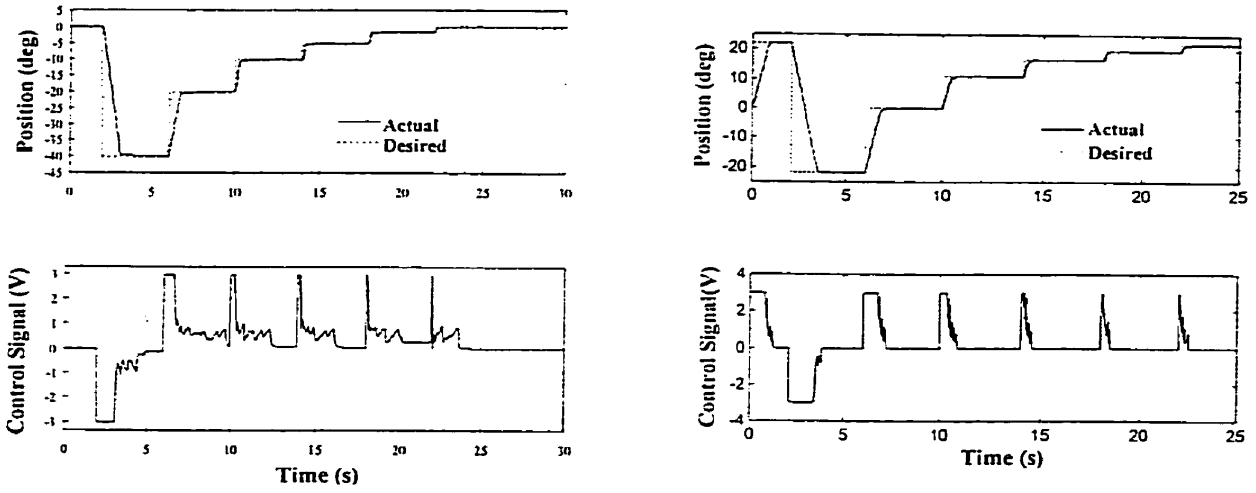

(a) (b)

Fig. 4.49. Performance of NPI controller in large step regulation:
(a) experiment, **(b)** simulations

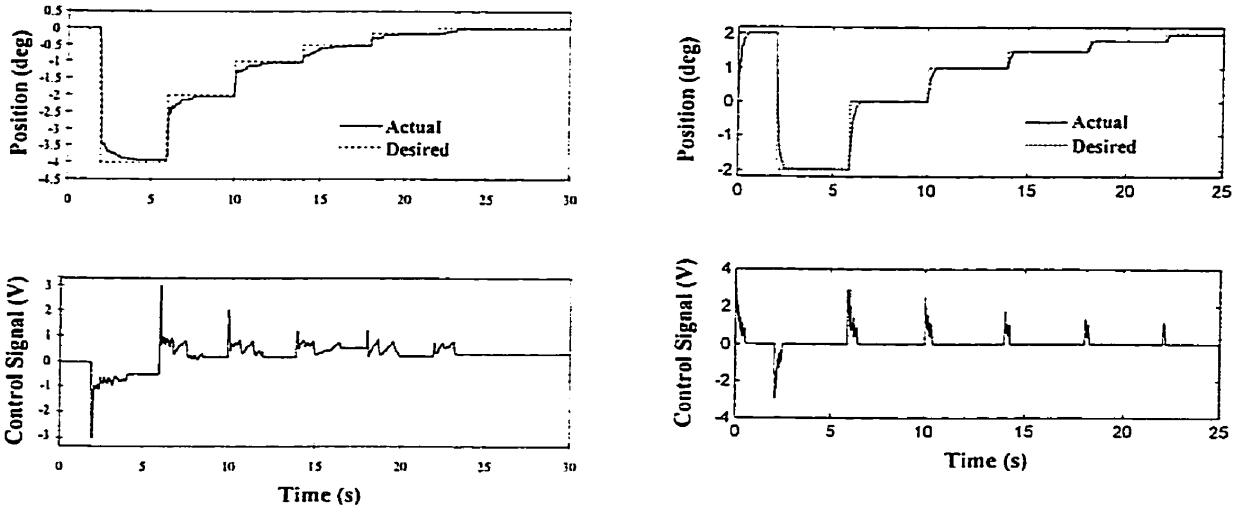

(a) (b)

Fig. 4.50. Performance of NPI controller in small step regulation:
(a) experiment, **(b)** simulations

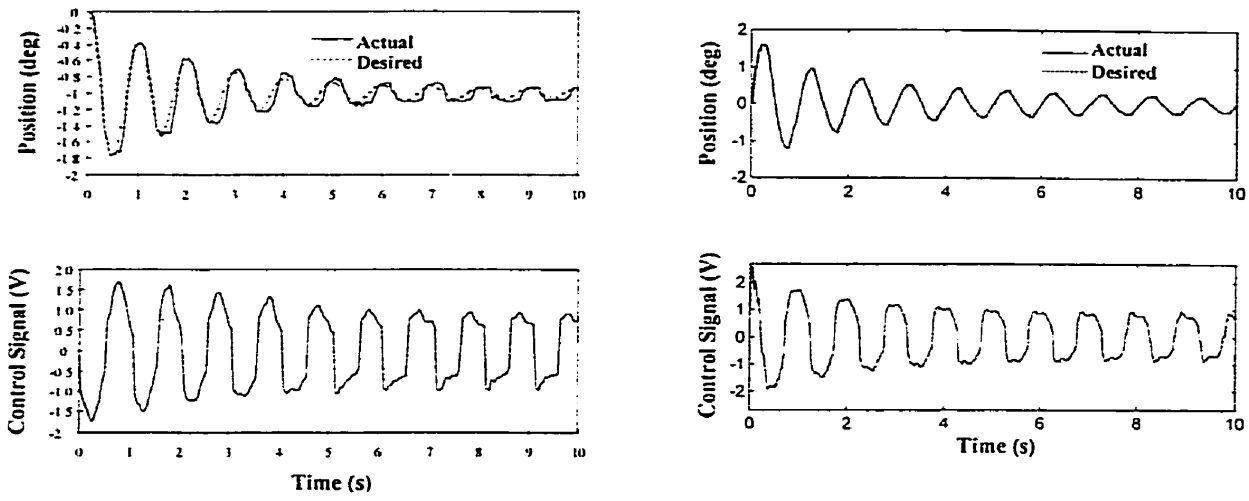

Fig. 4.51. Performance of NPI controller in tracking a diminishing sine wave: **(a)** experiment, **(b)** simulations

4.3 Impedance Control Evaluation Tests

The final position controller previously developed was nested in the position-based impedance controller shown in Fig. 4.1, and three different sets of tests were performed as performance assessments. The experimental results in this part are taken from the M.Sc. thesis by B. Heinrichs (1995) and are shown along with the simulation result.

4.3.1 Free Space Force Response

The free space force response tests involved a step change in the force set-point, f_r, when the end-effector is far from any obstacles (actual force $f = 0$). This is similar to the test Field and Stepanenko (1993) used to assess their model reference impedance controller.

The purpose of this set of tests was to ensure that the apparent manipulator impedance matches the target impedance under a simple step input. Fig. 4.52 shows, both in simulation and experiment, that the impedance controller successfully replaces the existing manipulator dynamics with the specified under-damped target impedance. It was observed (although not shown here) that the dynamics of the manipulator are successfully replaced by those of the critically damped and over-damped target impedances as well.

4.3.2 Tracking/Regulating Force Control

The regulating and tracking force control tests were conducted on an environment with a stiffness of $k_e \approx 7200$ N/m. The end-effector was positioned to be firmly in contact with the aluminum plate, and the force set-point was changed using a 150N step for the regulation test and a 0.1Hz sine wave with 100N amplitude for the tracking test. Assuming that the position controller works perfectly (i.e., x follows x_d precisely), the inner loop (position-controlled arm) can be simplified to unity and the block diagram of the impedance controlled system of Fig. 4.1 reduces to Fig. 4.53. The closed-loop transfer function of this system is:

$$\frac{F}{F_r} = \frac{m_e s^2 + c_e s + k_e}{(M + m_e)s^2 + (C + c_e)s + (K + k_e)} \tag{4.14}$$

According to the above transfer function, the steady-state value of the actual force is

$$f_{ss} = \frac{k_e}{K + k_e} f_r \tag{4.15}$$

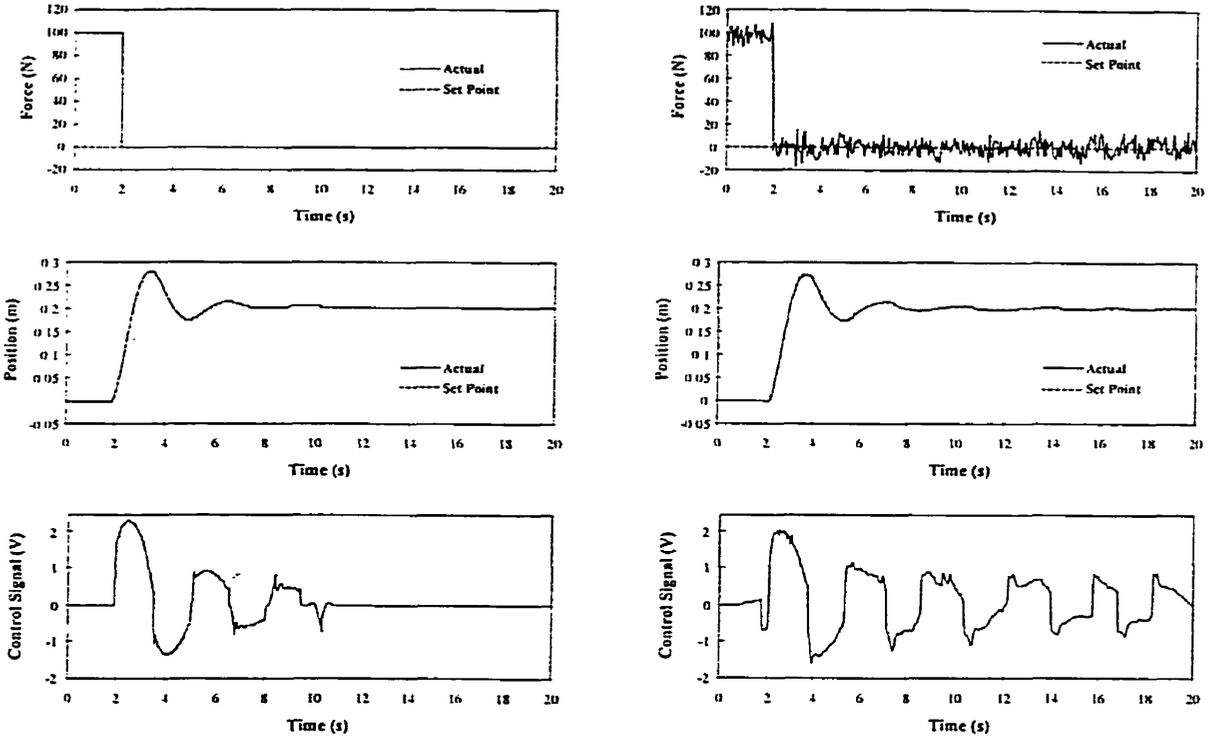

Fig. 4.52. Free space force response of PBIC (M=125kg, ζ=0.3, K=500N/m) (**a**) simulations, (**b**) experiment

It is seen that we need to pre-amplify the desired force by a factor of $(K+k_e)/k_e$ in order to have no steady-state error. Assuming that the environment parameters are known and not varying, the parameters (mass, damping and stiffness) of the impedance model can be adjusted for a designed dynamic response. However, in most practical cases the environment parameters are variable or unknown and in many cases even the location of the undeformed environment is not known or may vary. Figures 4.54 and 4.55 show simulation and experimental results of typical force regulation/tracking with reference force readjustment.

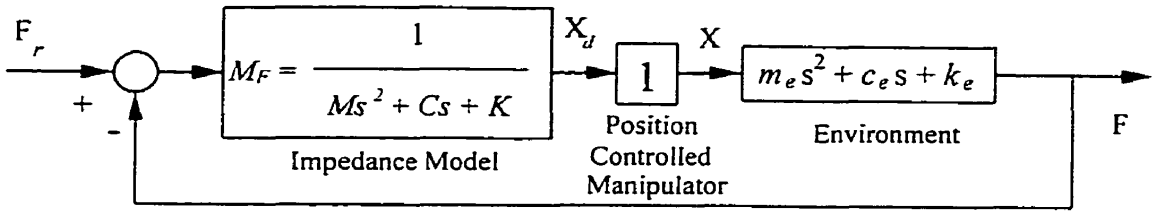

Fig. 4.53. Simplified position-based impedance control block diagram

4.3.3 Interrupted Position Trajectory Tracking

The interrupted position trajectory tracking test (Heinrichs et al., 1996) entailed commanding the end-effector to follow a circular trajectory in the vertical (XZ) plane while the aluminum plate was placed to cut the nominal trajectory circle in half. This provided a test of the impedance controller's response to sudden and large changes in environmental admittance, as well as tested its ability to control position in one direction and deal with forces of interaction in another. This test has been widely used by Hogan (1987), Lu and Meng (1991) and Tsia and Orin (1986).

The impedance model parameters are set differently for the interrupted trajectory test than for the previous cases because the task requirements are different. Instead of controlling the force, the goal is to minimize the force of interaction while remaining as close to the nominal position trajectory as possible. This required a low target stiffness and fast dynamics (high natural frequency).

4.4 Summary

Three nonlinear modifications to a conventional linear PI controller, as applied to an industrial hydraulic manipulator, increased its high-frequency low-amplitude tracking capability by an order of magnitude. The resultant positioner was able to accurately track

position trajectories down to seven encoder resolutions of error (~0.2°), and regulate static trajectories to within two encoder resolution widths (~0.05°). This level of accuracy was observed in spite of large manipulator inertia, joint stiction, actuator deadband and other nonlinearities, and over two orders of magnitude of step, ramp and sine wave trajectories.

This positioner was then used to implement a position-based impedance controller (PBIC) on the Unimate hydraulic robot. The PBIC was tested in free space, in regulating and tracking force, and in applications involving trajectory tracking in environments with highly discontinuous admittances. In all tests, the impedance controller successfully masked the actual, highly nonlinear robot dynamics and replaced them with those of the target impedance. The impedance controller proved to be capable of regulating and tracking forces, impact force reduction and multi-dimensional coordinated position control and force regulation.

All the experimental results were compared with simulation results to confirm that the observations made from the experiments truly reflect the nature of the controller and not some intrinsic properties inherent to any real-world industrial system. This comparison also confirmed that the simulation model developed during the course of this thesis is indeed accurate and represents all the nonlinearities inherent in the hydraulic manipulator under investigation. Therefore the simulation model can be used with confidence in the next chapter to study various force regulating schemes within the context of PBIC.

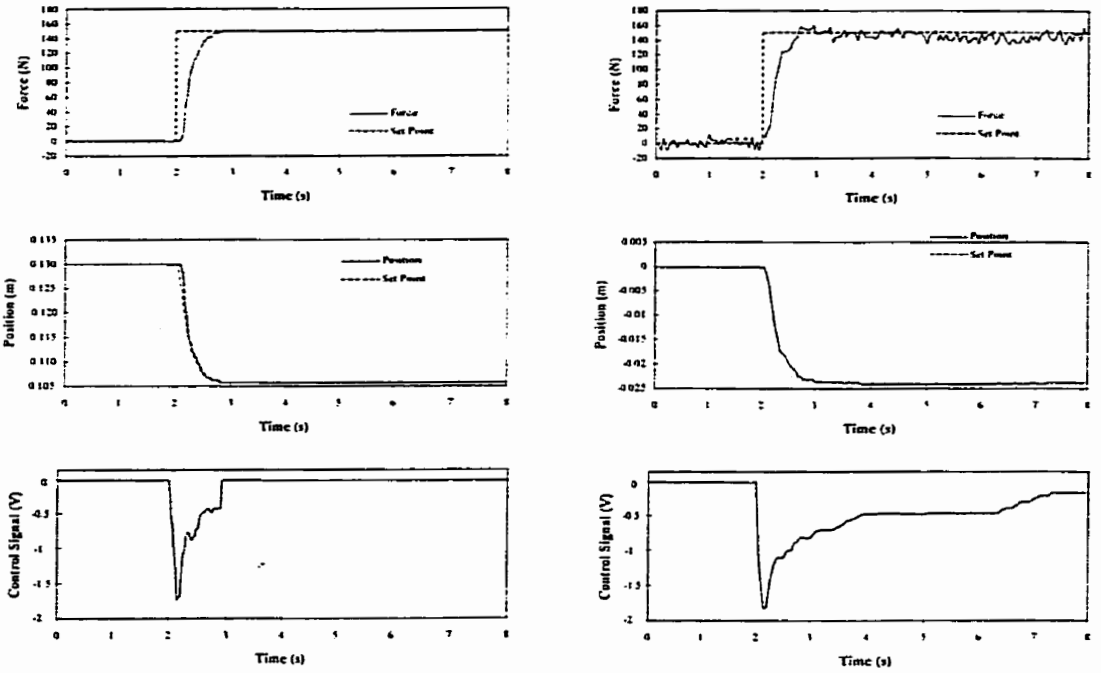

(a) **(b)**

Fig. 4.54. Force regulation with PBIC on low environmental stiffness ($k_e \approx 7200$N/m) (M=500kg, ζ=1.2, and K=50kN/m): (**a**) simulations, (**b**) experiment

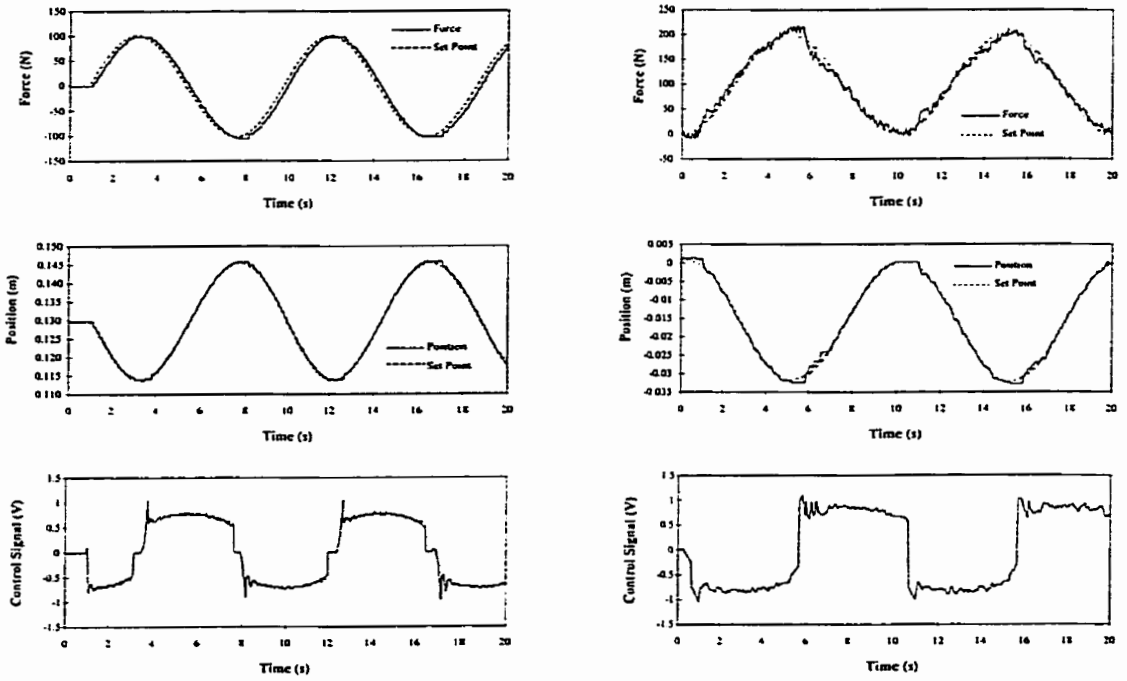

(a) **(b)**

Fig. 4.55. Force tracking with PBIC on low environmental stiffness ($k_e \approx 7200$N/m) (M=500kg, ζ=1.2, and K=50kN/m): (**a**) simulations, (**b**) experiment

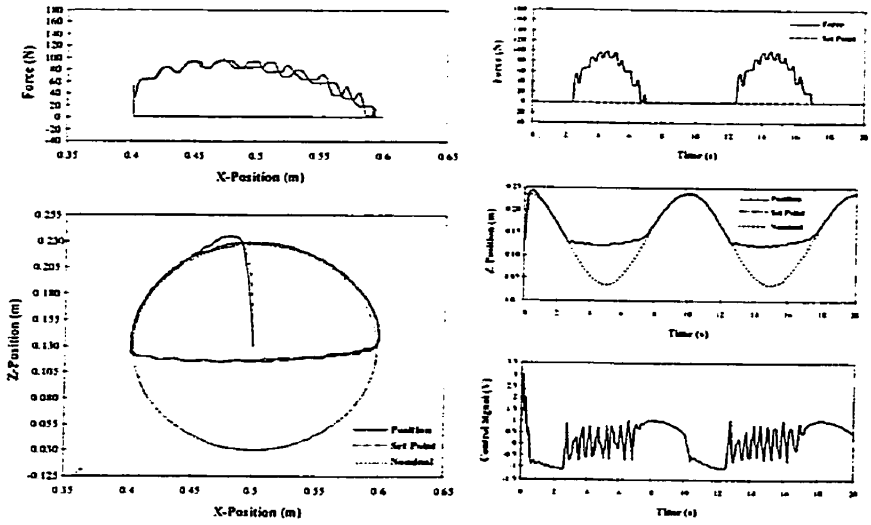

Fig. 4.56. Response of PBIC to changes in environmental admittance (k_e = 7200N/m): simulations: (M=50kg, ξ=1.0, and K=1000N/m)

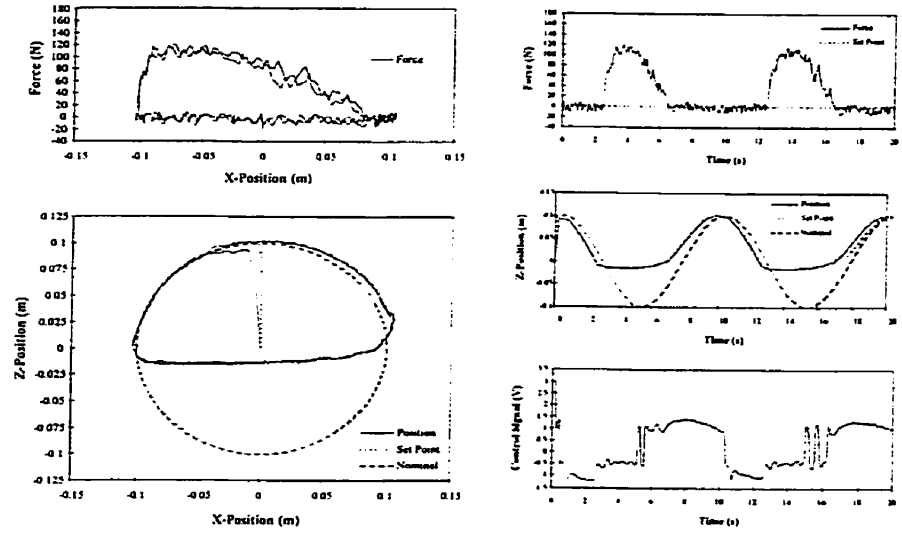

Fig. 4.57. Response of PBIC to changes in environmental admittance (k_e = 7200N/m): experiment: (M=50kg, ξ=1.0, and K=1000N/m)

Chapter 5

Force Regulation

in Impedance Control

5.1 Introduction

Force control capability of position-based impedance control, as applied to hydraulic manipulators, is investigated in this chapter. It is shown that impedance control by itself is not capable of regulating the end-effector force, and various sources of force error are discussed. It is then shown that the end-effector force can be regulated using position-based impedance control, if accurate information about the environmental parameters (i.e., stiffness and location) are available. Existing methods that seemed to be applicable in this study are adopted or modified as required, and are implemented within the PBIC framework to improve its force control capability as applied to hydraulic manipulators. A simple off-line environmental parameters estimation method by Lu and Goldenberg (1995), is modified and shown to produce accurate stiffness and location of the environment. An indirect adaptive scheme, as presented by Seraji and Colbaugh (1997), is adapted to estimate the environmental parameters on-line. The simple integral-based method, as presented by Lasky and Hsia (1993), is implemented to modify the position

reference on-line. Finally a direct adaptive controller, as presented by Seraji and Colbaugh (1997), is adapted to modify the position reference on-line for the purpose of force control. Performance of all the above mentioned force control schemes are compared and discussed.

5.2 *Problem of Force Tracking in Impedance Control*

Consider a single degree-of-freedom impedance controlled actuator shown in Fig. 5.1.

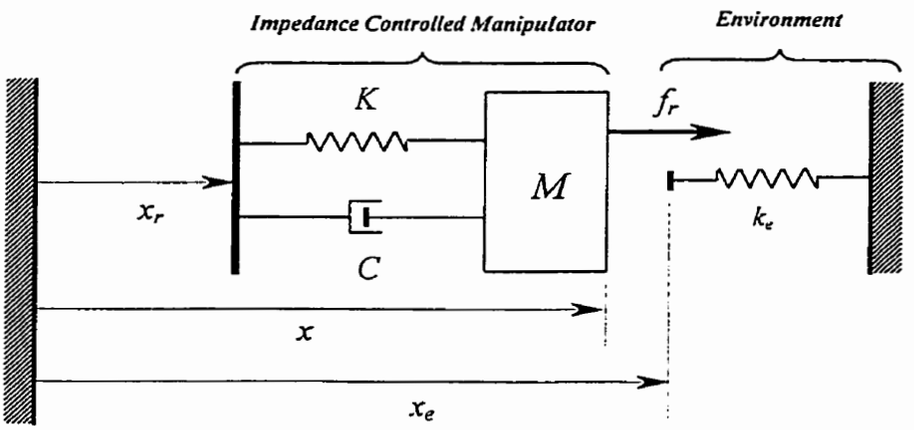

Fig. 5.1. Simplified model of impedance controlled robot and environment

Let x and x_r denote the actual and the reference end-position trajectories, respectively. Let f represent the contact force. The environment is represented by a linear spring, and hence the contact force is simply

$$f = \begin{cases} k_e(x - x_e) & (x \geq x_e) \\ 0 & (x < x_e) \end{cases} \tag{5.1}$$

where k_e is the equivalent stiffness of the environment and the force sensor mounted at the end-effector, and x_e denotes the location of the undeformed environment. This simple model is representative of many practical situations in which the stiffness term dominates the interaction dynamics, and has been widely adopted by several researchers (Khatib and Burdick, 1986; Lawrence and Stoughton, 1987; Ishikawa et al., 1989; Seraji and Colbaugh, 1997). To produce a constant contact force, f_r, the reference position, x_r, is specified to penetrate into the environment by a constant amount; thus $\dot{x}_r = \ddot{x}_r = 0$ and the target impedance model, described by Eq. (2.4a), can be used:

$$M\ddot{x} + C\dot{x} + K(x - x_r) = e \tag{5.2}$$

Using the environment model (5.1), x can be expressed in terms of e as

$$x = \frac{1}{k_e} f + x_e = \frac{1}{k_e}[f_r - e] + x_e \tag{5.3}$$

Equations (5.2) and (5.3) yield the following force-error differential equation

$$M\ddot{e} + C\dot{e} + (K + k_e)e = M\ddot{f}_r + C\dot{f}_r + Kf_r - k_e K(x_r - x_e) \tag{5.4}$$

Since f_r is constant, the steady-state force error is obtained from Eq. (5.4) as

$$e_{ss} = \frac{K}{K + k_e}[f_r + k_e(x_e - x_r)] = k_{eq}\left[\frac{f_r}{k_e} + x_e - x_r\right] \tag{5.5}$$

where $k_{eq} = \left(K^{-1} + k_e^{-1}\right)^{-1} = \dfrac{Kk_e}{K + k_e}$ is the equivalent stiffness of the target impedance and the environment. The steady-state contact force exerted on the environment can then be obtained as

$$f_{ss} = f_r - e_{ss} = \left(K^{-1} + k_e^{-1}\right)^{-1}\left[\frac{f_r}{K} + x_r - x_e\right]$$
$$= k_{eq}\left[\frac{f_r}{K} + x_r - x_e\right] \tag{5.6}$$

It is seen that the steady-state contact force, f_{ss}, is a function of both the reference position, x_r, and the force set-point, f_r. Now, from (5.5), it is observed that when the reference position trajectory is chosen precisely as

$$x_r = x_e + \frac{f_r}{k_e} \tag{5.7}$$

the steady-state force error becomes

$$e_{ss} = k_{eq}\left[\frac{f_r}{k_e} + x_e - \left(x_e + \frac{f_r}{k_e}\right)\right] = 0 \tag{5.8}$$

In other words, if the precise location of the environment, x_e, and the exact value of the environmental stiffness, k_e, are known a priori, the reference position trajectory, x_r, can be synthesized according to Eq. (5.7) to exert the desired contact force, f_r, on the environment. Note that, from Eq. (5.7), the reference trajectory, x_r, penetrates into the environment by the amount $\frac{f_r}{k_e}$, which is precisely the end-effector penetration needed to produce the desired contact force, f_r.

In practice, however, the values of x_e and k_e are unknown. Suppose that there are discrepancies between the actual (x_e, k_e) and the assumed $(\hat{x}_e, \hat{k}_e)$ values for environmental parameters, i.e., $\Delta x_e = x_e - \hat{x}_e$ and $\Delta k_e = k_e - \hat{k}_e$. Then, using the

reference position $x_r = \hat{x}_e + \frac{f_r}{\hat{k}_e}$ [see Eq. (5.7)] will produce the following steady-state force error:

$$e_{ss} = \frac{K}{K + k_e}\left[k_e \Delta x_e - \frac{\Delta k_e}{\hat{k}_e} f_r\right] \tag{5.9}$$

Furthermore, in implementation of position-based impedance control, there will be a residual position tracking error associated with the end-effector. For instance, with reference to Fig. 4.1, the target impedance filter is driven by the force error e and the reference position, x_r, and generates the desired position trajectory, x_d, which the end-effector is commanded to track. Due to the existence of residual position error, $\varepsilon = x_d - x$, the force error differential equation [Eq. (5.4)] becomes

$$M\ddot{e} + C\dot{e} + (K + k_e)e = k_e K x_e + M\ddot{f}_r + C\dot{f}_r + Kf_r + k_e\left[M\ddot{\varepsilon} + C\dot{\varepsilon} + K(\varepsilon - x_r)\right] \tag{5.10}$$

Provided that the inner-loop position control system is stable, during the steady-state response, $\dot{\varepsilon} = \ddot{\varepsilon} = 0$ and for constant f_r, Eq. (5.10) yields to

$$e_{ss} = k_{eq}\left[\frac{f_r}{k_e} + x_e + \varepsilon - x_r\right] \tag{5.11}$$

It is seen that the residual position error ε also contributes to the force error e_{ss}.

A knowledge of the environmental parameters is also essential when addressing the selection of the target impedance. For the system in Fig. 5.1, the natural frequency and damping ratio of the single degree of freedom system, as a function of the target impedance parameters, are:

$$\omega_n = \sqrt{\frac{K}{M}}\ , \qquad \zeta = \frac{C}{2\sqrt{KM}} = \frac{C}{2M\omega_n} \tag{5.12}$$

When this system interacts with the environment, an external force is produced, the amount of which is based upon the environmental impedance, modeled here as a spring, k_e. This provides the manipulator with a dynamic response that is different from the original design specifications:

$$\omega_n = \sqrt{\frac{K + k_e}{M}} \tag{5.13}$$

An increase in the natural frequency directly affects the damping ratio of the coupled manipulator-environment dynamics:

$$\zeta = \frac{C}{2M\omega_n} \tag{5.14}$$

The target damping of the compensated robot controller is therefore

$$C = 2\zeta\sqrt{M(K + k_e)} \tag{5.15}$$

Apparently the performance of the impedance-controlled manipulator improves if the desired impedance includes a model of the environment.

5.3 *Force Regulation Based on Off-line Estimation*

5.3.1 *Derivation of the Method*

The previous section showed that the problem of force regulation for an impedance-controlled robot can be reduced to choosing a suitable target impedance and an appropriate position reference, x_r, such that the contact force tracks the desired force, f_r, as closely as possible. The choice of position reference, x_r, is highly dependent on

information about environmental parameters, x_e and k_e. Inspired by the work done by Lu and Goldenberg (1995), consider that the reference position, x_r, is chosen as

$$x_r = \hat{x}_{ei} \tag{5.16}$$

where $\hat{x}_{ei}$ is an initial estimated value of x_e (environmental location as shown in Fig. 5.1). Substituting Eq. (5.16) into (5.6) leads to the steady-state force as

$$\begin{aligned} f_{ss} &= \left(K^{-1} + k_e^{-1}\right)^{-1}\left(K^{-1} f_r + \delta x_e\right) \\ &= k_{eq}\left(\frac{f_r}{K} + \delta x_e\right) \\ &= \frac{k_{eq}}{K} f_r + k_{eq}\delta x_e \end{aligned} \tag{5.17}$$

where, $\delta x_e = \hat{x}_{ei} - x_e$. In the above equation, f_{ss} can be separated into two parts:

$$f_{ss}(f_r, \delta x_e) = f_1 + f_2 \tag{5.18}$$

where

$$f_1 = f_{ss}(f_r, 0) = \frac{k_{eq}}{K} f_r = \frac{k_e}{K + k_e} f_r \tag{5.19}$$

and

$$f_2 = f_{ss}(0, \delta x_e) = k_{eq}\delta x_e = \frac{K \cdot k_e}{K + k_e} \cdot \delta x_e \tag{5.20}$$

From (5.19) and (5.20), it is noted that f_1 is a function of only f_r, and f_2 is a function of only δx_e. Using this feature, x_e and k_e can be identified using the following steps:

(i) Assign a certain value to $\hat{x}_{ei}$ and set f_r to zero. Implement the position-based impedance controller and measure the environmental force [f_2 in Eq. (5.20)].

(ii) Assign a value to f_r and use the same value of $\hat{x}_{et}$ as in (i). Implement the controller once more and measure the steady-state force, $f_{ss}(f_r, \delta x_e)$. f_1 is then obtained from Eq. (5.18):

$$f_1 = f_{ss}(f_r, \delta x_e) - f_2$$

(iii) Using f_1 and f_2, the estimated values of $\hat{k}_e$ and $\hat{x}_e = \hat{x}_{ei} - \delta x_e$, are then determined by simultaneously solving Eqs. (5.19) and (5.20) as follows:

$$\hat{k}_e = K\left(\frac{f_1}{f_r - f_1}\right) \tag{5.21}$$

$$\begin{aligned} \hat{x}_e &= \hat{x}_{et} - \left(\hat{k}_e^{-1} + K^{-1}\right) \cdot f_2 \\ &= \hat{x}_{et} - \frac{K + k_e}{K \cdot k_e} \cdot f_2 \end{aligned} \tag{5.22}$$

The estimated environmental parameters can then be used in Eq. (5.7) for the purpose of force control.

5.3.2 Simulation Study

The method described in Section 5.3.1 was first tested in the simulation program. The benchmark test was the application of a desired force of 1000N to an environment with a pure stiffness of 70000N/m. The environment was located at $x_e = 0.13\,\text{m}$ (refer to Fig. 3.2 for coordinates information) and the end-effector was initially just in touch with the environment.

With reference to Fig. 5.2, using the impedance model (2.4c), the implement was first commanded to penetrate 2cm into the environment ($\hat{x}_{et} = 0.11\,\text{m}$) while the force set-point was set to zero ($f_r = 0\,\text{N}$). The steady-state force was then measured

as $f_2 = 173\,\text{N}$. After 10s the force reference changed to $f_r = 1000\,\text{N}$. The steady-state end-effector force reached $f(f_r, \delta x_e) = f_1 + f_2 = 1047\,\text{N}$. From Eqs. (5.21) and (5.22), the environmental parameters were estimated as:

$$\hat{x}_e = 0.1298\,\text{m} \;,\; \hat{k}_e = 69365\,\text{N/m}$$

Note that the accuracy of the estimations depends on obtaining steady-state force responses. To ensure this, the damping ratio of the target impedance must be high.

The environmental parameters estimated above were then used along with Eq. (5.7) to determine the reference position in order to regulate end-effector force. The result is shown in Fig. 5.3. Figure 5.4 shows the response for a different impedance model [model (2.4a)]. In both cases, the steady-state force was accurately regulated, although the transient responses were different as expected.

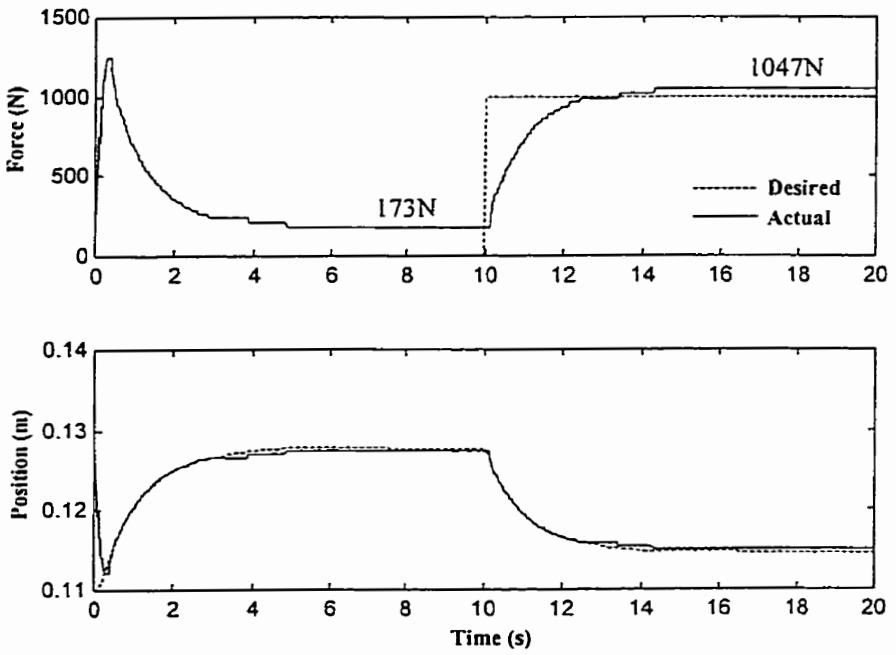

Fig. 5.2. Off-line environmental parameters identification (simulations)

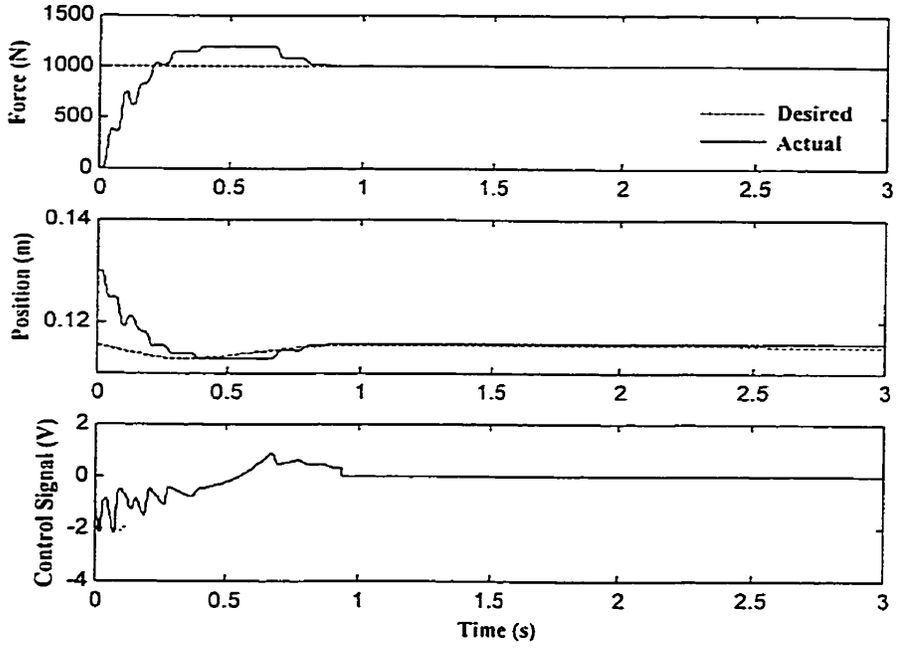

Fig. 5.3. Force control using estimated environmental parameters from Fig.5.2 and impedance model 2.4c (simulations)

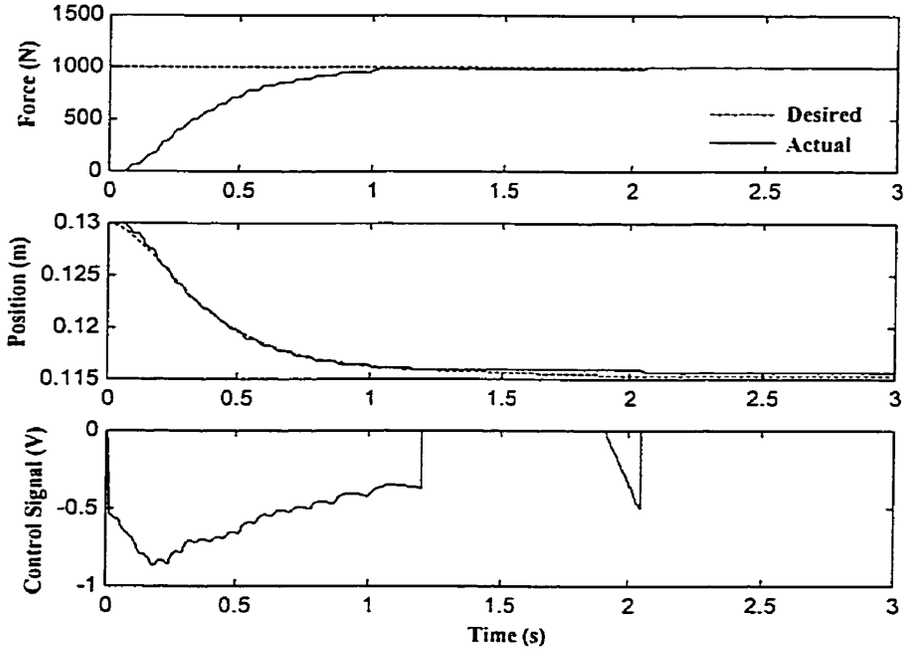

Fig. 5.4. Force control using estimated environmental parameters from Fig.5.2 and impedance model 2.4a (simulations)

5.3.3 Experimental Evaluations

This method was also applied to the hydraulic test station described in Chapter 3. The benchmark test was to apply a 500N force to two types of springy environments: a low stiffness environment ($k_e \approx 10000\,\text{N/m}$) and a high stiffness environment ($k_e \approx 42000\,\text{N/m}$). The end-effector was initially placed approximately 0.5 to 2cm away from the environment.

Figure 5.5 shows the results of off-line identification pertaining to the low stiffness environment. The manipulator was commanded to first move $\hat{x}_{et} = -0.050\,\text{m}$, in the vertical direction, towards the environment (i.e., 3cm into environment); then, change the reference force from zero to $f_r = 500\,\text{N}$. Following the same procedure as outlined in the simulation study, the environmental parameters were determined as:

$$\hat{x}_e = -0.0222\,\text{m} \;,\; \hat{k}_e = 11739\,\text{N/m}$$

The results of the force regulation, using the above values are shown in Fig. 5.6.

The results pertaining to the high stiffness environment are shown in Figs. 5.7 and 5.8. As is seen from Fig. 5.7, using $\hat{x}_{et} = -0.030\,\text{m}$ and $f_r = 600\,\text{N}$ leads to the following parameters:

$$\hat{x}_e = -0.0050\,\text{m} \;,\; \hat{k}_e = 40000\,\text{N/m}$$

Figure 5.8 shows the force control response using the above parameters. Control signals pertaining to Figs. 5.6 and 5.8 are compared in Fig. 5.9.

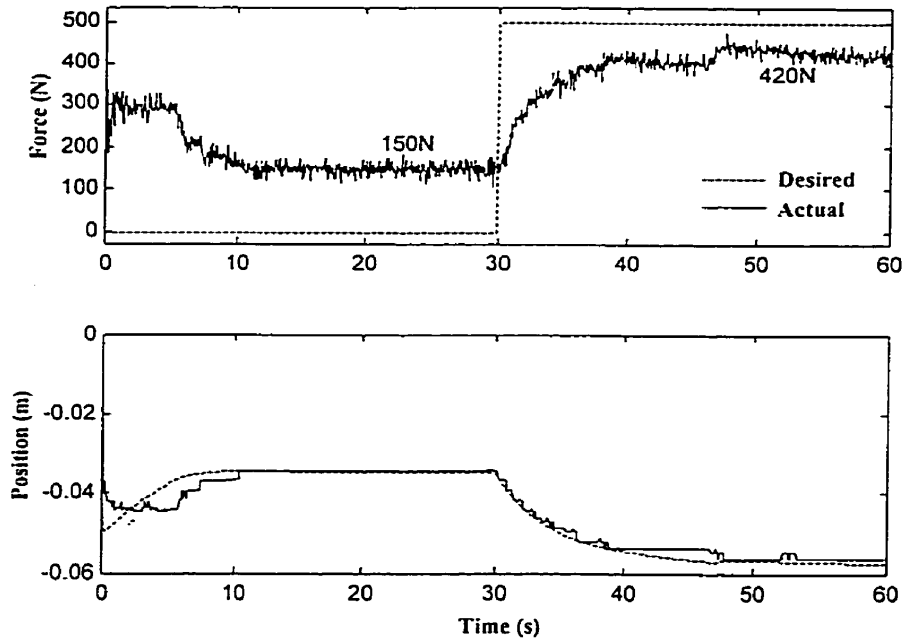

Fig. 5.5. Off-line environmental parameters identification for low stiffness environment (experiment)

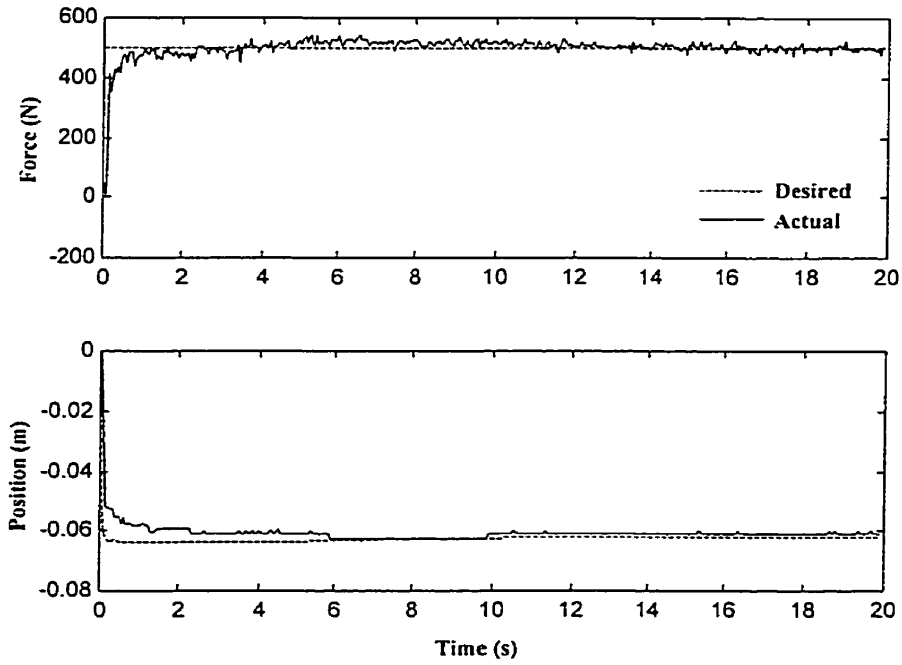

Fig. 5.6. Force control using estimated environmental parameters from Fig. 5.5 (experiment)

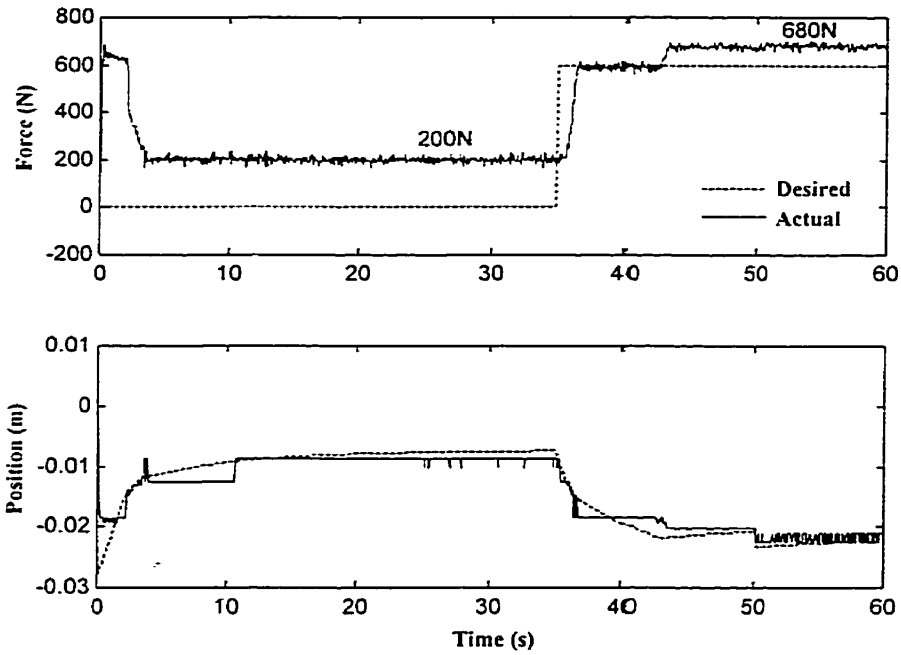

Fig. 5.7. Off-line environmental parameters identification for high stiffness environment (experiment)

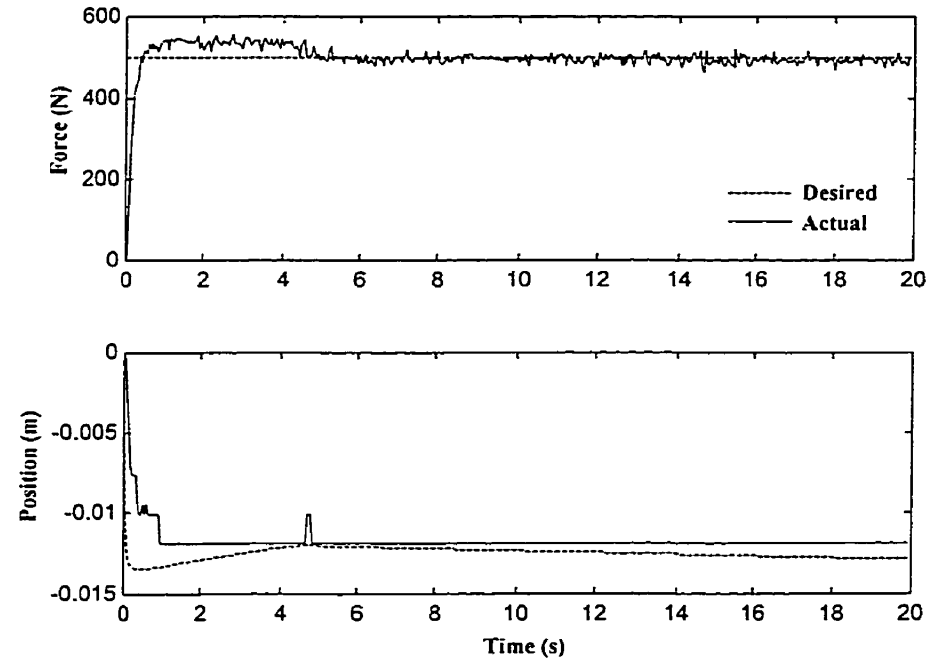

Fig. 5.8. Force control using estimated environmental parameters from Fig. 5.7 (experiment)

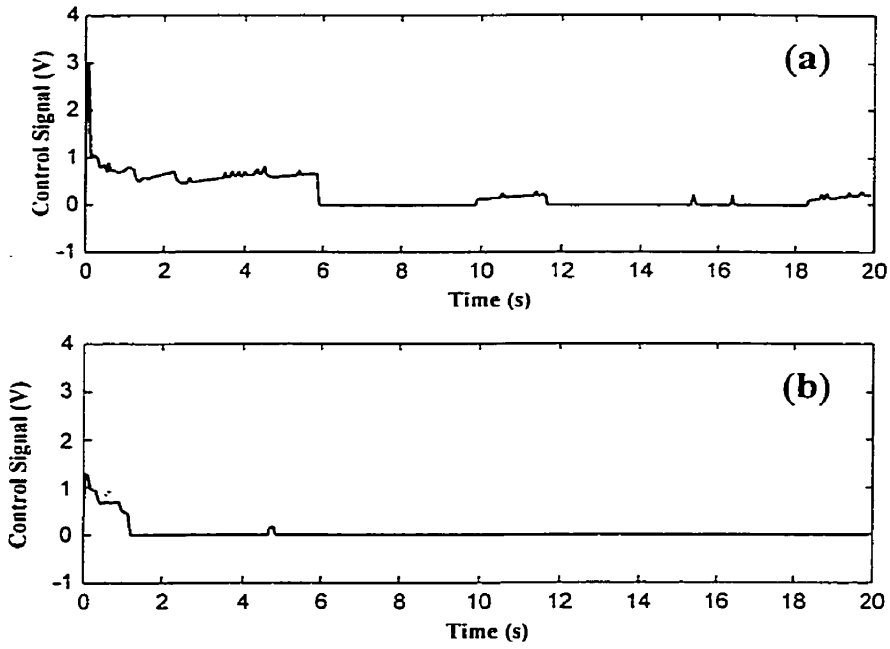

Fig. 5.9. Control signals pertaining to:
(a) Low stiffness environment (Fig. 5.6)
(b) High stiffness environment (Fig. 5.8)

5.4 Force Control using On-line Parameters Estimation

5.4.1 Derivation of the Method

The method described above, although quite simple, requires the estimation to be done off-line. Thus, it is prone to fail for cases whereby the properties of the environment vary during the operation. Furthermore, for stiff environments, large forces are normally required to generate enough deformation for identification purposes. In this section, we explore the idea of estimating the environmental parameters k_e and x_e on-line, and computing the required reference position, x_r, in real-time. Recall from Section 5.1 that

if x_e and k_e are known a priori, then specifying x_r as $x_r = x_e + \frac{f_r}{k_e}$ yields perfect force regulation. This observation suggests defining x_r as

$$x_r = \hat{x}_e + \frac{1}{\hat{k}_e} f_r \tag{5.23}$$

where $\hat{x}_e$ and $\hat{k}_e$ are estimates of x_e and k_e, respectively. Following the formulation developed by Seraji and Colbaugh (1997), consider the following relationships based on Eq. (5.1):

$$f = k_e(x - x_e) = k_e x - k_x \tag{5.24}$$

$$\hat{f} = \hat{k}_e(x - \hat{x}_e) = \hat{k}_e x - \hat{k}_x \tag{5.25}$$

where $\hat{k}_x = \hat{k}_e \hat{x}_e$ is an estimate of $k_x = k_e x_e$ and $\hat{f}$ can be viewed as a 'prediction' of f based on the current environmental estimates $\hat{k}_e$ and $\hat{x}_e$. Let $\phi_k = \hat{k}_e - k_e$, $\phi_x = \hat{k}_x - k_x$ and $\phi = [\phi_k \quad \phi_x]^T$. Differencing Eqs. (5.24) and (5.25) yields

$$\hat{f} - f = [x \quad -1]\phi \tag{5.26}$$

The objective is to devise a scheme for adjusting $\hat{k}_e$ and $\hat{k}_x$, based on the 'prediction error' $\hat{f} - f$, such that $\hat{f} \to f$ as $t \to \infty$. The desirability of the objective $\hat{f} \to f$ is demonstrated as follows. From Eqs. (5.24) and (5.25) with $\hat{f} = f$, we have

$$f = \hat{k}_e x - \hat{k}_e \hat{x}_e = -\hat{k}_e(x_r - x) + f_r \tag{5.27}$$

where Eq. (5.23) is used. Employing the target impedance as described by Eq. (2.4c), removing $(x_r - x)$ dependence in Eq. (5.27) and noting that if $\hat{f} = f$, then $\hat{k}_e$ is constant, gives the following relation:

$$M\ddot{e} + C\dot{e} + (K + \hat{k}_e)e = 0 \tag{5.28}$$

so that if $\hat{f} \to f$ then $f \to f_r$ or $\hat{k}_e \to -K$. The latter situation is easily avoidable since $k_e > 0$, so $\hat{k}_e$ can be restricted to positive estimates. Thus, $\hat{f} \to f$ implies $f \to f_r$ as desired.

The update laws for $\hat{k}_e$ and $\hat{k}_x$ to ensure $\hat{f} \to f$, and thus $f \to f_r$, are derived using a Lyapunov-based approach. We first define a positive scalar Lyapunov function candidate

$$V = \phi^T \Gamma \phi \tag{5.29}$$

where Γ is a (2×2) symmetric positive definite constant matrix. If $\dot{\phi}$ is specified as

$$\dot{\phi} = -\Gamma^{-1} \begin{bmatrix} x \\ -1 \end{bmatrix} (\hat{f} - f) \tag{5.30}$$

and differentiating (5.29) using Eqs. (5.30) and (5.26) gives

$$\dot{V} = 2\phi^T \Gamma \dot{\phi} = -2\phi^T \begin{bmatrix} x \\ -1 \end{bmatrix} (\hat{f} - f) = -2(\hat{f} - f)^2 \tag{5.31}$$

which is negative semi-definite. Eqs. (5.29) and (5.31) suggest that if ϕ is adjusted according to Eq. (5.30), then $\hat{f} \to f$ as $t \to \infty$, which implies $f \to f_r$ as $t \to \infty$. By definition we know that

$$\phi = \begin{bmatrix} \phi_k \\ \phi_x \end{bmatrix} = \begin{bmatrix} \hat{k}_e - k_e \\ \hat{k}_x - k_x \end{bmatrix} = \begin{bmatrix} \hat{k}_e - k_e \\ \hat{k}_e \hat{x}_e - k_e x_e \end{bmatrix} \tag{5.32}$$

Therefore,

$$\dot{\phi} = \begin{bmatrix} \dot{\hat{k}}_e \\ \dot{\hat{k}}_e \hat{x}_e + \hat{k}_e \dot{\hat{x}}_e \end{bmatrix} = -\Gamma^{-1} \begin{bmatrix} x \\ -1 \end{bmatrix} (\hat{f} - f) \tag{5.33}$$

and

$$\begin{bmatrix} \frac{1}{\gamma_1} & 0 \\ 0 & \frac{1}{\gamma_2} \end{bmatrix} \begin{bmatrix} \dot{\hat{k}}_e \\ \dot{\hat{k}}_e \hat{x}_e + \hat{k}_e \dot{\hat{x}}_e \end{bmatrix} = \begin{bmatrix} -x \\ 1 \end{bmatrix} (\hat{f} - f) \tag{5.34}$$

where $\Gamma = \begin{bmatrix} \frac{1}{\gamma_1} & 0 \\ 0 & \frac{1}{\gamma_2} \end{bmatrix}$ and, γ_1 and γ_2 are positive scalar constants. The above relation leads to the following set of equations:

$$\begin{aligned} \dot{\hat{k}}_e &= -\gamma_1 x (\hat{f} - f) \\ \dot{\hat{x}}_e &= \frac{(\hat{f} - f)}{\hat{k}_e} (\gamma_1 x \hat{x}_e + \gamma_2) \end{aligned} \tag{5.35}$$

Thus, the complete force-tracking scheme, based on on-line identification, can be summarized as

$$\begin{aligned} x_r &= \hat{x}_e + \frac{1}{\hat{k}_e} f_r \\ \hat{k}_e(t) &= \hat{k}_e(0) - \gamma_1 \int_0^t x (\hat{f} - f) dt \\ \hat{x}_e(t) &= \hat{x}_e(0) + \gamma_1 \int_0^t \frac{(\hat{f} - f)}{\hat{k}_e} \left(x \hat{x}_e + \gamma_2 / \gamma_1 \right) dt \\ \hat{f} &= \hat{k}_e (x - \hat{x}_e) \end{aligned} \tag{5.36}$$

5.4.2 Discussion

1. The above scheme uses a certainty equivalence approach, i.e., the environmental parameters x_e and k_e are estimated on-line, and the estimates $\hat{x}_e$ and $\hat{k}_e$ are used to compute x_r in Eq. (5.23). Note that the preceding analysis demonstrates that $f \to f_r$ as $t \to \infty$ using this approach, whether x_e and k_e are identified or not. Narendra and Annaswamy (1989) discussed that such schemes tend to be robust to unmodeled effects and sensor noise which is very attractive for the purpose of this study. The dynamics of the hydraulic system in the Unimate robot are highly nonlinear and contain many uncertainties that cannot be adequately modeled. Furthermore, the force sensor used in this thesis is a rugged, in-house built sensor with a ±15N noise level.
2. Substituting Eq. (5.26) into (5.30),

$$\dot{\phi} = -\Gamma^{-1}\begin{bmatrix} x \\ -1 \end{bmatrix}\begin{bmatrix} x & -1 \end{bmatrix}\phi \tag{5.37}$$

and differentiating Eq. (5.29) using Eq. (5.30) yields

$$\dot{V} = -2\phi^T\begin{bmatrix} x^2 & -x \\ -x & 1 \end{bmatrix}\phi \tag{5.38}$$

$\dot{V}$ is negative semi-definite in ϕ; thus, convergence of the parameter error, ϕ, to zero cannot be guaranteed. Indeed, convergence of ϕ requires a persistent excitation condition that is very unlikely to be realized in practice, because x typically varies very little during contact with the environment. This is the reason for minimizing the prediction error, $\hat{f} - f$, as the control objective since it is obtainable and ensures $f \to f_r$, as desired. Furthermore, Eqs. (5.36) may not ensure the boundedness of ϕ

in the presence of unmodeled effects, and so does not guarantee that $\hat{k}_e$ and $\hat{x}_e$ remain bounded. Therefore, it is necessary to keep these estimates in the compact sets $\hat{k}_e \subset \left[\hat{k}_e^-, \hat{k}_e^+\right]$ and $\hat{x}_e \subset \left[\hat{x}_e^-, \hat{x}_e^+\right]$, which is a common practice in parameter estimation methods. It is noted that selecting lower and upper bounds for $\hat{k}_e$ and $\hat{x}_e$ is practical, since this requires only very conservative information concerning k_e and x_e.

3. Eqs. (5.36) ensures that x_r, $\dot{x}_r$, and $\ddot{x}_r$ remain bounded, provided f_r is bounded. This is important because the boundedness of the reference trajectory and its derivatives is a necessary condition for stability of virtually any proposed impedance controller.

5.4.3 Simulation Study

The above controller has been tested in the simulation. The benchmark test was same as the one described in Section 5.3.2. Figure 5.10 illustrates the force regulating capability of the presented method as applied to an environment with a stiffness of $k_e = 70000\,\text{N/m}$. Environmental parameters were initially estimated to be $\hat{x}_e(0) = 0.15\,\text{m}$ and $\hat{k}_e(0) = 35000\,\text{N}$ and the two controller parameters, $\gamma_1 = 2$ and $\gamma_2 = 1$, were adjusted to provide the best possible performance for this environment. Figure 5.11 illustrates how the estimated parameters change in this scheme. With respect to this figure, the steady-state values of the estimated parameters are:

$$\hat{x}_e = 0.1446\,\text{m} \quad , \quad \hat{k}_e = 34956\,\text{N/m}$$

These estimations are obviously far away from the actual environmental parameters ($x_e = 0.13\,\text{m}$ and $k_e = 70000\,\text{N/m}$). It was observed that these estimates are highly dependent on the values of the initial estimations. Nevertheless, the end-effector force is regulated accurately. This is due to the fact that convergence of the prediction error, $\hat{f} - f$, was the control objective. Therefore, the scheme always works with the combination of values of environmental position and stiffness to determine the appropriate reference position. For example, given the exact parameters, the reference position, to regulate $f_r = 1000\,\text{N}$ at the end-point, is determined as:

$$x_r = x_e + \frac{f_r}{k_e} = 0.13 - \frac{1000}{70000} = 0.1157\,\text{m}$$

Given the estimates of the parameters, the reference position is determined as

$$x_r = \hat{x}_e + \frac{f_r}{\hat{k}_e} = 0.1446 - \frac{1000}{34956} = 0.1160\,\text{m}$$

which provides an end-effector force, $f = k_e(x - x_e) = 980\,\text{N}$, at the end-point.

Figures 5.12 and 5.13 show the performance of the controller in regulating the end-effector forces on low stiffness and high stiffness environments, respectively. The same initial and controller parameters as in the previous test were used. Both tests produced good force regulating performances. The slow response for the low stiffness test and hunting for the high stiffness environment were quite expected. For example, with reference to Fig. 4.1, we have

$$\frac{F}{X_r} = \frac{M_x(Ms^2 + Cs + K)(m_e s^2 + c_e s + k_e)}{(M + m_e)s^2 + (C + c_e)s + (K + k_e)}$$

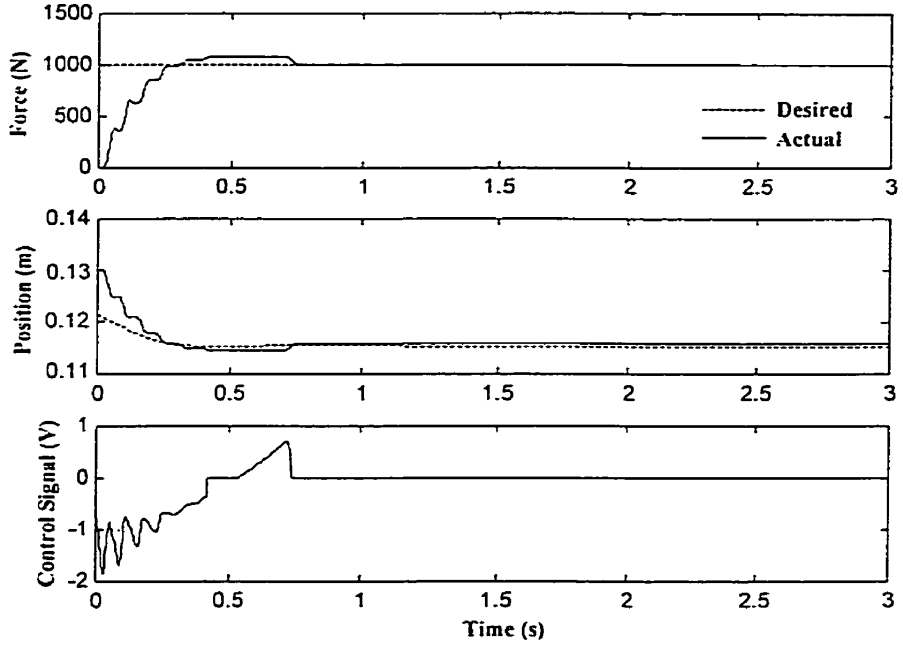

Fig. 5.10. On-line parameters estimation method force response for benchmark environment ($k_e = 70000\,\text{N/m}$) (simulations)

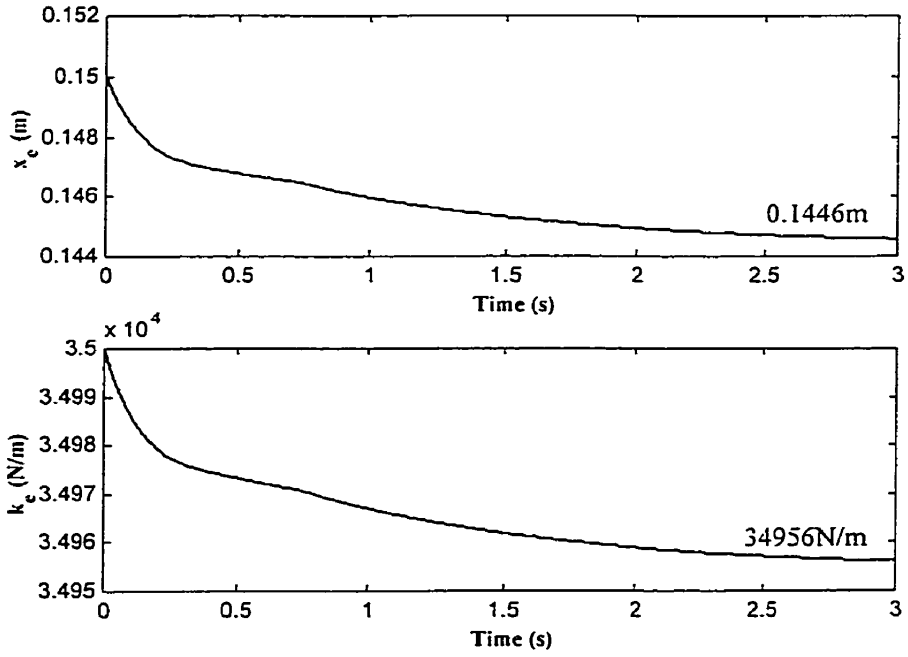

Fig. 5.11. Environment parameters estimation pertaining to Fig. 5.10

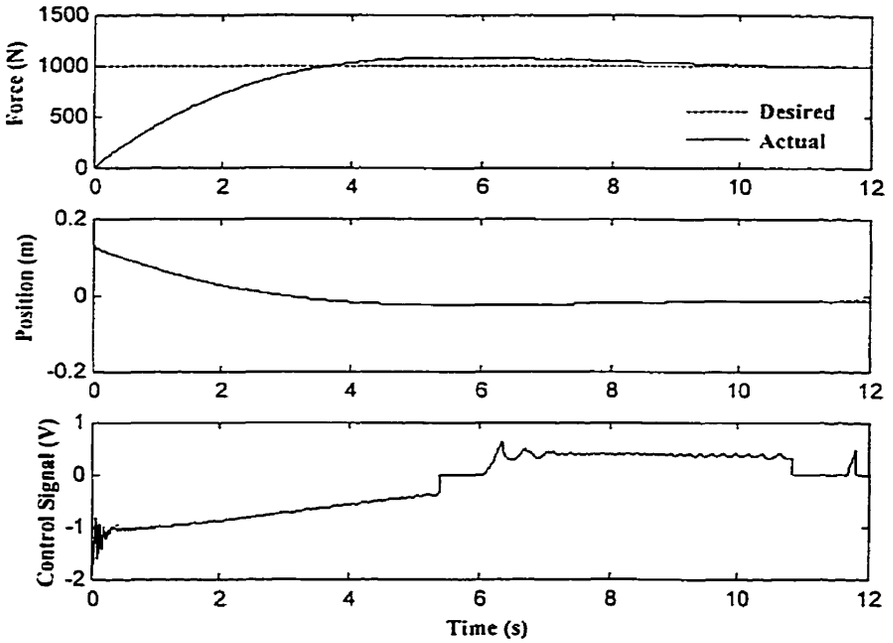

Fig. 5.12. On-line parameters estimation method force response for low stiffness environment ($k_e = 7000\,\text{N/m}$) (simulations)

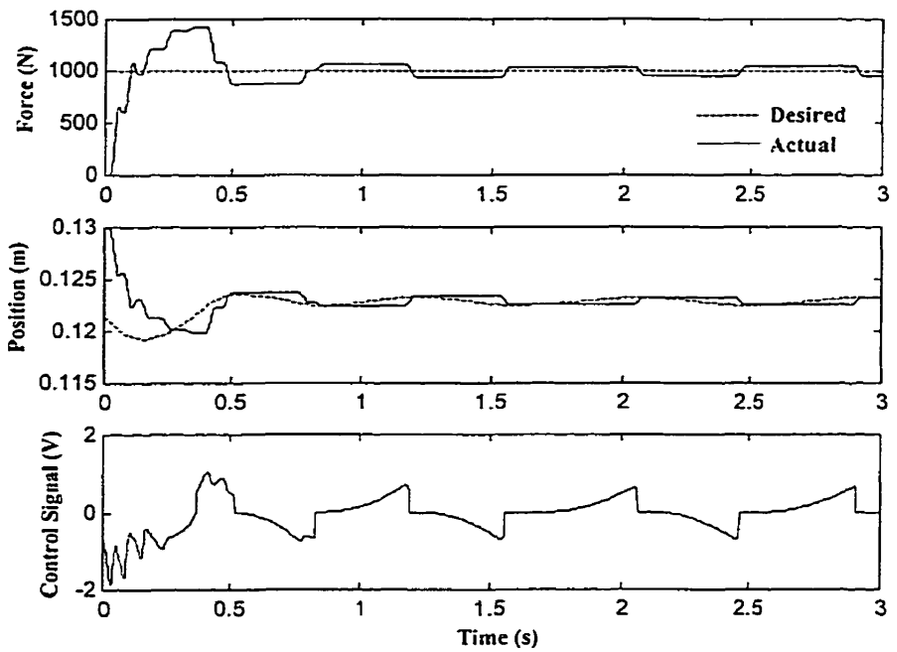

Fig. 5.13. On-line parameters estimation method force response for high stiffness environment ($k_e = 140000\,\text{N/m}$) (simulations)

It is seen that an increase in environmental stiffness increases the undamped natural frequency of the system and decreases the damping ratio. Together with small unavoidable positioning errors due to the imperfect NPI position controller, the results exhibit an overshoot and some sustained oscillations.

To bring further insight into the performance of the controller described above, more simulations were performed using variations on the values of the controller parameters, γ_1 and γ_2, as well as the initial estimates. Figure 5.14 shows the system's response when the end-effector was initially positioned 7cm away from the environment's free surface. Figure 5.15 shows the response when the end-effector was already positioned almost 3cm into the environment's free surface (contact force was $\approx 2000\,\mathrm{N}$). These results can be compared with Fig. 5.10 in which the end-effector was placed just in contact with the environment. Figure 5.14 illustrates a stable contact even though the control signal shows saturation at the start of the motion, meaning that the end-effector approaches the environment with full speed.

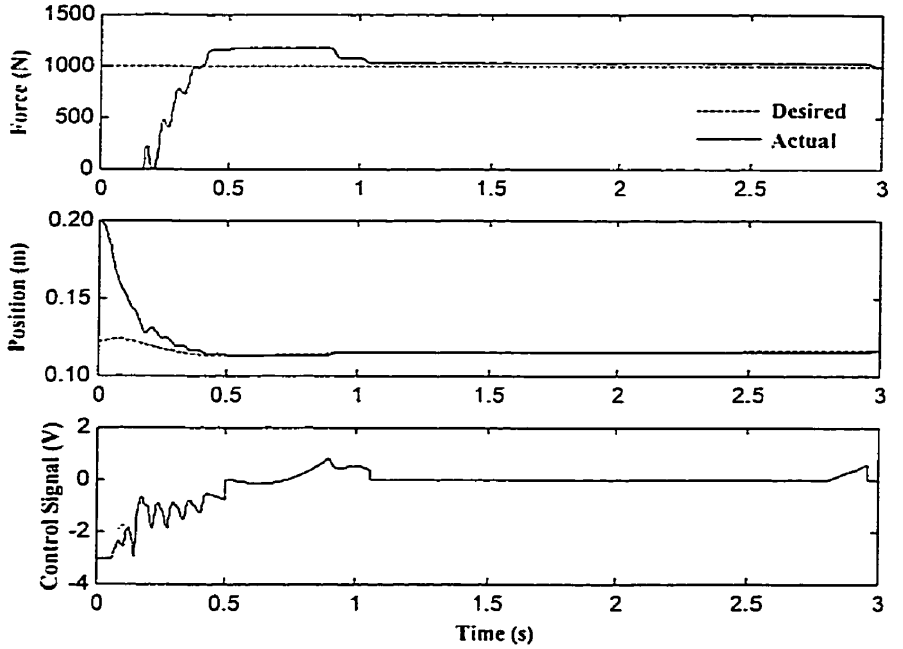

Fig. 5.14. On-line parameters estimation method force response for benchmark environment (k_e = 70000 N/m) and end-effector initially ~7cm away from the environment surface (simulations)

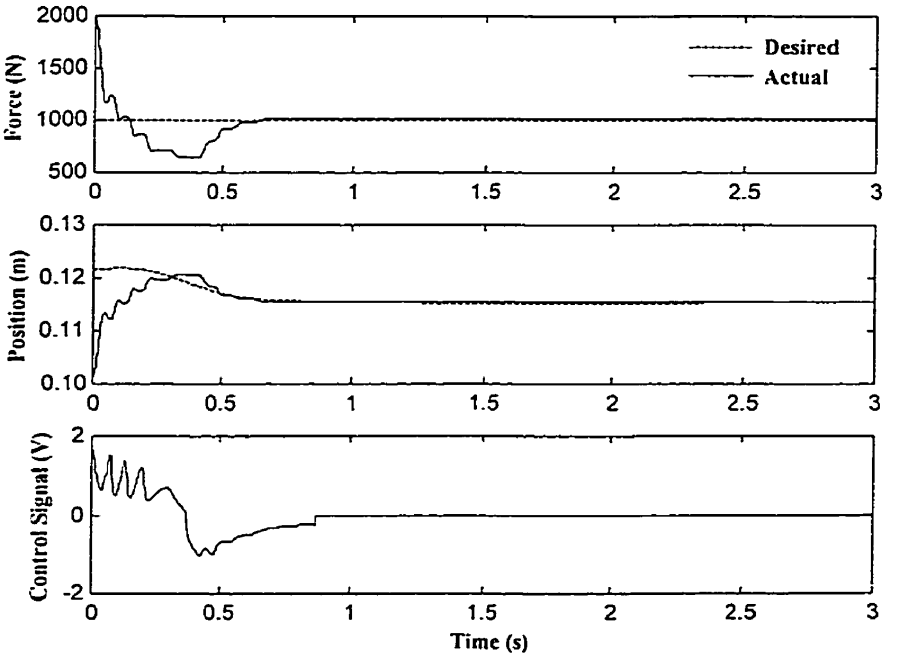

Fig. 5.15. On-line parameters estimation method force response for benchmark environment (k_e = 70000 N/m) and end-effector initially ~3cm into the environment surface (simulations)

Figures 5.16 and 5.17 show the effect of the variation of the initial estimation of the environmental stiffness, $\hat{k}_e(0)$, on the force regulating response. From Eq. (5.23), $\hat{k}_e$ inversely affects the position reference, x_r; thus, $\hat{k}_e(0)$ inversely affects the resulting contact force at the start of the motion. Since the initial estimation of the environment location, $\hat{x}_e(0)$, was 2cm away from the actual location of environment, an over-estimation of initial environmental stiffness (see Fig. 5.16) causes the position reference to initially move even farther away from the environment's free surface. This can produce a delay in establishing contact. On the other hand, under-estimating the environmental stiffness may cause the position reference to penetrate into the environment more than required, giving rise to an overshoot (see Fig. 5.17). Therefore, if a large overshoot is to be avoided, environment stiffness should initially be over-estimated rather than under-estimated.

Figures 5.18 and 5.19 show the effect of the initial estimation of the environmental location, $\hat{x}_e(0)$. From Eq. (5.23), $\hat{x}_e$ directly affects both the position reference, x_r, and consequently the resulting contact force. If the environmental location is initially estimated as being far away from the actual location, x_e, this introduces a delay in the force response in a similar manner as over-estimating $\hat{k}_e(0)$. On the other hand, if the environment location is initially estimated to be deep within the actual environment location, this may cause a large overshoot as seen in Fig. 5.19. Therefore, to avoid force overshoot, the initial estimation of environment location should be away from the actual environment location.

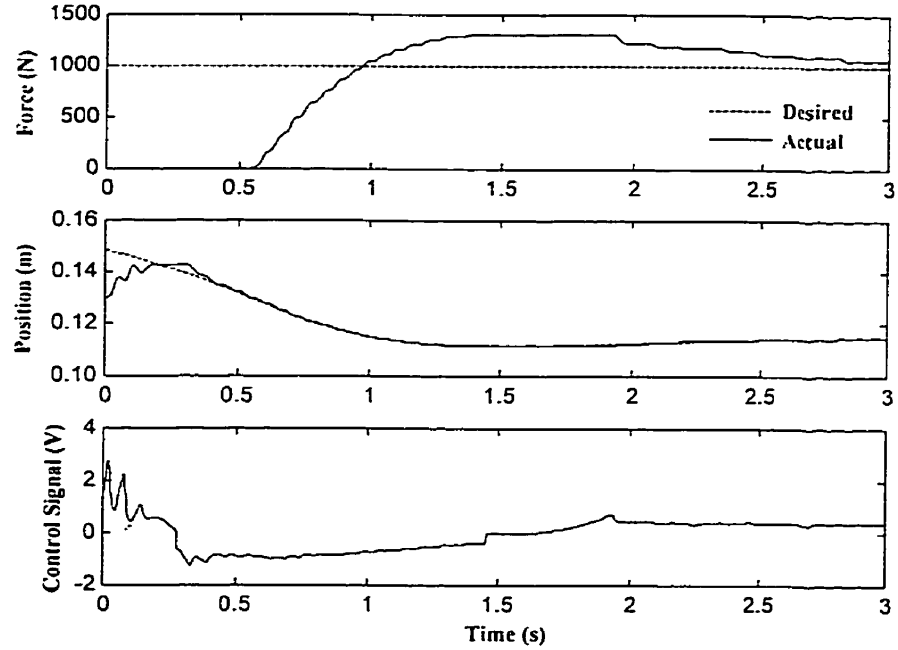

Fig. 5.16. On-line parameters estimation method force response for benchmark environment ($k_e = 70000\,\text{N/m}$) and initially over-estimated environmental stiffness ($\hat{k}_e(0) = 10 \times k_e$)

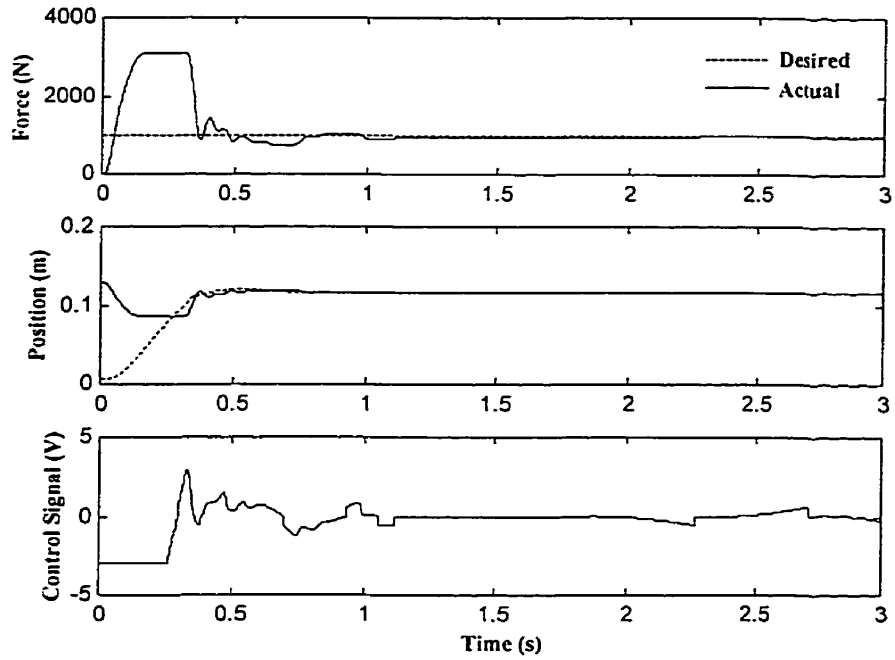

Fig. 5.17. On-line parameters estimation method force response for benchmark environment ($k_e = 70000\,\text{N/m}$) and initially under-estimated environmental stiffness ($\hat{k}_e(0) = 0.1 \times k_e$)

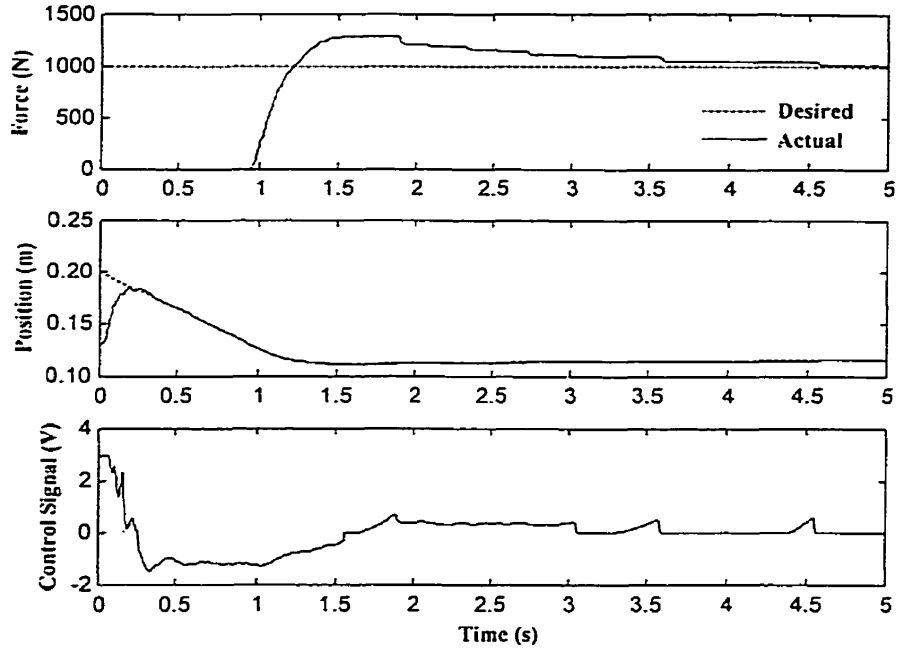

Fig. 5.18. On-line parameters estimation method force response for benchmark environment ($k_e = 70000$ N/m) and environmental location initially estimated 10cm away from its actual location ($\hat{x}_e(0) = x_e + 0.100$)

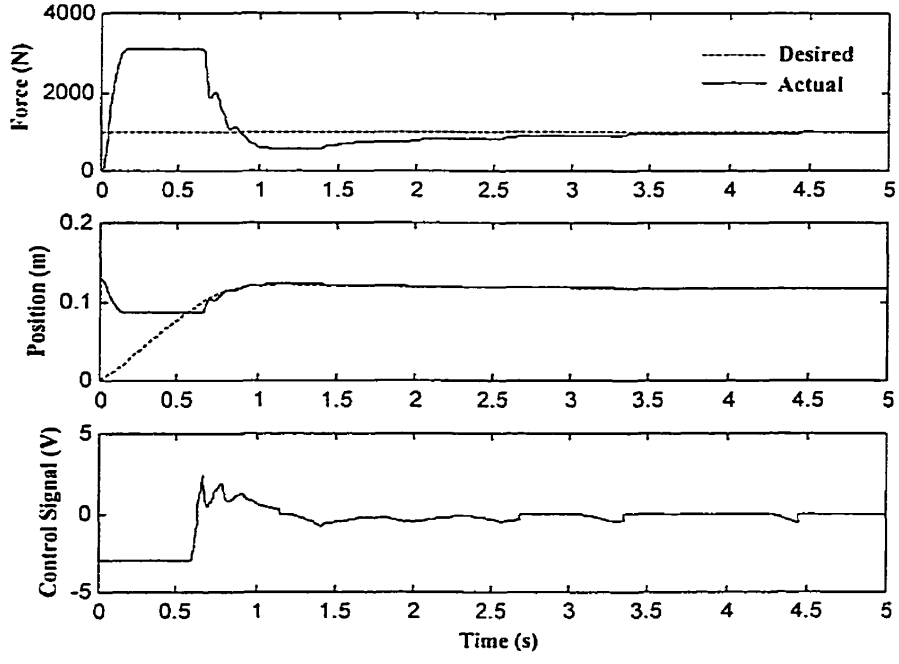

Fig. 5.19. On-line parameters estimation method force response for benchmark environment ($k_e = 70000$ N/m) and environmental location initially estimated 10cm beyond its actual location ($\hat{x}_e(0) = x_e - 0.100$)

Figures 5.20 and 5.21 show the effect of the variation of controller parameter γ_1. As is seen from these figures, the controller is rather insensitive to the variation of this parameter. The effect of γ_2 on the response was also studied. Figures 5.22 to 5.25 show the results of changing γ_2. With reference to Fig. 5.22, it is seen that even eliminating this gain, i.e., $\gamma_2 = 0$, has no significant effect on the performance of the controller. However, increasing γ_2, though still rather insensitive (see Fig. 5.24), may lead to sustained oscillations during the steady-state case (see Fig. 5.25). This is evidenced by the observation that γ_2 partly acts as a gain to the integral of force error [see Eq. (5.36)].

5.4.4 Experimental Evaluations

The control algorithm described by (5.36) was applied to the hydraulic test station. The controller parameters were set to $\gamma_1 = 2$ and $\gamma_2 = 1$ which provided the best possible response for the low stiffness environment (~10,000N/m). The response for the high stiffness environment (~42,000N/m) was then evaluated using the same controller gains. The benchmark tests from Section 5.3.3 were applied here. Fig. 5.26 shows the test result for force control on the low stiffness environment. Initial estimations of $\hat{k}_e(0) = 7000\text{N/m}$ and $\hat{x}_e(0) = 0.02\,\text{m}$ were used for this environment. The high stiffness environment was tested with initial estimations of $\hat{k}_e(0) = 35000\,\text{N/m}$ and $\hat{x}_e(0) = 0.02\,\text{m}$. Figure 5.27 shows the experimental force control response on the high stiffness environment. Figure 5.28 compares the control efforts. Note that the control signals are smooth and do not chatter.

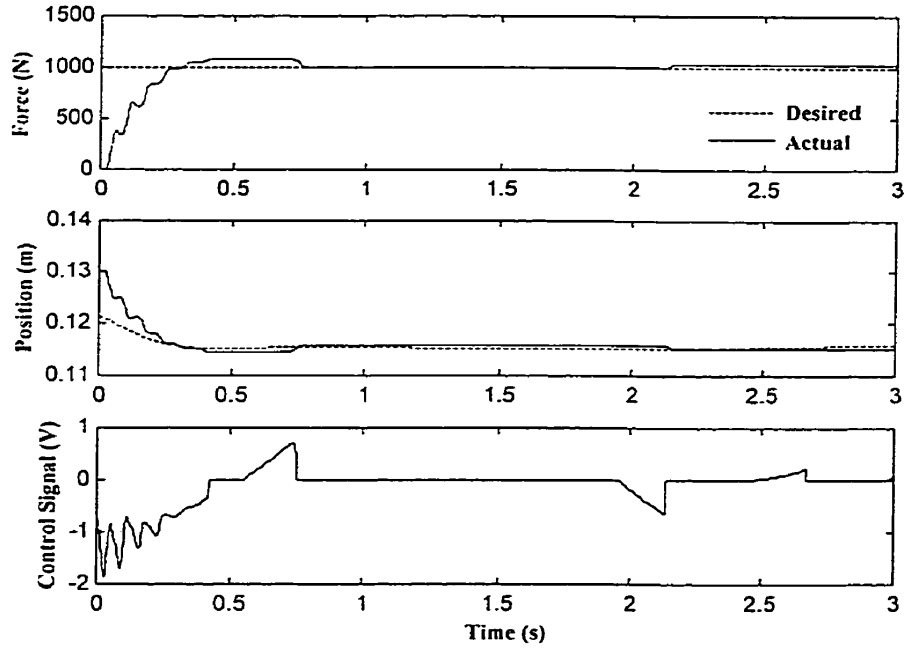

Fig. 5.20. Effect of reducing γ_1 ($\gamma_1 = 2 \times 0.01$) in on-line parameters estimation method force response

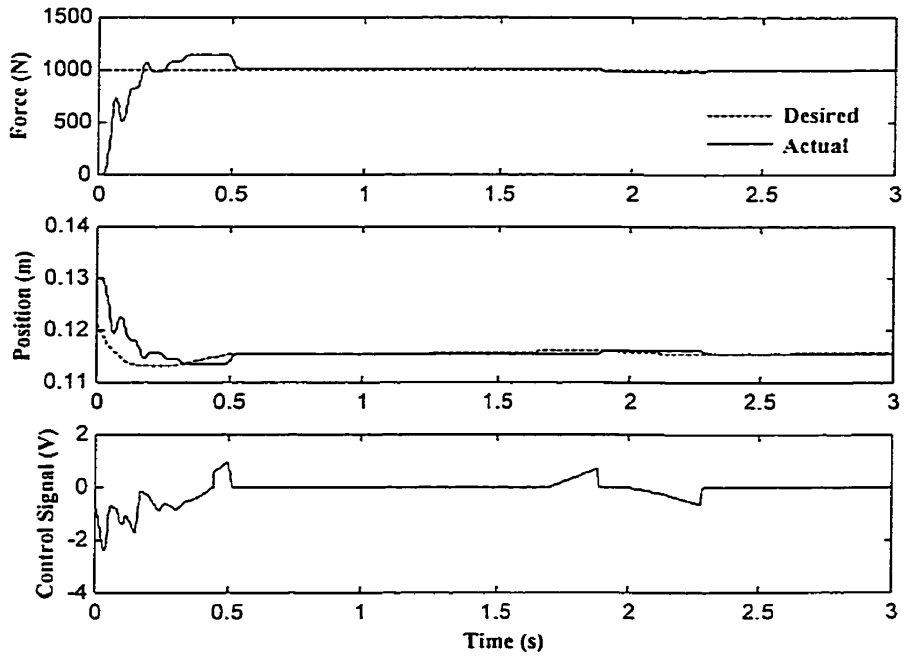

Fig. 5.21. Effect of increasing γ_1 ($\gamma_1 = 2 \times 100$) in on-line parameters estimation method force response

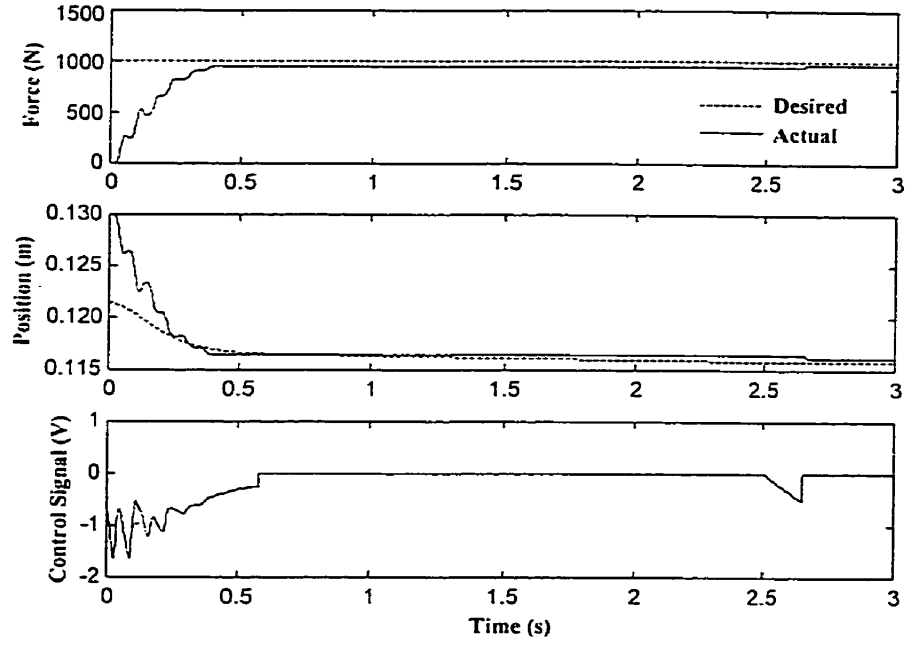

Fig. 5.22. Effect of extremely reducing γ_2 ($\gamma_2 = 0$) in on-line parameters estimation method force response

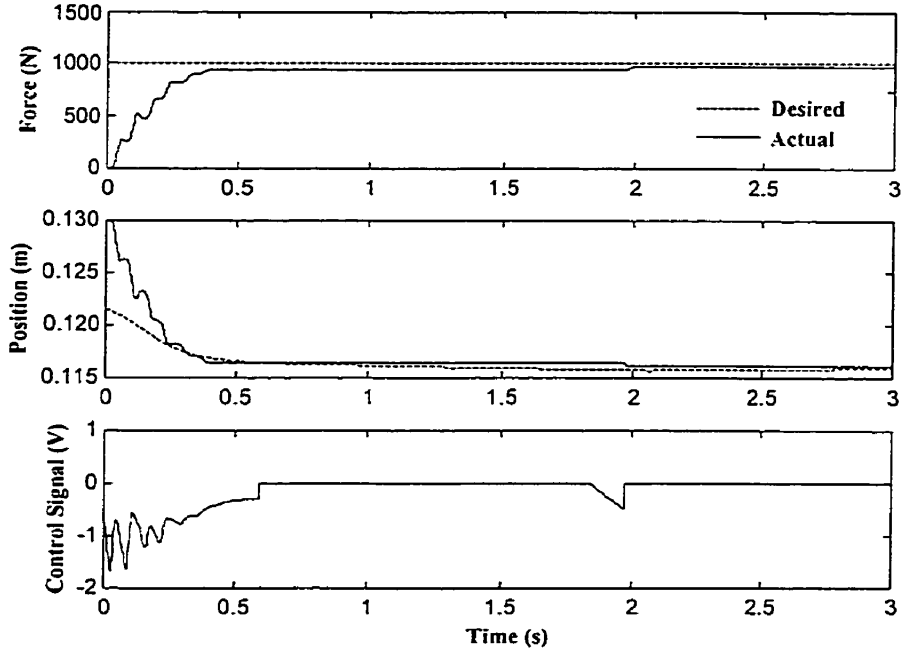

Fig. 5.23. Effect of reducing γ_2 ($\gamma_2 = 1 \times 0.025$) in on-line parameters estimation method force response

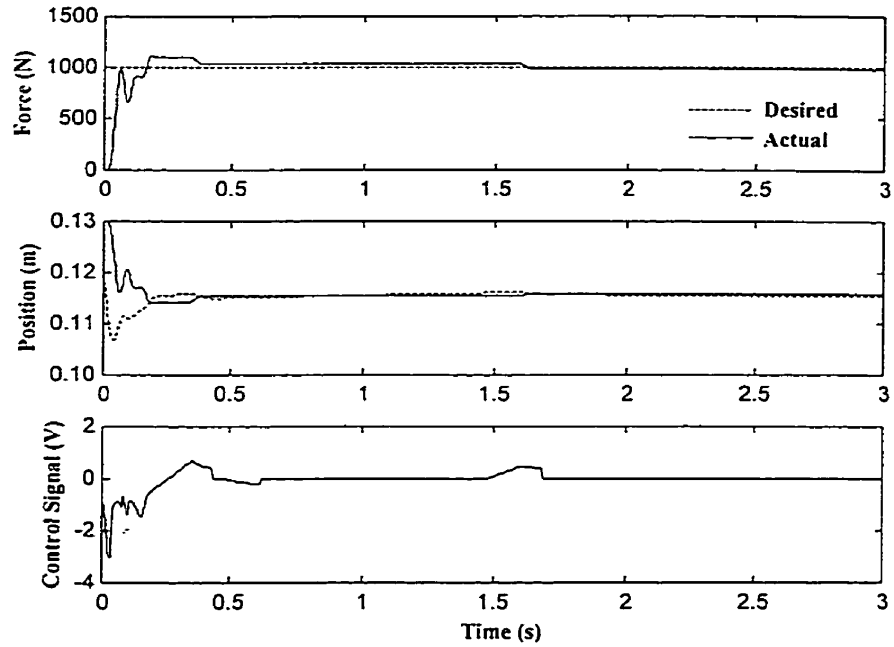

Fig. 5.24. Effect of increasing γ_2 ($\gamma_2 = 1 \times 40$) in on-line parameters estimation method force response

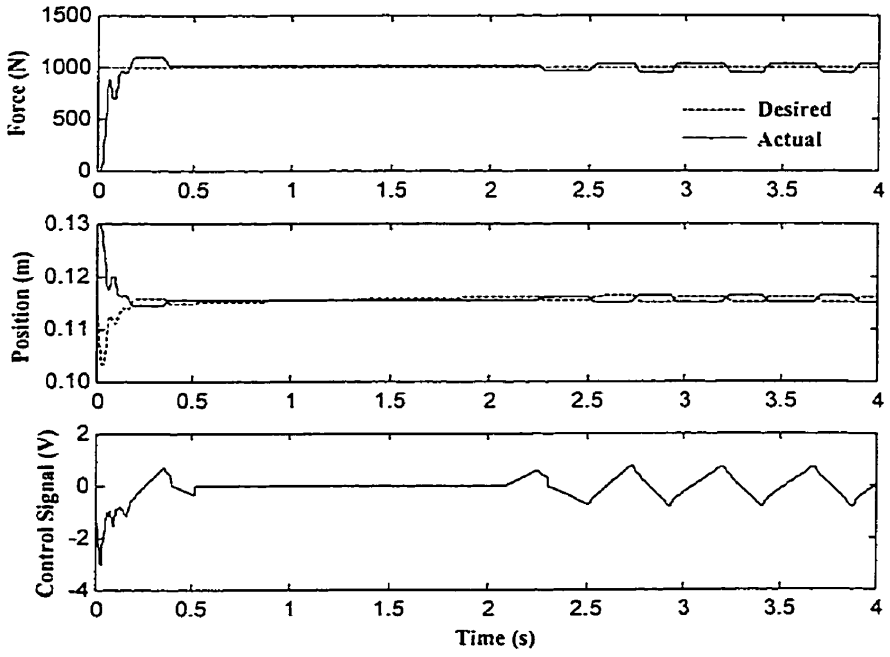

Fig. 5.25. Effect of extremely increasing γ_2 ($\gamma_2 = 1 \times 100$) in on-line parameters estimation method force response

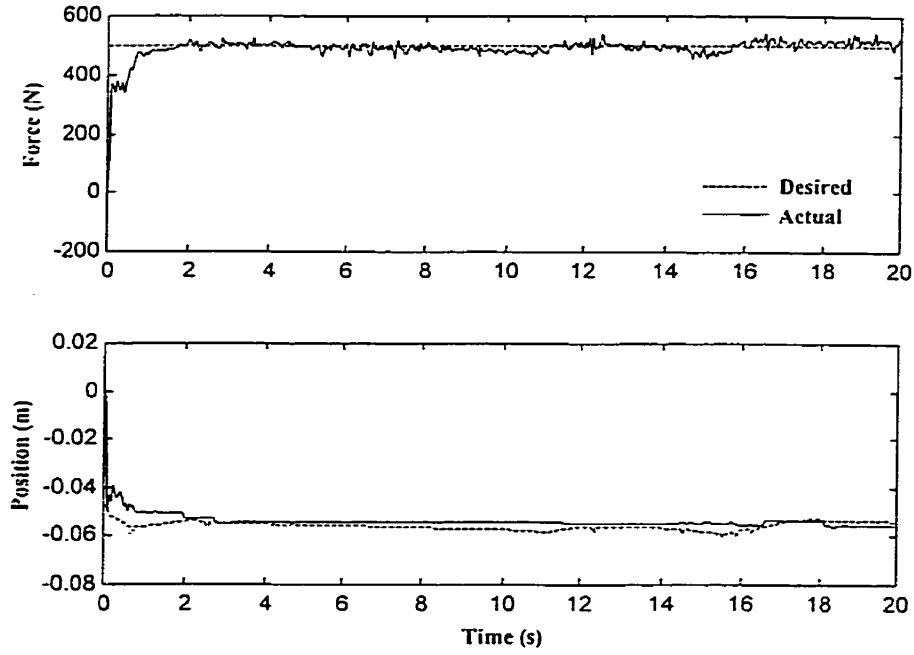

Fig. 5.26. On-line parameters estimation method force response on a low stiffness environment ($k_e \approx 10000\,\text{N/m}$) (experiment)

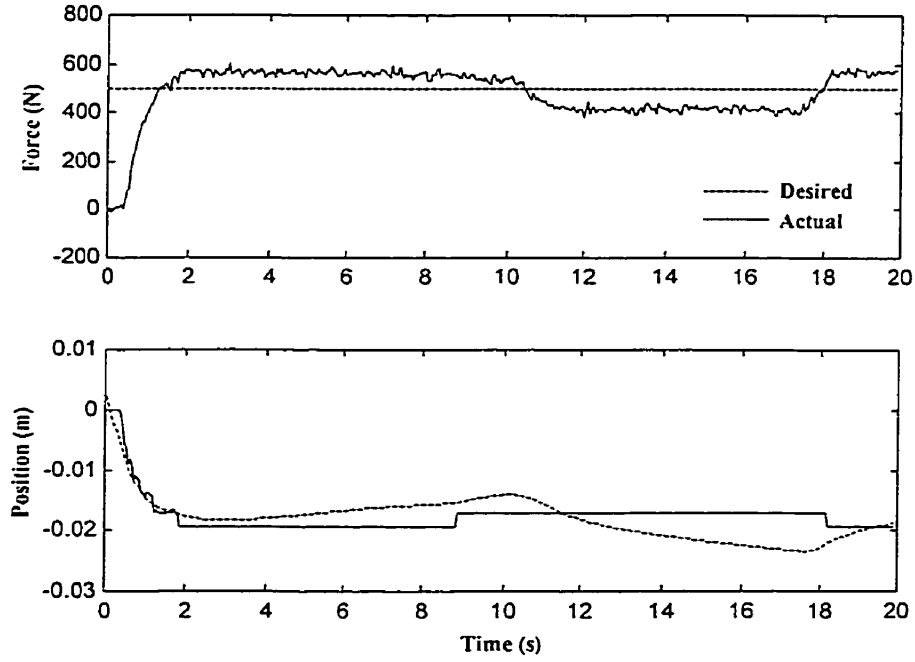

Fig. 5.27. On-line parameters estimation method force response on a high stiffness environment ($k_e \approx 42000\,\text{N/m}$) (experiment)

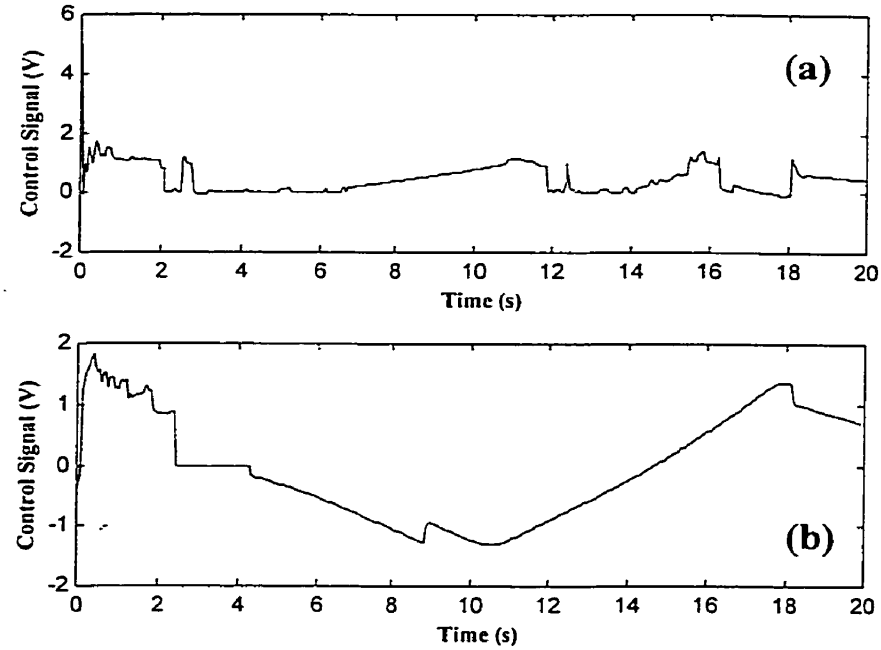

Fig. 5.28. Control signals pertaining to:
(a) Low stiffness environment (Fig. 5.26)
(b) High stiffness environment (Fig. 5.27)

5.5 Force Control Without Explicit Parameters Estimation

5.5.1 Derivation of the Method

In the previous section, it was shown that on-line estimation of the environmental parameters, k_e and x_e, do not necessarily converge to the correct values. However, the combined estimated parameters, when used within Eq. (5.23), produce an appropriate position reference to regulate the contact force.

This section focuses on generating the reference position directly and without explicit identification of the environmental parameters. An extensive literature survey identified the direct adaptive scheme developed by Seraji and Colbaugh (1997) as the only method

suitable to be adopted for force control of PBIC of hydraulic actuators. Therefore, this method is explored here.

The underlying concept of this scheme is the generation of the reference position, x_r, on-line as a function of force tracking error, $e = f_r - f$:

$$x_r(t) = g(t) + k_p(t)e(t) + k_d(t)\dot{e}(t) \tag{5.39}$$

where $k_p(t)$ and $k_d(t)$ are adaptive gains acting on the force error $e(t)$ and the error rate $\dot{e}(t)$, respectively. $g(t)$ is the auxiliary signal to be generated by an adaptation scheme. The target impedance given in (2.4a) is used here, since using the impedance models (2.4b) and (2.4c) result in the appearance of $\dot{x}_r$ and $\ddot{x}_r$ terms in the error dynamics equation which is undesirable for the subsequent control-law development. Rewriting the error dynamics equation (5.4),

$$M\ddot{e} + C\dot{e} + (K + k_e)e = K(f_r + k_e x_e) - Kk_e x_r \tag{5.40}$$

and substituting x_r from the control law (5.39) into the error dynamics (5.40), yields

$$\ddot{e}(t) + a(t)\cdot\dot{e}(t) + b(t)\cdot e(t) = f(t) \tag{5.41}$$

where

$$\begin{aligned} a(t) &= \frac{C + Kk_e k_d(t)}{M} \\ b(t) &= \frac{K + k_e + Kk_e k_p(t)}{M} \\ f(t) &= \frac{K(f_r + k_e x_e) - Kk_e g(t)}{M} \end{aligned} \tag{5.42}$$

$a(t)$, $b(t)$, $f(t)$ in (5.42) contain both fixed system parameters and adjustable controller gains. Force error dynamics (5.41) can be written in state space as

$$\dot{E} = \begin{bmatrix} 0 & 1 \\ -b & -a \end{bmatrix} E + \begin{bmatrix} 0 \\ f \end{bmatrix} \tag{5.43}$$

where $E(t) = \begin{bmatrix} e(t) & \dot{e}(t) \end{bmatrix}^T$ is the 2×1 force/force-rate error vector or the state vector of the adjustable system. Now let the desired behavior of $e(t)$ be described by the following second-order homogeneous differential equation:

$$\ddot{e}_m(t) + 2\zeta\omega \cdot \dot{e}_m(t) + \omega^2 \cdot e_m(t) = 0 \tag{5.44}$$

where e_m is the desired behavior of the force tracking error, and ς and ω are the user-specified damping ratio and undamped natural frequency of the force error dynamics, respectively. Rewriting (5.44) in state space, the following 'reference model' is obtained:

$$\dot{E}_m = \begin{bmatrix} 0 & 1 \\ -\omega^2 & -2\zeta\omega \end{bmatrix} E_m = DE_m \tag{5.45}$$

where $E_m(t) = \begin{bmatrix} e_m(t) & \dot{e}_m(t) \end{bmatrix}^T$ is the 2×1 desired force error and force error rate vector. Since the reference model (5.45) is stable, there exist symmetric positive-definite constant 2×2 matrices $P = \begin{bmatrix} p_1 & p_2 \\ p_2 & p_3 \end{bmatrix}$ and $Q = \begin{bmatrix} q_1 & q_2 \\ q_2 & q_3 \end{bmatrix}$ which satisfy the Lyapunov equation for the reference model (5.45), i.e.,

$$\mathrm{PD} + \mathrm{D}^{\mathrm{T}}\mathrm{P} = \mathrm{P}\begin{bmatrix} 0 & 1 \\ -\omega^2 & -2\zeta\omega \end{bmatrix} + \begin{bmatrix} 0 & -\omega^2 \\ 1 & -2\zeta\omega \end{bmatrix}\mathrm{P} = -Q \tag{5.46}$$

The initial values of the desired and actual responses are often the same, and hence the initial error is usually zero, i.e.,

$$E_m(0) = \begin{bmatrix} e_m(0) \\ \dot{e}_m(0) \end{bmatrix} = 0 \tag{5.47}$$

Thus, the solution of the homogeneous equation (5.44) is identically zero: $E_m(t) = 0$ for all t. Now, the goal is to find the appropriate time functions $a(t)$, $b(t)$ and $f(t)$ such that the state of the adjustable system (5.41), i.e., $[e(t) \quad \dot{e}(t)]^T$, tends to that of the reference model (5.44), i.e., $[e_m(t) \quad \dot{e}_m(t)]^T$, asymptotically. Subtracting (5.44) from (5.41),

$$(\ddot{e} - \ddot{e}_m) + 2\zeta\omega\,(\dot{e} - \dot{e}_m) + \omega^2\,(e - e_m) = f + (2\zeta\omega - a)\,\dot{e} + (\omega^2 - b)\,e \tag{5.48}$$

is obtained, or in the state-space form,

$$\dot{\boldsymbol{E}} = \begin{bmatrix} 0 & 1 \\ -\omega^2 & -2\zeta\omega \end{bmatrix} \boldsymbol{E} + \begin{bmatrix} 0 & 0 \\ \omega^2 - b & 2\zeta\omega - a \end{bmatrix} \begin{Bmatrix} e \\ \dot{e} \end{Bmatrix} + \begin{Bmatrix} 0 \\ f \end{Bmatrix} \tag{5.49}$$

where $\boldsymbol{E} = E - E_m = [(e - e_m) \quad (\dot{e} - \dot{e}_m)]^T$ is the adaptation error vector. Defining a scalar positive-definite Lyapunov function candidate

$$V = \boldsymbol{E}^T P\, \boldsymbol{E} + Q_0 \left(f - f^*\right)^2 + Q_1 \left(\omega^2 - b + b^*\right)^2 + Q_2 \left(2\zeta\omega - a + a^*\right)^2 \tag{5.50}$$

where Q_0, Q_1 and Q_2 are arbitrary constant positive scalars, P is given by (5.46), and a^*, b^* and f^* are functions of time to be specified later.

Differentiating V with respect to time, we obtain

$$\dot{V} = \dot{\boldsymbol{E}}^T P \boldsymbol{E} + \boldsymbol{E}^T P \dot{\boldsymbol{E}}$$
$$+ 2Q_0 (f - f^*)(\dot{f} - \dot{f}^*)$$
$$+ 2Q_1 (\omega^2 - b + b^*)(-\dot{b} + \dot{b}^*)$$
$$+ 2Q_2 (2\zeta\omega - a + a^*)(-\dot{a} + \dot{a}^*)$$

or

$$\dot{V} = \left(\boldsymbol{E}^T \begin{bmatrix} 0 & -\omega^2 \\ 1 & -2\zeta\omega \end{bmatrix} + \begin{bmatrix} e & \dot{e} \end{bmatrix} \begin{bmatrix} 0 & (\omega^2 - b) \\ 0 & (2\zeta\omega - a) \end{bmatrix} + \begin{bmatrix} 0 & f \end{bmatrix} \right) P \boldsymbol{E}$$
$$+ \boldsymbol{E}^T P \left(\begin{bmatrix} 0 & 1 \\ -\omega^2 & -2\zeta\omega \end{bmatrix} \boldsymbol{E} + \begin{bmatrix} 0 & 0 \\ (\omega^2 - b) & (2\zeta\omega - a) \end{bmatrix} \begin{bmatrix} e \\ \dot{e} \end{bmatrix} + \begin{bmatrix} 0 \\ f \end{bmatrix} \right)$$
$$+ 2Q_0 (f - f^*)(\dot{f} - \dot{f}^*)$$
$$+ 2Q_1 (b - \omega^2 - b^*)(\dot{b} - \dot{b}^*)$$
$$+ 2Q_2 (a - 2\zeta\omega - a^*)(\dot{a} - \dot{a}^*)$$

Rearranging:

$$\dot{V} = \boldsymbol{E}^T \left(\begin{bmatrix} 0 & -\omega^2 \\ 1 & -2\zeta\omega \end{bmatrix} P + P \begin{bmatrix} 0 & 1 \\ -\omega^2 & -2\zeta\omega \end{bmatrix} \right) \boldsymbol{E}$$
$$+ \left(\begin{bmatrix} e & \dot{e} \end{bmatrix} \begin{bmatrix} 0 & (\omega^2 - b) \\ 0 & (2\zeta\omega - a) \end{bmatrix} + \begin{bmatrix} 0 & f \end{bmatrix} \right) P \boldsymbol{E}$$
$$+ \boldsymbol{E}^T P \left(\begin{bmatrix} 0 & 0 \\ (\omega^2 - b) & (2\zeta\omega - a) \end{bmatrix} \begin{bmatrix} e \\ \dot{e} \end{bmatrix} + \begin{bmatrix} 0 \\ f \end{bmatrix} \right)$$
$$+ 2Q_0 (f - f^*)(\dot{f} - \dot{f}^*)$$
$$+ 2Q_1 (b - \omega^2 - b^*)(\dot{b} - \dot{b}^*)$$
$$+ 2Q_2 (a - 2\zeta\omega - a^*)(\dot{a} - \dot{a}^*)$$

in which,

$$\left(\begin{bmatrix} e & \dot{e} \end{bmatrix} \begin{bmatrix} 0 & (\omega^2 - b) \\ 0 & (2\zeta\omega - a) \end{bmatrix} + \begin{bmatrix} 0 & f \end{bmatrix} \right) P \boldsymbol{E} = \left(f + e(\omega^2 - b) + \dot{e}(2\zeta\omega - a) \right) \left(p_2 (e - e_m) + p_3 (\dot{e} - \dot{e}_m) \right)$$

$$\boldsymbol{E}^T P \left(\begin{bmatrix} 0 & 0 \\ (\omega^2 - b) & (2\zeta\omega - a) \end{bmatrix} \begin{bmatrix} e \\ \dot{e} \end{bmatrix} + \begin{bmatrix} 0 \\ f \end{bmatrix} \right) = \left(f + e(\omega^2 - b) + \dot{e}(2\zeta\omega - a) \right) \left(p_2 (e - e_m) + p_3 (\dot{e} - \dot{e}_m) \right)$$

Substituting from (5.46) and (5.47) and summarizing:

$$\begin{aligned}\dot{V} = &-\boldsymbol{E}^T Q \boldsymbol{E} \\ &+ 2(p_2 e + p_3 \dot{e})\Big(f + e(\omega^2 - b) + \dot{e}(2\zeta\omega - a)\Big) \\ &+ 2Q_0(f - f^*)(\dot{f} - \dot{f}^*) \\ &+ 2Q_1(b - \omega^2 - b^*)(\dot{b} - \dot{b}^*) \\ &+ 2Q_2(a - 2\zeta\omega - a^*)(\dot{a} - \dot{a}^*)\end{aligned}$$

or

$$\begin{aligned}\dot{V} = -\boldsymbol{E}^T Q \boldsymbol{E} &+ [2Q_0 f(\dot{f} - \dot{f}^*) + 2qf - 2Q_0 f^*(\dot{f} - \dot{f}^*)] \\ &+ [2Q_1(b - \omega^2)(\dot{b} - \dot{b}^*) - 2q(b - \omega^2)e - 2Q_1 b^*(\dot{b} - \dot{b}^*)] \\ &+ [2Q_2(a - 2\zeta\omega)(\dot{a} - \dot{a}^*) - 2q(a - 2\zeta\omega)\dot{e} - 2Q_2 a^*(\dot{a} - \dot{a}^*)]\end{aligned} \tag{5.51}$$

where $q = p_2 e + p_3 \dot{e}$ is the weighted force/force-rate error. Now, for the adaptation error $\boldsymbol{E}$ to vanish asymptotically, $\dot{V}$ must be negative-definite in $\boldsymbol{E}$. For this purpose, it is considered that the following relations hold:

$$\begin{aligned}2Q_0 f(\dot{f} - \dot{f}^*) + 2qf = 0 \quad &\rightarrow \quad \dot{f} - \dot{f}^* = -\frac{1}{Q_0} q \\ 2Q_1(b - \omega^2)(\dot{b} - \dot{b}^*) - 2q(b - \omega^2)e = 0 \quad &\rightarrow \quad \dot{b} - \dot{b}^* = \frac{1}{Q_1} qe \\ 2Q_2(a - 2\zeta\omega)(\dot{a} - \dot{a}^*) - 2q(a - 2\zeta\omega)\dot{e} = 0 \quad &\rightarrow \quad \dot{a} - \dot{a}^* = \frac{1}{Q_2} q\dot{e}\end{aligned} \tag{5.52}$$

which causes the time derivative of the Lyapunov function to be reduced to:

$$\dot{V} = -\boldsymbol{E}^T Q \boldsymbol{E} + 2f^* q - 2b^* qe - 2a^* q\dot{e} \tag{5.53}$$

Now, let f^*, b^* and a^* be defined as follows:

$$\begin{aligned} f^* &= -Q_0^* q \\ b^* &= Q_1^* qe \\ a^* &= Q_2^* q\dot{e} \end{aligned} \tag{5.54}$$

where Q_0^*, Q_1^*, and Q_2^* are zero or positive constants. $\dot{V}$ then simplifies to

$$\dot{V} = -\boldsymbol{E}^T Q \boldsymbol{E} - 2Q_0^* q^2 - 2Q_1^* (qe)^2 - 2Q_2^* (q\dot{e})^2 \tag{5.55}$$

which is negative-definite in $\boldsymbol{E}$, and hence the system described by (5.49) is stable. From (5.52) and (5.54), the laws for adjusting f, a and b are:

$$\begin{aligned} \dot{f} &= -\frac{1}{Q_0} q - Q_0^* \frac{d}{dt}(q) \\ \dot{b} &= \frac{1}{Q_1} qe + Q_1^* \frac{d}{dt}(qe) \\ \dot{a} &= \frac{1}{Q_2} q\dot{e} + Q_2^* \frac{d}{dt}(q\dot{e}) \end{aligned} \tag{5.56}$$

or,

$$\begin{aligned} f(t) &= f(0) - \frac{1}{Q_0} \int_0^t q(t)dt - Q_0^* q(t) \\ b(t) &= b(0) + \frac{1}{Q_1} \int_0^t q(t)e(t)dt + Q_1^* q(t)e(t) \\ a(t) &= a(0) + \frac{1}{Q_2} \int_0^t q(t)\dot{e}(t)dt + Q_2^* q(t)\dot{e}(t) \end{aligned} \tag{5.57}$$

where, $q(t) = \omega_p e(t) + \omega_d \dot{e}(t)$, $\omega_p = p_2$ and $\omega_d = p_3$. Substituting (5.42) into (5.57), the adaptation gains to be used in the control law (5.39) are found as follows:

$$
\begin{aligned}
g(t) &= g(0) + \alpha_1 \int_0^t q(t)dt + \alpha_2 q(t) \\
k_p(t) &= k_p(0) + \beta_1 \int_0^t q(t)e(t)dt + \beta_2 q(t)e(t) \\
k_d(t) &= k_d(0) + \gamma_1 \int_0^t q(t)\dot{e}(t)dt + \gamma_2 q(t)\dot{e}(t) \\
q(t) &= \omega_p e(t) + \omega_d \dot{e}(t)
\end{aligned}
\tag{5.58}
$$

where ω_p and ω_d are the positive position and velocity weighting factors. α_1, β_1 and γ_1 are the positive integral adaptation gains. α_2, β_2 and γ_2 are the nonnegative proportional adaptation gains. $g(0)$, $k_p(0)$ and $k_d(0)$ are the initial values chosen to provide an appropriate initial reference position signal and initial proportional and derivative gains for the control system.

Substituting terms from (5.58) into control law (5.39), one arrives at the following relation:

$$
x_r(t) = x_r(0) + k_p^*(t)e(t) + k_I^*(t)\int e(t)dt + k_d^*(t)\dot{e}(t) \tag{5.59}
$$

where $k_p^*(t) = \alpha_1\omega_d + \alpha_2\omega_p + k_p(t)$ is the proportional gain, $k_I^* = \alpha_1\omega_p$ is the integral gain, $k_d^*(t) = \alpha_2\omega_d + k_d(t)$ is the derivative gain, and $x_r(0) = g(0)$. By studying Eq. (5.59), one can observe that the reference position trajectory, $x_r(t)$, is actually generated by a PID controller driven by the force tracking error, $e(t)$. Further, it is well known that the contact force, f, measured by the sensor is often a noisy signal. Hence, direct differentiation of this signal to obtain $\dot{e} = \dot{f}_r - \dot{f}$ is undesirable. One approach is to filter the signal to remove the high frequency noise, and then to differentiate the

filtered force signal (Volpe, 1990). An alternative approach is to replace $\dot{e}$ in (5.58) and (5.59) by $-k_e\dot{x}$ as detailed below (Khatib and Burdick, 1986):

$$\dot{e} = \dot{f}_r - \dot{f} = 0 - k_e\dot{x} = -k_e\dot{x} \tag{5.60}$$

Substituting (5.60) into (5.58) and (5.59), the final control law is given below:

$$\begin{aligned}
x_r(t) &= g(t) + k_p(t)e(t) - k_v(t)\dot{x}(t) \\
g(t) &= g(0) + \alpha_1 \int_0^t q(t)dt + \alpha_2 q(t) \\
k_p(t) &= k_p(0) + \beta_1 \int_0^t q(t)e(t)dt + \beta_2 q(t)e(t) \\
k_v(t) &= k_v(0) - \lambda_1 \int_0^t q(t)\dot{x}(t)dt - \lambda_2 q(t)\dot{x}(t) \\
q(t) &= \omega_p e(t) - \omega_v \dot{x}(t)
\end{aligned} \tag{5.61}$$

where $\lambda_1 = \gamma_1 k_e$, $\lambda_2 = \gamma_2 k_e$ and $\omega_v = \omega_d k_e$.

5.5.2 Simulation Study

The controller was first tested in simulations. The test benchmark was the same as in Section 5.3.2, i.e., to regulate a 1000N force on an environment with a pure stiffness of $k_e = 70000\,\text{N/m}$, located at $x_e = 0.13\,\text{m}$. The end-effector was initially placed to be just in touch with the environment. The controller parameters were set to:

$\omega_p = 5\times10^{-5}$	$\omega_v = 1\times10^{-7}$	
$g(0) = 0$	$\alpha_1 = 2$	$\alpha_2 = 1\times10^{-3}$
$k_p(0) = 0$	$\beta_1 = 1\times10^{-5}$	$\beta_2 = 1\times10^{-5}$
$k_v(0) = 5.5\times10^{-5}$	$\lambda_1 = 2\times10^{-6}$	$\lambda_2 = 1.2\times10^{-8}$

which provided the best possible performance for the benchmark test. Figure 5.29 shows the response. The response for the low stiffness and high stiffness environments were

then evaluated using the same controller gains. Figures 5.30 and 5.31 show the responses.

The effect of positioning the end-effector was also studied. Figure 5.32 shows the system's response when the end-effector was initially positioned 7cm away from the environment's free surface. Figure 5.33 shows the response when the end-effector was positioned ≈3cm into the surface of the environment (which produced a 2000N contact force). Figure 5.32 illustrates a stable contact in spite of a non-zero approach velocity with respect to the environment. Figure 5.33 shows a smooth transition to a 1000N desired force without losing contact.

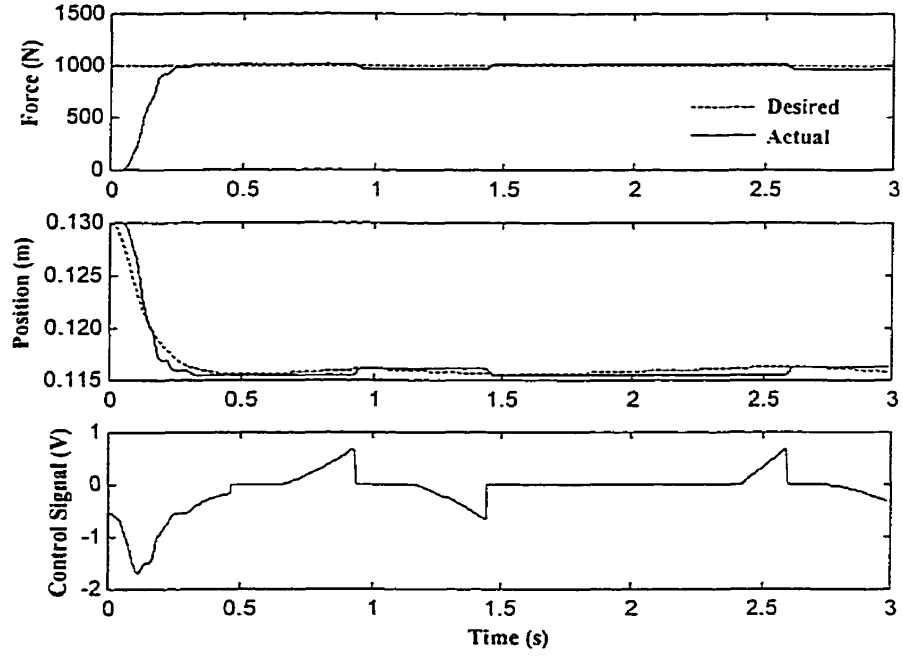

Fig. 5.29. Direct adaptive force control response for benchmark environment (k_e = 70000 N/m) (simulations)

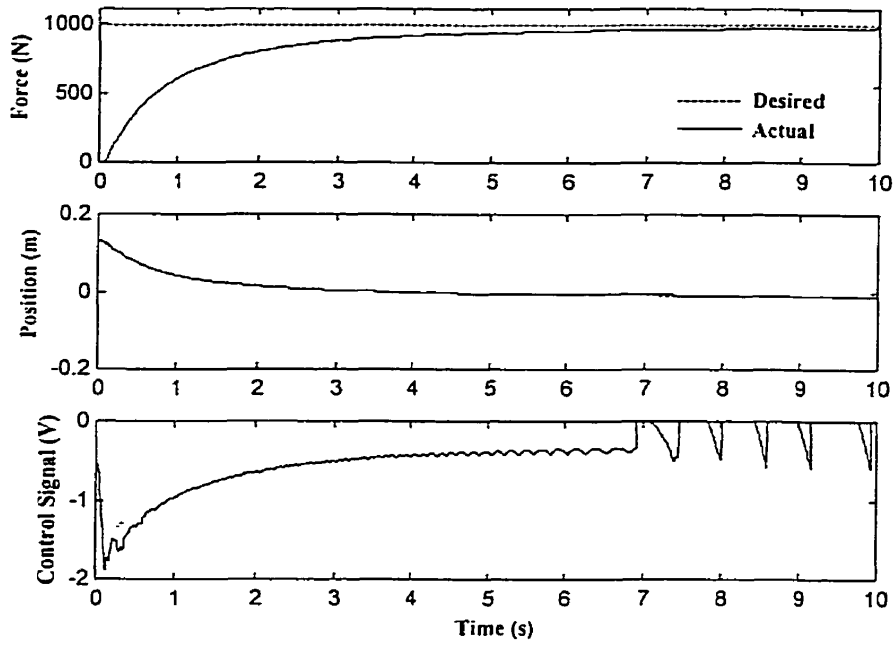

Fig. 5.30. Direct adaptive force control response for low stiffness environment ($k_e = 7000$) (simulations)

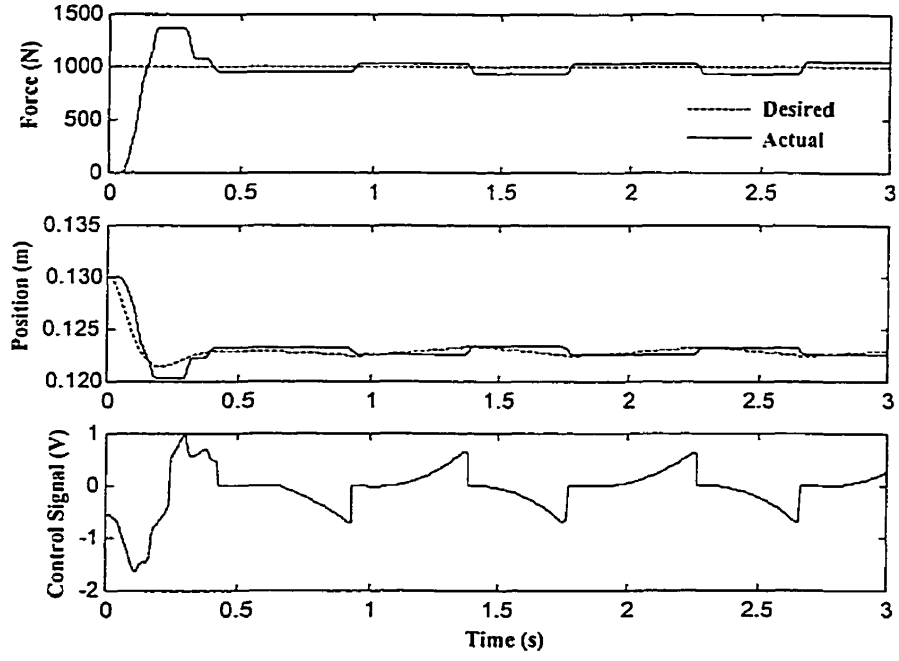

Fig. 5.31. Direct adaptive force control response for high stiffness environment ($k_e = 140000$ N/m) (simulations)

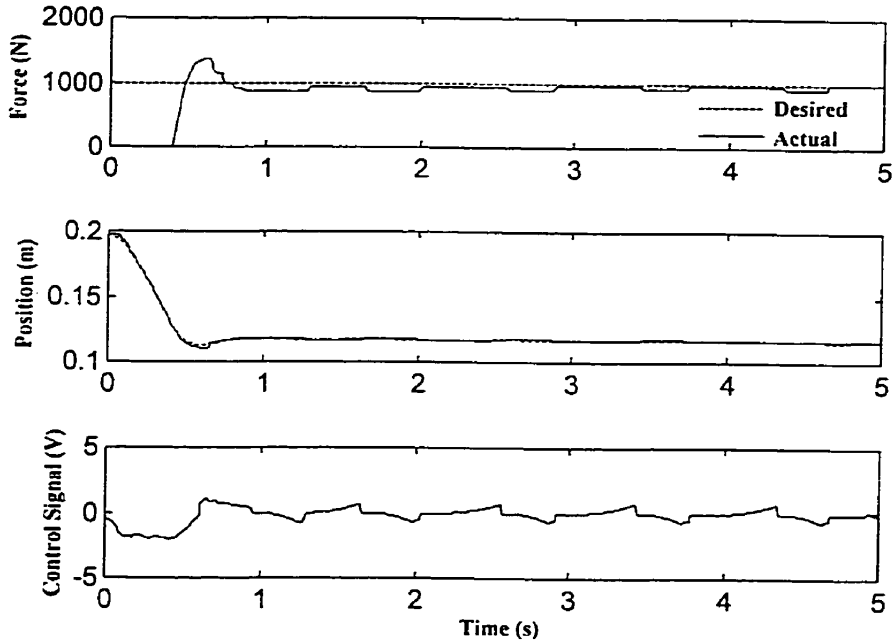

Fig. 5.32. Direct adaptive force control response for benchmark environment (k_e = 70000 N/m) and end-effector initially ≈7cm away from the environment surface (simulations)

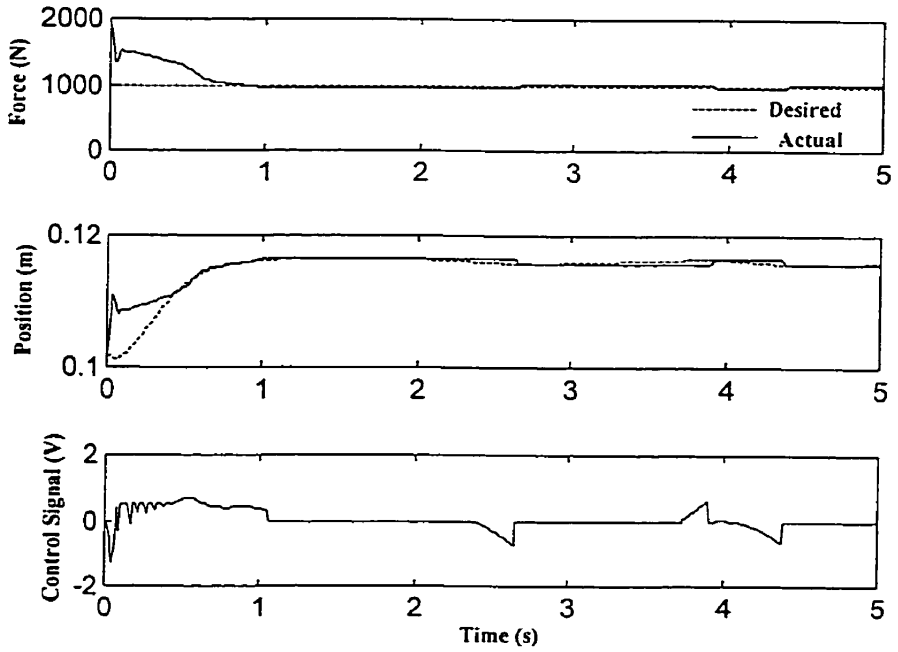

Fig. 5.33. Direct adaptive force control response for benchmark environment (k_e = 70000) and end-effector initially ≈3cm into the environment surface (simulations)

As in the previous controller, to bring further insight into the performance of this controller, the effects of all control gains were studied using the benchmark test.

Sensitivity to ω_p and ω_v: These two parameters are gains which affect all three adaptation gains, $g(t)$, $k_p(t)$, $k_v(t)$ in (5.61). The effect of increasing or decreasing ω_p on the response are shown in Figs. 5.34 and 5.35. It is seen that ω_p acts more or less like the gain of a proportional controller. Increasing ω_p increases the speed of response and may cause an overshoot; decreasing it, on the other hand, slows the response. Figures 5.36 and 5.37 show that ω_v acts more or less like the gain of a derivative controller. It actually affects the damping ratio of the system response.

Sensitivity to initial values of adaptation gains, $g(0)$, $k_p(0)$ and $k_v(0)$: Figures 5.38 and 5.39 show the response of the controller to variation in $g(0)$. $g(0)$ reflects the initial value of the position reference, x_r. Increasing $g(0)$ initially moves the end-effector farther from the environment (note the positive direction is assumed to be upward). This may cause a slower response (see Fig. 5.38). On the other hand, a small $g(0)$ tends to move the end-effector closer to the environment. With reference to Fig. 5.39, an overshoot may be inevitable when g(0) is chosen to be small.

Figure 5.40 shows the response when the initial value for the P-type adaptation gain, $k_p(0)$, was increased. This caused $k_p(t)$ in (5.61) to stay large for a long period of time. A large value for $k_p(t)$, as expected, causes an oscillatory output (position reference) and therefore an oscillatory force response. The higher the value of $k_p(t)$, the higher the frequency of the oscillations and the larger the overshoot (see Fig. 5.41).

The effect of increasing and decreasing $k_v(0)$, on the response is seen in Figs. 5.42 and 5.43, respectively. $k_v(0)$ essentially changes the velocity feedback term of the controller and therefore mainly influences the damping of the response.

Sensitivity to α_1 and α_2: Figures 5.44 and 5.45 show the effect of variation of α_1. With reference to (5.61), α_1 ultimately affects terms in the controller that are essentially proportional to, or integral of the force error. Therefore, increasing α_1 tends to induce oscillations.

Considering the controller (5.61) as a PID controller with adaptive gains, α_2 directly affects proportional and derivative gains with opposite effects on the response. Tests with a relatively wide range of α_2 showed that the response has no significant sensitivity to this parameter. This is seen from Figs. 5.46 and 5.47 whereby α_2 increased up to 10000 times.

Sensitivity to β_1, β_2, λ_1 and λ_2: With reference to Eq. (5.61), the effect of these parameters on the controller performance is rather complicated and not straightforward. Extensive simulations were performed which only allowed arriving at very general understanding of the effect of these parameters. With respect to Figs. 5.48 and 5.49, the response is not sensitive to β_1. A very high value for this parameter, however, promotes sustained oscillations. On the other hand, the controller performance was found more sensitive to β_2. Increasing β_2 by a factor of five caused a noticeable overshoot (see Fig. 5.50); decreasing it by a factor of five produced a significantly slowed response (see Fig. 5.51). Therefore, great care should be taken when choosing a value for this parameter. Similarly, more care should be taken in choosing λ_1 than in choosing λ_2 (see Figs. 5.52 to 5.55).

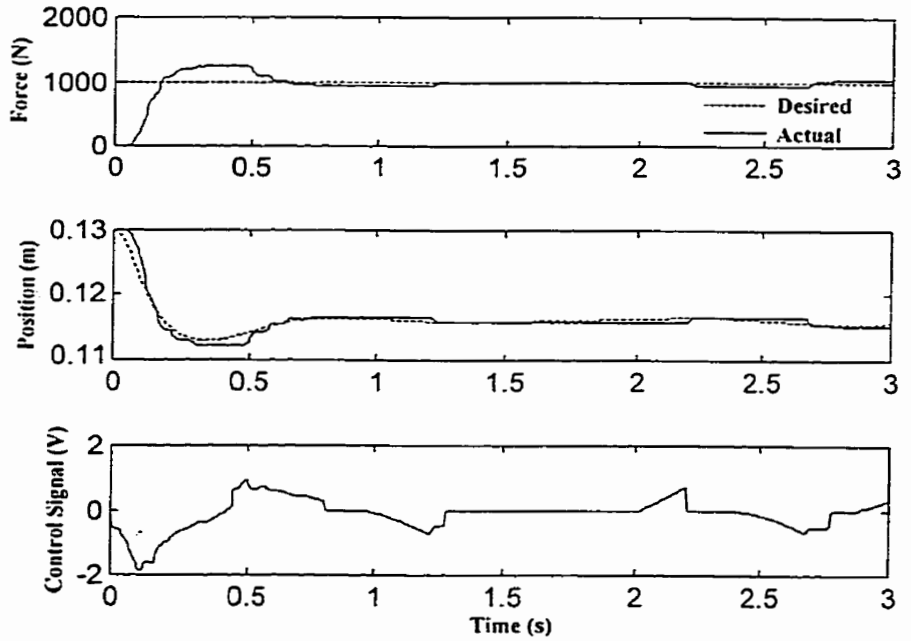

Fig. 5.34. Direct adaptive force control response for benchmark environment ($k_e = 70000$ N/m) and large $\omega_p = 1.20 \times (5 \times 10^{-5})$: simulations

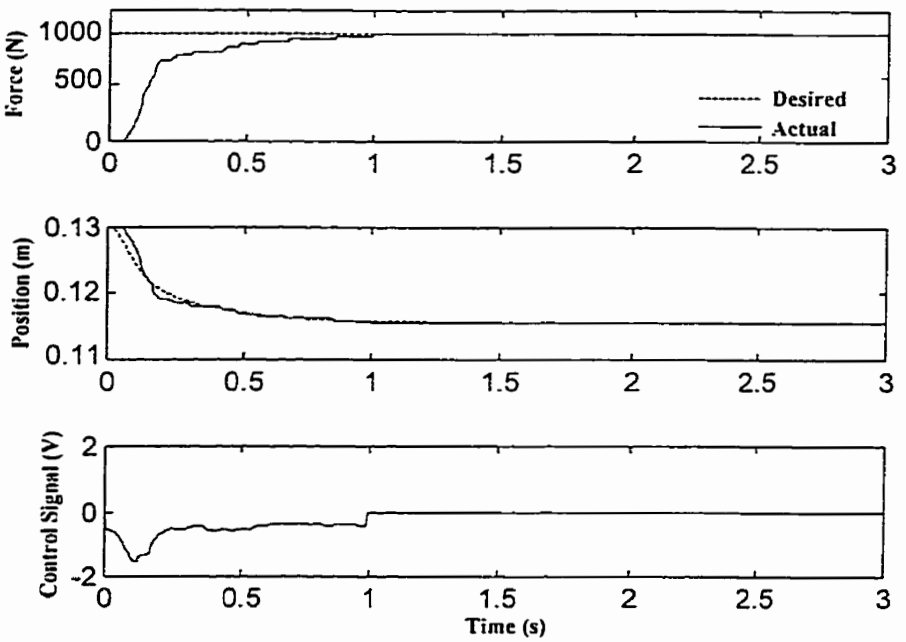

Fig. 5.35. Direct adaptive force control response for benchmark environment ($k_e = 70000$ N/m) and small $\omega_p = 0.80 \times (5 \times 10^{-5})$: simulations

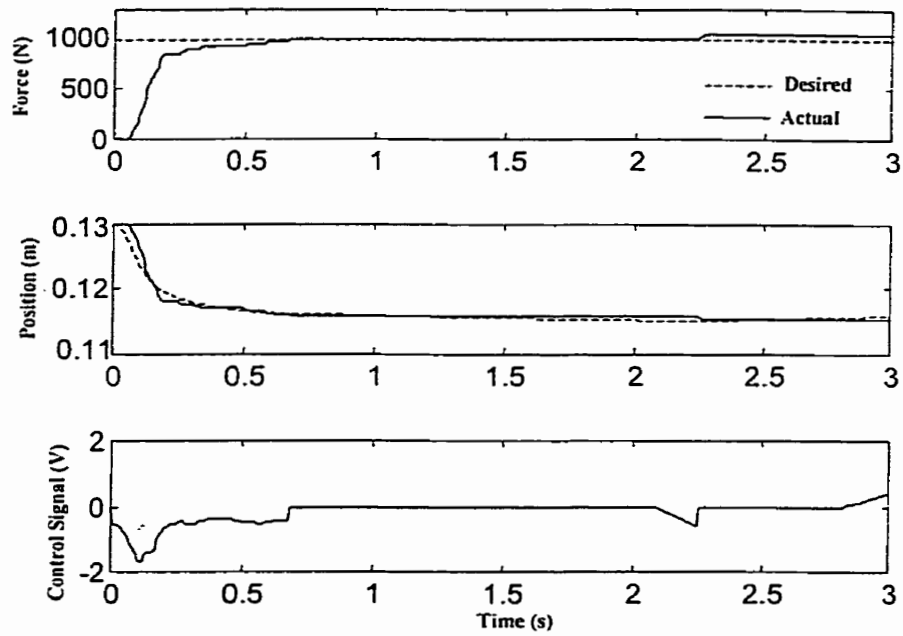

Fig. 5.36. Direct adaptive force control response for benchmark environment ($k_e = 70000\,\text{N/m}$) and large $\omega_v = 10 \times (1 \times 10^{-7})$: simulations

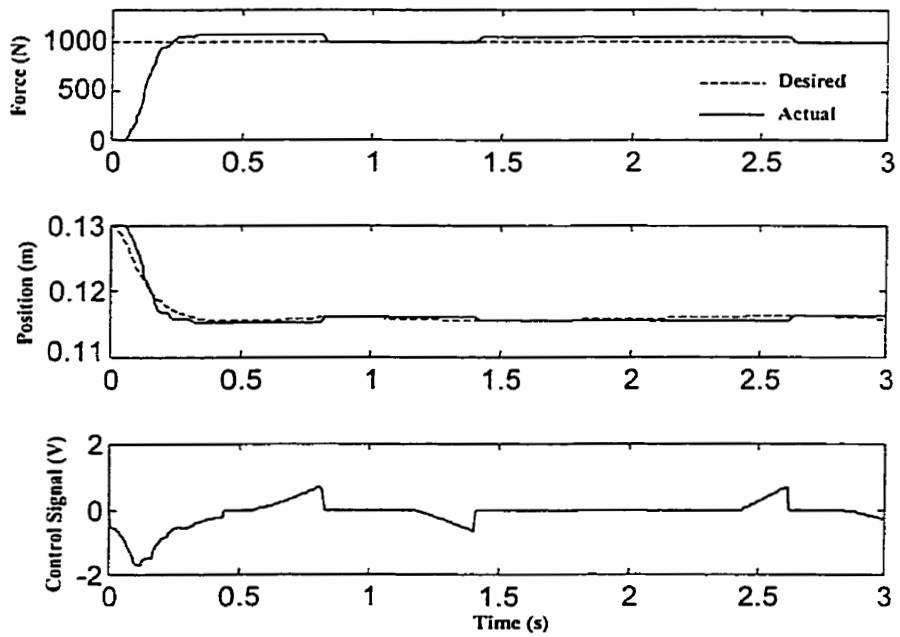

Fig. 5.37. Direct adaptive force control response for benchmark environment ($k_e = 70000\,\text{N/m}$) and small $\omega_v = 0.1 \times (1 \times 10^{-7})$: simulations

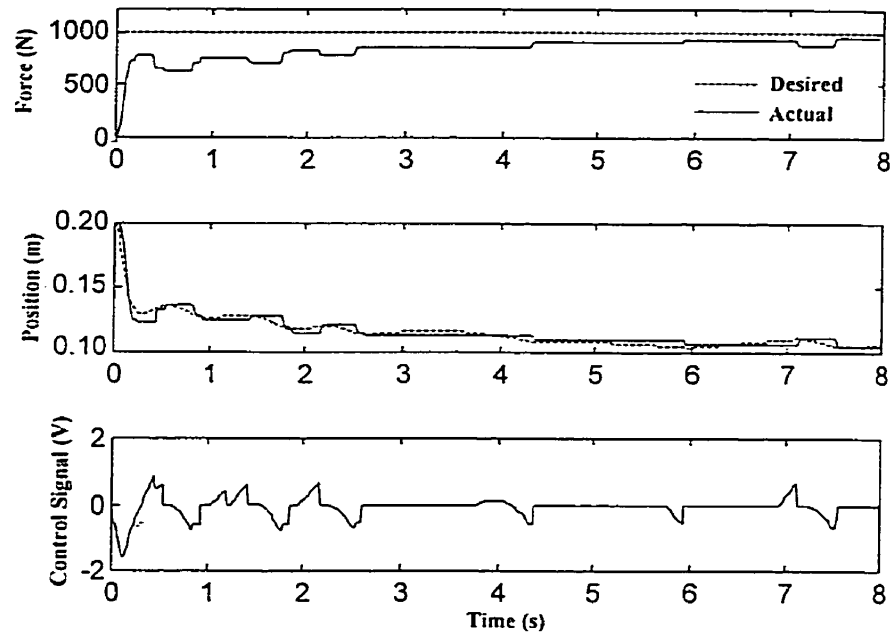

Fig. 5.38. Direct adaptive force control response for benchmark environment ($k_e = 70000\,\text{N/m}$) and $g(0)$ set far from the environment ($g(0) = 0.13 + 0.07$): simulations

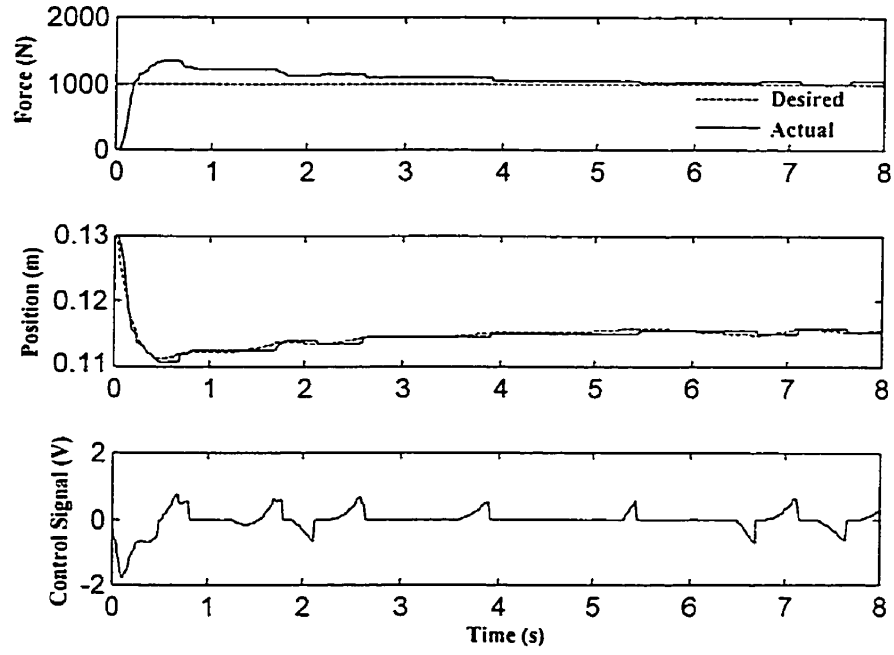

Fig. 5.39. Direct adaptive force control response for benchmark environment ($k_e = 70000\,\text{N/m}$) and $g(0)$ set into the environment ($g(0) = 0.13 - 0.07$): simulations

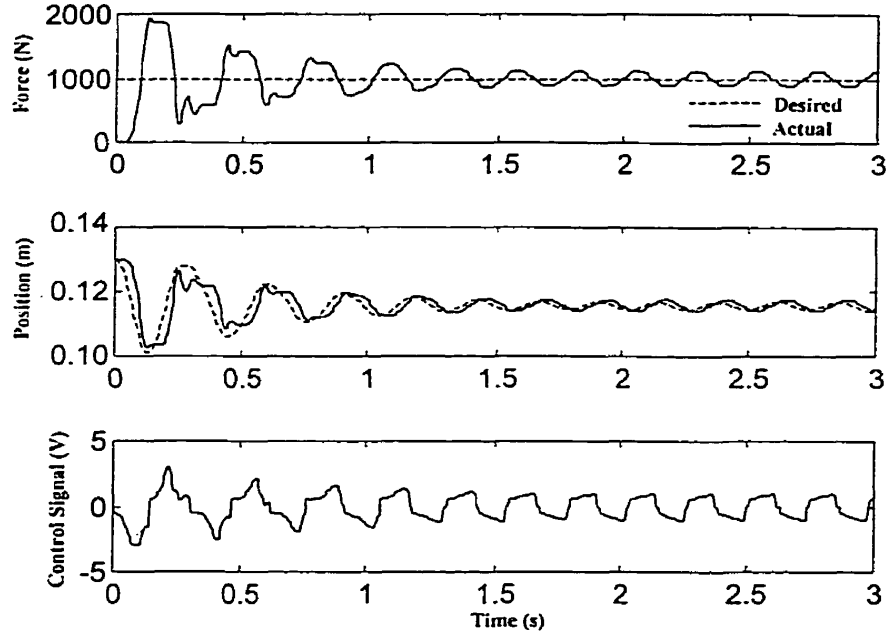

Fig. 5.40. Direct adaptive force control response for benchmark environment ($k_e = 70000\,\text{N/m}$) and large $k_p(0) = 0.0 + 0.002$: simulations

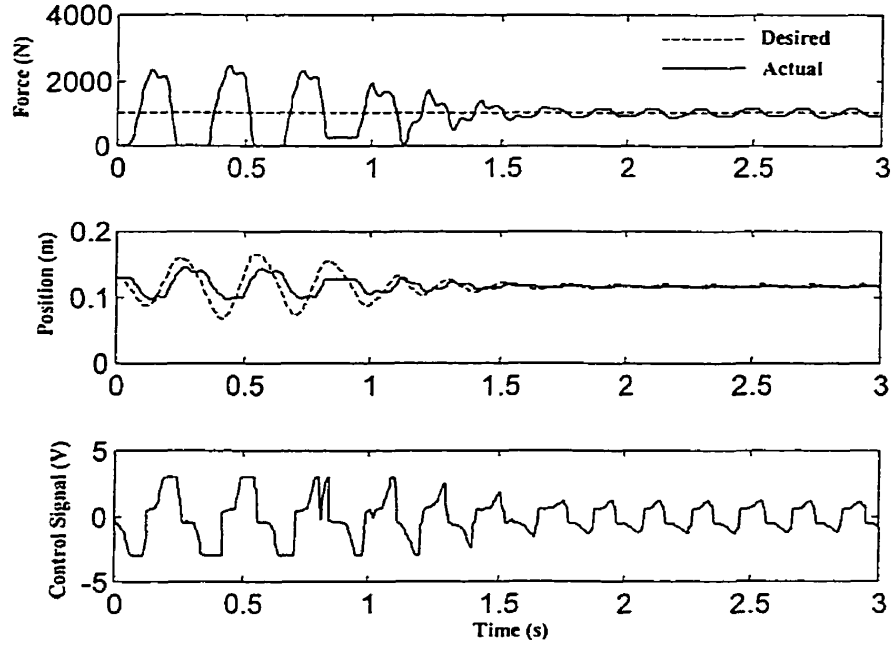

Fig. 5.41. Direct adaptive force control response for benchmark environment ($k_e = 70000\,\text{N/m}$) and very large $k_p(0) = 0.0 + 0.004$: simulations

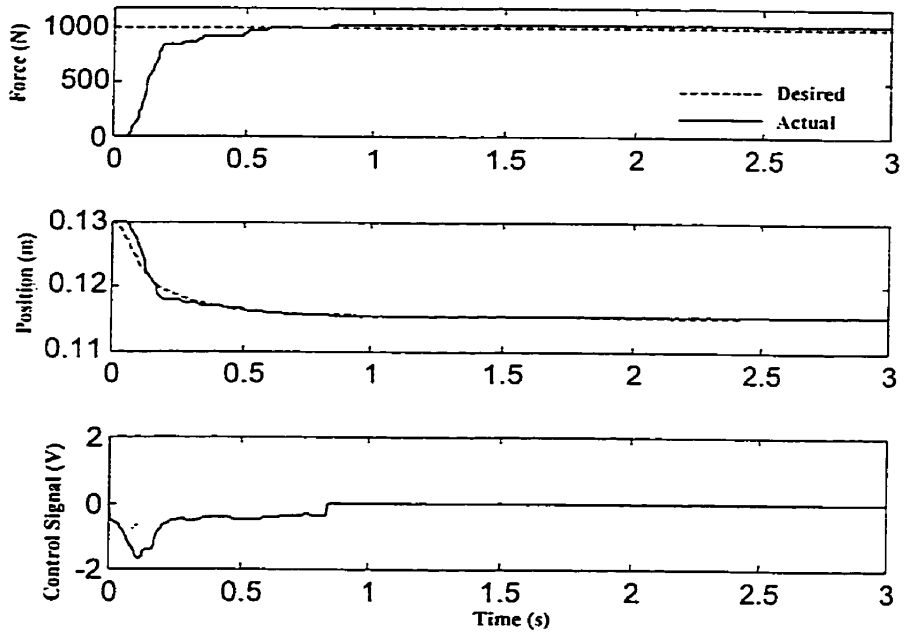

Fig. 5.42. Direct adaptive force control response for benchmark environment ($k_e = 70000\,\text{N/m}$) and large $k_v(0) = 1.20 \times (5.5 \times 10^{-5})$: simulations

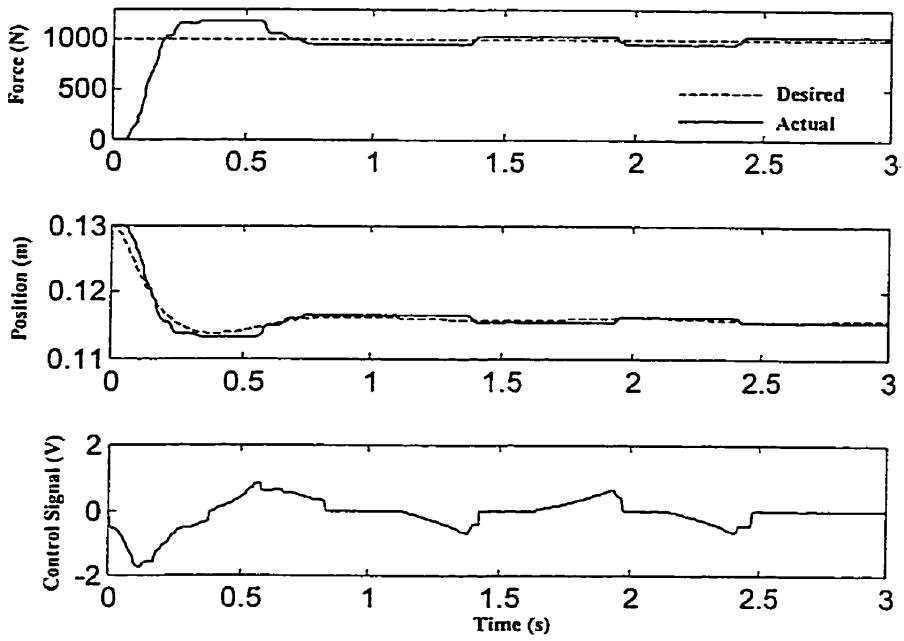

Fig. 5.43. Direct adaptive force control response for benchmark environment ($k_e = 70000\,\text{N/m}$) and small $k_v(0) = 0.80 \times (5.5 \times 10^{-5})$: simulations

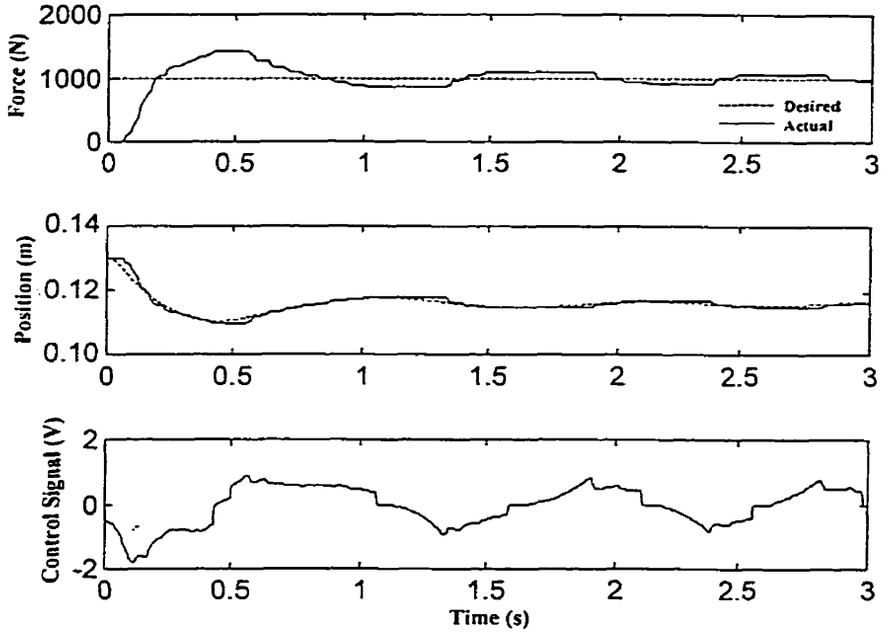

Fig. 5.44. Direct adaptive force control response for benchmark environment ($k_e = 70000\,\text{N/m}$) and large $\alpha_1 = 10 \times 2$: simulations

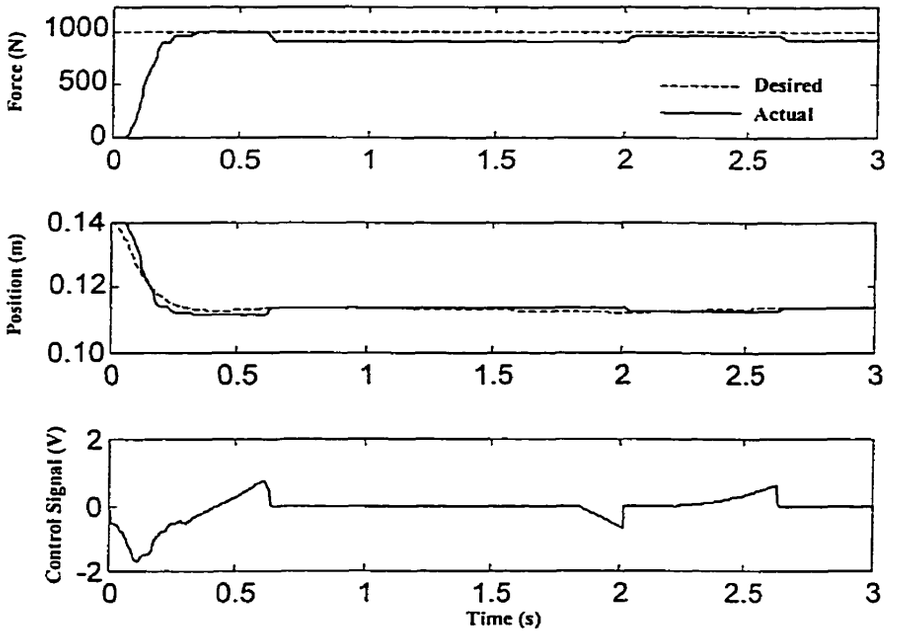

Fig. 5.45. Direct adaptive force control response for benchmark environment ($k_e = 70000\,\text{N/m}$) and small $\alpha_1 = 0.1 \times 2$: simulations

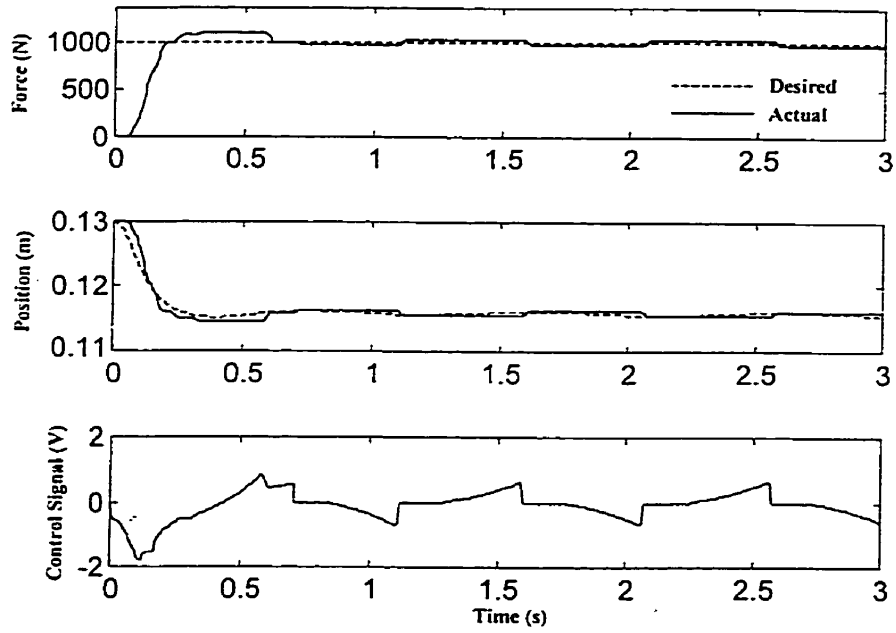

Fig. 5.46. Direct adaptive force control response for benchmark environment ($k_e = 70000\,\text{N/m}$) and large $\alpha_2 = 1000 \times (1 \times 10^{-3})$: simulations

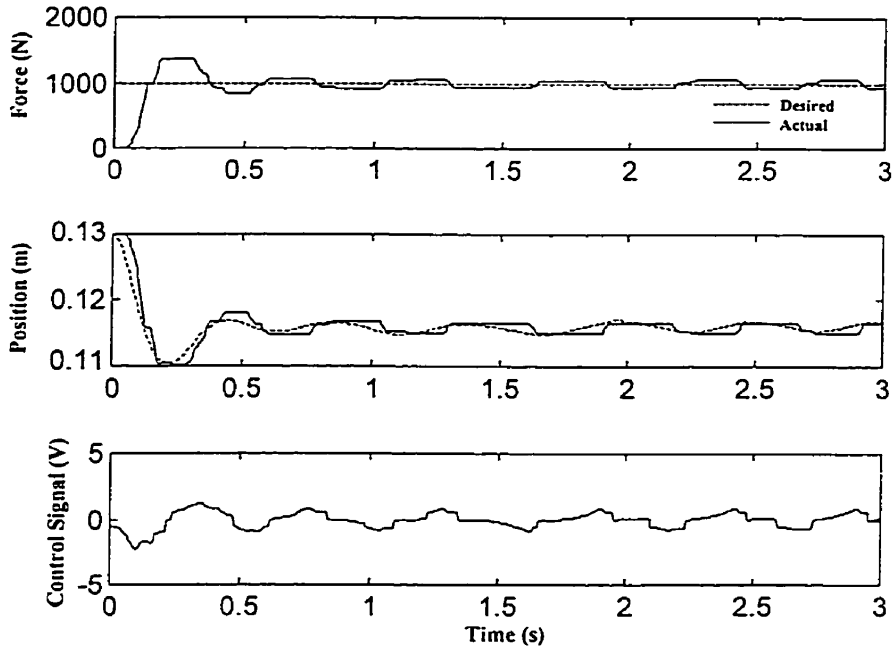

Fig. 5.47. Direct adaptive force control response for benchmark environment ($k_e = 70000\,\text{N/m}$) and very large $\alpha_2 = 10000 \times (1 \times 10^{-3})$: simulations

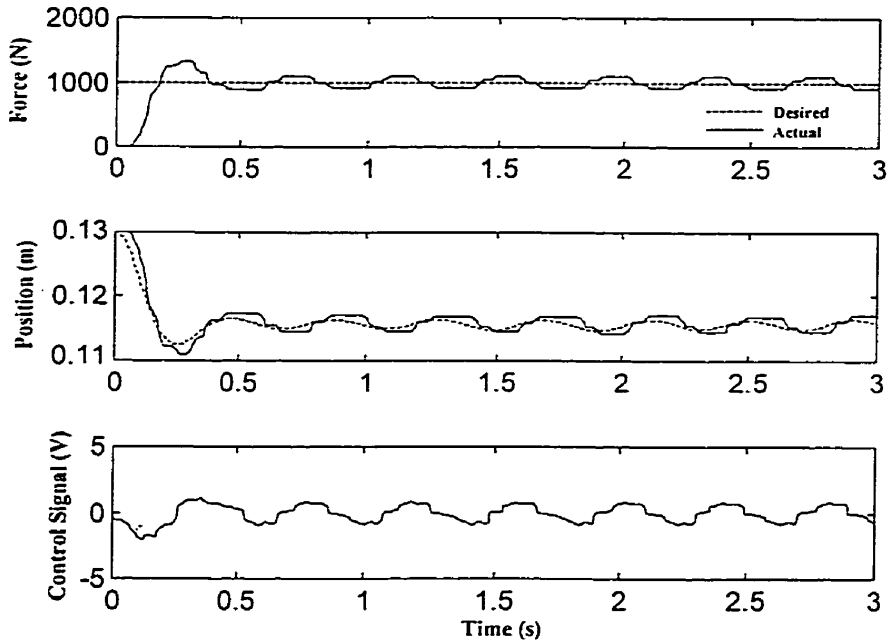

Fig. 5.48. Direct adaptive force control response for benchmark environment ($k_e = 70000\,\text{N/m}$) and large $\beta_1 = 10 \times (1 \times 10^{-5})$: simulations

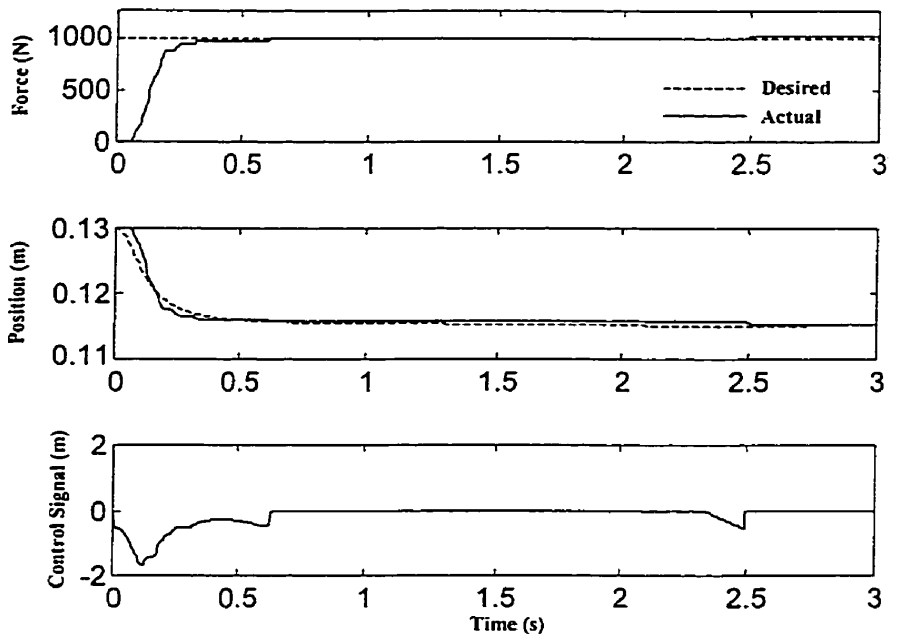

Fig. 5.49. Direct adaptive force control response for benchmark environment ($k_e = 70000\,\text{N/m}$) and small $\beta_1 = 0.1 \times (1 \times 10^{-5})$: simulations

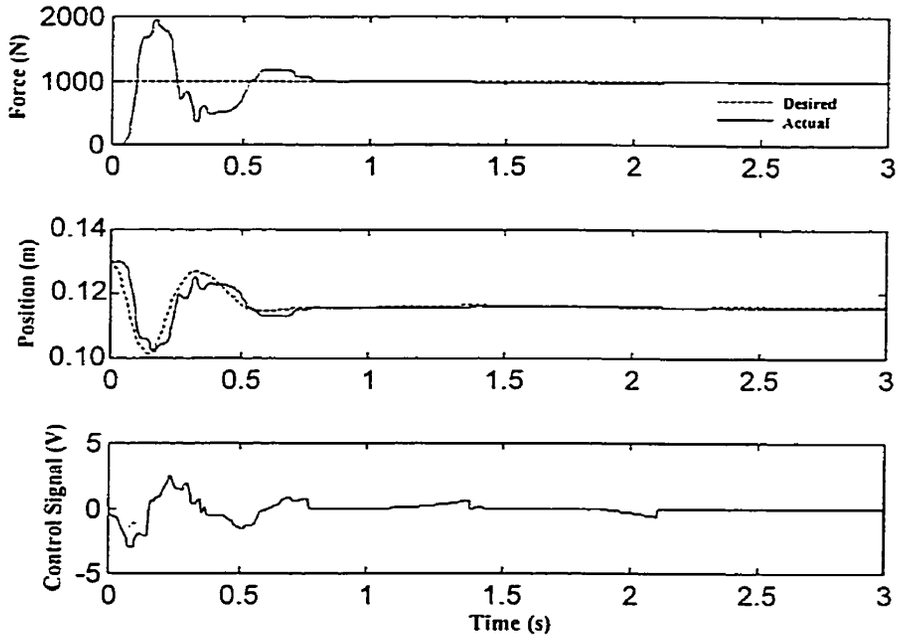

Fig. 5.50. Direct adaptive force control response for benchmark environment ($k_e = 70000\,\text{N/m}$) and large $\beta_2 = 5\times(1\times10^{-5})$: simulations

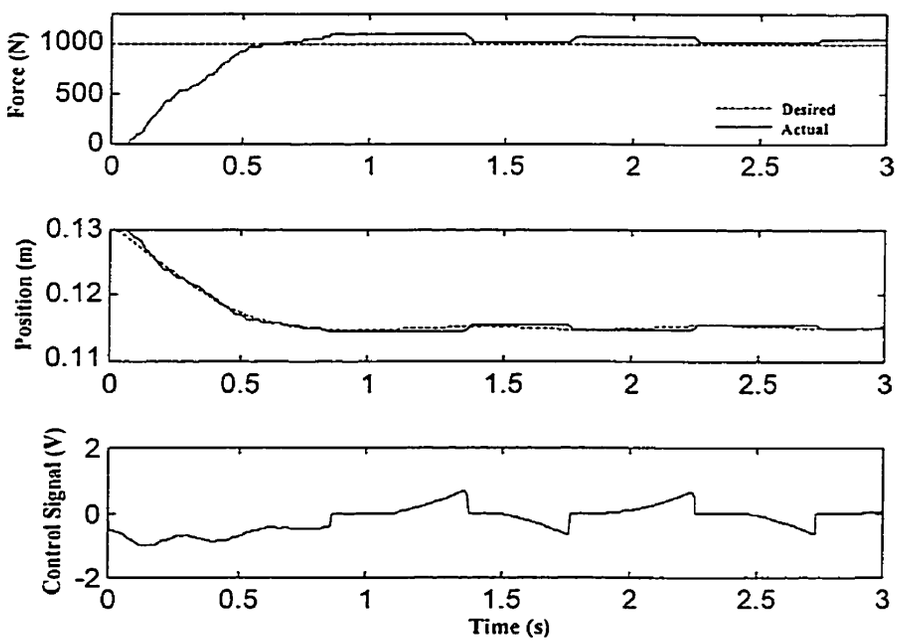

Fig. 5.51. Direct adaptive force control response for benchmark environment ($k_e = 70000\,\text{N/m}$) and small $\beta_2 = \frac{1}{5}\times(1\times10^{-5})$: simulations

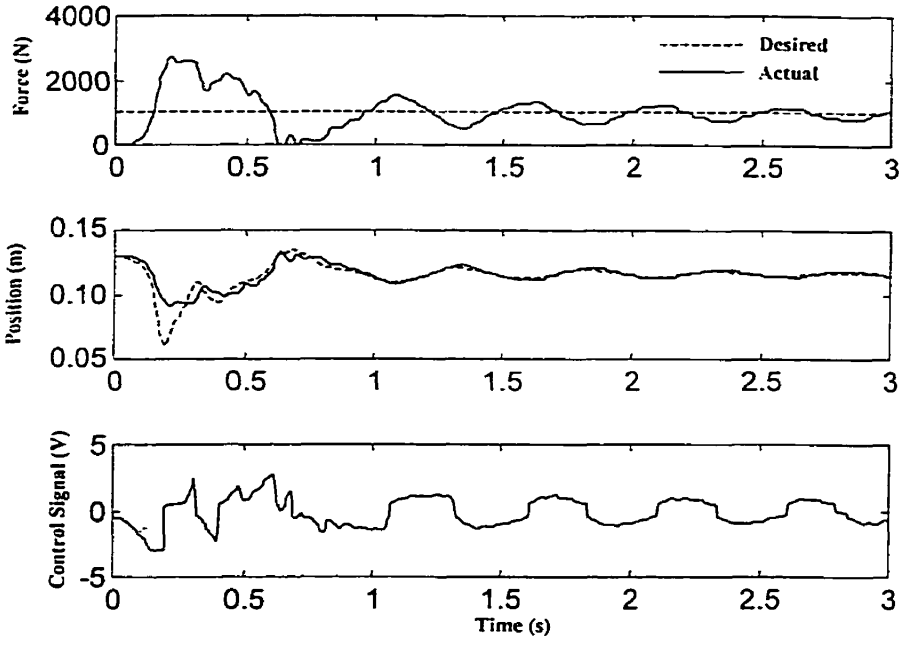

Fig. 5.52. Direct adaptive force control response for benchmark environment ($k_e = 70000\,\text{N/m}$) and large $\lambda_1 = 10 \times (2 \times 10^{-6})$: simulations

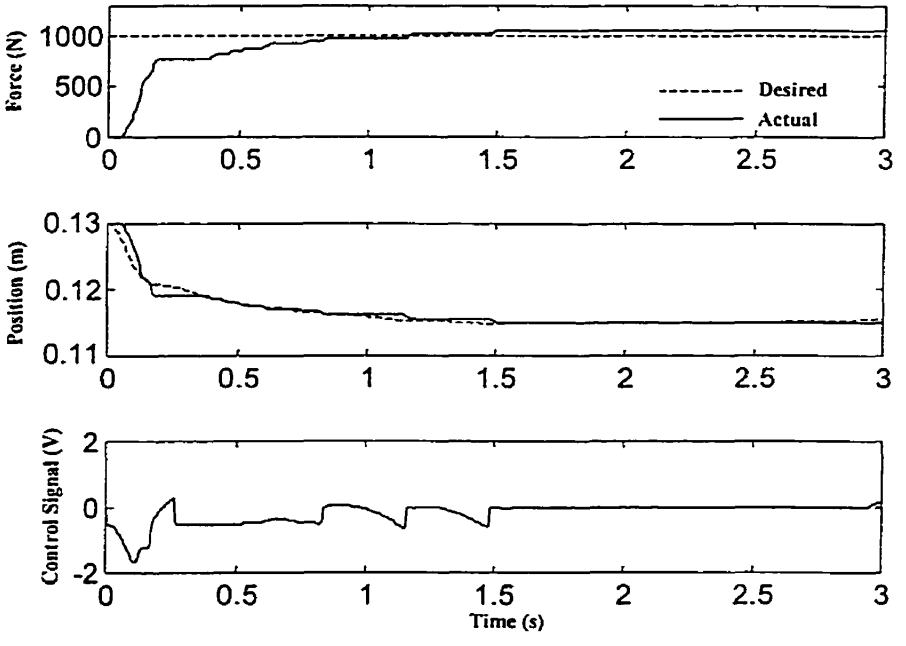

Fig. 5.53. Direct adaptive force control response for benchmark environment ($k_e = 70000\,\text{N/m}$) and small $\lambda_1 = 0.1 \times (2 \times 10^{-6})$: simulations

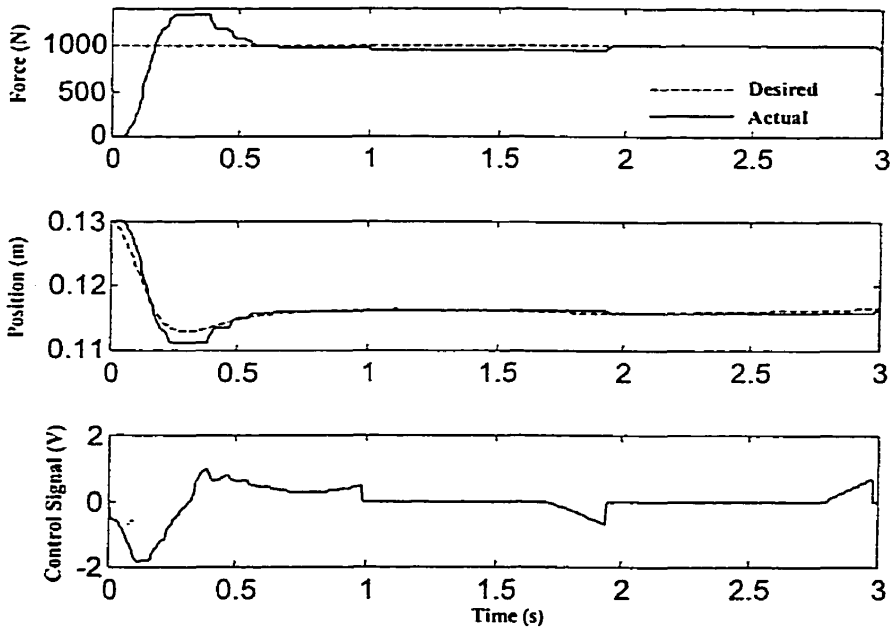

Fig. 5.54. Direct adaptive force control response for benchmark environment ($k_e = 70000\,\text{N/m}$) and large $\lambda_2 = 10 \times (1.2 \times 10^{-8})$: simulations

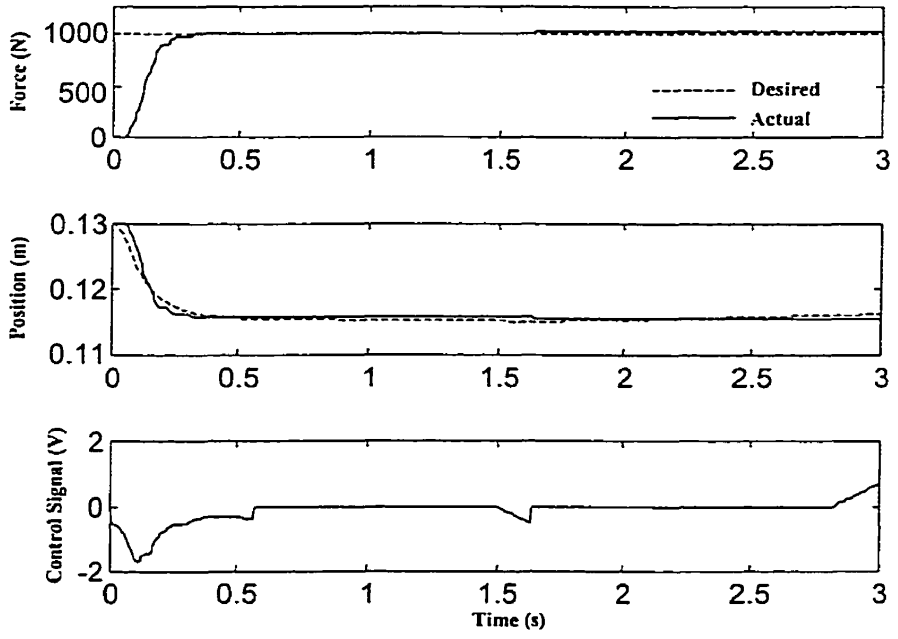

Fig. 5.55. Direct adaptive force control response for benchmark environment ($k_e = 70000\,\text{N/m}$) and small $\lambda_2 = 0.1 \times (1.2 \times 10^{-8})$: simulations

5.5.3 Experimental Evaluations

The control algorithm described by (5.61) was then applied to the hydraulic test station. The controller parameters were chosen as:

$\omega_p = 7\times10^{-6}$ $\omega_v = 1\times10^{-7}$

$g(0) = 0.02$ $\alpha_1 = 9$ $\alpha_2 = 1\times10^{-2}$

$k_p(0) = 1\times10^{-4}$ $\beta_1 = 1\times10^{-4}$ $\beta_2 = 1\times10^{-6}$

$k_v(0) = 1\times10^{-4}$ $\lambda_1 = 5\times10^{-6}$ $\lambda_2 = 7\times10^{-7}$

These parameters were adjusted to provide the best response for the low stiffness environment (~10,000N/m). The response for the high stiffness environment (~42,000N/m) was then evaluated using the same controller gains. Although the scheme did not need estimation of environmental parameters, there were too many parameters to be adjusted in this method. The same benchmark tests as in Section 5.3.3 were applied here. Figures 5.56 and 5.57 show the test results for low stiffness and high stiffness environments, respectively. Figure 5.58 shows the control efforts. The controller did not require knowledge of the environmental parameters, x_e and k_e, and the control terms were adjusted, on-line, based on the force tracking performance through e and $\dot{e}$. The response for the high stiffness environment is faster and generally has a lower damping ratio than the case of the low stiffness environment. Recall the relationship between the reference force and the actual end-effector force in PBIC [Eq. (4.14)]:

$$\frac{F}{F_r} = \frac{m_e s^2 + c_e s + k_e}{(M + m_e)s^2 + (C + c_e)s + (K + k_e)}$$

Evidently when the environmental stiffness, k_e, increases, the undamped natural frequency of the PBIC increases and the damping ratio decreases. Furthermore, from

Fig. 5.57 it is seen that the hunting effect is inevitable for high stiffness environments. This is due to the accuracy of the NPI position controller developed here. Position error of ≈0.2° (see Chapter 3) for link 2 corresponds to ≈4.5mm error in the vertical position of the end-effector. This error, for an environment with a stiffness of $k_e \approx 10000\,\text{N/m}$, produces ≈45N force error.

Finally, due to the difficulty and limitations in tuning the eleven controller parameters during the experiment, the experimental results were much slower; and the controller did not perform as well as it did in simulations.

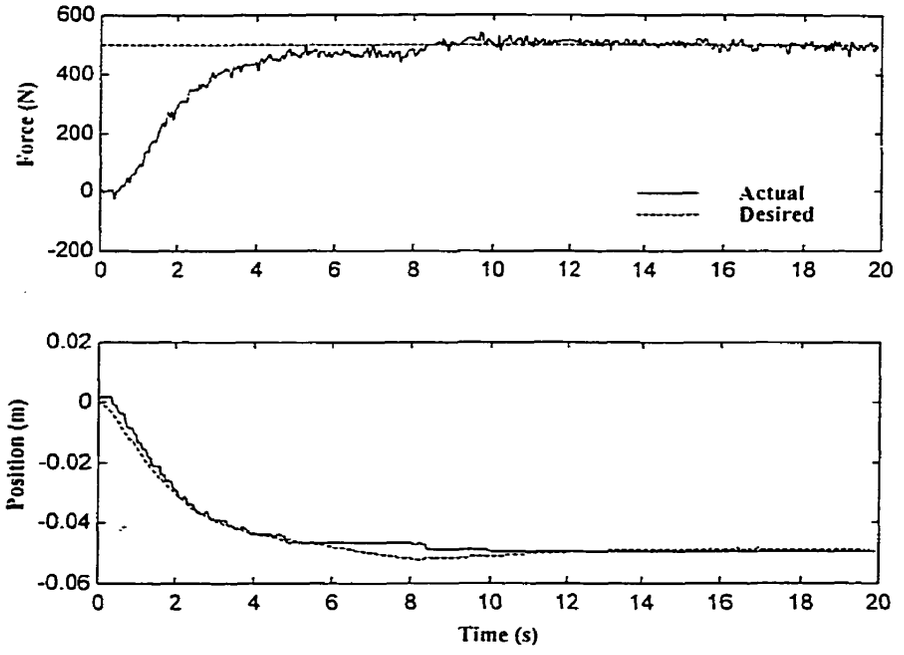

Fig. 5.56. Force control using direct adaptive scheme for low stiffness environment ($k_e \approx 10000$ N/m): experiment

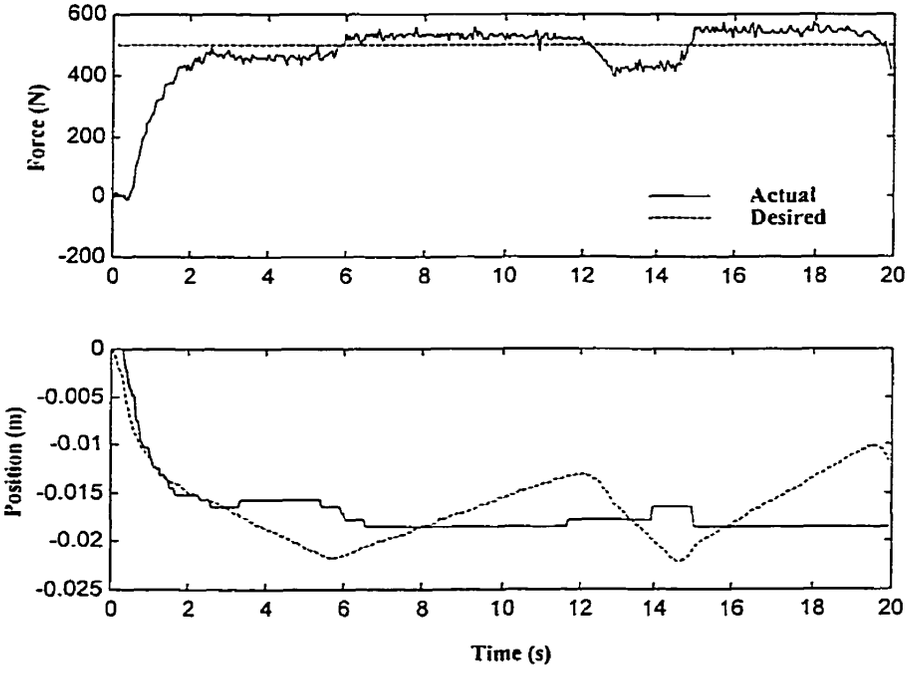

Fig. 5.57. Force control using direct adaptive scheme for high stiffness environment ($k_e \approx 42000$ N/m): experiment

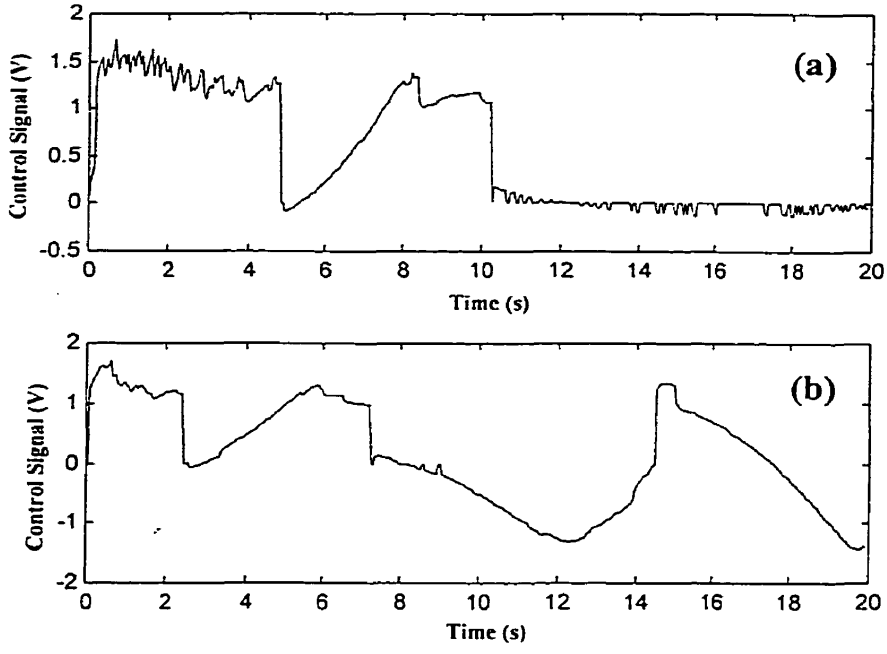

Fig. 5.58. Control signals pertaining to: **(a)** Low stiffness environment (Fig. 5.56) **(b)** High stiffness environment (Fig. 5.57)

5.6 Integral-based Position Reference Modification

Motivated by the discussion at the beginning of this chapter, we show here that force regulation in PBIC can be achieved by simply adding the integral of force error to the position reference. We therefore derive the formulation and evaluate this method with the goal of signifying the utilization of more advanced control techniques as outlined in the previous sections.

5.6.1 Derivation of the method

Let the reference position trajectory, x_r, be determined as

$$x_r(t) = x_r(0) + \Delta x_r \tag{5.62}$$

where the role of Δx_r is to modify $x_r(0)$ in such a way that the resulting x_r will drive the end-effector to produce a desired contact force, f_r, in steady-state. Δx_r should be generated on-line to enable f to converge to f_r. Defining the quadratic performance function ψ as

$$\psi = \frac{1}{2}(f_r - f)^2 \tag{5.63}$$

which needs to be minimized with respect to Δx_r. The force f, in steady-state, is given by Eq. (5.6) as

$$\begin{aligned} f &= \left(K^{-1} + k_e^{-1}\right)^{-1}\left(x_r - x_e + \frac{f_r}{K}\right) \\ &= k_{eq}\left(x_r - x_e + \frac{f_r}{K}\right) \end{aligned} \tag{5.64}$$

Assuming that the position controller of the PBIC (refer to Fig. 4.1) is fast enough, one can then use the steady-state f from (5.64) in the performance function ψ:

$$\psi(\Delta x_r) = \frac{1}{2}\left(f_r - k_{eq}\left(x_r(0) + \Delta x_r - x_e + \frac{f_r}{K}\right)\right)^2 \tag{5.65}$$

Δx_r should be appropriately selected to minimize $\psi(\Delta x_r)$ along the trajectory x_r. Since $\psi(\Delta x_r)$ is quadratic, we can use a simple steepest descent algorithm to adjust Δx_r,

i.e. $\Delta \dot{x}_r = -\beta\eta$, where β is the step size and η is the gradient of ψ with respect to Δx_r. Each component of η can be easily shown to be

$$\eta = \frac{\partial \psi}{\partial \Delta x_r} = -k_{eq}(f_r - f) \tag{5.66}$$

and finally,

$$\Delta \dot{x}_r = \Gamma(f_r - f) \tag{5.67}$$

where $\Gamma = \beta k_{eq}$ is a constant non-negative gain. This algorithm is actually Whitney's accommodation strategy (1977), with the addition of a reference force. It was first used by Lasky and Hsia (1991) for force regulation of direct drive robots employing torque-based impedance control.

5.6.2 Simulation Study

The benchmark test for the simulation was the same as the one that was used in Section 5.3.2, i.e., to regulate a 1000N force on an environment with a pure stiffness of $k_e = 70000$N/m, located at $x_e = 0.13$m. The end-effector was initially placed to be just in touch with the environment, and the value for $x_r(0)$ was set to the current location of the end-effector, i.e., $x_r(0)$=0.13m. The gain of the integrator, Γ, was adjusted to 7×10^{-5} to give the best possible response for the environment with the stiffness of $k_e = 70000$N/m (the benchmark test). The response for low stiffness, $k_e = 7000$N/m, and high stiffness, $k_e = 140000$N/m, environments were then evaluated using the same gain.

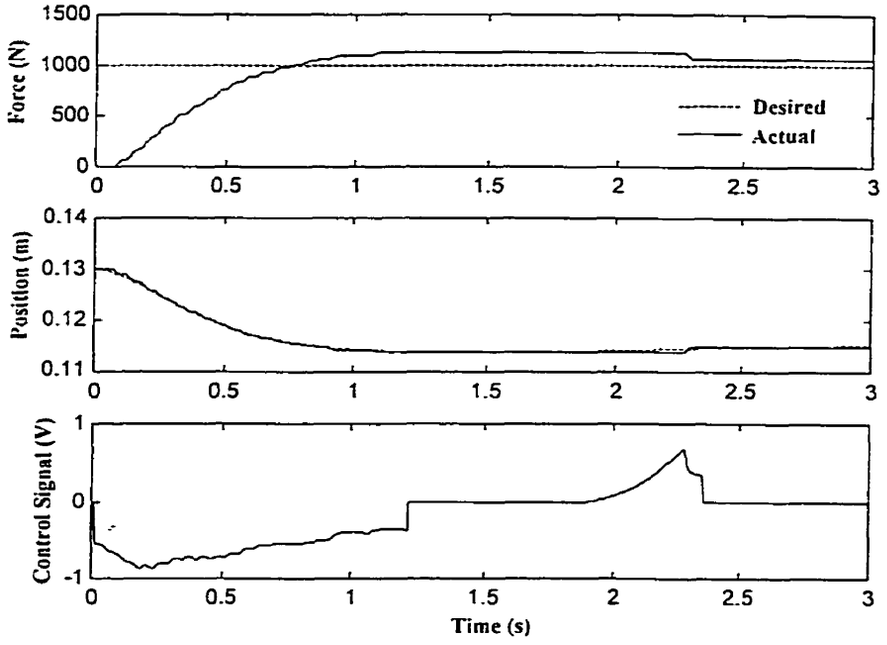

Fig. 5.59. Force control using integral-based position reference modification method for benchmark environment ($k_e = 70000\,\text{N/m}$)

Fig. 5.59 illustrates the force regulating capability of the method as applied to an environment with stiffness of $k_e = 70000\,\text{N/m}$. As is seen, this simple method can regulate the force properly. However, like any other pure integral controller, the integral gain has to be kept small to avoid overshoot. This may result in a slow response as seen in Fig. 5.59. Figures 5.60 and 5.61 show the performance of the scheme for low and high stiffness environments, respectively.

Figure 5.62 shows the system's response when the end-effector was initially positioned 7cm above the environment's free surface. Figure 5.63 shows the response when the end-effector was positioned almost 3cm penetrated into the environment's free surface (contact force was initially 2000N). In all these tests, the initial value for the position

reference was set to the initial location of the end-effector. With reference to Fig. 5.62, when the end-effector is located far away from the environment, the controller system keeps integrating a large force error until the end-effector comes into contact with the environment. This causes an overshoot.

Figures 5.64 and 5.65 illustrate the effects of increasing and decreasing the integral gain, Γ, by a factor of 10, respectively. Figure 5.64 exhibits a large overshoot and a very oscillatory response as expected from an integral controller with high integral gain. A very small integral gain, on the other hand, leads to a very slow response as seen in Fig. 5.65.

5.6.3 Experimental Evaluations

The control algorithm was also applied to the hydraulic test station. The integral gain of the controller was set to $\Gamma = 5 \times 10^{-6}$, which provided the best possible response for the low stiffness environment ($\approx$10,000N/m). The response for the high stiffness environment ($\approx$42,000 N/m) was then evaluated using the same controller gain. The same benchmark tests as in Section 5.3.3 were applied here. Figure 5.66 shows the test result for force control on the low stiffness environment. Figure 5.67 shows the experimental force control response on the high stiffness environment. Figure 5.68 compares the control efforts. As is seen, the control signals are smooth and do not chatter.

In short, this method is simple and works for regulating force in steady-state. However, since it simply uses a pure integral of the force error to modify the trajectory, it does not have a very good transient response especially for a wide range of environmental stiffnesses.

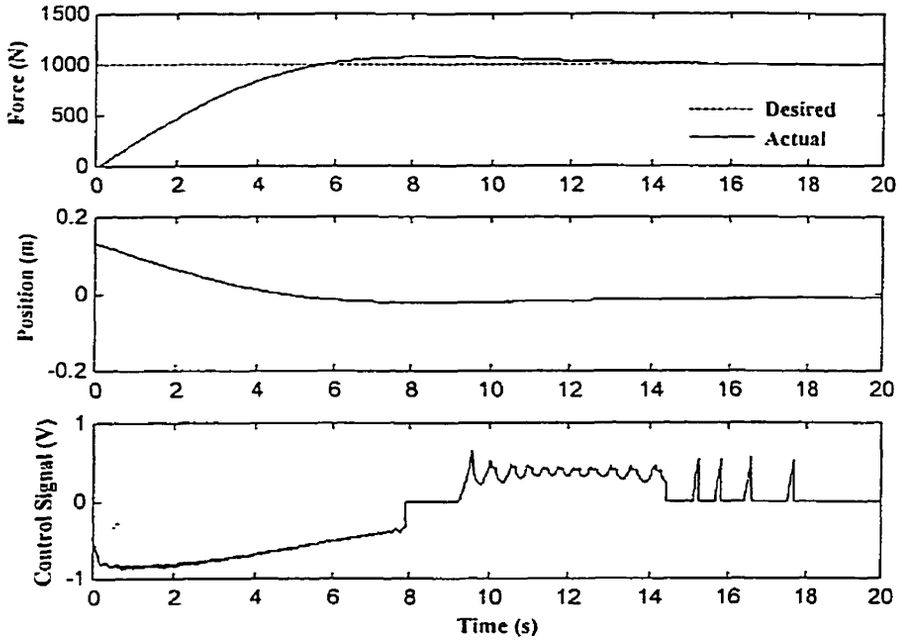

Fig. 5.60. Force control using integral-based position reference modification method for low stiffness environment (k_e = 7000 N/m): simulations

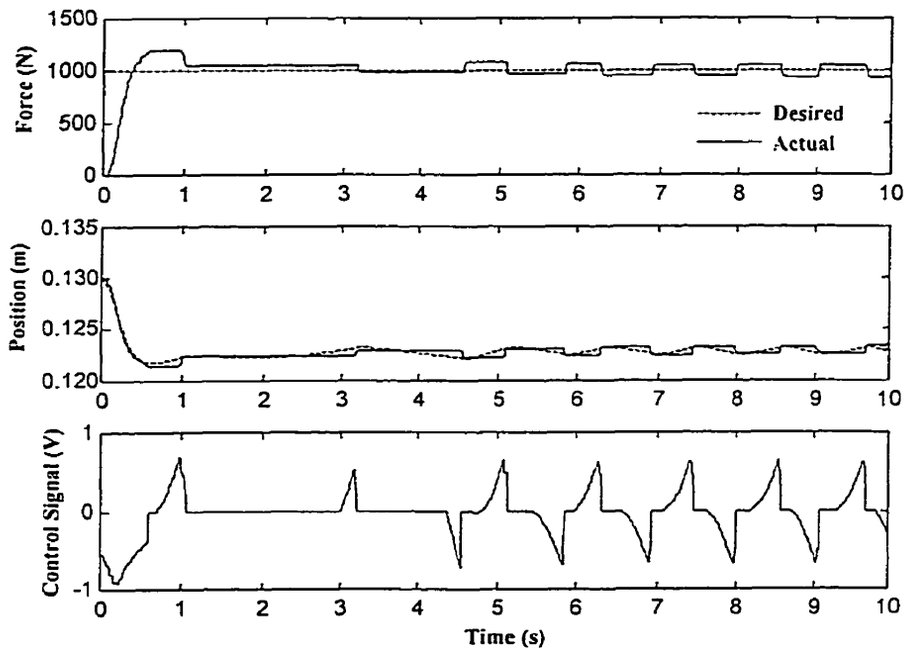

Fig. 5.61. Force control using integral-based position reference modification method for high stiffness environment (k_e = 140000 N/m): simulations

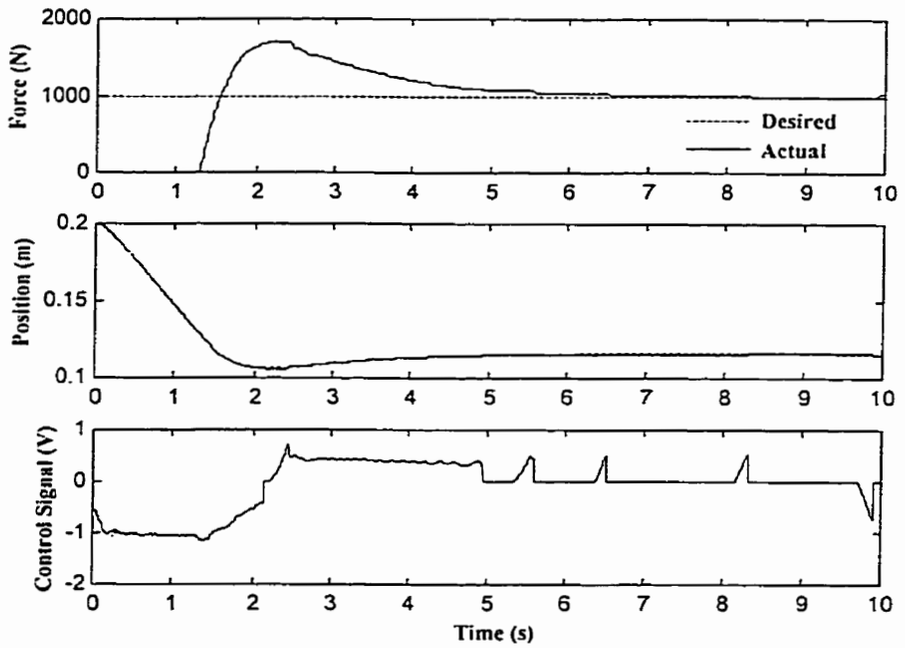

Fig. 5.62. Force control using integral-based position reference modification method for benchmark environment ($k_e = 70000$ N/m) and end-effector initially 7cm away from environment surface: simulations

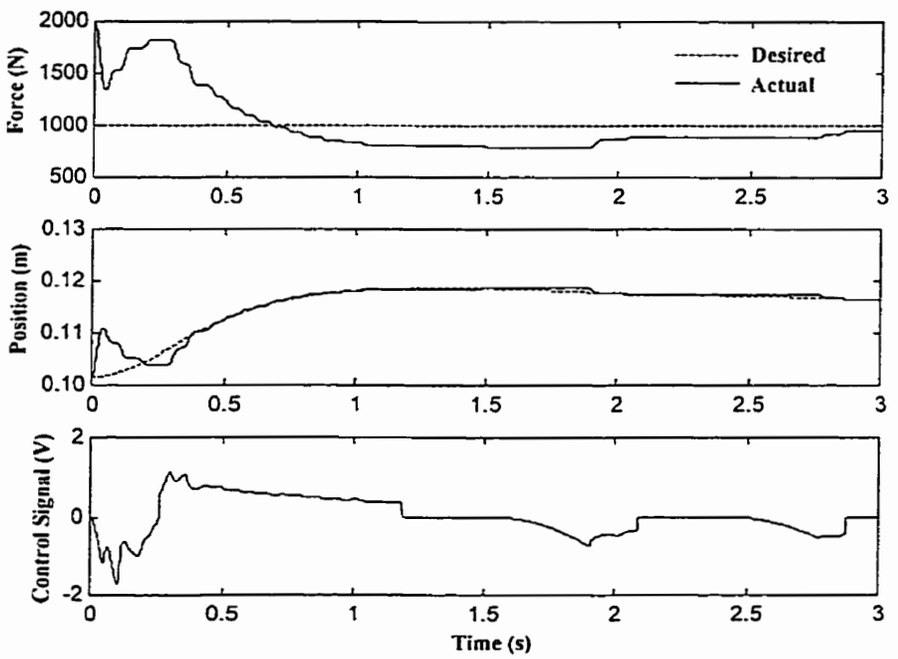

Fig. 5.63. Force control using integral-based position reference modification method for benchmark environment ($k_e = 70000$ N/m) and end-effector initially 3cm into the environment surface: simulations

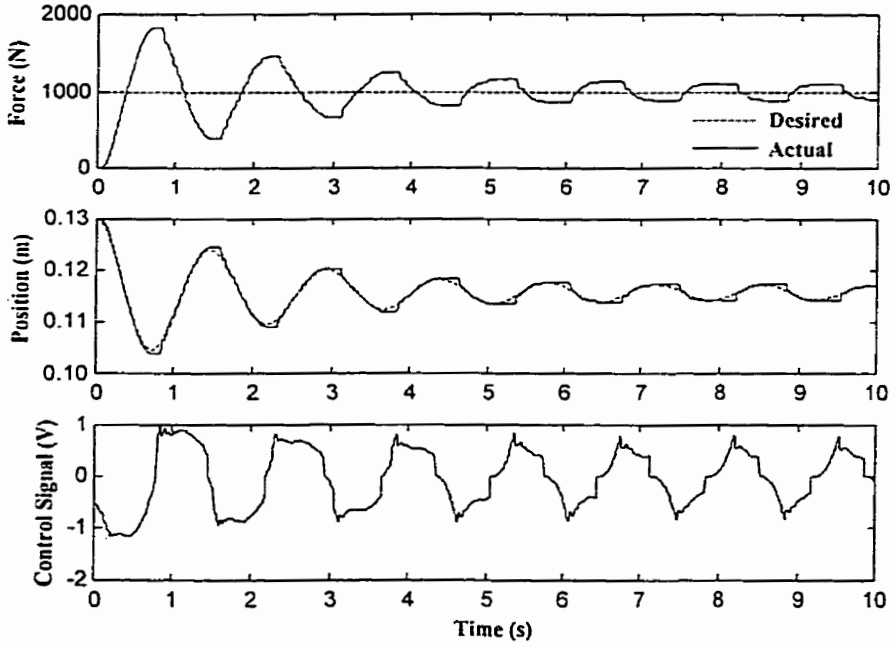

Fig. 5.64. The effect of increasing integral gain ($\Gamma = 10 \times (7 \times 10^{-5})$) on integral-based force control response: simulations

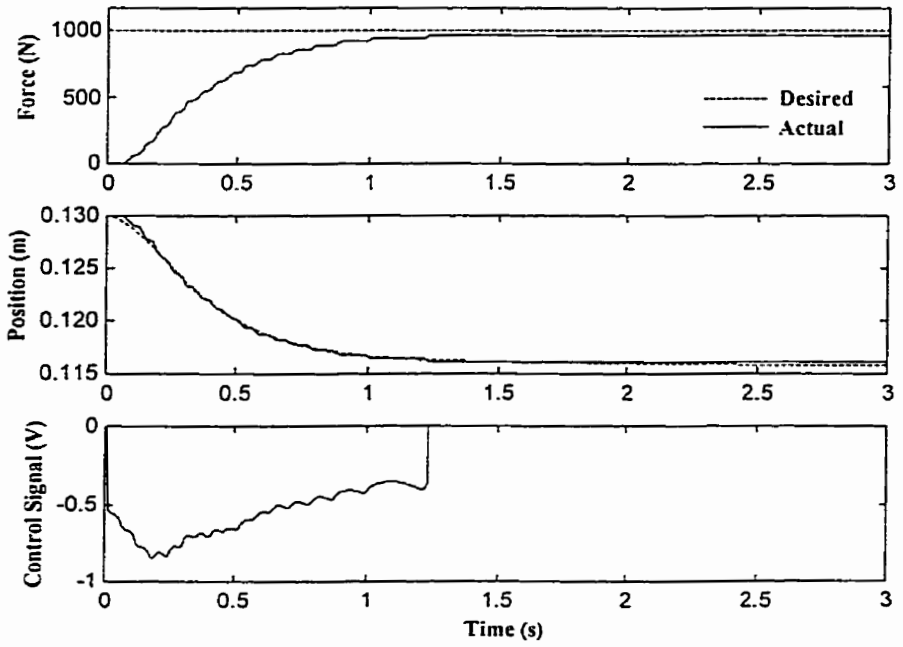

Fig. 5.65. The effect of decreasing integral gain ($\Gamma = 0.1 \times (7 \times 10^{-5})$) on integral-based force control response: simulations

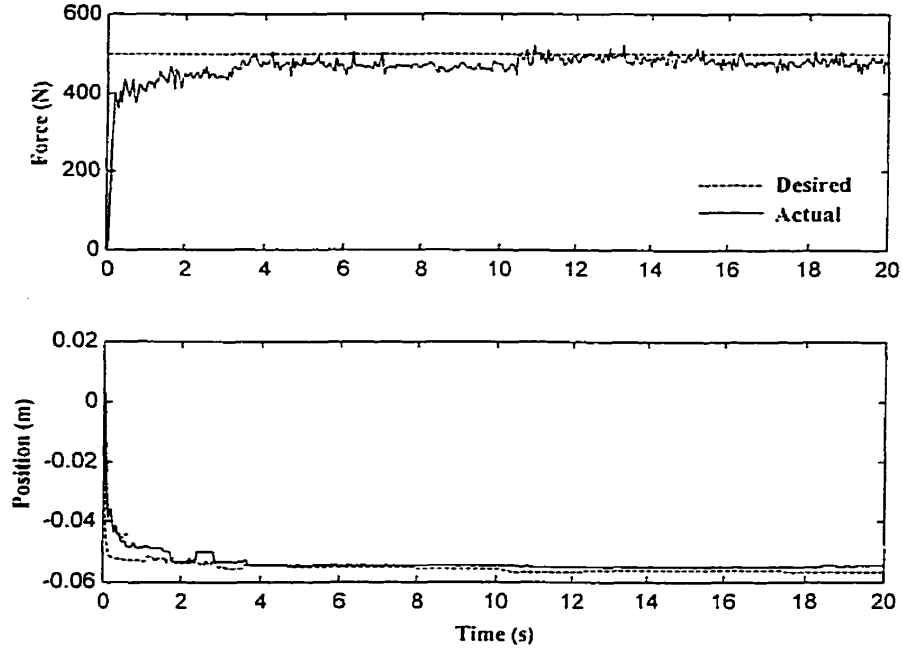

Fig. 5.66. Force control using integral-based position reference modification method for low stiffness environment ($k_e \approx 10000$ N/m): experiment

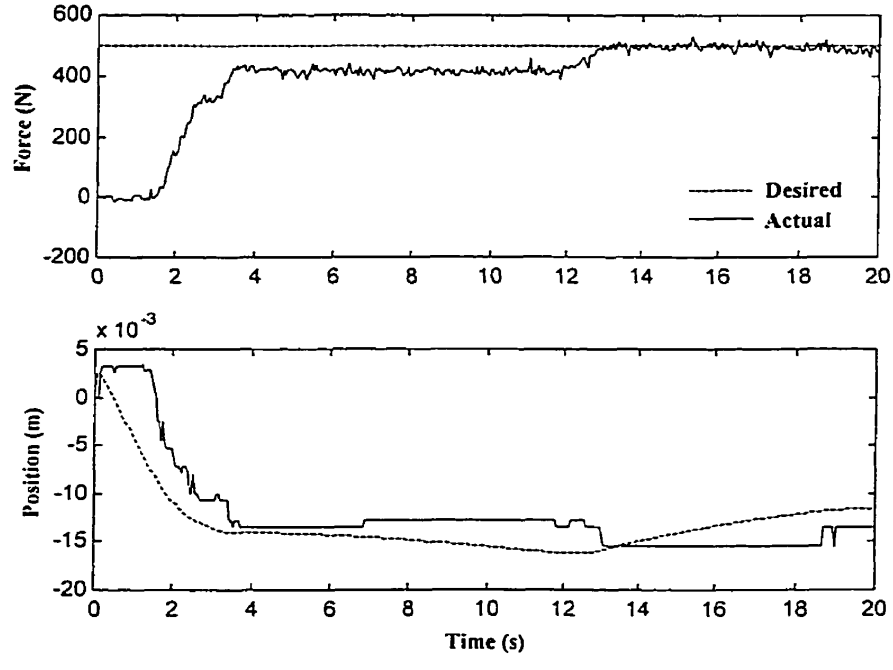

Fig. 5.67. Force control using integral-based position reference modification method for high stiffness environment ($k_e \approx 42000$ N/m): experiment

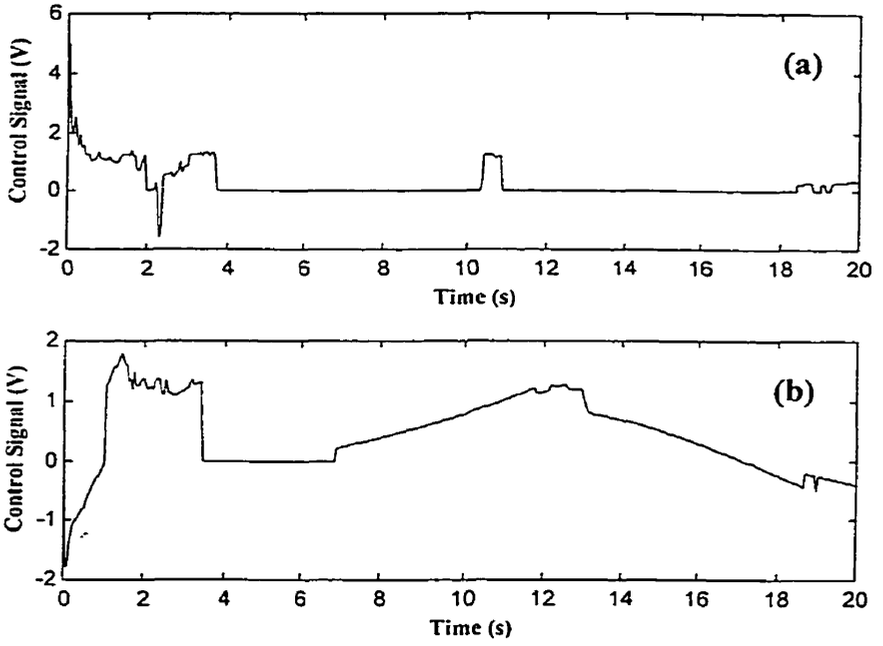

Fig. 5.68. Control signals pertaining to: **(a)** Low stiffness environment (Fig. 5.66) **(b)** High stiffness environment (Fig. 5.67)

5.6.4 Modification to the Integral-Based Method

As was discussed in Section 4.2.4, the rate-varying integral method has shown better performance than the conventional integral method by providing the opportunity to use a much higher integral rate while preventing overshoot significantly. Therefore, this method is incorporated into the integral-based controller introduced earlier with the goal of improving its performance. Recall from (5.67)

$$\Delta x_r = \Gamma \int (f_r - f) dt \tag{5.68}$$

or

$$\Delta x_r = \Delta x_r + \Gamma (f_r - f) \Delta t \tag{5.69}$$

Adding the rate-varying factor leads to

$$\Delta x_r = \frac{\alpha}{\alpha + \dot{x}^2}\left(\Delta x_r + \Gamma(f_r - f)\Delta t\right) \tag{5.70}$$

where $\dot{x}$ is the Cartesian velocity of the end-effector and α is a constant. This simple modification to the integral-based force control method was tested in both simulations and experiments. Typical results are shown in Figs. 5.69 to 5.71. Figure 5.69 illustrates the simulation results of the modified integral on the benchmark test. The controller parameters were $\alpha = 0.08$ and $\Gamma = 7 \times 10^{-4}$, which produced the best response. Figure 5.70 shows the system's response when the end-effector was initially positioned 7cm away from the environment's free surface. Figure 5.71 shows the response when the end-effector was already positioned almost 3cm penetrated into the environment's free surface (contact force is initially 2000N). Finally, Fig. 5.72 compares these three results with those obtained from the original integral-based method. This comparison shows some improvement over the original integral method. However, due to the nonlinearity involved in the modified method and the fact that the integral gain increases during the steady-state, the responses exhibit hunting phenomenon.

Finally, Figs. 5.73 and 5.74 show the experimental results of the rate-varying integral method for controlling a 500N force on low stiffness ($k_e \approx 10000$ N/m) and high stiffness ($k_e \approx 42000$ N/m) environments, respectively. Both results show improvement over the previous controller. Figure 5.75 shows the control signals pertaining to these experimental tests.

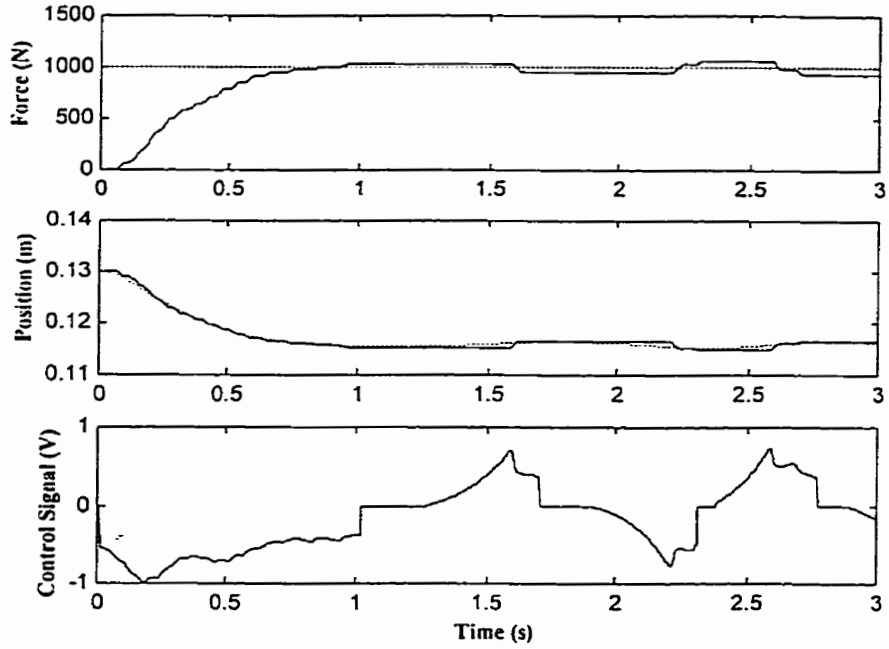

Fig. 5.69. Force control using rate-varying integral-based position reference modification method for benchmark environment ($k_e = 70000$ N/m): simulations

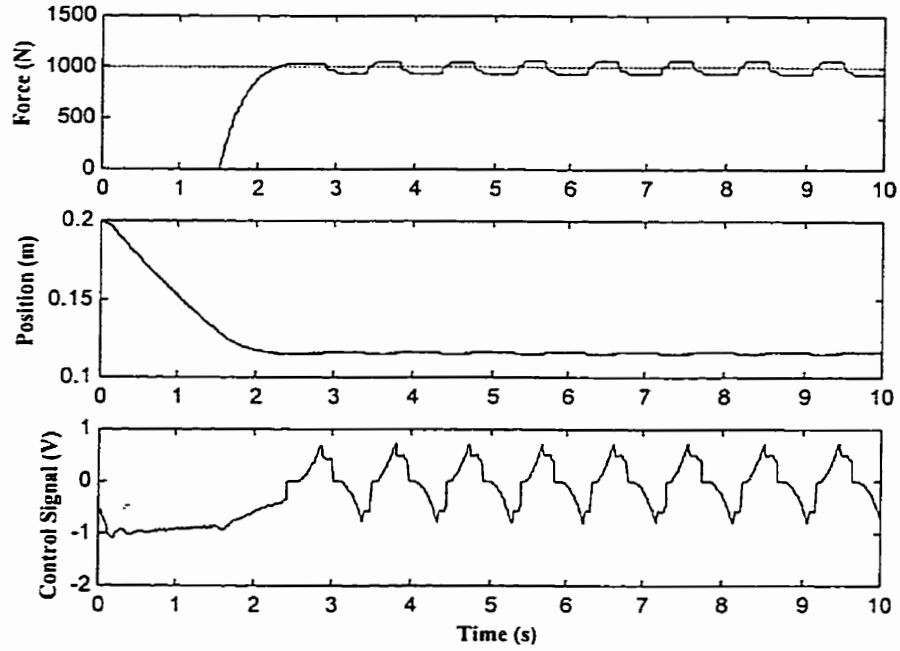

Fig. 5.70. Force control using rate-varying integral-based position reference modification method for benchmark environment (k_e = 70000 N/m) and end-effector initially 7cm away from environment surface: simulations

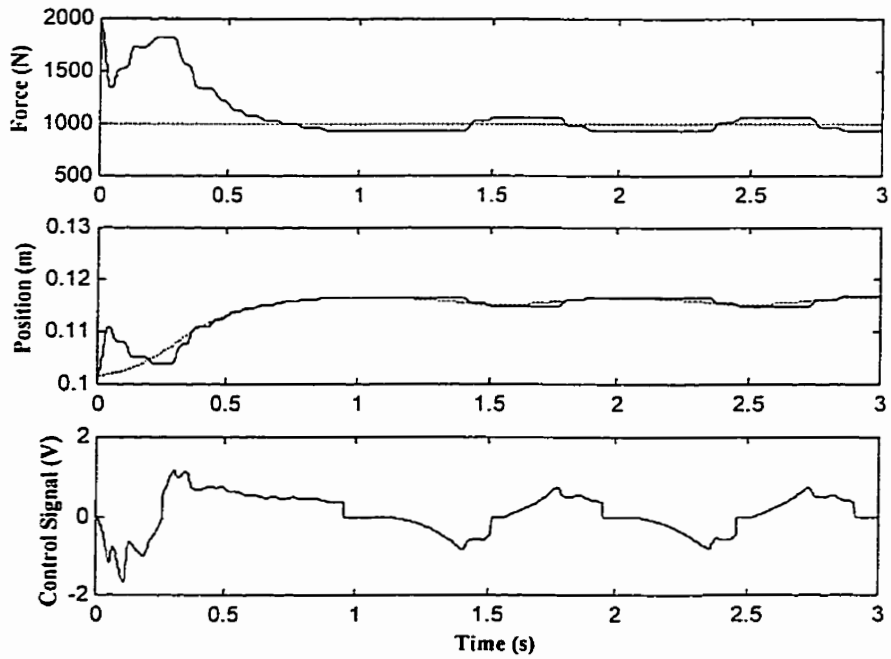

Fig. 5.71. Force control using rate-varying integral-based position reference modification method for benchmark environment (k_e = 70000 N/m) and end-effector initially 3cm into the environment surface: simulations

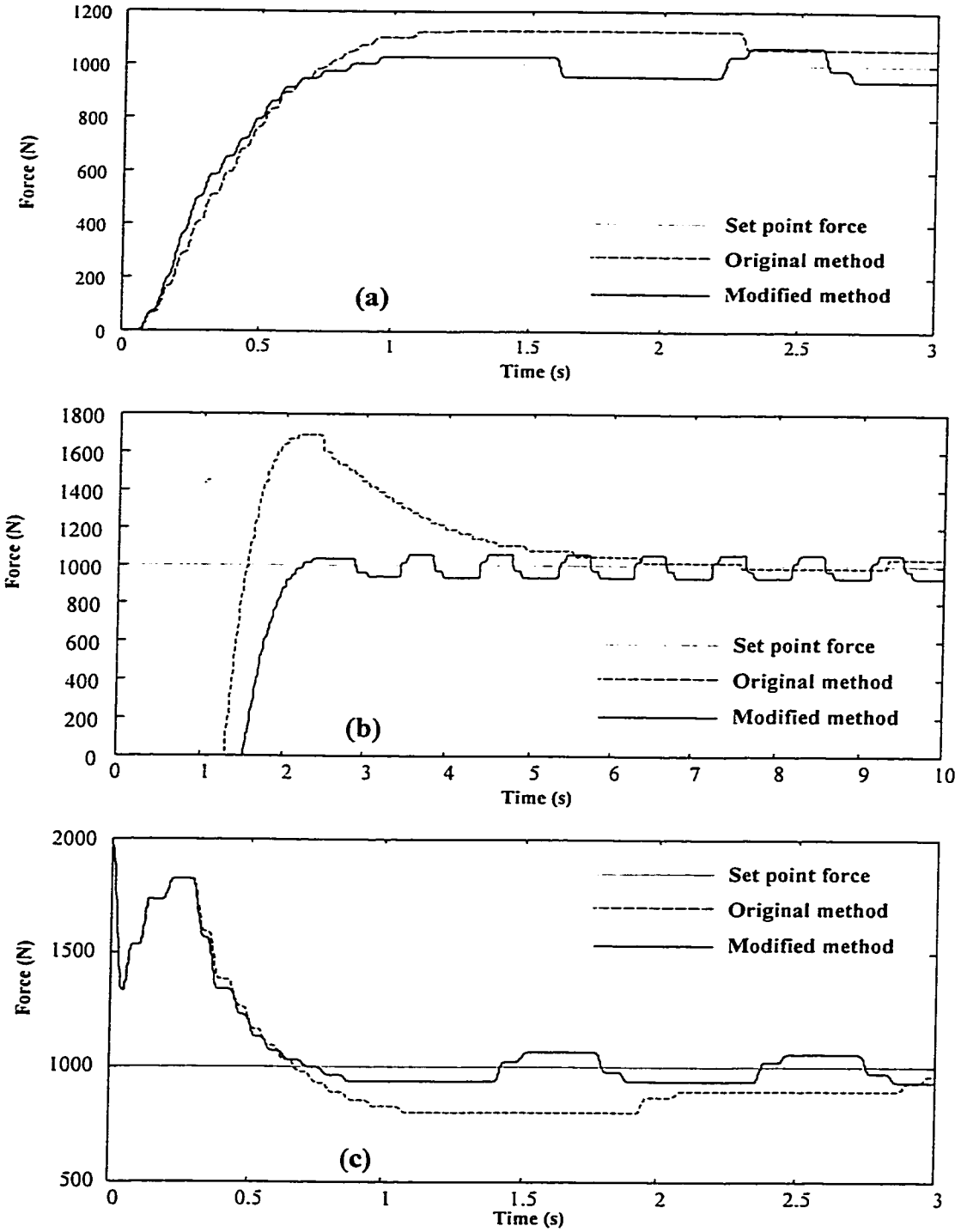

Fig. 5.72. Rate-varying integral and original integral-based position reference modification method for benchmark environment (k_e = 70000 N/m): simulations:
(a) Benchmark test
(b) End-effector initially 7cm away from the environment surface
(c) End-effector initially 3cm into the environment surface

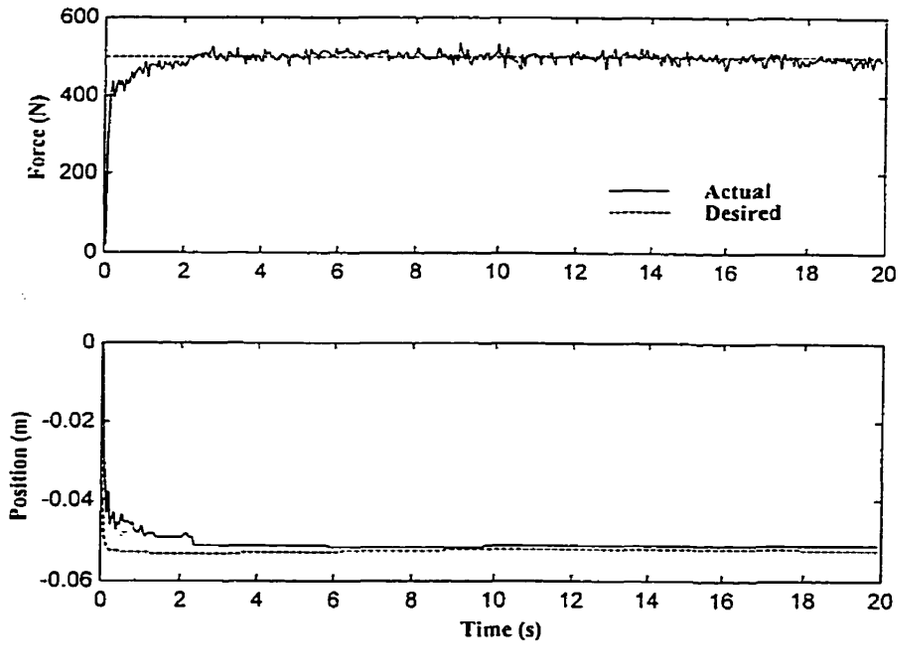

Fig. 5.73. Force control using rate varying integral-based position reference modification method for low stiffness environment ($k_e \approx 10000$ N/m): experiment

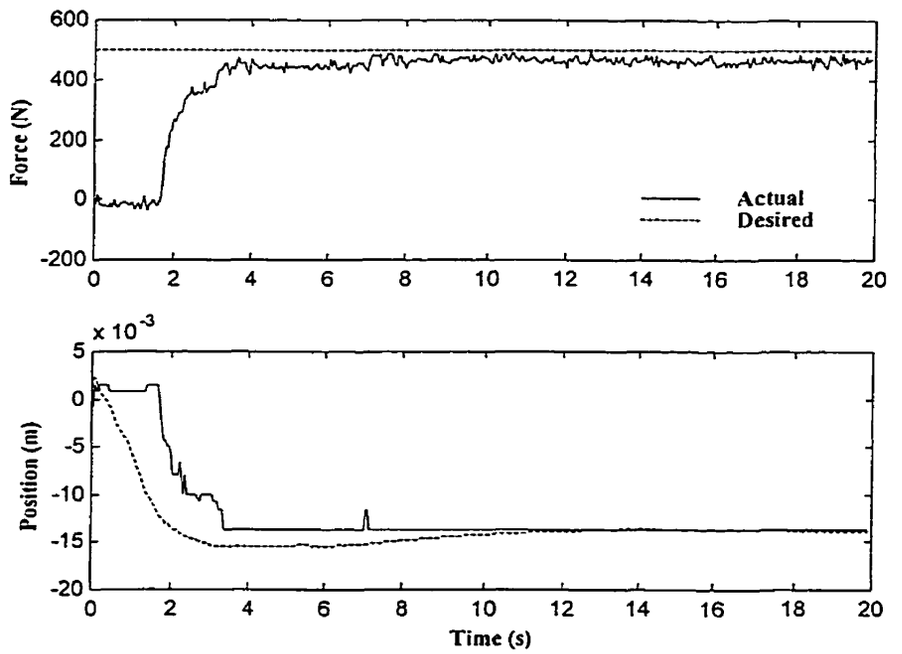

Fig. 5.74. Force control using rate varying integral-based position reference modification method for high stiffness environment ($k_e \approx 42000$ N/m): experiment

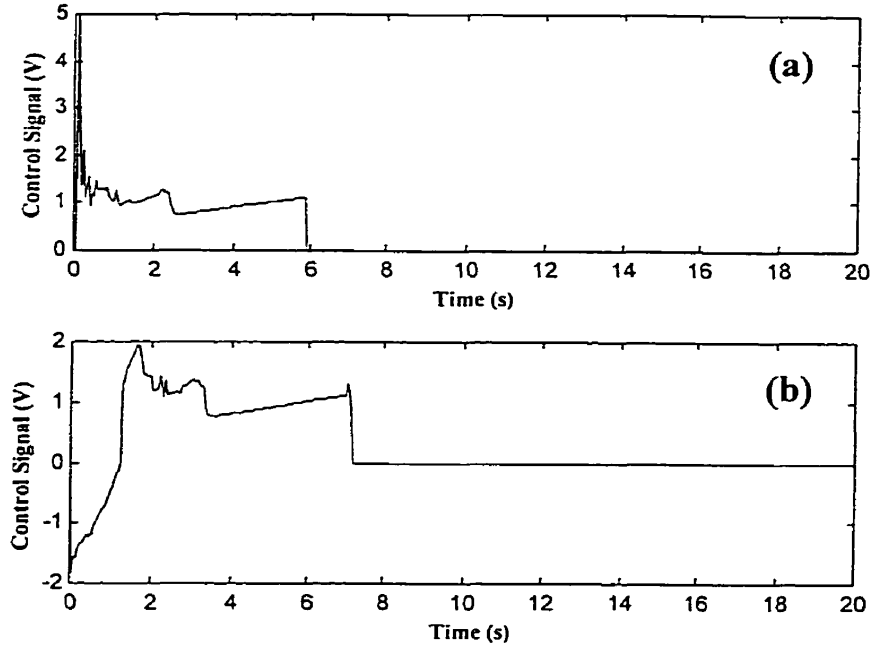

Fig. 5.75. Control signals pertaining to: **(a)** Low stiffness environment (Fig. 5.73) **(b)** High stiffness environment (Fig. 5.74)

5.7 Summary

In this section the drawback of using impedance control to regulate the end-effector force was outlined. It was then shown that if knowledge about the environment's position and stiffness exists, one may use it to adjust the reference trajectory to achieve the desired force tracking/regulation. Existing techniques for force regulation, using the impedance control concept, were adapted and modified as required to improve the force control capability of the PBIC. Comprehensive simulation studies were performed followed by experiments, through formally designed set of tests, aiming at evaluating their capability in force regulation of hydraulic manipulators. In particular, the effect of environmental

stiffness and, to a certain extent, discontinuity at the work-piece contact were studied. These experiments have allowed us to draw some useful conclusions about the performance of all four techniques in the context of a specific task.

The first method was based on the off-line environmental estimation by Lu and Goldenberg (1995). This method was simple and effectively estimated the location and stiffness of various environments through a two-step identification process. However, since it is an off-line method, it cannot work well for cases where the environmental parameters vary during the operation. Furthermore, for stiff environments, large forces are required to generate measurable deformations for reliable identification.

The on-line environmental estimation scheme by Seraji and Colbaugh (1997) was then employed within the context of hydraulic functions to modify the position reference in real-time. This scheme, named the indirect adaptive scheme, with only two controller parameters and two initial estimates of the environmental parameters, was found to be quite simple to apply and produced better performance. However, it did not converge to the actual environmental parameters. Nevertheless, the scheme performed very well in regulating the end-effector force both in low stiffness and in high stiffness environments without adjusting the controller gains.

A variation of the above scheme, named the direct adaptive scheme (Seraji and Colbaugh, 1997), for modifying the position reference was also implemented. The controller contained eleven parameters and was found to be very sensitive to some of the parameters. It was therefore very hard to tune and subsequently produced experimental results no better than its indirect counterpart.

An integral based position-reference modification method was also employed which modifies the position reference by simply adding the integral of the force error to it. This method was simple and produced results with poor transient responses. Further modification to this simple method, using the concept of rate-varying integration, improved the transient responses. However, the final results did not show any improvement over the indirect adaptive scheme.

Chapter 6

Summary and Conclusions

The present study is concerned with the problem of enabling a Unimate MK-II hydraulic manipulator to interact with environments within an impedance control framework. Impedance control was preferred over hybrid control because of its known ability to accommodate stable transition between unconstrained and constrained motions. A position-based formulation of impedance control is best suited to this application because of the difficulty in implementing controlled torques on hydraulic actuators. It was discussed that the quality of a position-based impedance controller highly depends on the tracking and regulating performances of its nested positioner. Three novel nonlinear modifications to a conventional proportional-integral (PI) controller increased its high-frequency low-amplitude tracking capability by an order of magnitude, as applied to the rugged Unimate hydraulic manipulator. The resulting nonlinear PI positioner accurately tracked position trajectories to within seven encoder resolutions (0.2°), and regulated static trajectories to within only two encoder resolution widths (0.05°). Using this positioner, the position-based impedance controller (PBIC) was successfully

implemented. Various tests including trajectory tracking in environments with highly discontinuous admittances were performed. In all these tests, the impedance controller successfully replaced the actual manipulator dynamics with those of the target impedance.

Further study revealed that force regulation within the impedance control framework is difficult because the manipulator/environment contact force can only be controlled indirectly by an appropriate choice of the reference position trajectory. It was also shown that one may use knowledge of the environmental parameters (position and stiffness) to adjust the reference trajectory in order to achieve the desired force. In this study, previously existing techniques for force regulation within the impedance control framework have been adapted and modified in order to improve force control capability of the PBIC in hydraulic manipulators. In modifying the reference position trajectory, two scenarios were examined. In one scenario, the reference position trajectory was updated based on the estimation (obtained via off-line or on-line methods) of the environmental parameters. In the other, the estimation was skipped through direct adjustment of the reference trajectory. The existing techniques for force regulation within the impedance control framework were then compared for their capability to regulate the hydraulic manipulator's force. The test results indicated that the off-line environmental estimation method is simple and effective in estimating the location and stiffness of various environments. However, its application needs to be limited to cases in which the environmental parameters would not change during the operation. The on-line environmental estimation method, also known as the indirect adaptive scheme, with few controller parameters was quite simple to apply. This method, however, failed to

converge to the actual environmental parameters. Nevertheless, the scheme successfully regulated the end-effector force both in low and high stiffness environments. The method of direct adaptive position reference modification contained too many parameters to tune, and appeared to be too sensitive to some of these parameters. Therefore, the method was difficult to tune for its best performance. The integral-based position-reference modification method, like any other conventional integral controller, produced results with poor transient responses. The responses improved somewhat as a result of using the concept of rate-varying integration. However, it did not show any improvement over the indirect adaptive scheme. This justifies the use of advanced control techniques for the force control problem of hydraulic manipulators within the context of PBIC.

One contribution of this thesis is that all force-regulating techniques were, for the first time, implemented on an existing hydraulic robot (both in simulation and in experiment) in similar environments and the results were compared. In particular, the influence resulting from the change in the physical parameters in the model or the controller was independently studied using the simulation program. The simulations also confirmed that the observations made from the experiments truly reflected the nature of the controller, and not some unstructured properties inherent in any real-world industrial system. The simulation program closely resembled the real system. All non-idealities such as nonlinear hydraulic functions, saturation, flow deadband and stick-slip friction were included in the simulation program.

Future work should include studying the effect of hydraulic compliance, valve bandwidth, control saturation and dry friction on each of the aforementioned force tracking approaches. These effects have not been explored, in the context of position-

based impedance control of hydraulic manipulators. Furthermore, the choice of target impedance model/parameters will affect the performance of each approach. The research reported in this thesis, can be continued by first studying the influence of second-order target impedance parameters on the responses. Finally, a target impedance model with fixed gains may perform poorly during the transition from unconstrained to constrained motion; this aspect can also be investigated.

REFERENCES

Anderson, R.J., and Spong, M.W., 1987, "Hybrid Impedance Control of Robotic Manipulators", *Proc. IEEE Int. Conf. on Robotics and Automation*, pp. 1073-1080.

Aström, K.J., and Hägglund, T., 1994, *Automatic Tuning of PID Controllers*, Instrument Society of America, Research Triangle Park, NC.

Bohn, C., and Atherton, D.P., April 1995, "An Analysis Package Comparing PID Anti-Windup Strategies", *IEEEE Control Systems*, Vol. 15, pp. 34-40.

Brambilla, A., Scali, C., and Chen, S., 1989, "Tuning of Conventional Controllers for Robust Performance", *Proc. IFAC Symposium in Low Cost Automation*, Milan, Italy, pp. 123-128.

Chan, S.P., Yao, B., Gao, W.B., and Cheng,M., 1991, "Robust Impedance Control of Robot Manipulators", *Int. Journal of Robotics and Automation*, Vol. 6, No. 4, pp. 220-227.

Chen, Y.N., Lee C.B., and Tseng C.H., 1990, "A Variable Structure Controller Design for an Electro-Hydraulic Force Control Servo System", *Journal of the Chinese Society of Mechanical Engineers*, Vol. 11, No. 6, pp. 520-526.

Cohen, M., and Flash, T., 1991, "Learning Impedance Parameters for Robot Control Using an Associative Search Network", *IEEE Trans. on Robotics and Automation*, Vol. 7, No. 3, pp. 382-389.

Colbaugh, R., Seraji, H. and Glass, K., 1993, "Direct Adaptive Impedance Control of Robot Manipulators", *Journal of Robotics Systems*, Vol. 10, No. 2, 217-248.

Colgate, J.E., and Hogan, N., July 1988, "Robust Control of Dynamically Interacting Systems", *Int. Journal of Control*, Vol. 48, No. 1, pp. 65-88.

Conrad, F., and Jensen, C.J.D., 1987, "Design of Hydraulic Force Control Systems with State Estimate Feedback", *Proc. IFAC 10th Triennial World Congress*, Munich, FRG, pp. 307-312.

Dawson, D.M., Lewis, F.L., and Dorsey, J.F., August 1992, "Robust Force Control of a Robot Manipulator", *The Int. Journal of Robotics Research*, Vol. 11, No. 4, pp. 312-319.

D'Souza, A. F., 1988, *Design of Control Systems*, Prentice-Hall, New Jersey, p. 240.

Eitelberg, E., 1987, "A Regulating and Tracking PI(D) Controller", *Int. Journal of Control*, Vol. 45, pp. 91-95.

Eppinger, S.D., and Seering, W.P., 1987, "Understanding Bandwidth Limitations in Robot Force Control", *Proc. IEEE Conf. on Robotics and Automation*, pp. 904-909.

Field, G., and Stepanenko, Y., 1993, "Model Reference Impedance Control of Robotic Manipulators", *Proc. IEEE Pacific Rim Conference*, pp. 614-617.

Goldenberg, A.A., 1988, "Implementation of Force and Impedance Control in Robot Manipulators", *Proc. IEEE Conf. on Robotics and Automation*, pp. 1626-1632.

Heinrichs, B., Khayyat, A.A., Sepehri, N., and Thornton-Trump, A.B., 1996, "A Nonlinear PI Controller for Accurate Positioning with Application to Impedance Control", *Proc. World Automation Congress (WAC 96)*, Montpellier, France, pp. 293-300.

Hogan, N., March 1985, "Impedance Control: An Approach to Manipulation Parts I, II and III", *ASME Journal of Dynamic Systems, Measurement, and Control*, Vol. 107, pp. 1-24.

Hogan, N., 1987, "Stable Execution of Contact Tasks using Impedance Control", *Proc. IEEE Conf. on Robotics and Automation* , pp. 1047-1054.

Hogan, N., December 1988, "On the Stability of Manipulators Performing Contact Tasks", *IEEE Journal of Robotics and Automation*, Vol. 4, No. 6, pp. 677-686.

Ishikawa, H., Sawada, C., Kawasa, K., and Takata, M., May 1989, "Stable Compliance Control and Its Implementation for a 6 DOF Manipulator", *Proc. IEEE Int. Conf. on Robotics and Automation*, Scottsdale, Arizona USA, pp. 98-103.

Johansson, R., and Spong, M.W., 1994, "Quadratic Optimization of Impedance Control", *Proc. IEEE Conf. on Robotics and Automation*, pp. 616-621.

Kazerooni, H., 1985, "A Robust Design Method for Impedance Control of Constrained Dynamics Systems", *Ph.D. thesis, Massachusetts Institute of Technology, Department of Mechanical Engineering.*

Kazerooni, H., Sheridan,T.B., and Houpt, P.K., 1986, "Robust Compliant Motion for Manipulators, parts I and II - The Fundamental Concepts of Compliant Motion", *IEEE Journal of Robotics and Automation*, Vol. 2, No. 2, pp. 83-105.

Khatib, O., and Burdick, J., 1986, "Motion and Force Control of Robot Manipulators", *Proc. IEEE Int. Conf. on Robotics and Automation*, Los Alamitos, CA: IEEE Computer Society Press, pp. 1381-1386.

Khayyat, A.A., Heinrichs, B., and Sepehri, N., 1996, "A Modified Rate-Varying Integral Controller", *Int. Journal of Mechatronics*, Vol. 6, No. 3, pp. 367-376.

Lasky, T.A., and Hsia, T.C., April 1991, "On Force-Tracking Impedance Control of Robot Manipulators", *Proc. IEEE Conf. on Robotics and Automation*, Los Alamitos, CA: IEEE Computer Society Press, pp. 274-280.

Lawrence, D.A., and Stoughton, R.M., 1987, "Position-Based Impedance Control: Achieving Stability in Practice", *Proc. AIAA Guidance Navigation Control Conf.*, pp. 221-226.

Liu, R., and Alleyne, A., March 2000, "Nonlinear Force/Pressure Tracking of an Electro-Hydraulic Actuator", *ASME Journal of Dynamic Systems, Measurement, and Control*, Vol. 122, pp. 232-237.

Lu, W.S., and Meng, Q.H., June 1991, "Impedance Control with Adaptation for Robotics Manipulations", *IEEE Trans. on Robotics and Automation*, Vol. 7, No. 3, pp. 408-415.

Lu, Z., and Goldenberg, A., June 1995, "Robust Impedance Control and Force Regulation: Theory and Experiments", *Int. Journal of Robotics Research*, Vol. 14, No. 3, pp. 225-254.

McCormic, W., and Schwartz, H.M., October 1993, "An Investigation of Impedance Control for Robot Manipulators", *Int. Journal of Robotics Research*, Vol. 12, No. 5, pp. 473-489.

Merrit, H.E., 1967, *Hydraulic Control Systems*, John Wiley & Sons, New York.

Morse, R.A., Day, C.P., Troy, K., and Stoddard, K.A., Feb. 23, 1988, "Position Control Method and System Utilizing Same", United States Patent Number 4727303.

Nakashima, M., Yakabe, H., Maruyama, Y., Yano, K., Morita, K., and Nakagaki, H., 1995, "Application of Semi-Automatic Robot Technology on Hot-Line Maintenance Work", *Proc. IEEE Int. Conf. on Robotics and Automation*, pp. 843-850.

Narendra, K., and Annaswamy, A., 1989, *Stable Adaptive Systems*, Englewood Cliffs, NJ: Prentice-Hall.

Pelletier, M., and Daneshmend, L., 1990, "An Adaptive Compliant Motion Controller for Robot Manipulators Based on Damping Control", *Proc. IEEE Int. Conf. on Robotics and Automation*, Los Alamitos, CA: IEEE Computer Society Press, pp. 78-83.

Pelletier, M., and Doyon, M., 1994, "On the Implementation and Performance of Impedance Control on Position Controlled Robots", *Proc. IEEE Conf. on Robotics and Automation*, pp. 1228-1233.

Raibert, M.H., and Craig J.J., June 1981, "Hybrid Position/Force Control of Manipulators", *ASME Journal of Dynamic Systems, Measurement, and Control*, Vol. 102, pp. 126-133.

Salisbury, J.K., December 1980, "Active Stiffness Control of a Manipulator in Cartesian Coordinates", *Proc. 19th IEEE Conf. on Decision and Control*, pp. 95-100.

Sepehri, N., Heinrichs, B., and Khayyat, A.A., September 1997, "Nonlinear Proportional-Integral Controller", United States Patent Number 5721477.

Sepehri, N., Khayyat, A.A., and Heinrichs, B., 1997, "Development of a Nonlinear PI Controller for Accurate Positioning of an Industrial Hydraulic Manipulator", *Int. Journal of Mechatronics*, Vol. 7, No. 8, pp. 683-700.

Seraji, H., April 1989, "Decentralized Adaptive Control of Manipulators: Theory, Simulation, and Experimentation", *IEEE Trans. On Robotics and Automation*, Vol. 5, No. 2, pp. 183-201.

Seraji, H., and Colbaugh, R., February 1997, "Force Tracking in Impedance Control", *Int. Journal of Robotics Research*, Vol. 16, No. 1, pp. 97-117.

Tsai, C.K., and Orin, D.E., July 1986, "Modified Hybrid Control for an Electro-Hydraulic Robot Leg", *Proc. ASME Int. Computers in Engineering Conf. and Exhibition*, Vol. 1, pp. 95-100.

Volp, R., and Khosla, P., August 1993, "A Theoretical and Experimental Investigation of Impact Control for Manipulators", *Int. Journal of Robotics Research*, Vol. 12, No. 4, pp. 351-365.

Volp, R., and Khosla, P., June 1994, "Analysis and Experimental Verification of a Fourth Order Plant Model for Manipulator Force Control", *IEEE Robotics and Automation Magazine*, pp. 4-13.

Whitney, D.E., June 1977, "Force Feedback Control of Manipulator Fine Motions", *ASME Journal of Dynamic Systems, Measurement, and Control*, Vol. 102, pp. 91-97.

Ziaei, K., Sepehri, N., and Khayyat, A.A., 1997, "Hardware Implementation and Evaluation of Environmental Effect in Force Control of Hydraulic Manipulators", *Proc. 16th Canadian Congress of Applied Mechanics (CANCAM 97)*, Quebec, Canada, pp. 509-510.

Appendix

Inertial Terms D_i , D_{ij} and D_{ijk} for the Unimate MK-II Hydraulic Manipulator

This appendix summarizes the inertial terms D_i , D_{ij} and D_{ijk} that appear in the manipulator dynamics for the Unimate MKII 2000.

The dynamics of the manipulator is defined by equations (3.11):

$$\tau_i = \sum_{j=1}^{3} D_{ij}\ddot{\theta}_j + I_{a_i}\ddot{\theta}_i + \sum_{j=1}^{3}\sum_{k=1}^{3} D_{ijk}\dot{\theta}_j\dot{\theta}_k + D_i + (\boldsymbol{J}^T F)_i \tag{3.11}$$

where the last term, $\boldsymbol{J}^T F$, is the effect of end-point forces on joint torques/forces and the inertial terms are given by Eq. 3.12:

$$\begin{cases} D_{ij} = \sum\limits_{p=\max(i,j)}^{3} Trace\left(\dfrac{\partial \boldsymbol{T}_p}{\partial \theta_j}\boldsymbol{J}_p\dfrac{\partial \boldsymbol{T}_p^T}{\partial \theta_i}\right) \\ D_{ijk} = \sum\limits_{p=\max(i,j,k)}^{3} Trace\left(\dfrac{\partial^2 \boldsymbol{T}_p}{\partial \theta_j \partial \theta_k}\boldsymbol{J}_p\dfrac{\partial \boldsymbol{T}_p^T}{\partial \theta_i}\right) \\ D_i = \sum\limits_{p=i}^{3} -m_p\, \boldsymbol{g}^T \dfrac{\partial \boldsymbol{T}_p}{\partial \theta_i}\, {}^p\bar{\mathbf{r}}_p \end{cases} \tag{3.12}$$

where $\boldsymbol{J}_p = \begin{bmatrix} \dfrac{-I_{xx_p} + I_{yy_p} + I_{zz_p}}{2} & I_{xy_p} & I_{xz_p} & m_p\bar{x}_p \\ I_{xy_p} & \dfrac{I_{xx_p} - I_{yy_p} + I_{zz_p}}{2} & I_{yz_p} & m_p\bar{y}_p \\ I_{xz_p} & I_{yz_p} & \dfrac{I_{xx_p} + I_{yy_p} - I_{zz_p}}{2} & m_p\bar{z}_p \\ m_p\bar{x}_p & m_p\bar{y}_p & m_p\bar{z}_p & m_p \end{bmatrix}$ (3.13)

τ_i is the joint torque/force at joint i, I_{a_i} is the joint/link i actuator inertia, $\boldsymbol{J}_p$ is the pseudo inertia matrix of link p, $\boldsymbol{g} = [g_x \quad g_y \quad g_z \quad o]^T$ is the gravitational acceleration vector in the base coordinate system and ${}^p\bar{\mathbf{r}}_p = [\bar{x}_p \quad \bar{y}_p \quad \bar{z}_p \quad 0]^T$ is the coordinates of the center of gravity of link p with respect to the same link coordinate system.

Terms $\boldsymbol{D_{ii}}$ represent the effective inertia at joint $\boldsymbol{i}$ and terms $\boldsymbol{D_{ij}}$ $(i \neq j)$ represent the coupling inertia between joints $\boldsymbol{i}$ and $\boldsymbol{j}$.

$$
\begin{aligned}
D_{11} = {} & I_{a_1} + \frac{I_{xx_2} + I_{xx_3}}{2} + I_{yy_1} + \frac{I_{zz_2} + I_{zz_3}}{2} \\
& - \bar{x}_2 a_2 m_2 - \bar{x}_3 a_2 m_3 + \frac{a_2^2 (m_2 + m_3)}{2} + \bar{z}_3 d_3 m_3 + \frac{d_3^2 m_3}{2} \\
& + d_2^2 (m_2 + m_3) + 2 d_2 (\bar{y}_2 m_2 + \bar{y}_3 m_3) \\
& + \left[I_{xx_2} + I_{xx_3} - I_{zz_2} - I_{zz_3} \right] \frac{\cos(2\theta_2)}{2} \\
& - \left[a_2^2 m_2 + a_2^2 m_3 - d_3^2 m_3 \right] \frac{\cos(2\theta_2)}{2} \\
& + \left[\bar{x}_2 a_2 m_2 + \bar{x}_3 a_2 m_3 + \bar{z}_3 d_3 m_3 \right] \cos(2\theta_2) \\
& - \left[I_{xz_2} + I_{xz_3} - \bar{z}_2 a_2 m_2 - \bar{z}_3 a_2 m_3 + \bar{x}_3 d_3 m_3 - a_2 d_3 m_3 \right] \sin(2\theta_2)
\end{aligned}
$$

$$
\begin{aligned}
D_{12} = D_{21} = {} & \left[I_{xy_2} + I_{xy_3} - \bar{y}_2 a_2 m_2 - \bar{y}_3 a_2 m_3 \right] \cos(\theta_2) \\
& + \left[I_{yz_2} + I_{yz_3} + \bar{y}_3 d_3 m_3 \right] \sin(\theta_2) \\
& + \left[\bar{x}_2 d_2 m_2 - a_2 d_2 m_2 + \bar{x}_3 d_2 m_3 - a_2 d_2 m_3 \right] \cos(\theta_2) \\
& + \left[\bar{z}_2 d_2 m_2 + \bar{z}_3 d_2 m_3 + d_2 d_3 m_3 \right] \sin(\theta_2)
\end{aligned}
$$

$$D_{13} = D_{31} = -(\bar{y}_3 + d_2) m_3 \cos(\theta_2)$$

$$D_{22} = I_{a_2} + I_{yy_2} + I_{yy_3} + a_2^2 m_2 + a_2^2 m_3 + d_3^2 m_3 - 2\bar{x}_2 a_2 m_2 - 2\bar{x}_3 a_2 m_3 + 2\bar{z}_3 d_3 m_3$$

$$D_{23} = D_{32} = (a_2 - \bar{x}_3) m_3$$

$$D_{33} = I_{a_3} + m_3$$

Terms D_{ijj} represent the centripetal forces at joint i due to velocity at joint j and terms D_{ijk} ($j \neq k$) represent the Coriolis forces at joint i due to velocities at joints j and k.

$$D_{111} = 0$$

$$D_{112} = D_{121} = -\left[I_{xx_2} + I_{xx_3} - \bar{z}_2 a_2 m_2 - \bar{z}_3 a_2 m_3 + \bar{x}_3 d_3 m_3 - a_2 d_3 m_3\right]\cos(2\theta_2) - \left[I_{yy_2} + I_{yy_3} - I_{zz_2} - I_{zz_3} - a_2^2 m_2 - a_2^2 m_3 + d_3^2 m_3\right]\frac{\sin(2\theta_2)}{2} - \left[\bar{x}_2 a_2 m_2 + \bar{x}_3 a_2 m_3 + \bar{z}_3 d_3 m_3\right]\sin(2\theta_2)$$

$$D_{113} = D_{131} = m_3\left[(d_3 + \bar{z}_3)\cos(\theta_2) + (a_2 - \bar{x}_3)\sin(\theta_2)\right]\cos(\theta_2)$$

$$D_{122} = \left[I_{yz_2} + I_{yz_3} + \bar{y}_3 d_3 m_3\right]\cos(\theta_2) - \left[I_{xy_2} + I_{xy_3} - \bar{y}_2 a_2 m_2 - \bar{y}_3 a_2 m_3\right]\sin(\theta_2) + d_2\left[\bar{z}_2 m_2 + \bar{z}_3 m_3 + d_3 m_3\right]\cos(\theta_2) - d_2\left[\bar{x}_2 m_2 - a_2 m_2 + \bar{x}_3 m_3 - a_2 m_3\right]\sin(\theta_2)$$

$$D_{123} = D_{132} = (\bar{y}_3 + d_2) m_3 \sin(\theta_2)$$

$$D_{133} = 0$$

$$D_{211} = \left[I_{xx_2} + I_{xx_3} - \bar{z}_2 a_2 m_2 - \bar{z}_3 a_2 m_3 + \bar{x}_3 d_3 m_3 - a_2 d_3 m_3\right]\cos(2\theta_2) + \left[I_{yy_2} + I_{yy_3} - I_{zz_2} - I_{zz_3} - a_2^2 m_2 - a_2^2 m_3 + d_3^2 m_3\right]\frac{\sin(2\theta_2)}{2} + \left[\bar{x}_2 a_2 m_2 + \bar{x}_3 a_2 m_3 + \bar{z}_3 d_3 m_3\right]\sin(2\theta_2)$$

$$D_{212} = D_{221} = 0$$

$$D_{213} = D_{231} = 0$$

$$D_{222} = 0$$

$$D_{223} = D_{232} = m_3(d_3 + \bar{z}_3)$$

$$D_{233} = 0$$

$$D_{311} = -m_3\left[(d_3 + \bar{z}_3)\cos(\theta_2) + (a_2 - \bar{x}_3)\sin(\theta_2)\right]\cos(\theta_2)$$

$$D_{312} = D_{321} = 0$$

$$D_{313} = D_{331} = 0$$

$$D_{322} = -m_3(d_3 + \bar{z}_3)$$

$$D_{323} = D_{332} = 0$$

$$D_{333} = 0$$

Terms $\boldsymbol{D_i}$ represent the gravity loading at joint $\boldsymbol{i}$.

$$D_1 = 0$$

$$D_2 = -gm_2\left[\bar{z}_2\cos(\theta_2) - \bar{x}_2\sin(\theta_2) + a_2\sin(\theta_2)\right] - gm_3\left[\bar{z}_3\cos(\theta_2) + d_3\cos(\theta_2) - \bar{x}_3\sin(\theta_2) + a_2\sin(\theta_2)\right]$$

$$D_3 = -gm_3\sin(\theta_2)$$